Optimization, stabilization and optical phase control of a high-repetition rate laser-wakefield accelerator

Lucas Rovige

To cite this version:

Lucas Rovige. Optimization, stabilization and optical phase control of a high-repetition rate laser-wakefield accelerator. Optics [physics.optics]. Institut Polytechnique de Paris, 2022. English. NNT : 2022IPPAE011 . tel-04329734

HAL Id: tel-04329734

https://theses.hal.science/tel-04329734v1

Submitted on 7 Dec 2023

INSTITUT
POLYTECHNIQUE
DE PARIS

NNT : 2022IPPAE011

Thèse de doctorat

Optimization, stabilization and optical phase control of a high-repetition rate laser-wakefield accelerator

Thèse de doctorat de l'Institut Polytechnique de Paris
préparée au Laboratoire d'Optique Appliquée

École doctorale n°626 École doctorale de l'Institut Polytechnique de Paris (EDIPP)
Spécialité de doctorat : Physique

Thèse présentée et soutenue à Palaiseau, le 18 Novembre 2022, par

LUCAS ROVIGE

Composition du Jury :

Julien Fuchs Directeur de Recherche, CNRS (LULI)	Président
Sophie Kazamias Professeure, Université Paris-Saclay (IJC Lab)	Rapporteur
Philippe Balcou Directeur de Recherche, CNRS (CELIA)	Rapporteur
Xavier Davoine Chercheur, CEA	Examinateur
Victor Malka Professeur, Weizmann Institute of Science	Examinateur
Olle Lundh Professeur, Lund University	Examinateur
Jérôme Faure Directeur de recherche, CNRS (LOA)	Directeur de thèse

Remerciements

Cette thèse conclut trois heureuses années de recherche, d'expériences et de travail d'équipe au sein du Laboratoire d'Optique Appliquée, et je tiens à remercier tous ceux qui, au labo ou en dehors, ont rendu cela possible.

Tout d'abord, merci à mon directeur de thèse, Jérôme Faure, qui a su me guider dans mon travail, toujours avec pédagogie et bienveillance, tout en m'accordant suffisamment d'indépendance et de confiance au fil du temps. J'ai beaucoup appris à tes côtés, et je t'en suis extrêmement reconnaissant.

Merci à Aline Vernier, grâce à qui j'ai tant appris sur l'expérience ! Ta patience, ta bonne humeur et tes jeux de mots inimitables ont rendu bien moins effrayant mes premiers pas en salle de manip. Merci également à mon compère Julius Huijts, qui a été présent pendant mes trois années de thèse et avec qui j'ai eu le plaisir de réaliser la plupart des expériences de ce manuscrit. Ton entrain et ta sympathie quotidienne ont rendu toutes ces heures en salle Orange et en salle de contrôle à la fois joyeuses et fructueuses ! J'espère que tu perpétueras les expressions et mots inventées que je t'ai appris. Je tiens également à remercier Igor Andriyash pour toute l'aide apporté sur les études numériques, et tes explications détaillées sur les rouages des codes PIC. Merci également à Joséphine Monzac et ses facéties, arrivée un peu plus tard pour prendre la relève, qui je n'en doute pas, est assurée ! Je remercie aussi Slava Smartsev, arrivé vers la fin de ma thèse, pour les nombreuses pauses cafés et thé (tea time !) que l'on a instauré avec toi.

Toute l'équipe de PCO a également été partie prenante de ma thèse et de la vie quotidienne au LOA, et je les remercie pour ça. Merci Rodrigo pour le super laser de la Salle Noire, et pour des discussions toujours animées. Thank you also to the laser wizards, Marie, Jaismeen, Zhao and Antoine, for all the patient help you have provided during our (many) struggles, and for the huge work you achieved on the laser system that made possible the results presented here. Merci également à Louis et Stefan de m'avoir accueilli dans la très sélect confrérie du café de PCO, et merci au café, sans qui rien de tout cela n'aurait été possible.

Je remercie également ceux qui étaient déjà là quand je suis arrivé, et qui m'ont accueilli à bras ouverts, Neil, Isabel et Jb. C'était très triste de vous voir partir une petite année seulement après mon arrivée. Merci également à Alessandro, Marco, Émilie et Rachel avec qui j'ai eu l'occasion de travailler lors de l'expérience de radiobiologie, pour votre énergie et le plaisir que j'ai eu à découvrir ce domaine grâce à vous.

Merci à tous ceux qui m'ont aidé et que j'ai côtoyé avec plaisir pendant cette thèse, Cédric, Kim, Julien, François, Davide, et envers notre directeur Stéphane et ses inarrêtable projets de constructions. Merci au service technique, Seb, Thomas, Adam, Bernard, Maxence et Mouhcine, et également à notre équipe administrative de choc, Catherine, Sandrine, Patricia et Magali, pour votre aide toujours teinté de bienveillance. Merci également à toute l'équipe des jeunes et fringants : Adeline, Pablo, Kosta, Ginevra, Pierre, Dan et ceux arrivés plus tard, que j'aurais aimé avoir rencontré plus tôt : Thomas et Juliette mes compagnons canadairs, Ronan, Aimé, Amélie, Lorenzo et Camilla.

Je suis reconnaissant envers les membres de mon jury : les rapporteurs Sophie Kazamias et Philippe Balcou, qui ont lu avec attention mon manuscrit, le président Julien Fuchs, et les examinateurs Xavier Davoine, Victor Malka et Olle Lundh. Merci pour tous vos commentaires et nos discussions intéressantes lors de la soutenance.

Je tiens également à remercier tous mes amis qui ont participés à rendre ces trois années fantastiques. D'abord, merci à Bayane pour tous ces trajets de retour du labo, tantôts euphoriques, tantôts moroses, à la faveur de nos résultats, et pour ces ballades confinées qui m'ont épargné la démence. Ton soutien quotidien à tant compté. Merci également à tous les autres copains de PPF, Albertine, Victor, Olivier, Jonas, Antonin et Flo (PPF de cœur) pour ces soirées au Hall of Beer à partager nos galères. Et bien sûr, merci à toute la famille de supop' : Perrine, Elo, Matal, JB, Cerise, Raph, Flex, Titi, Célia, Anouk, Jerem, Alice, Tutu, Magui. Vous êtes des amis incroyables et vous avez illuminés mes week-ends et vacances ! Merci à ceux qui sont là depuis le Lycée, Alban et Barry, et puis Cédric, depuis la maternelle.

Et enfin, merci à ma famille, mes parents et mes sœurs Jeanne et Marou, pour tout ce que vous m'avez apporté depuis 26 ans, et pour votre soutien et confiance indéfectibles. C'est grâce à vous si j'en suis là aujourd'hui.

Merci.

Résumé en Français

L'accélération par sillage laser dans un plasma (LWFA) est une technique qui permet d'accélérer des particules, et en particulier des électrons, à des vitesses relativistes en utilisant les très forts champs électriques associés à l'onde plasma générée dans le sillage d'une impulsion laser ultra-courte (fs) et très intense ($I > 1 \times 10^{18}\,\mathrm{W\,cm^{-2}}$). Les champs accélérateurs ainsi produits peuvent atteindre plus de 100 GV/m, soit trois ordres de grandeur supérieurs aux champs réalisables avec des accélérateurs conventionnels utilisant des cavités radiofréquence. Cela permet ainsi de réaliser des accélérateurs extrêmement compacts. Les expériences d'accélération laser-plasma utilisent typiquement des lasers de 100 térawatts à pétawatts avec plusieurs joules d'énergie par impulsion et une durée d'impulsion de 30 fs, pour accélérer des faisceaux d'électrons à plusieurs GeV, qui peuvent être utilisés par exemple pour générer des sources secondaires de rayons X femtosecondes. Mais ces systèmes laser à haute énergie ne fonctionnent qu'à un taux de répétition compris entre 0,1 et 10 Hz, ce qui limite considérablement le nombre d'expériences d'applications qu'un accélérateur laser-plasma serait en mesure de réaliser. Il est donc fondamental d'augmenter le taux de répétition des accélérateurs laser-plasma pour en faire une technologie compétitive pouvant être utilisée pour des expériences d'application.

Cette thèse de doctorat présente le travail expérimental sur le développement d'un accélérateur par sillage laser dans un plasma à haute taux de répétition (kHz) réalisé avec des impulsions d'énergie de quelques millijoules et une durée extrêmement courte de 3,5 fs (1,3 cycle optique). Ce nouveau régime d'interaction permet l'accélération de faisceaux d'électrons à une énergie de l'ordre du MeV sur une échelle micrométrique, avec une charge typique de quelques pC par tir, qui pourraient être utilisés dans des expériences de diffraction d'électrons ou pour l'irradiation d'échantillons biologiques. Nous explorons un large ensemble de paramètres expérimentaux pour optimiser l'accélérateur en contrôlant la densité et le profil du plasma, la durée des impulsions, le type de gaz et le mécanisme d'injection utilisés dans les expériences. Nous démontrons une amélioration significative des performances, notamment avec les progrès réalisés sur la stabilité et la fiabilité à long terme de l'accélérateur avec un fonctionnement continu et stable de l'accélérateur pendant plusieurs heures, accumulant ainsi un record de 18 millions de tirs consécutifs et également une bonne répétabilité du régime d'accélération d'un jour à l'autre. Nous obtenons ce gain de stabilité en utilisant un nouveau type de cible gazeuse qui produit un choc hydrodynamique oblique asymétrique permettant l'injection d'électrons dans la transition de densité descendante de la région choquée. En utilisant des simulations numériques de type particle-in-cell, les causes sous-jacentes menant à un régime d'accélération optimisé et stable sont étudiées. Nous constatons notamment que la zone de densité plus élevée induite par le choc favorise l'auto-focalisation du laser, augmentant son intensité juste avant la transition de densité où l'injection est facilitée par la combinaison du profil du plasma et de l'intensité accrue du laser. Ce résultat initie un changement de paradigme, faisant passer les accélérateurs laser-plasma d'expériences de preuve de principe où quelques bons tirs sélectionnés sont présentés, vers des installations fiables fournissant des faisceaux d'électrons pour des applications scientifiques. En effet, profitant de cette stabilité nouvellement acquise, nous avons réalisé une première expérience d'application avec notre accélérateur, où nous avons irradié des cellules cancéreuses avec des faisceaux d'électrons de quelques MeV pour mesurer leur taux de survie en fonction de la dose délivrée. Cette expérience de preuve de principe a démontré notre capacité à irradier des échantillons biologiques avec une dose contrôlée et un débit de dose moyen élevé d'environ 1 Gy/s, et appelle d'autres études prometteuses sur les effets temporels associés au dépôt de dose avec les sources par laser.

Dans un effort similaire d'amélioration des performances de l'accélérateur, l'énergie typique du faisceau d'électrons a également été multipliée par deux, passant de 4 MeV initialement à 8 MeV, avec une divergence du faisceau réduite à 3 mrad. Ce résultat a été obtenu en utilisant de l'hélium au lieu de l'azote comme gaz pour former le plasma. En effet, les nombreux niveaux d'ionisation de l'azote sont à l'origine d'une inhomogénéité de densité associée au profil d'intensité transverse du laser. Ce profil transverse du plasma, et son indice de réfraction correspondant, agissent comme une lentille défocalisante sur le laser réduisant ainsi l'intensité au foyer. Mais comme chaque molécule d'hélium fournit moins d'électrons que l'azote tout en offrant une efficacité de pompage plus faible, il a été nécessaire de développer un système de pompage différentiel pour pouvoir utiliser un flux continu et haute pression d'hélium dans la chambre d'interaction tout en conservant un niveau de vide suffisant pour la propagation du laser.

Un autre aspect important du travail présenté dans ce manuscrit est l'étude fondamentale de l'interaction d'impulsions à cycle quasi unique avec un plasma sous-dense qui se produit dans notre accélérateur. En effet, l'interaction d'impulsions de 30 fs à plusieurs cycles généralement utilisées dans l'accélération laser-plasma, est bien décrite dans le cadre de l'approximation pondéromotrice, où l'effet du champ électrique est moyenné sur le cycle optique. Dans cette approche, la réponse du plasma dépend uniquement de l'enveloppe de l'impulsion et est donc indépendante de la polarisation. Mais, lorsqu'on considère des impulsions beaucoup plus courtes dont la durée est proche du cycle optique, l'enveloppe et la porteuse de l'impulsion évoluent sur une échelle de temps similaire et l'approximation pondéromotrice n'est plus valable. Il est donc nécessaire de prendre en compte la forme réelle du champ électrique via la phase porteuse-enveloppe (CEP). Il a notamment été prédit que les impulsions monocycles peuvent conduire à une asymétrie transverse de l'onde plasma dans le plan de polarisation qui dépend de la CEP du laser, mais cela restait à observer expérimentalement. La CEP de nos impulsions proche du cycle optique est stabilisée et contrôlable, et nous observons et contrôlons expérimentalement pour la première fois les effets de la CEP dans un accélérateur par sillage laser dans un plasma, qui se manifestent par une dépendance du pointé du faisceau d'électrons à la phase optique initiale du laser. Nous observons également des variations de charge significatives (jusqu'à 30%) dans certains cas lorsque l'on change la valeur de la CEP. Les simulations numériques particle-in-cell indiquent que ces effets sont dus à l'injection périodique hors axe de plusieurs sous-faisceaux d'électrons déclenchée par l'oscillation de l'asymétrie de l'onde du

plasma dans la direction de la polarisation du laser en raison du glissement de la CEP pendant la propagation à cause de la dispersion dans le plasma. De plus, le rôle des imperfections de l'impulsion expérimentale est étudié en utilisant la tache focale mesurée expérimentalement dans les simulations, ce qui montre un couplage entre l'asymétrie dépendante de la CEP et l'asymétrie associée à l'impulsion imparfaite qui amplifie les variations des paramètres du faisceau. Enfin, des résultats préliminaires sur les effets de la CEP dans le cas de l'injection par ionisation sont présentées, notamment avec une variation importante du spectre des électrons mesurés en fonction de la valeur de la CEP du laser.

Contents

Introduction

Particle accelerators play an important role in fundamental scientific discoveries, notably with high energy colliders [1], but also through secondary light sources such as free-electron lasers [2] and synchrotrons [3]. Accelerated electron beams can also be used to probe fast dynamics in material science in electron diffraction experiments [4, 5]. Particle accelerators are also widely used for many industrial and medical applications such as non-destructive testing, radiation hardness studies and radiotherapy [6]. Conventional accelerators use radio-frequency (RF) electromagnetic fields synchronized with the propagation of particles to accelerate them to high energies. These RF cavities can support higher fields (10-100 MV/m) than when using electrostatic fields before electrical breakdown occurs between the electrodes. The two main types of accelerators are linear particle accelerators (LINAC) and synchrotrons, where particles are accelerated along a circular trajectory. The highest energies are achieved in synchrotrons because their geometry allows for the particles to be indefinitely accelerated, with the well known Large Hadron Collider (LHC) and its 27 km circumference being capable of accelerating protons up to an energy of 7 TeV. But, for accelerating electrons and positrons, LINACs are often preferred because of the loss of energy via synchrotron radiation that occurs when they travel in a circular trajectory, except when electrons are accelerated in synchrotrons specifically to induce X-ray light via synchrotron radiation. Indeed, the energy radiated by a particle scales with $E_{loss} \propto m^{-4}$ which limits the energy accessible by lighter particles in synchrotrons (*i.e.* electrons can be accelerated to 'only' 206 GeV at LHC). But in order to reach higher energies with LINACs, they must be scaled up to very large dimensions, for instance the linear accelerator at SLAC is 3.2 km long and accelerates electrons up to 50 GeV. The cost of these installations thus becomes considerable, and gaining a few orders of magnitude in energy seems prohibitively costly.

In 1979, Tajima and Dawson proposed laser-plasma acceleration [7] as a new scheme to bring particles, electrons in particular, to high energy. Their idea was to use an intense laser pulse propagating in a plasma to excite a high amplitude electronic wave (or plasma wave) via the ponderomotive force which expels the electrons from the high intensity zone. The charge separation induced by this plasma wave (the ions are too heavy to move in a first instance) can lead to massive longitudinal electric fields (100 GV/m), 3-4 orders of magnitude stronger than in radio-frequency accelerators, enabling the acceleration of electrons on very short distances. The plasma wave travels in the wake of the laser at the speed of light, leading to the name of laser-wakefield accelerator (LWFA) for this technique. The invention of the chirped-pulse amplification (CPA) technique [8] led to the development ultra-intense and ultra-short lasers that enabled experimental realization of laser-wakefield accelerator in the 90's, at first using the self-modulation of a few hundreds of femtoseconds laser pulses [9–11]. With the continuous progress in ultra-short laser development, and the advent of Joule-class, 30 fs titanium-sapphire lasers achieving relativistic intensities ($I > 10^{18}$ W/cm^2) and resonance with the plasma wave,

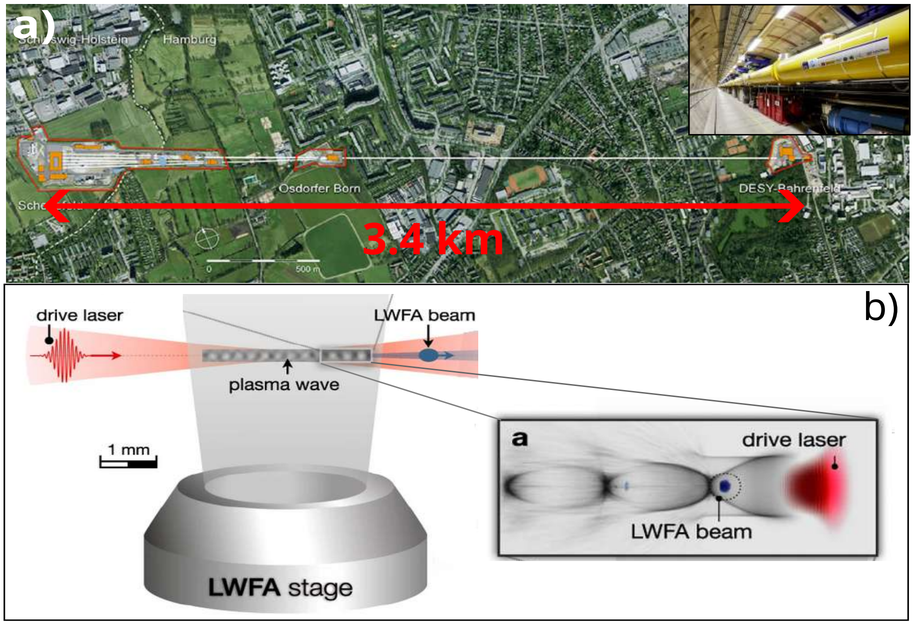

Figure 1 – a) Aerial view of the European XFEL LINAC accelerating electrons to 17.5 GeV and photo of the tunnel (top left corner) [from xfel.eu]. b) Schematic of laser wakefield acceleration taken from [20].

high-quality, monoenergetic, collimated laser-accelerated electron beams were obtained [12–14] with energies >100 MeV. Then, additional development in the injection techniques enabled the enhancement the quality of the beam [15], while the guiding of the pulse further increased the beam energy yielding the first GeV laser-accelerated electrons [16]. The use of guiding methods in combination with the new generation of PW-class lasers allowed to reach the current energy record of 8 GeV in a laser-plasma accelerator [17]. These advances made possible the demonstration of a long-time goal of LWFA: a free-electron laser driven by a laser-wakefield accelerator, but only with electron beams of few hundreds of MeV and not a the GeV level yet [18, 19].

All these results were achieved with lasers that operate at repetition rates between 0.1 Hz and 10 Hz, mostly due to thermal limitations of titanium-sapphire crystals. But using LPA for applications will require much higher repetition rates to acquire statistically meaningful data sets from scans on several parameters. For instance in colliders, the small cross sections often result in only a few collision events per beam crossing, depending on the particles and their energy. So in order to accumulate enough signal, the repetition rate of the accelerator must be large to amplify the signal which is why the LHC collider operates at 40 MHz. If we now look at the XFELs driven by LINACs, the LCLS at SLAC currently provides coherent X-ray pulses at 120 Hz, but its upgrade LCLS-II is supposed to reach 1 MHz repetition rate in a close future [21], while the European XFEL is currently operating at an average repetition rate of 27 kHz [22]. This means that actual applications of LPA as tools for science experiments and in industry will necessarily involve increasing their repetition rate to kilohertz and even megahertz levels in the long run. Additionally, a high-repetition rate will enable the use of active feed-back loops and on-line monitoring of the performances to further stabilize the accelerator.

High repetition rate laser-wakefield acceleration has thus been gaining interest in the past decade, taking advantage of existing multi-mJ, kilohertz laser systems. A first experiment at CUOS in Michigan achieved in 2013 to accelerate electrons to sub-relativistic energies (<100 keV) at 0.5 kHz using 8 mJ, 30 fs pulses [23, 24]. This was then followed by the acceleration of MeV electrons at 1 kHz by a group of the University of Maryland in 2017, using a <10 mJ, 30 fs laser and high plasma density $n_e > 4 \times 10^{20}\,\mathrm{cm}^{-3}$ to reach the self-modulated regime [25]. The same year, the APPLI group at LOA (that I later joined to carry out my research presented in this manuscript) achieved to accelerate electrons to 5 MeV at a kilohertz repetition rate, using the Salle Noire 2.0 few-mJ pulses post-compressed to nearly a single optical cycle duration $\tau = 3.5\,\mathrm{fs}$ at lower plasma density $n_e \sim 1 \times 10^{20}\,\mathrm{cm}^{-3}$ [26] achieving higher laser intensity and operating near the resonant bubble regime [27]. These are the first pioneer experiments operating at a kilohertz repetition rate, and because of the moderate pulse energy achievable with current kHz lasers, they yield relatively low energy electrons compared to the accelerators driven by 100 TW or PW lasers discussed earlier. But with future increase in power of high-repetition rate lasers, one can anticipate the production of kHz 100s of MeV and even GeV beams. Still, efforts remained to be made to bring this existing few-MeV source to the performances, stability and reliability necessary to use as an accelerator for applications.

Moreover, in this new acceleration regime using near-single cycle pulses, contrarily to multi-cycle pulses where the cycle-average ponderomotive framework applies, the optical phase or carrier-envelope phase (CEP) of the pulse can impact the response of the plasma and lead to asymmetries of the plasma wave [28]. And while the effects of CEP have been observed in laser-plasma experiments on solid targets [29–34] where the CEP has a fixed value on the surface of the target, it had yet to be demonstrated in laser-wakefield experiments in underdense plasma where the optical phase shifts during propagation due to dispersion in the plasma. Some preliminary results hinting for an effect of the CEP on the energy spectrum of the electrons were observed on the experiment prior to my arrival [35, 36] but were lacking repeatability and remained non-conclusive. The usual physical description of laser-wakefield acceleration largely relies on the ponderomotive approximation, so observing CEP effects in laser-plasma acceleration would be of fundamental interest, demonstrating an interaction beyond the ponderomotive force.

Motivations and comparison to other MeV sources

The motivation of my research, and more generally of our group is dual. Our goal is to develop a kilohertz LPA oriented towards applications and delivering high quality MeV electron beams. But in the meantime, we explore and study the specifics of the physical regime occurring during the interaction of near-single cycle pulses with an underdense plasma, notably through the impact of the carrier-envelope phase, but also other laser and plasma parameters. Originally, the main purpose of the electron source was to carry-out pump-probe ultrafast electron diffraction (UED) experiments to resolve the fast dynamics of phase transitions in crystalline solids. Conventional sources for such experiments are electron gun, constituted of a photo-cathode from which electron are extracted by a laser pulse and accelerated by an electric field to energies up to 100 keV [5]. But due to the relatively low energy of the electrons, the temporal resolution is limited by space charge dispersion of the bunch, and the bunch cannot be compressed much more than 100 fs. By using a RF cavity to accelerate the beam after the electron gun to few MeV, the bunch is not as much impacted by space charge and durations under 30 fs

RMS can be achieved [37] but timing jitter associated with shot-to-shot fluctuations of the RF amplitude and phase still limits the resolution to around 100 fs. In this context, a LWFA source capable to accelerate sub-5 fs electron bunches to a few MeV could provide an important platform to study the dynamics of phase transition of material in the 10-100 fs range, which was inaccessible to conventional UED experiments. However, during the course of my PhD, the temporal limitations associated with the jitter of RF cavities has been greatly reduced by using a magnetic bunching chicane that compressed the bunch and strongly reduced its jitter down to 25 fs [38] and to 8 fs RMS in another experiment [39] thus achieving a global UED resolution of 30 fs (RMS). While a LPA source for UED remains interesting and could still achieve a significantly higher temporal resolution, this progress of RF based electron source brings to light the importance to explore and direct the development of our kHz accelerator towards other potential applications such as radiobiology with a high mean dose rate (see section 4.4), or a X-ray source via Compton scattering [40, 41] that would require to increase the energy to >10 MeV to be of interest. Indeed a Compton source driven by 10-20 MeV electrons would be able to generate ultrashort X-rays in the 2-10 keV range at a kHz repetition rate.

Peak performances of the accelerator (having a higher charge, more energy, lower divergence) on a few selected shots are not the sole issue to solve in order to make LPA competitive sources for applications. Indeed, a fundamental aspect for application experiments is the stability, robustness and reliability of the source *i.e.* when an acceleration regime of interest is achieved, one should be able to obtain the same beam every shot for extended period of time, and consistently on several days/weeks/months. So this will also be a fundamental concern in the development and enhancement of our accelerator.

Outline of the thesis

This manuscript is organized as follows:

— Chapter 1 presents the global theoretical framework of laser-wakefield acceleration. The basic equations are detailed in the linear regime, and then the non-linear bubble regime is described. The scaling laws of laser-wakefield acceleration are detailed and applied to our millijoule laser driver. The question of injection of electrons in the plasma wave is addressed, and injection methods relevant to our work are discussed. Then, we study different effects impacting the propagation of ultra-intense, ultra-short pulses in a plasma. Finally, we present the theoretical predictions regarding the carrier-envelope phase effects that can be expected when using near-single cycle pulses to drive a LPA.

— Chapter 2 details the experimental set-up and methods used during my thesis. We start by presenting the Salle Noire 2.0 laser system, and then the LWFA set-up, with notably the electron beam diagnostics and plasma density characterization. We also details the characteristics of the particle-in-cell (PIC) code that was used to carry-out numerical simulations.

— In Chapter 3, we study theoretically and numerically oblique shocks in supersonic hydrodynamic flows. Computational fluid dynamics simulations are performed to study the impact of different parameters of symmetric shock gas nozzles on the flow. Then a new type of asymmetrically shocked gas target suitable for gradient injection is proposed, modeled and experimentally characterized.

- Chapter 4 details the experimental efforts made to optimize and stabilize the kilohertz LWFA. We start by performing an extensive scan in plasma density and laser pulse duration to study different acceleration regimes and determine the optimum. Then, the results of a 5h continuous hands-off operation of the LPA made possible by the use of the new type of shocked gas jets are presented and supported by PIC simulations. In addition, we demonstrate a significant increase in the electron energy by using helium gas instead of nitrogen for the plasma. Finally we show how the improved long-term stability and reliability enabled the use of our accelerator for a first application experiment in radiobiology.
- In Chapter 5, we study carrier-envelope phase effects in laser-wakefield acceleration driven by near-single cycle pulses. We observe CEP effects experimentally though the variation of the electron beam pointing with the laser optical phase, in a nitrogen plasma, and then in a helium plasma. PIC simulations are carried-out to understand in details the mechanisms leading to the observed effects. Then, we present preliminary results of the impact of the carrier-envelope phase in the context of ionization injection.
- Finally, we conclude on the work carried out during this thesis, and address the future perspectives for this experiment, but also for high-repetition rate laser-wakefield acceleration in general.

Chapter 1

Theory of laser-wakefield acceleration

Sommaire

The aim of this chapter is to summarize the main theoretical basis of the interaction of an ultra-short laser of relativistic intensity with an underdense plasma leading to the formation of a wakefield that can accelerate electrons to relativistic velocities.

1.1 Plasma formation: barrier-suppression ionization

First, we will see how the intense electric field of a laser can lead to ionization of a gas into a plasma. Let us consider the bound electron of an atom placed in an exterior electric field E. In the absence of electric field, the electron is simply bound to the atom by the Coulomb potential from the nucleus on the x axis taking into account the screening of other electrons [42]:

$$V_c = -\frac{Z^* e^2}{4\pi\epsilon_0 |x|} \tag{1.1}$$

Where Z^* is the effective atomic number taking into account the screening from remaining electrons. When adding an exterior electric field $\boldsymbol{E} = E\boldsymbol{e_x}$, its potential is added to the Coulomb potential, and the total potential seen by the electron is thus:

$$V_{tot} = -\frac{Z^* e^2}{4\pi\epsilon_0 |x|} - eEx \tag{1.2}$$

The maximum value of the total potential for x>0 is found by taking the derivative of V_{tot}: $(\partial V_{tot}/\partial x)$ and finding the position in x where it is zero: $x_m = \pm \left(\frac{Z^* e}{4\pi\epsilon_0 E}\right)^{1/2}$. The maximum value of the potential at this position x_m is thus:

$$V_{max}(x_m) = -2e \left(\frac{Z^* eE}{4\pi\epsilon_0}\right)^{1/2} \tag{1.3}$$

Therefore, for a sufficiently high amplitude electric field, the potential can be lower than the ionization level, $V_{max} < -E_i$ (see Fig. 1.1), and the electron becomes unbound: the atom is ionized. The electric field necessary to reach this barrier-supression is: $E_{bs} = \frac{\pi\epsilon_0 E_i^2}{Z^* e^3}$. This threshold electric field translates into the barrier-suppression intensity:

$$I_{bs} = \frac{\pi^2 c \epsilon_0^3 E_i^4}{2e^6 Z^{*2}} \tag{1.4}$$

That can be written in practical units:

$$I_{bs}\,[\mathrm{W\,cm^{-2}}] = 4 \times 10^9\, \frac{E_i^4 [eV]}{Z^{*2}} \tag{1.5}$$

We can then look at the intensity necessary to ionize different levels of atoms typically used in LWFA, showed in Table 1.1. We note that for hydrogen, helium, and the five first levels of nitrogen, a laser intensity of $I \sim 10^{16}\,\mathrm{W\,cm^{-2}}$ is sufficient to ionize them and therefore create a plasma. This level of intensity is two orders of magnitude lower than the typical relativistic peak intensities reached by the pulse, the plasma is thus created by the very front of the laser pulse. We also note that some higher ionization levels (such as N^{6+}, N^{7+}) require intensities higher than $10^{19}\,\mathrm{W\,cm^{-2}}$ to reach the barrier-suppression limit. This means that these levels will be, depending on the laser intensity, ionized only at the center of the pulse where the laser is most intense, or only marginally via tunnel ionization [43] (see. Fig. 1.1).

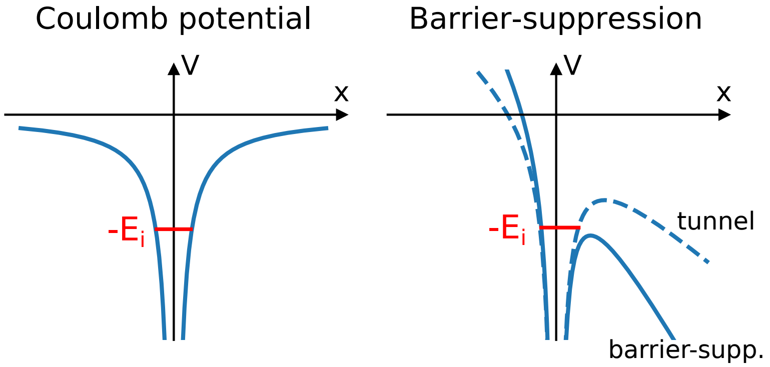

Figure 1.1 – a) Coulomb potential of a bound electron without external electric field. b) Potential on an electron with an external electric field over the barrier-suppression intensity (solid) and in the tunnel ionization regime (dashed).

		1^+	2^+	3^+	4^+	5^+	6^+	7^+
H	E_i (eV) I_{bs} (W cm^{-2})	13.6 1.4×10^{14}						
He	E_i (eV) I_{bs} (W cm^{-2})	24.6 1.5×10^{15}	54.4 8.8×10^{15}					
N	E_i (eV) I_{bs} (W cm^{-2})	14.5 1.7×10^{14}	29.6 7.7×10^{14}	47.4 2.3×10^{15}	77.5 9.0×10^{15}	97.9 1.5×10^{16}	552.1 1.0×10^{19}	667.0 1.6×10^{19}

Table 1.1 – Ionization energies and corresponding barrier-suppression intensities for hydrogen, helium and nitrogen [44].

1.2 Plasma wave generation

When focusing an intense, finite-extent laser pulse into an underdense plasma, the laser expels the electrons from the high-intensity zones through the ponderomotive force, while the ions remain still at the considered timescale due to their much larger inertia ($m_p = 1836 m_e$). This leads to the formation of an electron density perturbation, or plasma wave in the wake of the laser, co-moving with it at the laser group velocity v_g. This plasma wave, by creating an important charge separation, induces a structure of extremely strong longitudinal electric fields ($\sim 100\, GV/m$) traveling near the speed of light and capable of accelerating electrons to very high energies. In this section we develop the basic theory of plasma wave generation by an intense laser pulse in the linear regime, then we present a phenomenological analysis of the strongly non-linear bubble regime. We then discuss the problematic of electron trapping in the plasma wave and present different practical methods of injection.

1.2.1 Basic equations

Laser parameters

The laser is an electromagnetic field that satisfies Maxwell's equations:

$$\nabla \cdot \boldsymbol{E} = \frac{\rho}{\epsilon_0} \tag{1.6}$$

$$\nabla \cdot \boldsymbol{B} = 0 \tag{1.7}$$

$$\nabla \times \boldsymbol{E} = -\frac{\partial \boldsymbol{B}}{\partial t} \tag{1.8}$$

$$\nabla \times \boldsymbol{B} = \frac{1}{c^2}\frac{\partial \boldsymbol{E}}{\partial t} + \mu_0 \boldsymbol{j} \tag{1.9}$$

$$\tag{1.10}$$

where ϵ_0 is the vacuum permittivity, μ_0 the vacuum permeability, ρ the charge density, and $\boldsymbol{j}$ the current density in the propagation medium of the electromagnetic wave. We can rewrite the electric and magnetic fields using the vector and scalar potentials:

$$\boldsymbol{B} = \nabla \times \boldsymbol{A} \tag{1.11}$$

$$\boldsymbol{E} = -\nabla\Phi - \frac{\partial \boldsymbol{A}}{\partial t} \tag{1.12}$$

$$\tag{1.13}$$

We will use the Coulomb gauge $\nabla \cdot \boldsymbol{A} = 0$ so that the Poisson equation becomes:

$$\nabla^2\Phi = \frac{\rho}{\epsilon_0} \tag{1.14}$$

We define the normalized vector potential $\boldsymbol{a} = \frac{e\boldsymbol{A}}{m_e c}$ and $a_0 = \frac{e|\boldsymbol{A}|}{m_e c}$ its amplitude. We can write a_0 as a function of the laser intensity I_0 and wavelength λ_0:

$$a_0 = \left(\frac{e^2}{2\pi^2\epsilon_0 m_e^2 c^5} I_0 \lambda_0^2\right)^{1/2} = 0.85(I_{18}\lambda_{\mu\text{m}}^2)^{1/2} \tag{1.15}$$

Where I_{18} is the laser intensity measured in 10^{18} W.cm^{-2} and $\lambda_{\mu\text{m}}$ the wavelength expressed in microns.

For a laser propagating along the z axis and polarized along x, $\boldsymbol{a}$ is written as follow:

$$\boldsymbol{a} = \hat{a}(x, y, z - v_g t)\cos(kz - \omega t)\boldsymbol{e_x} \tag{1.16}$$

where k is the wave-vector and ω the pulsation of the laser, v_g the laser group velocity and $\hat{a}$ is an envelope function that represents the spatial distribution of the pulse.

Plasma equations

We will consider in our theoretical framework a cold and non-collisional plasma. This plasma can be modeled through Eulerian equations describing the motion of the fluid electrons. The ions are assumed to be immobile during the considered timescales due to their large inertia.

We start by writing the continuity and equation of motion:

$$\frac{\partial n}{\partial t} + \nabla(n\boldsymbol{v}) = 0 \tag{1.17}$$

$$\frac{\partial \boldsymbol{v}}{\partial t} + (\boldsymbol{v} \cdot \nabla)\boldsymbol{v} = -\frac{e}{m_e}(\boldsymbol{E_L} + \boldsymbol{v_e} \times \boldsymbol{B_L} - \nabla\Phi) \tag{1.18}$$

where the laser electric and magnetic field are given by $\boldsymbol{E_L} = \frac{\partial A}{\partial t}$ and $\boldsymbol{B_L} = \nabla \times \boldsymbol{A}$ and $\nabla\Phi$ is the plasma electrostatic field.

1.2.2 Ponderomotive force

In this section we will derive the expression of the ponderomotive force which is the driver of the wakefield during the interaction of the laser with the plasma. For additional clarity, in a first instance we will neglect the plasma fields, considering that the electrons only see the fields from the laser. The Euler equation is then written as follows:

$$\frac{\partial \boldsymbol{v}}{\partial t} + (\boldsymbol{v} \cdot \nabla)\boldsymbol{v} = -\frac{e}{m_e}(\boldsymbol{E_L} + \boldsymbol{v} \times \boldsymbol{B_L}) \tag{1.19}$$

We place ourselves in the linear regime, and consider only small perturbations of the electron velocity, that can be therefore written as follow: $v = v_1 + v_2$ where v_1 is the first-order component, and v_2 the second order non-linear term. So at the first order the equation of motion gives:

$$\frac{\partial \boldsymbol{v_1}}{\partial t} = -\frac{e}{m_e}\boldsymbol{E_L} \tag{1.20}$$

This equation tells us that the main, first order motion of the electrons is a transverse oscillation in the laser field at the laser frequency. Now by taking the curl of this expression, and using Maxwell-Faraday equation:

$$\frac{\partial \nabla \times \boldsymbol{v_1}}{\partial t} = -\frac{e}{m_e}\nabla \times \boldsymbol{E_L} = \frac{e}{m_e}\frac{\partial \boldsymbol{B_L}}{\partial t} \tag{1.21}$$

which gives $\boldsymbol{B_L} = m_e/e\nabla \times \boldsymbol{v_1}$. We can then plug this relation in the second order Euler equation:

$$\frac{\partial \boldsymbol{v_2}}{\partial t} + (\boldsymbol{v_1} \cdot \nabla)\boldsymbol{v_1} = \boldsymbol{v_1} \times \nabla \times \boldsymbol{v_1} \tag{1.22}$$

$$\frac{\partial \boldsymbol{v_2}}{\partial t} = -\nabla({\boldsymbol{v_1}}^2/2) \tag{1.23}$$

where we used the vector identity: $\nabla({\boldsymbol{v_1}}^2/2) = \boldsymbol{v_1} \times \nabla \times \boldsymbol{v_1} + (\boldsymbol{v_1} \cdot \nabla)\boldsymbol{v_1}$. By using the relation $\boldsymbol{v_1} = e\boldsymbol{A}/m_e$, we can replace: $\nabla({\boldsymbol{v_1}}^2/2) = c^2\nabla(\boldsymbol{a}^2/2)$. The equation of motion can now be written:

$$\frac{\partial \boldsymbol{v}}{\partial t} = -\frac{e}{m_e}\boldsymbol{E_L} - c^2\nabla\frac{\boldsymbol{a}^2}{2} \tag{1.24}$$

We can separate the dynamics between the very fast timescales (laser oscillations) and the slower timescales (evolution of the pulse envelope) by averaging on the laser optical cycle. This assumes that the envelope does not evolve during an oscillation of the electric field, meaning $\omega \gg 2\pi/\tau$. When averaging over the optical cycle, the contribution of the electric field disappears $\langle \boldsymbol{E_L} \rangle = 0$ but not the square of the normalized potential: $\langle \boldsymbol{a^2} \rangle = \hat{a}^2/2$, which yields:

$$\frac{\partial \boldsymbol{v_{slow}}}{\partial t} = -c^2 \nabla \frac{\hat{a}^2}{4} \tag{1.25}$$

where $\hat{a}$ is the spatial envelope of the laser pulse and $\boldsymbol{v_{slow}}$ the electron velocity averaged on the fast oscillations. This term on the right corresponds to the ponderomotive force, it pushes the electrons from the higher intensity zone towards the lower intensity zones. It depends purely on the envelope and therefore is polarization independent. This means that, even if a laser polarized linearly in one direction (*e.g* $\boldsymbol{e_x}$) could *a priori* induce an asymmetry between the x and y directions in the problem, the ponderomotive force which is the main driver of the plasma wave, enables the interaction to remain symmetric in the transverse direction. This is of course valid only upon the verification of the ponderomotive approximation that requires the envelope the beam to be much longer than the optical cycle.

1.2.3 Generation of the plasma wave in the linear regime

Once again, we place ourselves is the small perturbations linear regime ($a_0^2 \ll 1$). We write the local plasma density as the equilibrium density n_0 plus a small density perturbation δn: $n_e = n_0 + \delta n$. The Poisson equation is therefore written:

$$\nabla^2 \Phi = \frac{e}{\epsilon_0} \delta n \tag{1.26}$$

The linear continuity equation becomes:

$$\frac{\partial \delta n}{\partial t} + n_0 \nabla \boldsymbol{v_{slow}} = 0 \tag{1.27}$$

And without neglecting the plasma field, the motion equation 1.25 becomes:

$$\frac{\partial \boldsymbol{v_{slow}}}{\partial t} = -c^2 \nabla \frac{\hat{a}^2}{4} + \frac{e}{m_e} \nabla \Phi \tag{1.28}$$

By deriving 1.27 and using the Poisson and motion equation, we obtain the equation for the electron density perturbation:

$$\left(\frac{\partial}{\partial t} + \omega_p^2 \right) \frac{\delta n}{n_0} = c^2 \nabla^2 \frac{\hat{a}^2}{4} \tag{1.29}$$

The equation 1.29 shows that it is the ponderomotive force that drives the density perturbation, and creates the plasma wave. By using the Poisson equation 1.26 to replace the density perturbation by the potential, and defining a normalized potential $\phi = e\Phi/m_e c$, we can simplify the equation by removing the Laplace operators and get the potential equation:

$$\left(\frac{\partial}{\partial t}+\omega_p^2\right)\phi=\omega_p^2\frac{\hat{a}^2}{4} \tag{1.30}$$

Since the laser driver propagates at a velocity v_g, it is relevant to use longitudinal coordinate coupling z and t *via*: $\zeta = z - v_g t$. By performing the change of variables $(z,t) \rightarrow (\zeta, t')$, equation 1.30 becomes:

$$\left(\frac{\partial^2}{\partial t'^2}-2c\frac{\partial^2}{\partial\zeta\partial t'}+c^2\frac{\partial^2}{\partial\zeta^2}+\omega_p^2\right)\phi=\omega_p^2\frac{\hat{a}^2}{4} \tag{1.31}$$

We can then perform the quasistatic approximation, assuming that the laser pulse and the plasma wave only slowly evolve in time, meaning $\frac{\partial}{\partial t'} \ll v_g\frac{\partial}{\partial\zeta}$. The temporal derivative can therefore be neglected, which yields (with $k_p=\omega_p/c$):

$$\left(\frac{\partial^2}{\partial\zeta^2}+k_p^2\right)\phi(x,y,\zeta)=k_p^2\frac{\hat{a}^2}{4}(x,y,\zeta) \tag{1.32}$$

By solving this second order differential equation looking for solutions in the form $\phi(r,\zeta) = A(r,\zeta)\sin k_p\zeta + B(r,\zeta)\cos k_p\zeta$ we find:

$$\phi(r,\zeta)=-\frac{k_p}{4}\int_{-\zeta}^{\infty}\hat{a}^2\sin[k_p(\zeta-\zeta')]d\zeta' \tag{1.33}$$

The constant of integration has been chosen so that $\phi(r,\zeta)$ is zero before the pulse ($\zeta=+\infty$), and the wake appears behind the pulse where $\hat{a}=0$ so that we can extend the lower bound of the integral to $-\infty$:

$$\phi(r,\zeta)=-\frac{k_p}{4}\int_{-\infty}^{\infty}\hat{a}^2\sin[k_p(\zeta-\zeta')]d\zeta' \tag{1.34}$$

And by assuming that $\hat{a}$ is a pair function, finally we obtain the general solution for ϕ:

$$\phi(r,\zeta)=-\frac{k_p}{4}\sin(k_p\zeta)\int_{-\infty}^{\infty}\hat{a}^2\cos(k_p\zeta')d\zeta' \tag{1.35}$$

Gaussian laser driver

We can look at the case where the laser pulse is gaussian: $\hat{a}^2 = a_0^2\exp(-\zeta^2/L_0^2)\exp(-r^2/\sigma_r^2)$. Inserting this expression of $\hat{a}$ in the equation 1.35 yields:

$$\begin{aligned}\phi(r,\zeta) &= -\frac{k_p}{4}\exp(-r^2/\sigma_r)\int_{-\infty}^{\infty}a_0^2\exp(-\zeta'^2/L_0^2)\exp(ik_p\zeta')d\zeta' && (1.36)\\ &= -\sqrt{\pi}a_0^2\frac{k_pL_0}{4}\exp(-k_p^2L_0^2/4)\exp(-r^2/\sigma_r^2)\sin(k_p\zeta) && (1.37)\end{aligned}$$

We can then retrieve the electric field through $\frac{E}{E_0}=\frac{1}{k_p}\nabla\phi$, with $E_0 = m_e c\omega_p/e$. The longitudinal and radial electric fields are then:

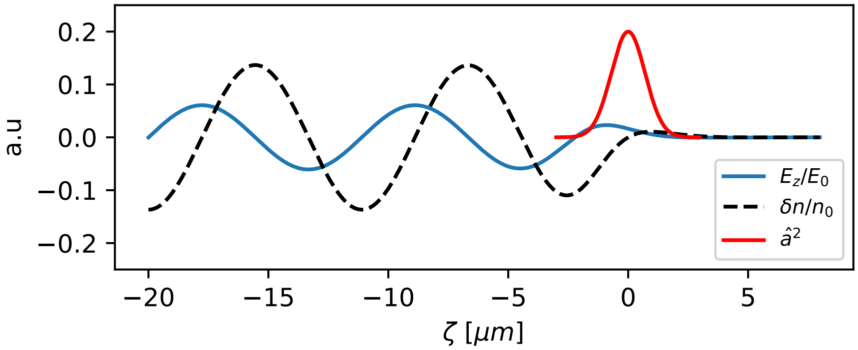

Figure 1.2 – On axis solution for the longitudinal electric field (blue) and density perturbation (black, dashed) in the wakefield for the linear regime, with a gaussian laser pulse (red).

$$E_z = E_0\sqrt{\pi}a_0^2\frac{k_pL_0}{4}\exp(-k_p^2L_0^2/4)\exp(-r^2/\sigma_r^2)\cos(k_p\zeta) \tag{1.38}$$

$$E_r = -E_0\sqrt{\pi}\frac{a_0^2}{2}\exp(-k_p^2L_0^2/4)\frac{L_0r}{\sigma_r^2}\exp(-r^2/\sigma_r^2)\sin(k_p\zeta) \tag{1.39}$$

The longitudinal and radial electric fields are dephased by $\pi/2$, which means that the plasma wave will be both accelerating and focusing on a quarter plasma wavelength. And finally, using the Poisson equation, we can retrieve the electron density perturbation:

$$\frac{\delta n}{n_0} = \sqrt{\pi}a_0^2\frac{k_pL_0}{4}\exp(-k_p^2L_0^2/4)\exp(-r^2/\sigma_r^2)\sin(k_p\zeta)\left[1+\frac{4}{\sigma_r^2k_p^2}\left(1-\frac{r^2}{\sigma_r^2}\right)\right] \tag{1.40}$$

We see from the equation 1.38 that there is a value of k_pL_0 maximizing the longitudinal (accelerating) electric field. This is called the resonance condition, and it is verified for:

$$\boxed{k_pL_0 = \sqrt{2}} \tag{1.41}$$

This condition indicates that the laser has to have a longitudinal extent on the order of half a plasma wavelength in order to be resonant and drive a high amplitude plasma wave.

1.3 The non-linear and blow-out regimes

Up until now, we have considered only small density perturbations, which allowed us to use the linearized fluid equations. Expanding this analytical theory to non-linear relativistic cases with $a_0 > 1$ is still possible but limited to a 1D description [45, 46]. In this non-linear, relativistic regime, the motion equation is now:

$$\frac{\partial}{\partial t}(\boldsymbol{p} - e\boldsymbol{A}) = e\nabla\Phi - m_ec^2\nabla\gamma \tag{1.42}$$

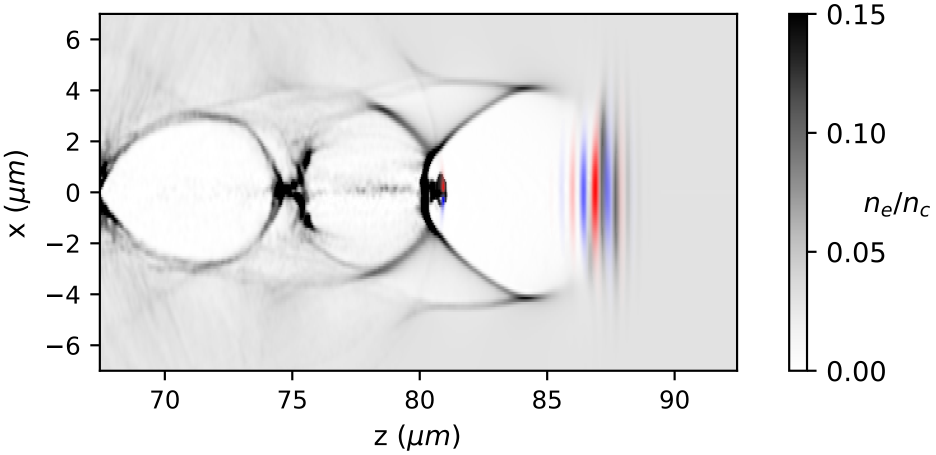

Figure 1.3 – Wakefield in the bubble regime obtained with a PIC simulation with the code FBPIC. The electron density is showed in gray, the laser electric field in a blue-red colormap. The parameters are $a_0 = 4$, $\tau = 5\,\mathrm{fs}$, $\lambda_0 = 800\,\mathrm{nm}$, the waist $w_0 = 4\ \mu\mathrm{m}$ and $n_e = 5 \times 10^{19}\,\mathrm{cm}^{-3}$

where $\gamma = \sqrt{1 + p^2/m_e^2c^2}$ is the Lorentz factor. Using the quasi-static approximation, the 1D fluid system of equation allows us to compute the following equation for the potential:

$$\frac{\partial^2\phi}{\partial\zeta^2} = k_p^2\gamma^2\left[\beta_p\left(1 - \frac{1+\hat{a}^2/2}{\gamma^2(1+\phi)^2}\right)^{-1/2} - 1\right] \tag{1.43}$$

where $\beta_p = v_p/c$ is the ratio of the plasma wave phase velocity to c. This equation has no analytical solution, but can be solved numerically. When using relativistic laser potentials $a_0 > 1$, the fields of the plasma wave steer away from the sinusoidal shape of the linear case and tend towards steeper profiles. When increasing a_0 the electron density perturbation becomes a succession of very fine high amplitude peaks, that can support very strong accelerating fields.

The 3D non-linear relativistic regime cannot be described analytically, and is therefore studied mainly through numerical particle-in-cell (PIC) simulations [27] where it has been observed that for relativistic intensities, the wake just behind the laser takes the form of a plasma cavity almost completely devoid of electrons, surrounded by a fine sheath of very high electronic density. This regime is known as the blow-out or bubble regime, and is particularly interesting because of the very strong accelerating fields it creates, and also because this bubble structure support fields that are both accelerating and focusing on a larger extent than only a quarter of the plasma wavelength. Reaching this regime experimentally has allowed to accelerate high quality electron beams [12–14] with a narrow energy spread and a low beam divergence. Figure 1.3 shows a snapshot of a wakefield driven by a laser with $a_0 = 4$ from a PIC simulation, highlighting the bubble regime. We can see the round-shaped cavity completely depleted from background electrons, and the high-density sheath around it. Due to the extremely high accelerating fields at the back of the cavity, as it it the case in Fig.1.3, electron can be self-injected in the plasma wave.

A phenomenological theory of the bubble regime has been developed by Lu *et al.* [47] and indicates the conditions necessary to achieve it. We detail and apply it to scale the bubble regime to our kilohertz laser in the next section.

1.4 Scaling the bubble regime to millijoule pulses

The phenomenological analysis developed by Lu *et al.* [47] and supported by PIC simulations, allows to retrieve simple and general scaling laws to reach the bubble regime depending on the experimental conditions, and the order of magnitude of the maximum energy at which the electron can be accelerated.

Firstly, the non-linearity condition require $a_0 > 2$ for the laser to be able to expel all the electrons from the axis through the ponderomotive force. Then we can estimate the optimal matching spot size by considering that the transverse ponderomotive force $k_p \nabla a_0^2/\gamma \sim a_0/(k_p R)$ where R is the bubble radius, is balanced by the restoring force of the ion cavity $E_r \sim k_p R$. This yields $k_p R \sim \sqrt{a_0}$, and the size of the bubble follows the laser waist so $k_p w_0 \sim \sqrt{a_0}$ for transverse matched conditions. Simulations indicate a slightly corrected version of this matching condition:

$$\boxed{k_p w_0 = 2\sqrt{a_0}} \tag{1.44}$$

Then we have to derive a condition on the longitudinal extent, or duration of the pulse. For this, we consider two important characteristics lengths describing the acceleration process. Firstly, during its interaction with the plasma the driving laser loses its energy and is depleted (or etched) on a length $L_{etch} \simeq \frac{c}{v_{etch}} c\tau_{fwhm}$ where v_{etch} is the velocity at which the front of the pulse driving the wake moves backward by etching. This etching velocity is estimated based on non-linear 1D theory in [48] as $v_{etch} \simeq c\omega_p^2/\omega_0^2$, which finally yields:

$$L_{etch} = \frac{\omega_0^2}{\omega_p^2} c\tau_{fwhm} \tag{1.45}$$

The second important length to consider is the dephasing length which is the wake propagation distance after which the injected electrons catch-up with the decelerating field of the bubble. The phase velocity of the wake is the laser group velocity, minus the etching velocity which lowers the actual velocity of the pulse: $v_\phi = v_g - v_{etch}$. The laser group velocity is $v_g = c\sqrt{1 - \frac{\omega_p^2}{\omega_0^2}} \simeq c(1 - \frac{1}{2}\frac{\omega_p^2}{\omega_0^2})$ for a strongly underdense plasma, so that the wake phase velocity is $v_\phi = v_g - v_{etch} \simeq c(1 - \frac{3}{2}\frac{\omega_p^2}{\omega_0^2})$. The electrons have to travel a blow-out radius to enter the decelerating phase, so the dephasing length can therefore be written:

$$L_d = \frac{c}{c - v_\phi} R \simeq \frac{2}{3}\frac{\omega_0^2}{\omega_p^2} R \tag{1.46}$$

In order to reach their maximal energy, the pulse should not be depleted before the electron reach the decelerating phase, meaning $L_{etch} > L_d$, which yields:

$$\boxed{c\tau_{fwhm} > \frac{2}{3} R} \tag{1.47}$$

Another condition to maintain the bubble regime on distances sufficiently long to accelerate electrons despite the diffraction of the laser is to overcome it by the relativistic self-focusing [49]. A typical assumption is to assume it is necessary for the laser power to exceed the relativistic self-focusing limit by a factor of 2 [47]:

$$\boxed{P > 2P_c = 2 \times 17 \frac{n_c}{n_e}\ [GW]} \tag{1.48}$$

where $n_c = \epsilon_0 m_e \omega_0^2 / e^2$ is the critical density

The maximum energy of the accelerated electrons is then estimated by using $\Delta E = qE_{LW}L_{acc}$, where E_{LW} is the average accelerating field in the bubble, and L_{acc} the accelerating length. We assume the electrons are accelerated during the whole dephasing length L_d. Lu *et al.* estimate $E_{LW} \simeq \frac{\sqrt{a_0}}{2}\frac{mc\omega_p}{e}$, which yields, using the matching condition and the expression of the dephasing length in 1.46:

$$\boxed{\Delta E = eE_{LW}L_d \simeq \frac{2}{3}mc^2 \left(\frac{\omega_0}{\omega_p}\right)^2 a_0 \simeq mc^2 \left(\frac{P}{m^2c^5/e^2}\right)^{1/3} \left(\frac{n_c}{n_e}\right)^{2/3}} \tag{1.49}$$

We can now apply these scaling laws numerically to existing laser systems. Firstly, we can look at the parameters of the typically used 50 TW lasers such as in *Salle Jaune* at LOA, with pulse duration $\tau \sim 30$ fs, and typical energy on target $E_{las} \sim 1$ J that operates at a typical repetition rate of 1 Hz. In order to reach $a_0 = 2.5$ (corr. to $I = 1.4 \times 10^{19}$ W cm^{-2}) it is necessary to focus the pulse to a spot with $w_0 = 13$ µm. The matching condition 1.44 then indicates that a plasma density of $n_e = 1.8 \times 10^{18}$ cm^{-3} is necessary to be resonant. The condition on the pulse duration 1.47 indicates an minimal pulse duration $\tau_{fwhm} = 27\, fs$ matching quite well the laser. These parameters yield a maximum energy gain for the electrons $\Delta E \simeq 800$ MeV using equation 1.49, on a typical acceleration length $\lambda_{acc} = 20$ mm. We note that the energy gain seems a bit overestimated with regard to experimental results achieved in this regime. Indeed, without external guiding, the typical maximum energy reached in Salle Jaune at LOA is more around 200-300 MeV [14, 15] mostly because the plasma densities that are necessary in these experiments are higher than the ones predicted by the scaling laws, leading to a shorter dephasing length.

Applying the same scaling laws to our kilohertz laser delivering typically 2.5 mJ energy on target with a pulse duration $\tau = 4$ fs, leads to (aiming for $a_0 = 2.2$): $w_0 = 2$ µm, $n_e = 7 \times 10^{19}$ cm^{-3} and an optimal $\tau_{fwhm} = 4.3\, fs$ to reach the bubble regime. These parameters yield a maximum energy gain for the electrons $\Delta E \simeq 19$ MeV on a typical acceleration length $\lambda_{acc} = 35$ µm. In our regime using near-single cycle pulses, some of these scaling laws might be limited to some extent. Firstly, the laser intensities we are able to reach are only mildly relativistic ($a_0 \sim 1.5$) and therefore we will not necessarily obtain a perfectly formed bubble. Additionally, the etching and self-guiding concept are not completely relevant to single-cycle pulses. Indeed, what we observe in simulations is not an etching of the laser pulse due to depletion, but on the contrary it extends longitudinally due to dispersion. This dispersion also competes with self-focusing, making self-guiding on extended lengths impossible. However, despite these apparent flaws, these scaling laws still succeed quite well at predicting optimal operating conditions and the achievable acceleration regime.

1.5 Injecting electrons in the wakefield

We have seen how the laser creates the plasma, and how it can drive non-linear plasma waves that can accelerate electrons to very high energies over small distances. The question of how to inject electrons at the right phase of the wakefield so that they can be trapped in the accelerating structure remains to address. There are many phenomena and techniques that can lead to electron injection, and the objective of this section is not to give an exhaustive picture of all these trapping mechanisms, but to describes the main injection situations that will be relevant in our experiments.

1.5.1 General Hamiltonian formalism of electron trapping

The Hamiltonian formalism is quite convenient to describe the trapping of an electron in a wakefield [50, 51]. Let us consider the case of an electron in 1D (z) plasma wave of potential Φ. Its Hamiltonian is:

$$H = \sqrt{1 + u_\perp^2 + u_z^2} - \phi(z - v_p t) \tag{1.50}$$

With $u_z = P_z/m_e c$ the normalized longitudinal momentum of the electron, v_p the phase velocity of the plasma wave, and $\phi = e\Phi/m_e c^2$ the normalized potential. We can transform this Hamiltonian by using the $\zeta = z - v_p t$ variable through the canonical transformation: $(z, u_z) \rightarrow (\zeta, u_z)$ using the generating function $F = u_z \times (z - v_p t)$:

$$H = \sqrt{1 + u_\perp^2 + u_z^2} - \phi(\zeta) - \beta_p u_z \tag{1.51}$$

The transverse momentum can be written as the sum of the electron initial momentum and the momentum gained through the laser: $u_\perp = u_{\perp,0} + a$. Because we consider a 1D case, the canonical transverse momentum is preserved: $-\partial H/\partial r = 0$ so H does not depend on the transverse direction. This means that $u_\perp = cst$ and assuming that the electron is initially at rest:

$$u_\perp = a \tag{1.52}$$

This Hamiltonian does not depend on time anymore, just on the spatial coordinate ζ, and therefore is invariant, meaning $H = H_0$, with H_0 a constant defined by the initial conditions. It can be written as a second order polynomial equation:

$$(H_0 + \phi + \beta_p u_z)^2 = 1 + u_z^2 + a(\zeta)^2 \tag{1.53}$$

Its solutions are:

$$u_z = \beta_p \gamma_p^2 (H_0 + \phi) \pm \gamma_p \sqrt{\gamma_p^2 (H_0 + \phi)^2 - \gamma_\perp^2} \tag{1.54}$$

These solutions are represented in Figure 1.4 for different initial values of the Hamiltonian H_0, corresponding to different initial momenta. Depending on their initial momentum, we can differentiate two different populations of electrons: the trapped orbits and the fluid orbits. The limit between the two is called the separatrix, and is represented in red in Fig. 1.4. If its energy is too low, the electron cannot be injected, its trajectory is open, and it simply oscillates

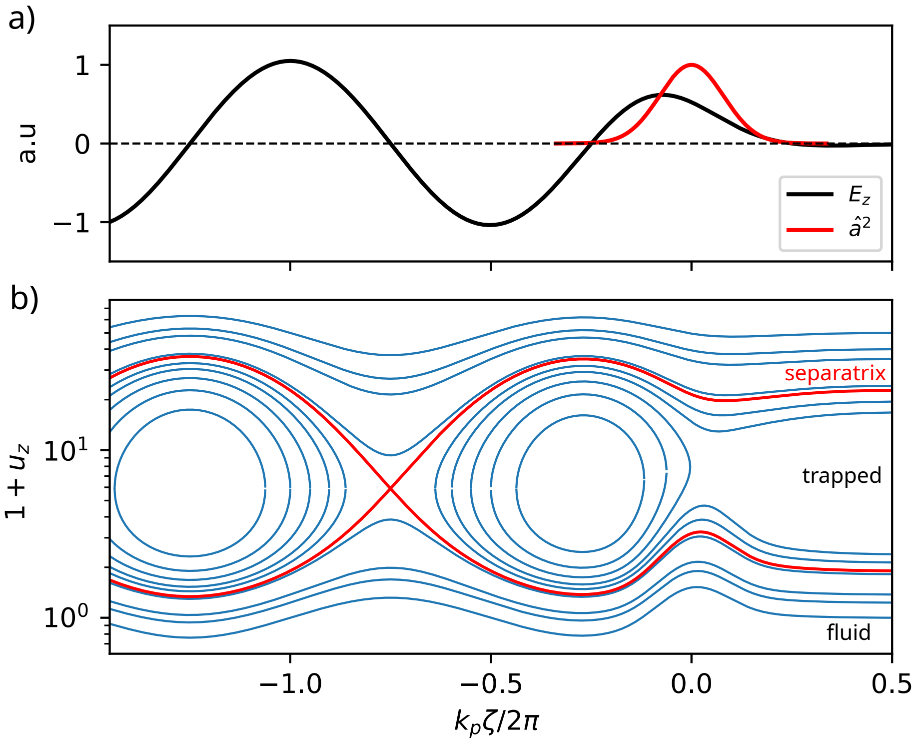

Figure 1.4 – a) Wakefield potential (black) and laser envelope (red) in the linear approximation with $a_0 = 1$. b) Electron phase-space for different initial energy of the electrons. The separatrix highlights the limit between the fluid and the trapped orbits.

in the plasma wave. Those electrons are the one forming the wakefield. But if the electron initial energy (in $\zeta = +\infty$) is between the lower and upper limits defined by the separatrix, it can be trapped in the plasma wave and can gain energy. The position of the separatrix can be found by assuming that at the minimum of the potential, the particle energy should be $\gamma = \gamma_p$ to be trapped. Its Hamiltonian is therefore $H_s = 1/\gamma_p - \phi_{min}$. This corresponds to an electron traveling at v_p at the position where $E_z = 0$ and thus it feels no force. The maximum and minimum of energy are obtained at the maximum and minimum of potential so that the extrema of momentum on the separatrix can be written assuming $\phi_{max} = -\phi_{min} = \phi_0$:

$$u_{z,min}^{max} = \beta_p\gamma_p(1+2\gamma_p\phi_0) \pm \gamma_p\sqrt{(1+2\gamma_p\phi_0)^2 - \gamma_\perp^2} \qquad (1.55)$$

Which yields the maximum momentum gain for an electron Δu_z (and its approximation when $\gamma_p\phi_0 \gg 1$:

$$\Delta u_z = 2\gamma_p\sqrt{(1+2\gamma_p\phi_0)^2 - \gamma_\perp^2} \simeq 4\gamma_p^2\phi_0 \qquad (1.56)$$

So we have seen that if they have a sufficiently high initial momentum, some electrons can interact with the accelerating phase of the wakefield for a sufficiently long time to catch up with its velocity and therefore be trapped in it, continuously gaining energy up to the point where they reach the decelerating phase of the plasma wave.

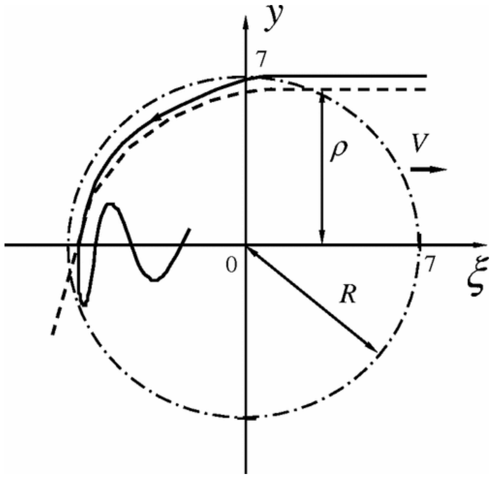

Figure 1.5 – Trajectories of trapped (solid) and untrapped (dashed) electrons in a spherical bubble taken from [55].

1.5.2 Self-injection

One of the most commonly used technique to trap electrons in the wake is self-injection, mainly because it is easy to implement as it occurs naturally in experiments, without the need of an external element. It occurs if the plasma wave is of sufficiently high amplitude and some conditions detailed later are met. An electron can be injected in the wakefield if its velocity is sufficiently high so that its momentum is comprised between the two separatrix in the phase space of Fig.1.4. In that case it can be trapped in the accelerating field and gain energy. But the plasma wave moves at the velocity very close to c (depending on n_e), and therefore the trapping velocity is much higher than the typical velocity of the plasma electrons. By adopting a fluid description of the wakefield, self-injection can be explained by the wave-breaking of the plasma wave. In the non-linear regime, the shape of the wakefield deviates from its sinusoidal shape and steepen up to a singularity point where the electric field reaches the wave-breaking threshold E_{WB}, fluid trajectories cross and the wave breaks [52, 53]. Even though both longitudinal and transverse wave-breaking can occur in multi-dimensional wakefields, it has been observed that transverse wave-breaking largely dominates in 3D structures [54]. The transverse wave-breaking of a multidimensional plasma wave can be seen as the point where the electron displacement ξ induced by the non-linear wave becomes of the order of the curvature of the wake phase surface. This means that during this displacement, the electron can enter the accelerating field from a transverse direction and gain longitudinal momentum, thus leading to the breaking of the wave and the injection of electrons.

An analytical model based on an Hamiltonian description of the trajectories of the electrons in the bubble regime [55] gives us more insight on the mechanism leading to self-injection. The electrons are pushed off-axis by the ponderomotive force, and recalled toward it by the field of the ion-cavity, leading to trajectories with a circular curvature leading to the formation of the sheath of the bubble. Depending on their trajectory, the electrons can be accelerated by the longitudinal field and be trapped when reaching the back of the bubble. Figure 1.5 shows two different trajectories leading to trapped and untrapped electrons. If the initial distance of the electron from the axis is close to the bubble radios $\rho \simeq R$, the electron will enter the bubble in its second half, and therefore will purely see the accelerating field. When reaching the back of the bubble, it has been sufficiently accelerated for its velocity to be higher than the wake phase velocity, and it is thus trapped in the bubble. For the other trajectories with $\rho < R$, the electron enter the bubble in a decelerating phase in which in will acquire negative longitudinal momentum before reaching the accelerating phase. In the end, its final momentum resulting from the sum of the decelerating and accelerating fields is not sufficient to be trapped in the bubble. This model is coherent with the observation in [54] where, in 3D-PIC simulations, the electrons from transverse self-injection originate from a ring of radius similar to the laser waist (and therefore the bubble radius). This analytical model also provides a condition on the radius of the bubble and the Lorentz factor of the wake in order to inject electrons:

$$k_p r \geq \sqrt{2}\gamma_p \tag{1.57}$$

Where r is the bubble radius. A numerical application of this formula for a plasma density $n_e = 1 \times 10^{20}\,\mathrm{cm}^{-3}$ yields $r_{min} = 3.1\,\mu\mathrm{m}$, and $n_e = 1 \times 10^{19}\,\mathrm{cm}^{-3}$ yields $r_{min} = 31\,\mu\mathrm{m}$. These values are overestimated because the bubble field enhancement at the back of the bubble associated with electron trajectory crossing [47, 53, 55]. The formula 1.57 indicates that the minimum radius at which self-injection is possible scales with n_e^{-1}, as higher densities lead to a slower wakefield which lowers the injection threshold. We also note that the Lorentz factor γ_p is the local factor at the back of the bubble, which can be different of the Lorentz factor at the front of the bubble if it is evolving in time. For instance, in the case of self-focusing, a_0 can increase sharply leading to an increase of the bubble radius while lowering the gamma factor at the back of the bubble due to the local slow down induced by its enhanced size, thus triggering self-injection. The formula 1.57 also indicates that the minimum injection radius scales with λ_0^{-1}, meaning higher laser wavelengths are favorable to injection because the laser, and therefore the wake will propagate at slower velocity. This means that the redshift of the laser during the propagation in the plasma can participate in reducing the threshold for self-injection.

Self-injection has been used in many experiments [12, 14, 56] because of its simplicity as it occurs spontaneously, and it enabled to obtain good quality, low-divergence, quasi-monoenergetic electrons beams. But it depends of strongly non-linear phenomena such as relativistic self-focusing and redshift of the laser that occur during the propagation in the plasma which makes it very difficult to control and can lead to strong shot-to-shot variations of the accelerator. A possibility to overcome this issue would be to control self-injection by triggering an increase of the bubble size through an external effect. This is addressed in the following section.

1.5.3 Injection in a density gradient

We observed in the previous section that the evolution of the bubble size could trigger injection [57] by lowering the threshold. A possibility to gain control over injection would be to trigger a longitudinal expansion of the plasma bubble through a controlled density downramp in the plasma profile [58, 59]. Depending on the size of the gradient scale relatively to the plasma wavelength λ_p, two different regimes can be identified.

Long density gradient $L_{grad} > \lambda_p$

When the gradient scale L_{grad} is larger than the plasma wavelength λ_p, the plasma wave will evolve progressively during its propagation in the gradient. As the plasma wavelength (or bubble size) scales with $n_e^{-1/2}$, it increases progressively while crossing the gradient. This leads to an effective slow-down of the back of the plasma bubble due to its expansion, with the wake phase velocity being in a density gradient [59]:

$$v_p = c\frac{1}{1+(z-ct)\frac{1}{k_p}\frac{dk_p}{dz}} \tag{1.58}$$

with $k_p(z) = \omega_p(z)/c \propto n_e^{1/2}(z)$. We see that for a density downramp ($dk_p/dz < 0$), the local phase velocity decreases in the co-moving frame with the laser co-moving coordinate $(z-ct)$. Therefore the phase velocity of the back of the bubble decreases. This lowered phase velocity decreases the wave-breaking threshold and therefore can trigger injection during the propagation in the density gradient. Additionally, this effect is not limited to the first bucket of the plasma wave, and the phase velocity decreases even more in the buckets that are further away from the laser. Indeed, the plasma wavelength expansion of each bucket in the front accumulates leading to a stronger slow-down which can lead to injection of electrons in many different buckets at the back of the laser pulse. This regime of injection was demonstrated experimentally in proof-of-principle experiments [60, 61] by focusing the laser downstream of a gas jet, in the density downramp.

Short density gradient $L_{grad} \leq \lambda_p$

When the density gradient is sharp, meaning $L_{grad} \leq \lambda_p$, the plasma bubble expands abruptly longitudinally when crossing the gradient, leading to the trapping of electrons of the plasma wave that end up in the accelerating phase of the wake at the back of the bubble. This regime is advantageous because the electron trapping is much more localized, and occurs in the first plasma bucket, which allows to accelerate higher quality electron beam, with low energy spread, and short bunch duration. This has been demonstrated in several experiments [62–64] with enhanced stability compared to uncontrolled self-injection.

1.5.4 Ionization injection

Ionization injection [65–68] is based on the fact that for certain high-Z atoms (e.g nitrogen) the barrier-suppression ionization of some higher levels occur only at the peak intensity of the pulse. For example, the ionization of nitrogen up to N^{5+} require a laser intensity of $I = 1.5 \times 10^{16}\,\mathrm{W\,cm^{-2}}$ (see sec. 1.1) which is reached quite far in the front of the pulse, but the levels of N^{6+} and N^{7+} require intensities respectively of $I = 1.0 \times 10^{19}\,\mathrm{W\,cm^{-2}}$ and $1.6 \times 10^{19}\,\mathrm{W\,cm^{-2}}$, which are reached only near the peak of the pulse. The ions being too heavy to be significantly impacted by the ponderomotive force at the considered timescales, they are not expelled and remain near the axis. Therefore, when the inner K-shell electrons are ionized by the high fields at the peak of the pulse, they are created already inside the plasma wake and can be injected even though they have zero initial longitudinal momentum. The behavior of the electrons depending on their ionization level is highlighted in Figure 1.6. The nitrogen L-shell electrons (from N^{1-5+}) are ionized well before the pulse, are will therefore be expelled

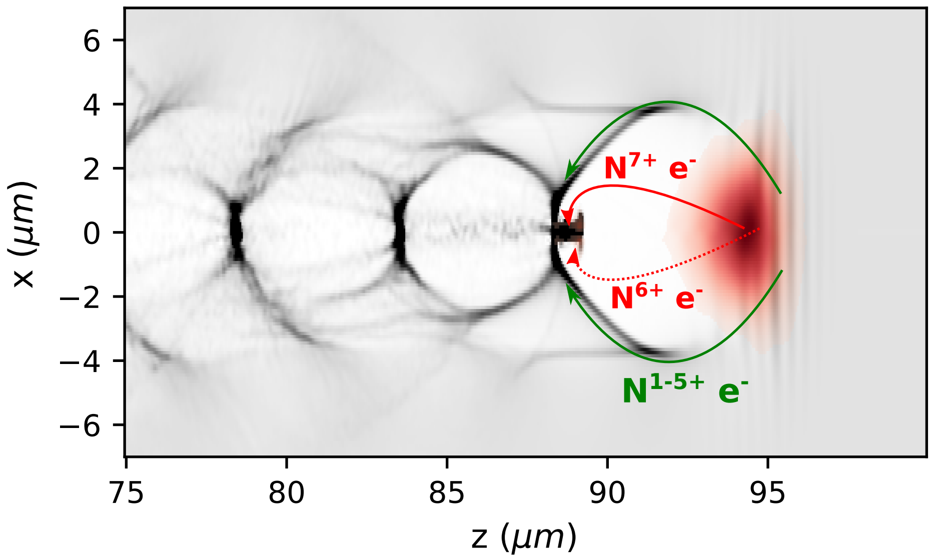

Figure 1.6 – Principle of ionization injection. The laser pulse envelope is showed in red scale. The typical trajectories of L-shell electrons (from N^{1-5+}) are displayed in green, the trajectories of injected K-shell electrons (from N^{6-7+}) are showed in red.

by the ponderomotive force and participate in the formation of the bubble (fluid trajectories). The K-shell shell electrons (from N^{6-7+}) are created near the peak of the pulse, already inside the bubble, they are trapped by the plasma fields and injected in the accelerating structure.

Ionization injection can be implemented by using pure nitrogen gas, but also by using a mixture of helium with a small percentage of nitrogen. This allows to limit ionization defocusing [69] induced by the numerous ionization levels of nitrogen, while still providing K-shell electrons for injection. This method can provide quite stable and reproducible beams, because the electrons are injected close to the laser axis, but as injection continues to occur as long as the intensity is higher than the threshold, it can lead to beams with large energy spreads because electrons are injected during an extended period of time. Additionally, the ionization process can lead to a residual transverse momentum of the electrons [68]. Indeed, when the electrons are ionized slightly away from the maximum of the electric field ($a = 0$ at E_{max}), they are created with a non-zero transverse momentum in the polarization direction which will usually result in a beam elongated on this axis.

1.6 Propagation of an ultra-intense, ultra-short laser pulse in an underdense plasma

When propagating into a plasma, an intense femtosecond pulse will experience several linear and non-linear phenomena that will modify its characteristics and behavior which can have a fundamental impact of the process of laser-wakefield acceleration. It is therefore important to know and quantify these effects in order to anticipate the actual state of the laser at the point of interaction, and its further evolution during the acceleration process.

1.6.1 Dispersion in a plasma

The refractive index of an underdense plasma is:

$$\eta = \sqrt{1 - \frac{\omega_p^2}{\omega_0^2}} \simeq 1 - \frac{1}{2}\frac{\omega_p^2}{\omega_0^2} = 1 - \frac{1}{2}\frac{n_e}{n_c} \tag{1.59}$$

We see that the refractive index depends on the laser frequency ω_0, and by considering the uncertainty relation $\Delta t \Delta\omega = 1/2$, ultra-short laser pulses have necessarily a large spectrum and therefore the dispersion of the plasma will be of importance, especially with near-single cycle pulses. Let us consider the electric field in the spectral domain:

$$E(\omega) = |E(\omega)| \exp(i\phi(\omega)) \tag{1.60}$$

where $\phi(\omega)$ is the spectral phase. We compute its derivative:

$$\frac{dE}{d\omega} = \left(\frac{d|E(\omega)|}{d\omega} + i\frac{d\phi}{d\omega}|E(\omega)| \right) \exp(i\phi(\omega)) \tag{1.61}$$

We can then compute the mean value $\langle t \rangle$:

$$\langle t \rangle = \int_{-\infty}^{+\infty} t|E(t)|^2 dt = -i\int_{-\infty}^{+\infty} E^*(t) itE(t) dt = -i\int_{-\infty}^{+\infty} E^*(\omega)\frac{dE}{d\omega}\frac{d\omega}{2\pi} \tag{1.62}$$

$$= -i\int_{-\infty}^{+\infty} |E(\omega)\frac{d|E(\omega)|}{d\omega}\frac{d\omega}{2\pi} + \int_{-\infty}^{+\infty} \frac{d\phi}{d\omega}\omega|E(\omega)|^2\frac{d\omega}{2\pi} \tag{1.63}$$

$$= -i\left[\frac{1}{2}|E(\omega)|^2|\right]_{-\infty}^{+\infty} + \langle\frac{d\phi}{d\omega}\rangle \tag{1.64}$$

The first term is zero so we can deduce:

$$\langle t \rangle = \langle\frac{d\phi(\omega)}{d\omega}\rangle \tag{1.65}$$

We can then compute the second moment $\langle t^2 \rangle$:

$$\langle t^2 \rangle = \int_{-\infty}^{+\infty} t^2|E(t)|^2 dt = \int_{-\infty}^{+\infty} |itE(t)|^2 dt = \int_{-\infty}^{+\infty} \left|\frac{dE}{d\omega}\right|^2 \frac{d\omega}{2\pi} \tag{1.66}$$

$$= \int_{-\infty}^{+\infty} \left(\frac{d|E(\omega)|}{d\omega}\right)^2 \frac{d\omega}{2\pi} + \int_{-\infty}^{+\infty} \left(\frac{d\phi(\omega)}{d\omega}\right)^2 |E(\omega)|^2\frac{d\omega}{2\pi} \tag{1.67}$$

$$= \langle t^2 \rangle_{\phi=0} + \langle\left(\frac{d\phi}{d\omega}\right)^2\rangle \tag{1.68}$$

The term $\langle t^2 \rangle_{\phi=0}$ is the square of the Fourier transform limited pulse duration in absence of spectral phase: $\Delta t_0^2 = \langle t^2 \rangle_{\phi=0}$. We can deduce the rms pulse duration after adding an arbitrary spectral phase From the expression 1.68:

$$\Delta t = \sqrt{\Delta t_0^2 + \Delta\tau_g^2} \tag{1.69}$$

Where $\tau_g = d\phi/d\omega$ is the the group delay, and $\Delta\tau_g^2 = \langle\tau_g^2\rangle - \langle\tau_g\rangle^2$. The propagation in a plasma of refractive index $\eta(z)$ on a distance z leads to the accumulation of the spectral phase:

$$\phi(z) = -\frac{\omega}{c}\int_0^z \eta(z)dz \tag{1.70}$$

If we assume a constant plasma density over the propagation distance z we can compute the pulse duration [70]:

$$\boxed{\Delta t = \Delta t_0\sqrt{1+\frac{z^2}{L_d^2}}} \tag{1.71}$$

With L_d the characteristic dispersion length:

$$L_d = \frac{2c\Delta t_0}{\omega_p^2}\left\langle\left(\frac{1}{\omega^2} - \left\langle\frac{1}{\omega^2}\right\rangle\right)^2\right\rangle^{-1/2} \tag{1.72}$$

Which can be simplified assuming a narrow distribution $\delta\omega \ll \omega_0$:

$$\boxed{L_d = 2c\Delta t_0^2\frac{\omega_0^3}{\omega_p^2}} \tag{1.73}$$

Note that the narrow spectrum approximation is at the limit of validity for near single cycle pulses, as for a 4 fs pulse, $\delta\omega/\omega_0 \simeq 1/3$. The pulse durations is taken as rms. The FWHM duration is therefore $\tau_{fwhm} = 2\sqrt{2\ln 2}\Delta t \simeq 2.355\Delta t$.

Let us first consider a 30 fs FWHM pulse propagating in a plasma of density $n_e = 5\times10^{18}\,\mathrm{cm}^{-3}$. After 10 mm of propagation, its duration is almost unchanged $\tau_{disp} = 30.2\,fs$, and therefore dispersion can be neglected in this regime. Let us consider now the propagation of a near-single pulse with $\tau_{fwhm} = 4$ fs in a plasma of density $n_e = 1\times10^{20}\,\mathrm{cm}^{-3}$. After a propagation of 100 µm, the pulse is stretched to a duration $\tau_{disp} = 6.9$ fs which corresponds to a 40% intensity loss.

But dispersion is a linear phenomenon, which can be compensated by applying the opposite dispersion beforehand, for example by propagating in a medium of index $\eta > 1$ such as fused silica (glass). We can compute the second order phase corresponding to the dispersion in a plasma:

$$\phi_2 = \left(\frac{\partial^2\phi}{\partial\omega^2}\right)_{\omega_0} \tag{1.74}$$

Where the phase accumulated by the propagation in the plasma is: $\phi(z) = -\omega/c\int_0^z \eta(z)dz \simeq -\omega/c\int_0^z[1-\omega_p^2/2\omega_0^2]dz$. By assuming a constant density and computing the second order derivative, we can express the chirp after a propagation distance z in a plasma:

$$\phi_2 = -\frac{z}{c}\frac{\omega_p^2}{\omega_0^3} \tag{1.75}$$

The quadratic phase (or chirp) accumulated during a 100 µm propagation in a $n_e = 1\times10^{20}\,\mathrm{cm}^{-3}$ plasma is therefore $\phi_2 = -8\,\mathrm{fs}^2$. The group velocity dispersion of fused silica at 800 nm is

$36\,\mathrm{fs}^2/\mathrm{mm}$ [71], therefore it is possible to pre-compensate the dispersion of the plasma by adding 220 µm of fused silica in the beam propagation beforehand.

1.6.2 Relativistic self-focusing

When a relativistic laser pulse propagates in an underdense plasma, two physical effects can contribute to modulate the refractive index radially with a maximum on axis, thus creating a self-focusing effect. First, the effective mass of the electrons is increased by the local Lorentz factor γ due to their transverse oscillation motion in the laser. Second, the ponderomotive force expels the electrons from the higher intensity zones, thus creating a radial density gradient. The refractive index is then written:

$$\eta = \sqrt{1 - \frac{\omega_p^2}{\gamma\omega_0^2}} = \sqrt{1 - \frac{n_e}{\gamma n_c}} \tag{1.76}$$

where $\gamma = (1 + u_\perp^2 + u_z^2)^{1/2}$. With $u_\perp = a$ and $u_z \ll u_\perp$, the Lorentz factor can be approximated as: $\gamma \simeq 1 + a^2/2$. By expanding this expression of the refractive index, and assuming a tenuous plasma, it can be expressed in first approximation as [72]:

$$\eta = 1 - \frac{1}{2}\frac{\omega_p^2}{\omega_0^2}\left(1 + \frac{\delta n_e}{n_e} - \frac{\langle a^2 \rangle}{2}\right) \tag{1.77}$$

Where $\delta n_e/n_e$ is the ponderomotive term, and $\langle a^2 \rangle/2$ the relativistic term. The threshold power at which the laser will self-focus can be expressed as [49, 73]:

$$P_c[GW] = 17.4\left(\frac{\omega}{\omega_p}\right)^2 = 17.4\left(\frac{n_c}{n_e}\right) \tag{1.78}$$

If $P < P_c$ the diffraction dominates and the laser is not self-focused, but if $P > P_c$ the laser self-focus and under the right conditions, diffraction and self-focusing can compensate and result in a self-guiding regime.

1.6.3 Self-compression and redshift of the pulse

We can now consider the longitudinal variations of the refractive index. While radial variations of the index can lead to self-focusing of the pulse, fast longitudinal variations can lead to a change in the instantaneous frequency of the pulse after a small propagation δz:

$$\omega = \frac{\partial \phi}{\partial t} = \omega_0 - \frac{\omega_0}{c}\frac{\partial n}{\partial t}\delta z \tag{1.79}$$

The frequency variation is thus:

$$\delta\omega = \omega - \omega_0 = -\frac{\omega_0}{c}\frac{\partial \eta}{\partial t}\delta z \tag{1.80}$$

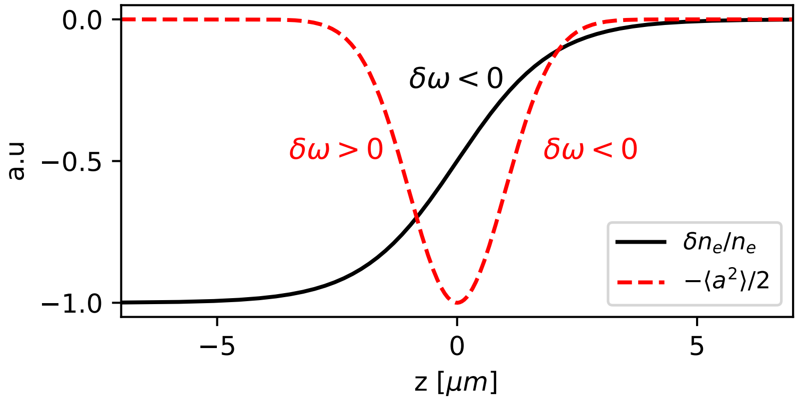

Figure 1.7 – Principle of the frequency shift $\delta\omega$ associated with the relativistic (red) and ponderomotive (black) terms

Which can be expressed in the laser co-moving frame ($\zeta = z - ct$):

$$\delta\omega = -\frac{\omega}{c}\frac{\partial\eta}{\partial\zeta}\frac{\partial\zeta}{\partial t}\delta z = \omega\frac{\partial\eta}{\partial\zeta}\delta z \tag{1.81}$$

Equation 1.81 indicates that if the refractive index decreases longitudinally, $\delta\omega < 0$, lower frequency are produced (redshift) and if it increases, $\delta\omega > 0$ and higher frequency are produced (blueshift). Now if we consider the refractive index from equation 1.77, the relativistic and ponderomotive terms will have different physical effects. The relativistic term $-\langle a^2\rangle/2$ leads to the redshift of the front (negative gradient) and blueshift of the back (positive gradient) of the pulse (see Fig.1.7). Then, due to dispersion in the plasma, the redshifted front will propagate at a slower velocity than the blueshifted back, which can lead to self-compression of the pulse and result in shorter duration than initially [74–76]. The term in $\delta n_e/n_e$ will induce a negative gradient of the index between the back and the front of the pulse: the back is inside the ion cavity, the local index is maximum. In the front, the electrons have not yet been expelled by the ponderomotive force, the local index is minimum (see Fig.1.7). If the pulse is sufficiently short compared to the plasma wavelength λ_p, this results in a global redshift of the pulse.

1.6.4 Ionization defocusing

When an intense laser pulse is focused in a gas jet, the very front of the pulse ionizes the atoms via barrier-suppression and the rest of the pulse propagates in a plasma. But, if the center of the pulse has a sufficiently high intensity to fully ionize helium and hydrogen, or ionize up to N^{5+} nitrogen, this is not necessarily the case further away from the axis where the laser intensity is lower. This results is a radial distribution of the plasma density which is maximum on-axis and decreases with r, with steps corresponding to the ionization levels. This means that the center of the beam will experience a lower refractive index than the edges thus creating a defocusing lens effect [69, 77]. It can prevent the laser to reach its diffraction-limited vacuum spot size, therefore reducing the maximum intensity. But this phenomenon strongly depends on the ionization levels of the gas used. Figure 1.8 shows a simplistic modeling of the radial plasma density by an intense laser, assuming a level is ionized if the laser intensity is

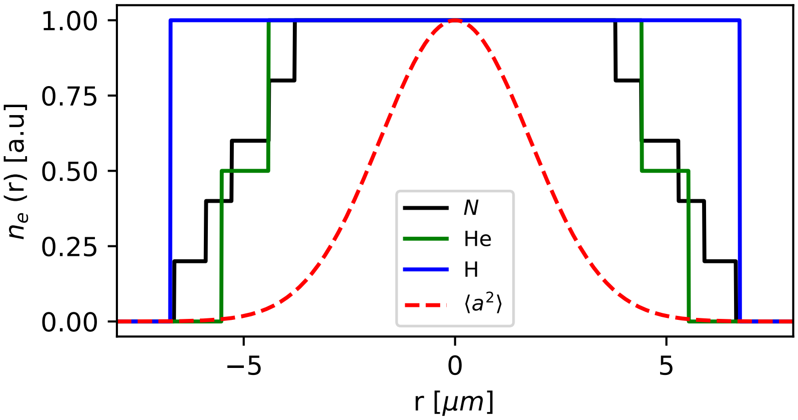

Figure 1.8 – Simplified modeling of the normalized radial plasma density for different molecules assuming a level is ionized when the laser intensity reaches its associated barrier suppression threshold $I > I_{bs}$.

over the barrier-suppression limit. It shows that, for nitrogen, the several ionization levels with the fifth being at relatively high intensity ($I_{bs} = 1.5 \times 10^{16}\,\mathrm{W\,cm^{-2}}$) lead to a decreasing radial density with several steps, therefore nitrogen will lead to strong defocusing. On the contrary, hydrogen has only one ionization level, at a lower intensity ($I_{bs} = 1.4 \times 10^{14}\,\mathrm{W\,cm^{-2}}$) and thus its defocusing effect will be much lower. Helium is intermediate, with two ionization levels at moderate intensities. This leads to two conclusions to minimize the detrimental effect of ionization defocusing: (i) using low-Z gas such as hydrogen or helium should yield better performances because of the lower number of ionization levels and the lower intensity necessary to reach it, (ii) the propagation in plasma before the focus should be limited in order to prevent the defocusing of the laser before self-focusing is able to compensate it.

Additionally, a similar step-profile associated with the different ionization levels is produced longitudinally associated with the temporal distribution of the laser intensity which can contribute to blueshift the front of the pulse.

1.7 Carrier-envelope phase effects: theoretical predictions

1.7.1 Context and general observations on CEP

Let us consider the expression of the electric field of a laser pulse with a gaussian envelope with a carrier frequency ω_0:

$$E(z,t) = E_0 \exp(-t^2/2\tau^2) \exp[i(kz - \omega_0 t + \phi_{CEP})] \tag{1.82}$$

The carrier-envelope phase (CEP) of the pulse is the phase ϕ_{CEP} between the carrier-wave of the electric field and its envelope. It is a global phase term, constant on the whole spectrum which does not result in a instantaneous frequency. While it is defined for any pulse length, CEP becomes a meaningful quantity when the number of optical cycle in the pulse becomes close to one. Indeed, for many cycles pulses such as showed in the top panel of figure 1.9, the

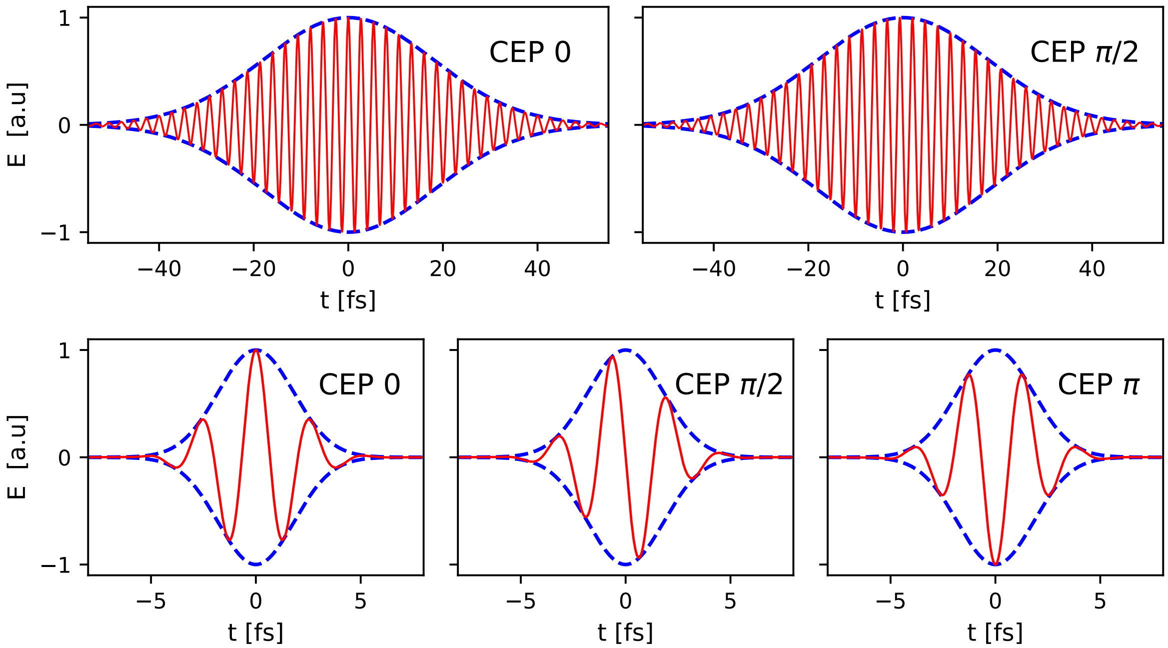

Figure 1.9 – Temporal electric field (red) and its envelope (blue) corresponding to a 30 fs (top) and a 3 fs (bottom) pulse at $\lambda_0 = 800\,nm$, for different carrier-envelope phases (CEP). Pulse duration is taken as FWHM of intensity.

envelope evolves slowly compared to the oscillations of the electric field. Therefore a different CEP induces only a small shift in the relative position of the carrier and the envelope, and the electric fields for the two different CEP in the 30 fs case are almost indistinguishable. But when considering a near-single cycle pulse (3 fs is 1.1 optical cycle at 800 nm), both the carrier and the envelope evolve on a similar timescale and different CEP lead to significantly different shapes of the electric field.

The break-down of the ponderomotive force

The usual description of the interaction between the laser and the plasma in a laser-wakefield accelerator is based on the effect of the ponderomotive force of the pulse which expels the electrons from the higher intensity zones and excite a plasma wave, as seen in section 1.2. And because the ponderomotive force depends solely on the envelope of the pulse, the interaction has an axial symmetry and is independent from the polarization. But in order to derive this ponderomotive force, we had to assume that two separate time scales govern the physics: a fast motion on the timescale of the electric field, and a slower one corresponding to the pulse envelope. This assumption is valid in the case of many cycle pulses, but breaks down for single cycle or near-single cycle pulses where the timescales for the electric field oscillations and the envelope variation are similar. It is therefore necessary to consider the actual shape of the waveform, taking into account the carrier-envelope phase, and a deviation from the axial symmetry usually imposed by the ponderomotive force can be anticipated.

The slippage of CEP in a plasma

When a laser pulse propagates in a plasma, its phase velocity $v_{ph} = c\left(1-\omega_p^2/\omega_0^2\right)^{-1/2}$ is higher than its group velocity $v_g = c\sqrt{1-\omega_p^2/\omega_0^2}$ because of the plasma dispersion. Therefore, the CEP changes during propagation, and the typical length after which it has slipped from 2π can be expressed as:

$$L_{2\pi} = \frac{c}{v_{ph}-v_g}\lambda_0 \simeq \frac{n_c}{n_e}\lambda_0 \qquad \left(\frac{n_e}{n_c} \ll 1\right) \tag{1.83}$$

If we consider a plasma density of $n_e = 1 \times 10^{20}\,\mathrm{cm}^{-3}$ typical of our kilohertz LWFA regime with near-single cycle pulses, the CEP slippage length is $L_{2\pi} = 14\,\mu\mathrm{m}$ which is a very short distance. This has several implications on a potential study of carrier-envelope phase effects in a laser-wakefield accelerator:

- The CEP value at the interaction point will necessarily be different from the initial CEP
- The value of the CEP will change significantly during the propagation and interaction, and will even perform several 2π loops
- In order to be able to observe an effect of different initial CEP on a process of the interaction (*e.g.* the injection), this process has to be localized on distance inferior to $L_{2\pi}$. If it is not the case, the effects associated with all the different instantaneous values of the shifting CEP will average out and no particular effect of the CEP on the electron beam will be detected.

The slippage of the carrier-envelope phase is one the main reasons for which observing effects of the CEP during the interaction of a laser with an underdense plasma remains a challenge, and require a very fine control of the parameters. On the other hand, it has been demonstrated in several experiments in the case of solid targets [29–34], in which the interaction is localized to the surface of the over-critical plasma, and therefore the CEP has a fixed value.

1.7.2 Transverse asymmetry of the plasma wave

The complex interaction of near-single cycle, or few-cycle laser pulses with an underdense plasma has been first studied in numerical simulations that pointed out a transverse oscillation of the plasma bubble and a modulation of the self-injected electron beam in the polarization plane [79, 80]. This effect was in a first instance attributed in [80] to the hosing instability of the laser pulse and the electron beam, but the standard description of this instability [81, 82] fits well in the cycle-averaged ponderomotive framework and fails to explain the observed polarization dependence. Nerush and Kostyukov [28] showed by using a perturbation development of the plasma response to a near-single cycle pulse up to the second order, that when considering higher-order terms, an asymmetry appears in the transverse momentum p_y of the electrons scattered by the laser pulse in the polarization direction (y). This asymmetry depends on the value of the laser carrier-envelope phase, and leads to the formation of an asymmetric bubble in the polarization plane, while it remains perfectly symmetric in the perpendicular direction. The authors define the quantity $\Lambda = p_y(y_0) + p_y(-y_0)$, the sum of the momenta of two electrons that have gone through the laser with an initial transverse position symmetric with respect to the propagation axis, in order to quantify the asymmetry. In absence of asymmetry,

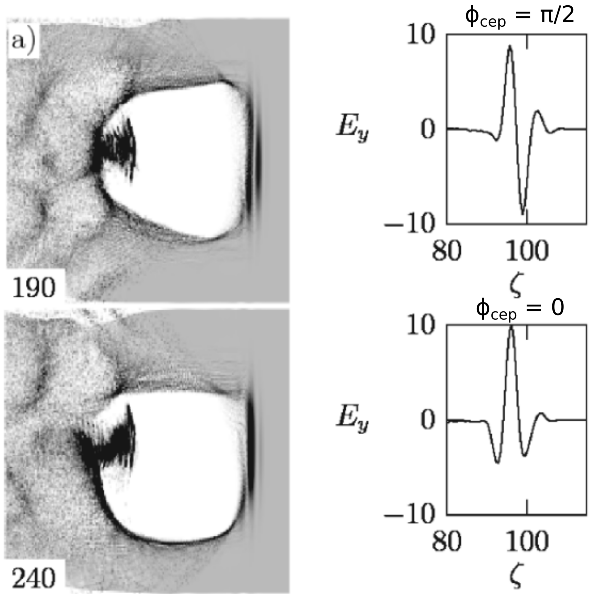

Figure 1.10 – Images of the bubble in the polarization plane from PIC simulations from [28] and the corresponding on-axis laser electric field at two different times of the simulation, corresponding to two different laser CEP.

$\Lambda = 0$. They find that the momentum asymmetry in the polarization direction scales as:

$$\Lambda \propto \frac{a_0^3}{w_0^2 \tau^2} \lambda_0^4 \cos(\phi_{cep}) \tag{1.84}$$

Where w_0 is the laser spot size, τ the pulse duration, λ_0 the laser central wavelength, and ϕ_{cep} the CEP. In the perpendicular direction, the bubble remains symmetric at the second order. A more convenient measurement of this asymmetry is the deviation of the centroid of the high density electron sheath forming the bubble, normalized to the laser waist, which can be expressed:

$$\Gamma_y = \frac{\int n_e y dy}{w_0 \int n_e dy} \tag{1.85}$$

Where n_e in the plasma density. It was observed from PIC simulations in [28] that Γ_y is proportional to Λ and therefore has the same scaling. From the scaling 1.84, we deduce that the asymmetry that arises in the polarization plane depends indeed on the value of the CEP, which is illustrated by the image of the wake in Fig. 1.10 for two different CEP. When $\phi_{cep} = \pi/2$, the positive and negative peaks of the electric field have the same amplitude, their effect on the electron compensate and it yields a symmetric bubble. When $\phi_{cep} = 0$, the positive peak of the electric field is higher amplitude than the the two negative peaks, the electrons will therefore be pushed slightly more towards the $y < 0$ and the bubble is shifted downward. A CEP of π will result in the opposite case of a bubble shifted upwards.

Now if we consider, as explained is the previous section, that the value of the CEP evolves during the propagation in the plasma due to the dispersion, it follows that the plasma bubble oscillates transversely in the polarization direction with a spatial period $L_{2\pi}$. This behavior was indeed observed in our PIC simulations carried out by Julius Huijts [78] (see Fig.

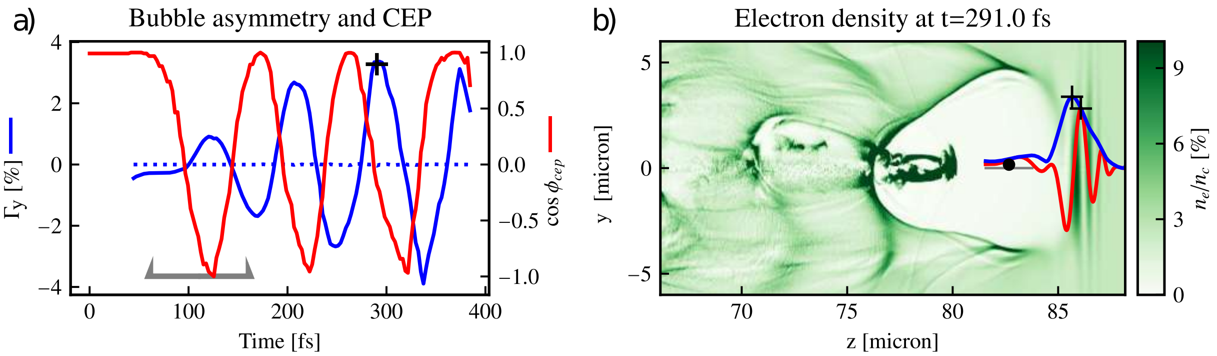

Figure 1.11 – PIC simulation from [78], with a 3 fs pulse at $\lambda_0 = 800\,\text{nm}$ focused to a 5 µm spot with $a_0 = 4$ in a plasma density $n_e = 4.3 \times 10^{19}\,\text{cm}^{-3}$. a) Asymmetry of the bubble (blue) in the polarization plane (solid) and in the perpendicular plane (dotted), and evolution of the carrier-envelope phase (CEP) of the laser driver (red). b) Snapshot of the asymmetric plasma wave in the polarization plane, as well as the laser electric field (red) and envelope (blue). From

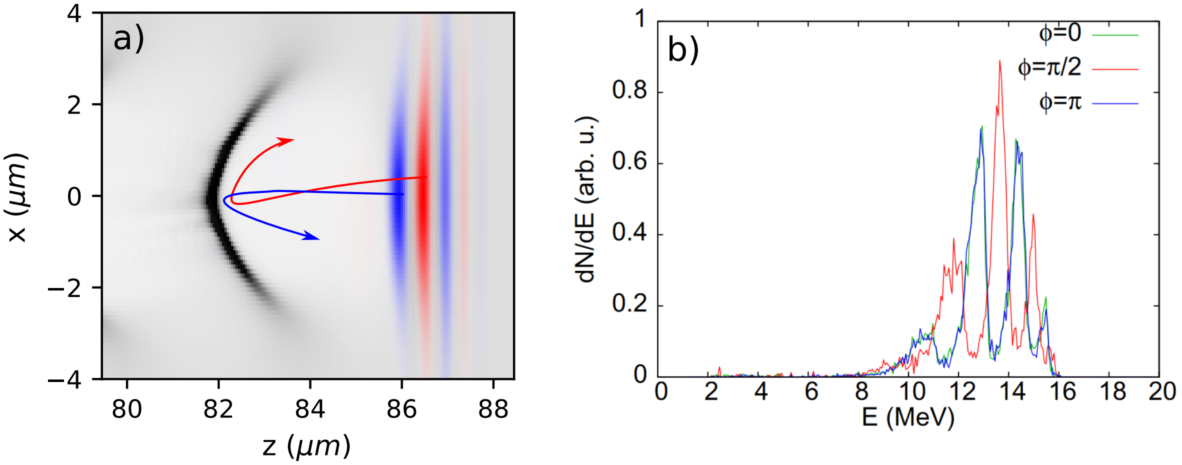

Figure 1.12 – a) Ionization injection with a near-single cycle pulse. Representation of the trajectories of electrons injected at different peaks of the electric field. b) Energy spectrum of electrons injected by ionization by a near-single cycle pulse for different initial laser CEP, from a PIC simulation from [84]

1.11) intended to determine the effects of carrier-envelope phase in a favorable high-intensity case with parameters quite different from the regime achieved in our experiment ($a_0 = 4$, $n_e = 4.3 \times 10^{19}\,\text{cm}^{-3}$). This work also identified the variation of the beam pointing as a key experimental observable associated with CEP effects in laser-wakefield acceleration. By using an Hamiltonian description, and a simplified model of this oscillating wakefield represented by a positively charged spherical bubble propagating at uniform velocity and oscillating vertically, Kim *et al.* [83] showed that this transverse oscillation of the accelerating structure can trigger periodic injection of electrons with a period $L_{2\pi}/2$.

1.7.3 CEP and ionization injection

Ionization injection occurs in a high-Z gas such as nitrogen in which the ionization of N^{5+} and N^{6+} levels requires a high intensity that can be reached solely near the peak of the pulse.

Additionally, ionization occurs preferably near the peaks of the electric field. So when the laser pulse is near-single cycle, only a few peaks will contribute to the injection, and the separation between each peak is significant compared to the whole pulse envelope. The injection will thus be discontinuous in space, with several separate bunches originating from different extrema of the electric field. Lifschitz and Malka [84] showed with PIC simulations that these bunches originating from different peaks of the electric field, and therefore from a different position relative to the bubble, end up with different energies because of their trajectories is associated to different initial conditions. This leads to an energy spectrum with several narrow peaks associated to different ionization peaks (see Fig. 1.12). When varying the laser CEP, the position of each peak is shifted (for example, when CEP is shifted from 0 to $\pi/2$, a position where E was 0 is now an ionizing extrema) which leads to different trajectories of the injected electrons and therefore shifted energy peaks (see Fig. 1.12b). Additionally, the initial residual transverse momentum $p_{\perp,i} = a_{ioniz}$, and thus the final pointing of each injected bunch depends on the sign of the ionizing electric field. So there is a clear correlation between the semi-cycle responsible for the ionization and the exit angle of a bunch in the polarization direction. Because different semi-cycles yield different energies, a correlation arises between the energy and the pointing direction of each bunch. This means that experimentally, we can expect to observe in case of ionization injection injection, oscillations in the beam pointing and a spectra of the electrons correlated with the angle of observation.

Chapter 2

Experimental set-up and methods

Sommaire

2.1 The Salle Noire 2 laser system

We have seen that in order to scale efficiently LWFA to kilohertz laser systems delivering pulse energies of a few millijoules, it is necessary to reduce the pulse duration close to one single optical cycle. This requirement was well in line with the goal of the PCO (*Physique du Cycle Optique*) group led by Rodrigo Lopez-Martens to develop a kilohertz laser system able to reach the so-called lambda-cubed regime [85]. In this regime, light is focused down to a $\sim \lambda$ spot size with a single cycle pulse duration, in order to drive efficient and high-repetition rate High Harmonic generation (HHG) from the interaction of the relativistic pulse with a plasma mirror. To achieve this, the PCO group developed a laser system with a global architecture that differs

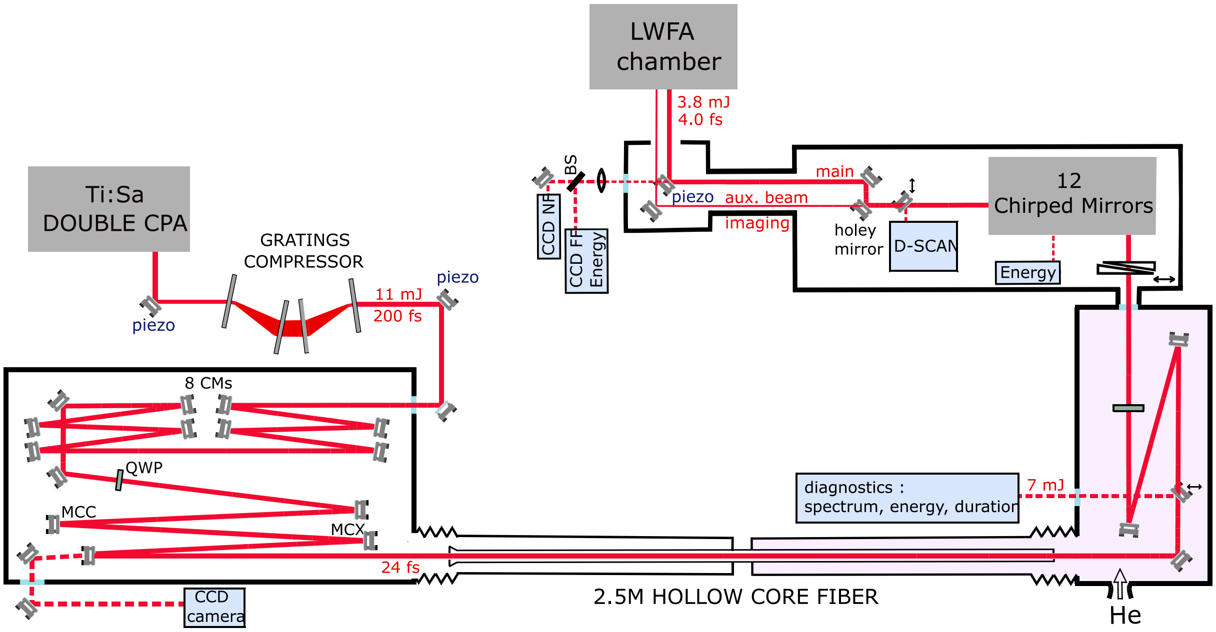

Figure 2.1 – Post-compression setup. CM: chirped mirror, QWP: quadri-wave plate, MCC: concave mirror (ROC=2.5m), MCX: convex mirror (ROC=-2m).

from usual multi-cycle 10s of TW or 100s of TW lasers. These standard titanium-sapphire systems amplify spectra with a bandwidth that do not support pulse durations much shorted than 20 fs. The goal of this section is to present an overview of this laser system and some of the diagnostics relevant to our experiment. A much more detailed description of the Salle Noire 2 system can be found in Marie Ouillé's thesis [86, 87].

2.1.1 Double CPA chain

The first brick of this laser, which is actually composed itself of many different elements, is a double CPA system that delivers 10 mJ, 25 fs pulses at a kilohertz repetition rate. To reach this point, we start from a commercially available oscillator (Rainbow, Femtolaser) that produces nJ-level pulses at 80 MHz. They are then amplified to 1.3 mJ by the first CPA stage which is a 10 pass Ti:Sa amplifier (Femtopower, Femtolaser), in which the repetition rate is brought down to 1 kHz by a Pockels cell. The next step is then to increase the temporal contrast of the pulse through a Cross-Wave Polarization (XPW) filter. The XPW technique [88] uses a third order non-linear effect that leads to the generation of a light wave with a polarization orthogonal from the incident one. The efficiency of the conversion scales with the cube of the incident intensity so that only the high intensity part of the pulse has its polarization rotated. A polarizer then selects the rotated wave, which cleans the pulse from its lower intensity parts. Finally, the pulse is sent through the second CPA, composed of two amplification stages: a 6 pass Booster (Femtolaser) that bring the energy to 3.3 mJ and a homemade 2 pass Power Amplifier. After recompression by the gratings, the energy is around 10 mJ per pulse, and the duration between 25 and 30 fs.

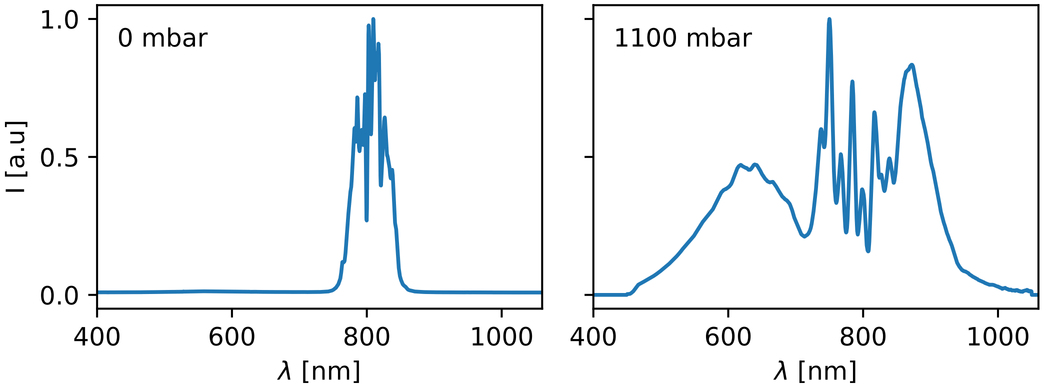

Figure 2.2 – Left: Spectra of the laser after the HCF in vacuum (no compression). Right: Spectra after the HCF filled with 1100 mbar of helium.

2.1.2 Post-compression in a hollow-core fiber

The double CPA laser system just described produces multi-cycle pulses of 25 fs, quite far for the near-single cycle, sub-5fs pulses for which we aim for to resonantly drive a wakefield with few millijoules of energy. It is therefore necessary to create additional frequency components to obtain a spectrum sufficiently broad to support a sub-5 fs Fourier-transform limited (FTL) pulse duration. This spectral broadening is obtained by focusing the pulse into a 536 µm diameter, 2.5 m long hollow-core fiber (HCF) filled with helium gas [89, 90], in which the laser will experience self-phase modulation resulting in the creation of new frequencies on each side of the spectrum.

More precisely, after the gratings the pulse is not perfectly compressed to prevent the apparition of non-linear effects on the gratings and through the following window, and it is then finely adjusted via a set of 8 chirped mirrors. The pulse is then focused into the hollow-core fiber and a fast beam-stabilization ensures that the pointing matches the position of the entrance of the fiber. The linear polarization is converted to circular with a quarter-waveplate in order to reduce the peak electric field in the fiber and thus limit ionization. A helium gradient is imposed in the fiber by setting a pressure value at the exit (typically 1000 mbar), and keeping the entrance chamber under vacuum by pumping it continuously. This ensures a more efficient coupling through the fiber while reducing ionization and self-focusing due to Kerr effect [91]. Figure 2.2 shows the laser spectra after the HCF when there is no compression ($P_{HCF} = 0$ mbar) and for maximum compression ($P_{HCF} = 1100$ mbar), corresponding to a pulse duration of 3.5 fs. In the latter case, the spectrum covers the whole 450-1000 nm range. The typical transmission of the HCF is around 50%. The polarization is then converted back to linear with a quarter-wave plate, and sent through a window to a vacuum chamber, where the dispersion accumulated in the fiber is compensated by a set a chirped mirrors (Initially 12, and then 16 after a modification). A pair of motorized wedges can be translated to fine tune the dispersion and achieve optimal compression, or slightly chirp the pulse. The pulse is then sent toward our experimental chamber. An interesting feature of post-compression using a HCF is that by changing the value of the pressure of helium in the fiber, we can continuously tune the pulse duration between 25 fs and 3.5 fs without impacting the other parameters such as pulse

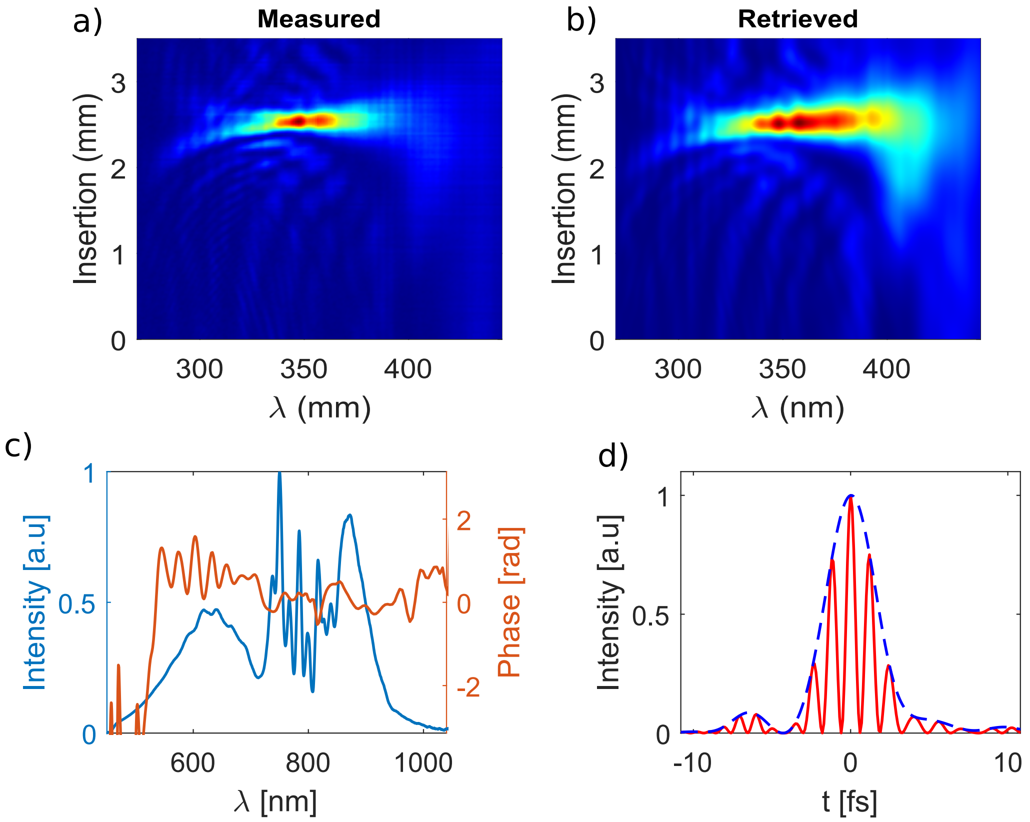

Figure 2.3 – a)-b) Measured and retrieved d-scan trace of the SHG spectrum as a function of the insertion of the wedges. c) Spectral intensity and phase retrieved by the d-scan measurement. d) Temporal intensity and squared electric field of the pulse measured by the d-scan. The pulse duration is 3.6 fs FWHM.

energy and size of the focal spot.

2.1.3 Pulse duration measurement with the d-scan

In order to measure the duration of pulses as short as the ones achieved in Salle Noire 2, that can go as low as 3.5 fs, we use a commercially available d-scan (Sphere Photonics [92]). It allows to characterize the pulse duration and spectral phase of the laser in a relatively user-accessible manner. The principle of the measurement is to frequency double the laser in a BBO crystal and measure the second harmonic spectrum as a function of the group-delay dispersion (GDD) by varying the insertion of motorized fused silica wedges in the beam. The optimal compression corresponds to the insertion of the wedges that yields the broadest SHG spectrum. An iterative algorithm [93] is used to retrieve the spectral phase. The complex electric field in the spectral domain can be written:

$$\tilde{E}(\omega) = |\tilde{E}(\omega)| \exp(i\phi(\omega)) \tag{2.1}$$

Where $|\tilde{E}(\omega)|$ is given by the fundamental spectrum, and $\phi(\omega)$ is the spectral phase. The temporal amplitude of the frequency doubled pulse is proportional to square of the electric field that propagated in a thickness z of glass beforehand:

$$U(t,z) \propto \left(\int_{-\infty}^{+\infty} \tilde{E}(\Omega) \exp(ik(\Omega)z) \exp(i\Omega t) d\Omega \right)^2 \tag{2.2}$$

Where U is the temporal amplitude of the SHG pulse, and $k(\Omega)$ the frequency dependent wavenumber of the pulse in fused silica. By Fourier transform we obtain the spectral intensity of the SHG pulse:

$$S(\omega,z) \propto \left| \int \left(\int_{-\infty}^{+\infty} \tilde{E}(\Omega) \exp(ik(\Omega)z) \exp(i\Omega t) d\Omega \right)^2 \exp(i\omega t) dt \right|^2 \tag{2.3}$$

The algorithm starts from an initial guess of the spectral phase, and retrieves the spectral intensity of the SHG for each insertion of the wedges with this method. The SHG trace is compared to the measured one, and a new guess of the spectral phase is performed using a minimization technique. After convergence the spectral phase of the pulse is thus characterized, while the spectral amplitude is measured with a spectrometer. Figure 2.3 shows the result of a d-scan measurement for a 1100 mbar pressure of helium in the HCF. The spectral phase is relatively flat on the whole spectrum, except for wavelength under 500 nm, where the signal is very low. Oscillations of the phase can be observed in the 550 nm-700 nm range of the spectrum and are most probably due to the phase response of the chirped mirrors. This data allows us to retrieve the temporal pulse shape, with a pulse duration in this case of 3.6 fs FWHM. Note that here, the pulse is arbitrarily represented with a carrier-envelope phase of 0 (maximum of the envelope synchronized with the maximum of the electric field) but the d-scan cannot measure the actual value of the CEP.

2.1.4 Estimation of the peak intensity

The laser peak intensity is an important parameter of the interaction with the plasma, as it informs us if the laser is sufficiently intense to drive a high amplitude wakefield for accelerating electrons. It integrates three different measurements of the laser parameters: the energy per pulse, the duration, and the spatial profile at focus. The pulse energy is measured using a laser calorimeter (gentc-EO) just before the final focusing parabola. The pulse duration measurement method has been described in the previous section. In order to obtain the focused laser spatial profile, we attenuate it first by the reflection on a glass plate, and then by inserting a pellicle attenuator in the beam. The focal spot is then imaged by a microscope objective onto a CCD camera providing us with the spatial distribution at focus.

We can express the laser energy as the integral in space and time of the intensity:

$$E_{las} = \iiint_{-\infty}^{+\infty} I(x,y,t) dx dy dt \tag{2.4}$$

By assuming a gaussian temporal and spatial profile , one can obtain:

$$E_{las} = \frac{I_0 \pi w_0}{2} \frac{\sqrt{\pi} \tau_{fwhm}}{\sqrt{4 \ln 2}} \tag{2.5}$$

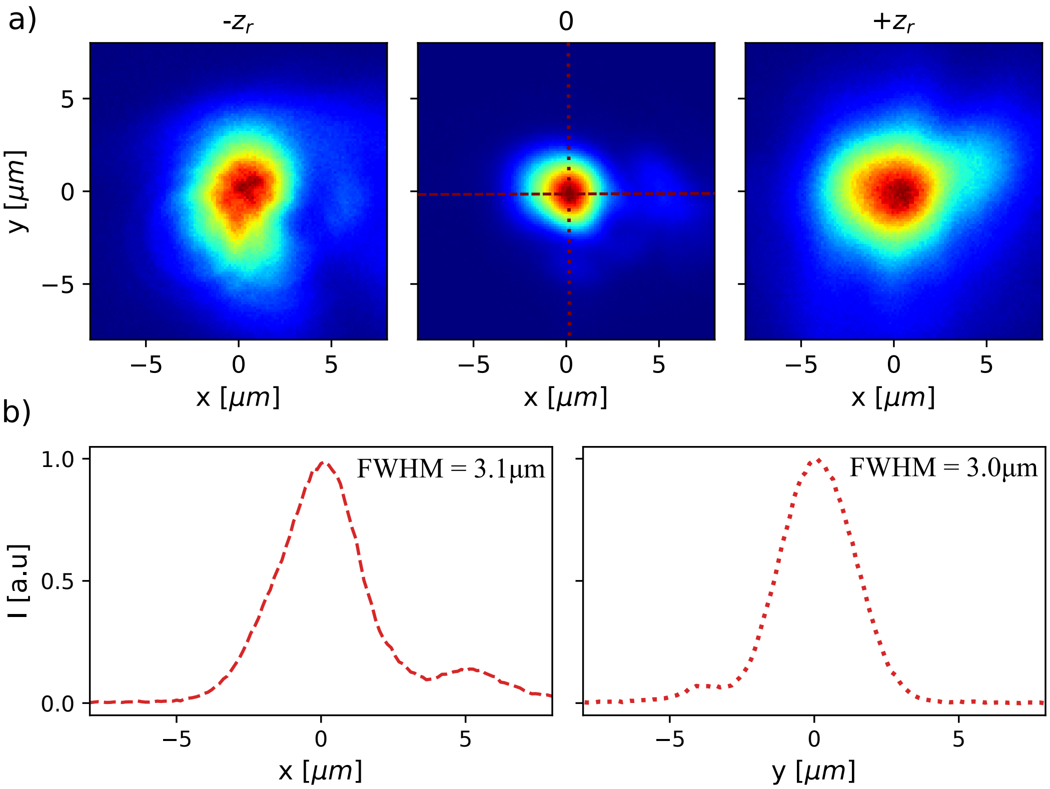

Figure 2.4 – a) Laser spots at: $z = -z_r$, $z = 0$ and $z = +z_r$. Here $z_r \sim 50\,\mu\text{m}$. b) Horizontal (left) and vertical (right) lineout of the intensity centered on the peak. The laser is focused with a f/2 (f'=50 mm) off-axis parabola.

Where w_0 is the waist of the laser, and τ_{fwhm} the full width half maximum pulse duration. And therefore:

$$I_0 = \frac{2E_{las}}{\pi w_0} \frac{\sqrt{4\ln 2}}{\sqrt{\pi}\tau_{fwhm}} \simeq \frac{2E_{las}}{\pi w_0 \tau_{fwhm}} \tag{2.6}$$

This is useful to have a rough idea of the peak intensity considering typical parameters, but it does not precisely describe the experimental reality where pulses can deviate significantly from the gaussian profile. To retrieve the real vacuum intensity from measured data, we neglect spatio-temporal couplings and therefore that we can write the intensity as:

$$I(x,y,t) = I_0 f(x,y) g(t) \tag{2.7}$$

Where f(x,y) is the normalized spatial intensity of the focal spot, given by the image from the camera, and g(t) the normalized temporal intensity measured with the d-scan. The laser energy is thus written:

$$E_{las} = I_0 \iint_{-\infty}^{+\infty} f(x,y)dxdy \int_{-\infty}^{+\infty} g(t)dt \tag{2.8}$$

And the peak intensity is obtained via:

$$I_0 = \frac{E_{las}}{\iint_{-\infty}^{+\infty} f(x,y)dxdy \int_{-\infty}^{+\infty} g(t)dt} \tag{2.9}$$

Which can be integrated numerically using experimental data.

Figure 2.4 shows the laser spot at focus and at a Rayleigh length on both sides, when using a f/2 off-axis parabola. The spatial profile is quite nice, mainly because the hollow-core fiber acts as a spatial filter that results in a clean laser profile. The spot is 3.1×3.0 µm FWHM. Using a measured on-target energy of 2.9 mJ, a pulse duration of 3.8 fs and integrating the spatial intensity of the pulse, we retrieve $I = 5.2 \times 10^{18}\,\mathrm{W\,cm^{-2}}$. An if we take into consideration the temporal profile measured with the d-scan and integrate over it, this yields the corrected intensity: $I_{exp} = 4.1 \times 10^{18}\,\mathrm{W\,cm^{-2}}$.

2.1.5 CEP stabilization

We have seen in section 1.7 that the carrier-envelope phase of the laser could impact the physics of laser-wakefield acceleration driven by near-single cycle pulses. In order to study these effects we need to measure and control the CEP of the laser. Stabilizing the CEP was an important part of Marie Ouille's PhD work, and it has enabled the results on CEP presented later in this manuscript. A thorough description of the details of CEP stabilization is presented in her manuscript [86], while we will simply give here a general picture of the method.

CEP stabilization of the oscillator

In an oscillator, the CEP shifts from one pulse to the other is associated to an offset of the frequency comb in the spectral domain [94]. If this offset is equal to the repetition rate of the oscillator (which is the distance between two peaks of the comb), two consecutive pulses will have the exact same spectra and therefore same CEP. In the temporal domain, this means that the CEP shift associated with a round trip in the dispersive medium of the cavity should be 2π so that two consecutive pulses have the same phase. In practice, it is not necessary that every consecutive pulse have the same CEP because the repetition rate of our laser (1 kHz) is much lower than the oscillator (80 MHz). The phase shift between two consecutive pulses is thus set to $\pi/2$ meaning every fourth pulse of the oscillator will have the same CEP which is largely sufficient in our case. The CEP of the oscillator is then stabilized by a feedback loop on the oscillator which modulates the power of the pump laser through an acousto-optic modulator (managed by an XPS800 by Menlo Systems, Garching, Germany). This modifies the strength of the Kerr-lens effect and therefore slightly changes the effective optical path in the cavity [94, 95].

Sources of CEP instabilities

We can distinguish three main sources of instability affecting the laser chain:

- A linear one associated with fluctuations in the optical path because of a change in the refractive index due to temperature variation, or of the traveled length due to vibrations and misalignment.

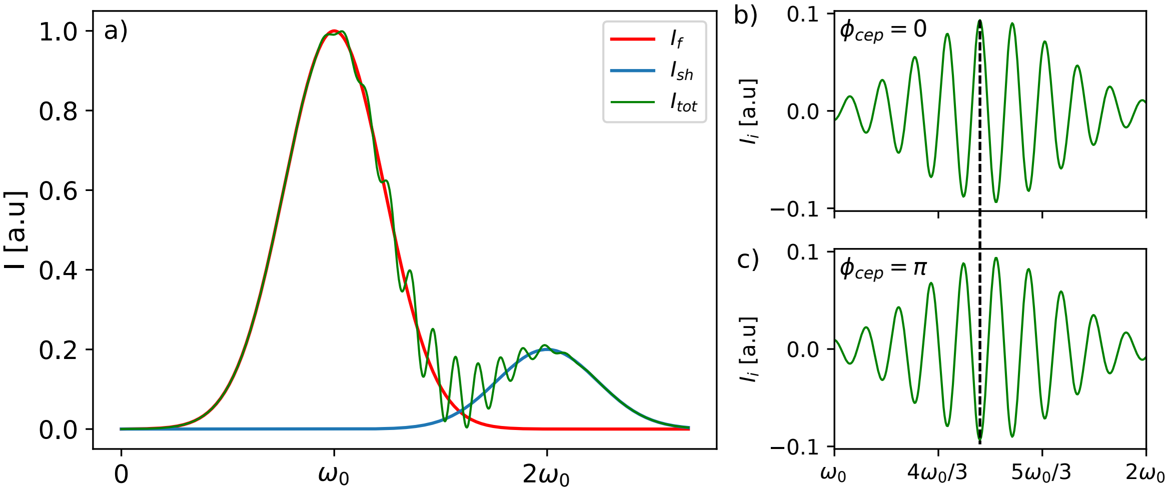

Figure 2.5 – Principle of the f-2f interferometer. a) Spectral intensities of the fundamental (red) the frequency doubled pulse (blue) and the resulting interferometry pattern (green). b)-c) Fringes intensity corresponding to $I_i = I_{tot} - I_f - I_{sh}$, for an initial CEP of 0 and π

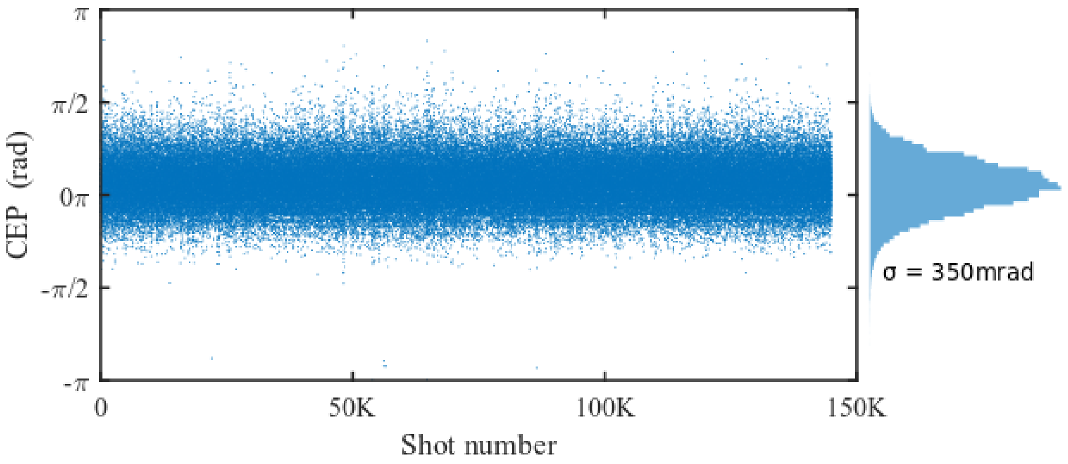

Figure 2.6 – Single-shot CEP stabilized and measured by the Fringeezz over 2 minutes. The typical stability here is 350 mrad RMS.

— A non-linear one coming from the change in the non-linear phase accumulated at high intensity due to variations of the energy or intensity.

— The amplification process can lead to phase changes associated to resonances in the medium. Therefore variations of the pump power can lead to CEP instability.

This means that even if the CEP is stabilized at the output of the oscillator, all these sources of noise further in the laser system will make the CEP very unstable. A solution is to add another feedback loop measuring the CEP at the end of the system.

f-2f interferometer and second feedback loop

In order to measure the CEP near the end of the system (after spectral broadening and compression), we send a wedge reflection of part of the beam into a f-2f interferometer [96]. A f-2f interferometer is based on spectral interferometry of the fundamental pulse at the frequency ω_0 with a frequency doubled pulse at $2\omega_0$. To do this, the fundamental is slightly chirped before the doubling so that the blue part from the fundamental and the frequency doubled pulse are separated by a time τ. Let us consider two components from the broad fundamental E_f at ω_0 and $2\omega_0$:

$$E_f(\omega_0) = E_0(\omega_0)\exp(-i\omega_0 t + i\phi_{cep}) \tag{2.10}$$

$$E_f(2\omega_0) = E_0(2\omega_0)\exp(-i2\omega_0(t-\tau) + i\phi_{cep}) \tag{2.11}$$

The component at ω_0 is then frequency doubled to $E_{sh}(2\omega_0)$:

$$E_{sh}(2\omega_0) = E_{sh0}(2\omega_0)\exp(-i2\omega_0 t + i2\phi_{cep}) \tag{2.12}$$

The two components around $2\omega_0$: $E_f(2\omega_0)$ and $E_{sh}(2\omega_0)$ interfere and yield an intensity:

$$I_{tot}(\omega) = I_f(\omega) + I_{sh}(\omega) + 2\sqrt{I_f(\omega)I_{sh}(\omega)}\cos(\omega\tau + \phi_{cep}) \tag{2.13}$$

As represented in Fig. 2.5 there are intensity fringes with a frequency interfringe $i_\omega = 2\pi/\tau$. We see from equation 2.13 and from Fig. 2.5b-c that a change of CEP will translate by the same phase change on the interference fringes, we can thus retrieve the relative CEP between pulses.

Our f-2f interferometer consists of a β-barium borate crystal for frequency doubling and a polarizer to project the fundamental and second harmonic polarizations onto the same axis. The interference spectrum is analyzed shot-to-shot by a Fringeezz [97] (Fastlite, Antibes, France) to measure changes in the CEP. This measurement is fed back to an acousto-optic programmable dispersive filter (Dazzler, Fastlite, Antibes, France) in the first amplification stage to stabilize the CEP.

The CEP single shot measurements for a stabilization over 2 minutes with a stability of 350 mrad RMS is showed in Fig. 2.6. During my PhD, the typical stability of the CEP ranged between 250 mrad and 500 mrad RMS, depending on various elements and changes in the laser chain. CEP is en extremely sensitive parameter, and therefore its control on a complex laser system such as in Salle Noire 2 requires steady efforts to maintain it to an acceptable level of stability.

2.2 LWFA experimental setup

A simplified representation of the experimental setup of LWFA experiments is showed in Figure 2.7. The main beam is focused by a 2" silver coated 90° off-axis parabola onto a continuously flowing gas jet. A plasma is created by the front of the pulse, and electrons are accelerated along the laser axis. The electron beam profile and charge can be directly measured by a fiber optic scintillator (FOS) which is imaged by a CCD (see Sec. 2.3.1). A motorized magnetic spectrometer composed of an array of pinholes and two permanent magnets (see sec. 2.3.2) can be inserted in the beam to measure the electron energy. A probe pulse, obtained using the leak

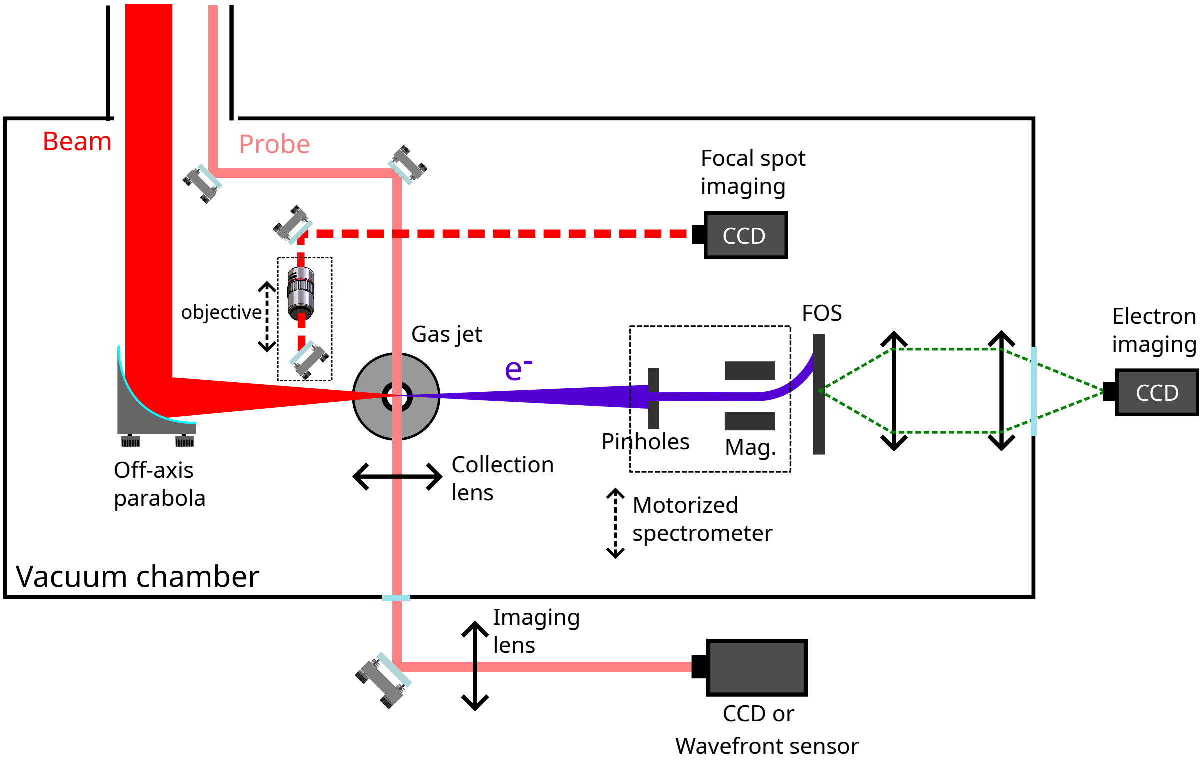

Figure 2.7 – Experimental setup of the LWFA experiments.

of the main beam through a mirror with a small hole, illuminates the plasma from the side. A system of lenses allows us to retrieve the shadowgraphic image of the plasma on a CCD, or to perform gas or plasma density measurements using a commercially available SID4-HR wavefront sensor from Phasics (see sec. 2.4). A pick-off mirror and a microscope objective are mounted on a motorized translation stage in order to image the focal spot of the attenuated main beam on a CCD.

2.3 Electron beam and plasma diagnostics

2.3.1 Beam profile and charge measurement

We discuss here the setup and method used to characterize the electron beam profile and charge. To achieve that, the magnetic spectrometer is removed from the axis of the electrons so as to let the whole beam pass. The electron beam arrives on a 2" CsI(Tl) scintillating screen with an array of fiber optics at the back (FOS for fiber optic scintillator). The energy of the electrons is converted into photons by the scintillator, which are then imaged by an optical system composed of two lenses onto a 14-bit CCD camera (QImaging EXi Blue) which permits to retrieve the electron beam profile. A 50 µm aluminum foil is placed in front of the screen to shield it from the light from the laser, and block the lower energy electrons (<120 KeV). Figure 2.8 shows a measurement of a laser-accelerated electron beam on the FOS scintillator. For the last experimental campaigns of my PhD, the FOS was replaced by a 3", 1 mm thick YAG crystal scintillator yielding more signal while allowing to measure the beam on a larger field of view.

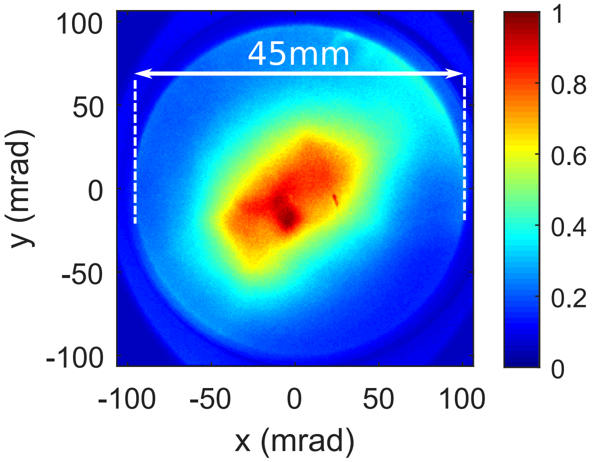

Figure 2.8 – Laser-accelerated electron beam measured on the FOS scintillator with a 2.3 pC/shot charge..

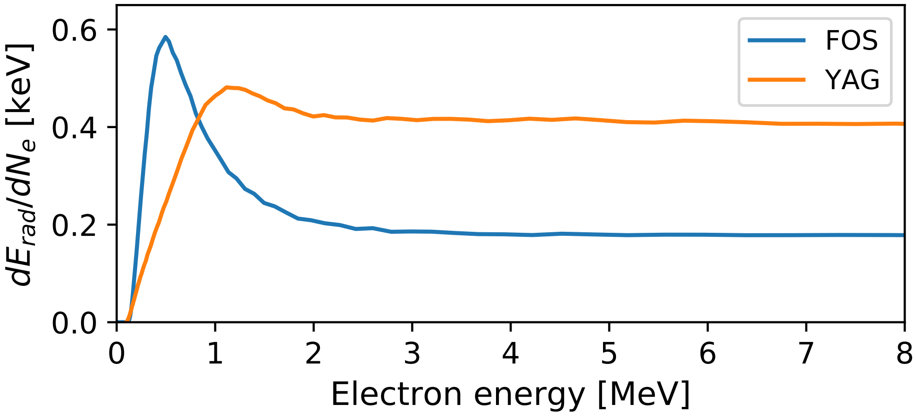

Figure 2.9 – Energy radiated by the scintillator as a function of the energy of the incident electron, for the FOS (blue) and the YAG (orange).

Obtaining a correspondence between the light collected by the system and the actual charge of the electron beam required a two-step calibration method performed before my arrival, which is detailed in Dominykas Gustas's thesis [35]. The first step consists in the estimation of the relative radiated light energy by the scintillator depending on the incident electron energy and the scintillator material. This is proportional to the curve of the energy deposited by the electrons as a function of their energy, which is estimated via Monte-Carlo simulations using the code GEANT4 [98]. The spectral distribution of the emission of the scintillator (given by the manufacturer), the transmission of the optical system and the efficiency of the CCD depending on the wavelength also have to be taken into account. Using all this information, we can deduce the relative quantity of counts measured by the camera per electron depending on their energy.

The second step consisted in estimating the coefficient linking the deposited energy and the radiated energy through an experimental calibration on a linear accelerator in Laboratoire de l'Accélérateur Linéaire. The whole imaging system was brought in order to preserve the original geometry. The accelerator at LAL was accelerating electrons to 3.8 MeV with a charge that could range from 30 pC to 70 pC. The exact charge from each shot was non-destructively measured with an integrating current transformer (ICT). Another scintillator composed of a YAG crystal was also calibrated using the same geometry. This measurement allowed to determine the absolute response of the scintillators which are plotted in figure 2.9. It shows that for both materials, the radiated energy strongly depends on the incident electron energy for energies <2 MeV, but remains constant for higher energies. The peak efficiency of the FOS is at 500 KeV where it yields three times more signal than at 3 MeV. Additionally, in the steady region for $E > 3$ MeV, the YAG yields 2.3 times more signal than the FOS.

In the last year of my PhD, we decided to change the geometry of the beam imaging system in order to use a 3" YAG crystal and 3" lenses for the imaging system. This enabled to have a wider field of view for the electrons, while collecting more light and having a better conversion efficiency at energies higher than 1 MeV. The energy radiated by the YAG had been calibrated during the LAL experiment, but not the new imaging system. We thus performed a cross calibration of the light collected by the two imaging systems using a radioactive tritium light source which has the particularity to be extremely stable and steady in time. We found that the new 3" geometry yielded 1.3 times more light than the previous 2" system. Therefore, this upgrade in the electron beam diagnostics allowed us to obtain 3 times more signal at energies >3 MeV taking into account the increased efficiency of the YAG.

But, this calibration method has some limitations, mainly of reliability over long (years) period of time. Indeed, using the LAL accelerator requires to move the whole setup in another lab, obtaining beam time and is valid only in the conditions in which the calibration has been done. Therefore, when changing things on the beam diagnostics (such as the change from 2" to 3" geometry) one has to limit to cross calibrations over the initial geometry. Moreover, it is possible that the efficiency of the scintillators, or the transmission of the optical system changes over long periods of time. All of this induces a significant uncertainty on the accelerated charge. In order to be able to calibrate frequently this diagnostics, it would be relevant to have our own ICT to measure the absolute beam charge, but they are expensive (30k€).

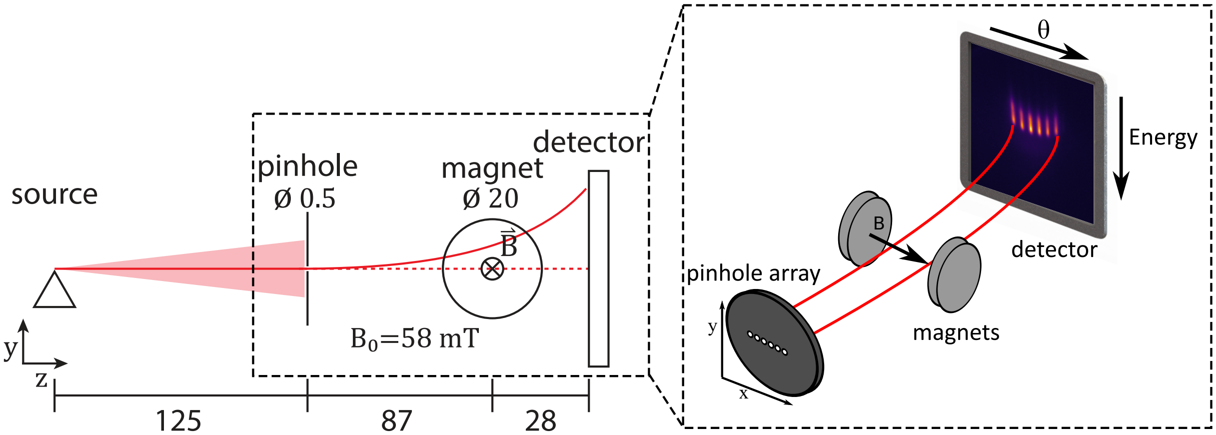

Figure 2.10 – Schematic representation of the electron spectrometer. The distances are given in mm, B_0 is the peak magnetic field.

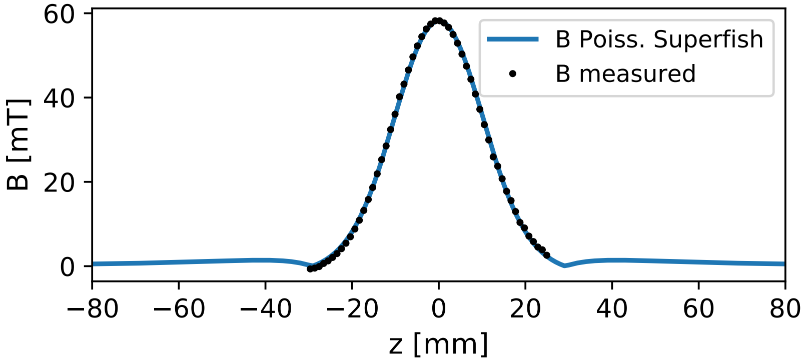

Figure 2.11 – On-axis magnetic field obtained with Poisson Superfish (blue) and measured experimentally (black), for 5mm thick magnets separated by 34mm.

2.3.2 Electron spectrometer

We measure the energy of the electrons with a magnetic spectrometer [99]. The electrons are sent in the magnetic field created by a dipole of two permanent magnets, the lower energy electrons are more deflected than the higher energy ones, and the dispersion on the scintillator thus corresponds to the energy spectrum. The electrons are moved due to the Lorentz force:

$$\boldsymbol{F}_L = -e\boldsymbol{v} \times \boldsymbol{B} \tag{2.14}$$

Which induces a circular trajectory in the plane perpendicular to the B field with a radius of gyration r_g:

$$r_g = \frac{\gamma m_e v}{eB} \tag{2.15}$$

If the extent of the magnetic field is lower than this gyration radius, the electron will just be deflected by an angle depending on their energy and continue in a straight line.

Figure 2.10 shows the geometry of the spectrometer. Pinholes of 500 µm diameter in a 3mm thick lead plate are placed at 125 mm from the electron source. The electrons are then deflected

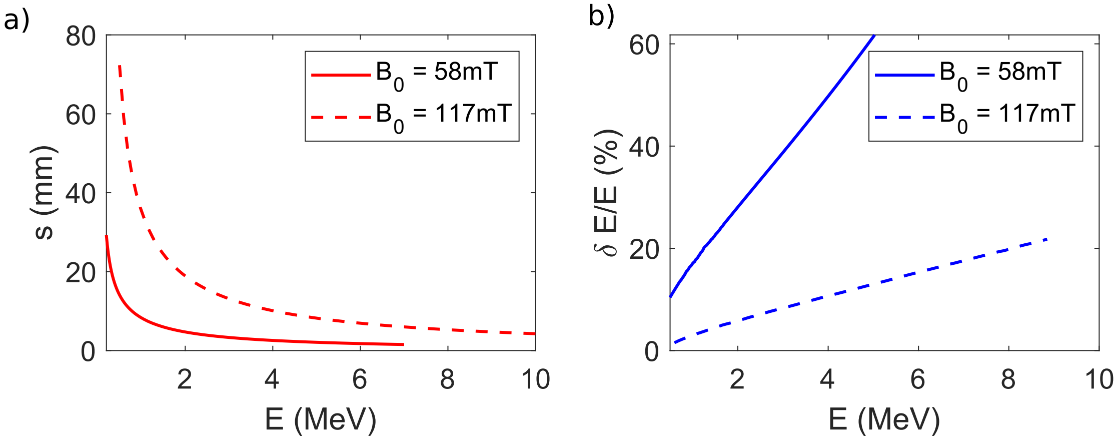

Figure 2.12 – a) Dispersion on the scintillator as a function of the electron energy simulated for two different peak magnetic fields B_0. b) Corresponding resolution of the spectrometer as a function of the electron energy.

vertically and measured on the scintillator. In order to associate a dispersion distance on the screen to a specific energy, it is necessary to compute the trajectories of the electrons in the magnetic field. We thus have to characterize the B-field of the magnetic dipole. To do so, we use the electro-magneto-static code Poisson Superfish [100] that calculates the static field $\boldsymbol{E}$ and $\boldsymbol{B}$ in 2D. We take advantage of the axial symmetry of our dipole to fully model it. Figure 2.11 shows the on-axis B-field computed from a Poisson Superfish simulation in the case of a dipole composed of two cylindrical permanent magnets of diameter 20 mm and thickness 5 mm, with a distance between the two magnets of 34 mm, yielding a maximum on-axis B-field of 58 mT. It also shows the experimental measurement of this on-axis field with a Hall probe, which matches extremely well the simulation. Note that the magnetic field increases when moving away transversally from the axis and getting closer to either of the magnets, meaning that the electrons passing through the off-centered pinholes will see a higher magnetic field and will be slightly more deflected.

Then we numerically solve the equation of motion for the electrons in the magnetic field for different energies, which allows us to retrieve the relation between the dispersion on the screen and the energy of the electrons. Figure 2.12 shows the modeled dispersion on the screen as well as the spectrometer resolution as a function of the electron energy. It highlights the fact that using a higher magnetic field significantly increases the resolution (at 5 MeV: 55% vs 15%), but then lower energy electrons are deflected too far to be detected on the 25 mm high half-screen of the 2" FOS. Depending on the typical regime achieved in the different experimental campaigns, we will therefore use different sets of magnets to obtain the best compromise between an adequate measurement range and spectrometer resolution.

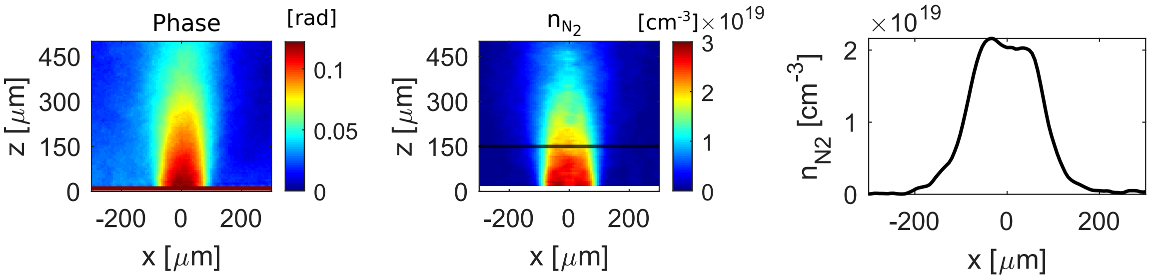

Figure 2.13 – a) Phase map obtained with the wavefront sensor, b) molecular density map retrieved via Abel inversion and c) density lineout at 150 µm from the nozzle's exit. The nozzle is a symmetric supersonic target with a backing pressure $P_{back} = 50$ bar of N_2 gas.

2.4 Density characterization and pumping system

To understand the physical processes occurring when the laser propagates in the plasma, and be able to explain the outcome of a laser-plasma experiment, it is important to measure the plasma density and characterize the profile of the target. To achieve this, a common method consist of illuminating the gas jet with a probe pulse and retrieving the phase shift associated with the refractive index of the gas via interferometry with a reference beam [101]. The gas density profile can then be retrieved using Abel inversion if the profile has an axial symmetry [102]. If the profile is asymmetric, it can be obtained through a tomographic reconstruction using measurements at different angles of rotation of the nozzle [103]. Another possibility is to directly measure the density of the ionized plasma column which still has axial symmetry [63, 104] which is the solution we implemented because tomography requires a very high level of precision in the rotation of the jet to be able to reconstruct the profile, which is quite complicated to achieve when using micrometer-scale targets.

The two cases of symmetric and asymmetric profiles are discussed in this section, as well as the pumping system that has been implemented to be able to support a continuous flow of gas in order to effectively run the accelerator at 1 kHz repetition rate.

2.4.1 Gas measurement of symmetric profiles

When the jet is symmetric, the molecular gas density can be directly retrieved from the 2D phase map via Abel inversion (see Fig. 2.13). To obtain the phase shift associated with the gas jet density, we use a commercially available quadri-wave lateral shearing interferometer [105, 106] (QWLSI) wavefront sensor (SID4-HR, Phasics) that is able to retrieve the local phase shifts thanks to the interference pattern of four tilted replica of the wavefront obtained by using a chessboard diffraction grating placed at a few millimeters from a CCD camera. This type of wavefront sensor allows to use a broadband, white LED lamp as a source for the transverse illumination of the gas jet. The gas density measurement is typically performed in nitrogen due to its high index of refraction that provides sufficient signal. Once the molecular density is obtained, the plasma density is obtained by assuming the laser ionizes the five first ionization levels of nitrogen, each molecule of N_2 thus releasing 10 electrons. Indeed, the threshold intensity for ionization up to N^{5+} is $I = 1.5 \times 10^{16}$ W cm^{-2} which is easily achieved during the whole propagation into the plasma, while the intensity necessary to ionize further is 1×10^{19} W cm^{-2}

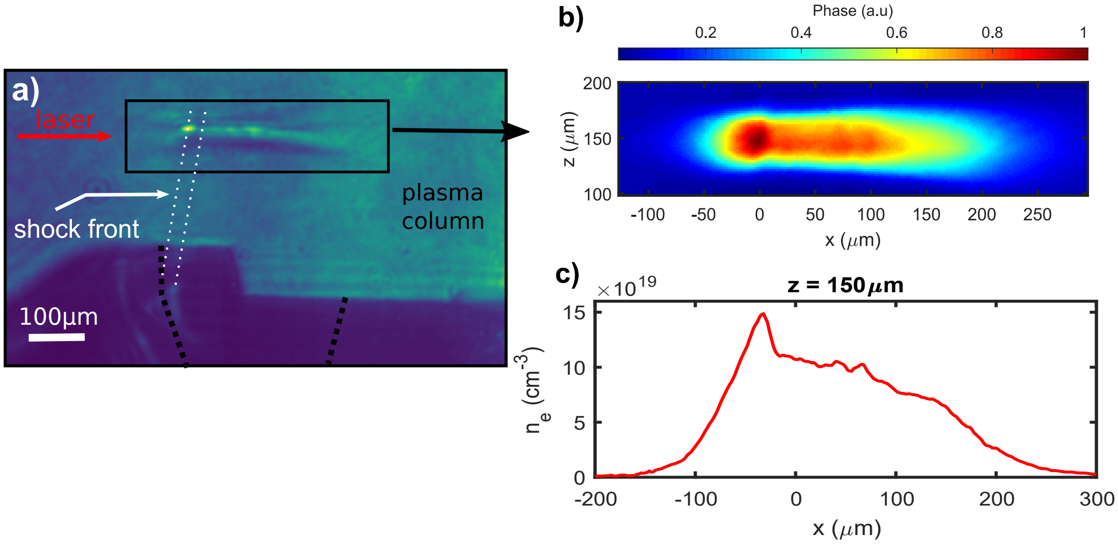

Figure 2.14 – a) Experimental shadowgraphic image of the plasma. The black dotted line suggests the inner walls of the nozzle, the white dotted lines suggest the position of the shock front. b) Normalized phase map of the plasma channel obtained by quadriwave lateral shearing interferometry at $z = 150\,\mu\text{m}$ from the nozzle's exit. c) Plasma density lineout at 150 µm from the nozzle's exit obtained via Abel inversion of the phase map.

(see sec. 1.1), which is higher than our laser peak intensity. When the measurement is performed in helium, full ionization into He^{2+} is assumed. For instance, the peak N_2 density measured at 150 µm from the exit of the nozzle (typical distance at which the laser is shot) in Figure 2.13 is $2.2 \times 10^{19}\,\text{cm}^{-3}$ for a backing pressure of $P_{back} = 50\,\text{bar}$. The corresponding plasma density will thus be $2.2 \times 10^{20}\,\text{cm}^{-3}$. Additionally, this density is expected to scale linearly with the backing pressure [107], we can therefore use this measurement to scale the density at other pressures. In practice, we found that some discrepancies in the density profile could arise for large pressure differences (e.g. 10 bar vs 150 bar), most likely due to boundary layer affects. It is thus preferable to perform several measurements at different pressures as references, and use the closest one to the pressure used in an experiment to rescale and retrieve the peak density and density profile.

2.4.2 Plasma measurement of asymmetric profiles

When the gas profile is not axially symmetric, Abel inversion cannot be performed and therefore the previous method cannot be used to characterize the density profile. To solve this issue, we restore an axial symmetry by measuring directly the phase shift associated with the plasma column ionized by the main beam, which is illuminated from the side by the laser probe beam. Indeed, the small radial extent of the plasma ($\sim 20\,\mu\text{m}$) allows us to neglect the density variation between each side of the laser axis and therefore assume a radial symmetry of the plasma. This way, the plasma density can be obtained by performing Abel inversion on the phase map of the plasma column along the laser propagation axis. Figure 2.14 shows an example of a plasma density measurement of an asymmetric gas jet with an oblique shock (the principle and physics of these nozzles is detailed in section 3). This time, the plasma density is directly measured instead of the gas density.

But this kind of measurement is significantly harder to perform than the gas density one. Firstly, it requires both laser main and probe beams to be synchronized, while the gas measurement requires only a white LED lamp. Additionally, the ionizing laser intensity has to be controlled quite precisely. Indeed, if the laser intensity is too high, the laser will self-focus, reaching very high intensities, and the light from Thomson scattering will perturb the measurement, while the effective Rayleigh length will be reduced due to the smaller dimensions of the laser spot. But if the intensity is too low, the laser will not be able to ionize the 5 first levels of nitrogen during the whole propagation, which would induced errors in the measurement. We aim for typical peak intensities reduced to $I \sim 2 - 5 \times 10^{17}\,\mathrm{W\,cm^{-2}}$, by using the uncompressed 25 fs pulse and reducing the beam energy using an iris (which also have the beneficial effect of increasing the Rayleigh length). This intensity range ensures that the first five levels of nitrogen are ionized on-axis over a few Rayleigh lengths while limiting the chaotic propagation and light emission associated with relativistic intensity.

2.4.3 Pumping system

In order to be able to operate the accelerator at the effective repetition rate of 1 kHz, the nozzle has to be continuously flowing. But, if the residual pressure in the chamber increases too much, it will impact negatively the propagation of the laser pulse, for instance through ionization defocusing. A strong pumping system able to evacuate the large quantity of gas continuously injected in the chamber and keep the residual pressure below $\sim 10^{-2}$ mbar is thus necessary.

Pumping system at the beginning of my PhD

When I started my PhD, the gas evacuation system on the experiment was organized as follows. The gas jet was flowing directly inside the large vacuum chamber, which was pumped by a large 4400 l/s turbo-molecular pump and a roots pump. Without influx of gas, this allows to bring the pressure inside the chamber down to $\sim 10^{-5}$ mbar. Using nitrogen gas, it could support the continuous flow of 100 µm diameter throat nozzles (the throat diameter imposes the mass flow) with backing pressures around 100 bar which is largely sufficient to reach plasma densities of a few $10^{20}\,\mathrm{cm^{-3}}$. But, in this configuration, using lighter gas such as helium was not possible, as its pumping is less efficient, and its requires higher operating pressures to achieve the wanted plasma density because it releases less electrons per atom.

Differential pumping system

We installed during the spring 2021 a differential pumping system in order to increase our capacity of pumping and be able to use continuous flows of helium in our experiments. In this new configuration, the gas jet does not flow in the large vacuum chamber anymore, but in a small centimeter-sized chamber pumped separately by another system of primary pumps (see Fig. 2.15). The small chamber is linked to the large vacuum chamber through two small 1 mm diameter openings to let the focused laser beam through. It also has two small windows on the sides to let the probe beam through. As highlighted by Figure 2.16, this largely increased the pumping capacity of our experiment, making the use of high pressure (>100 bar) of helium

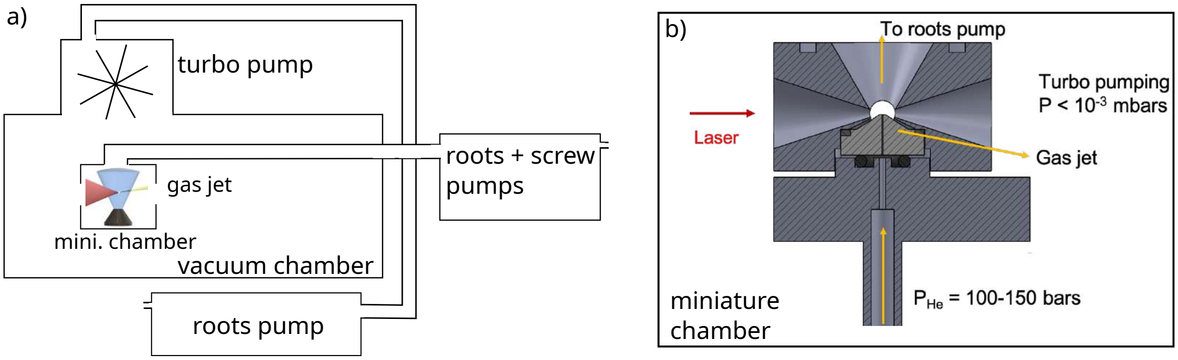

Figure 2.15 – a) Schematic representation of the differential pumping system. b) Drawing of the miniature chamber used in the differential pumping system, with a nozzle inside.

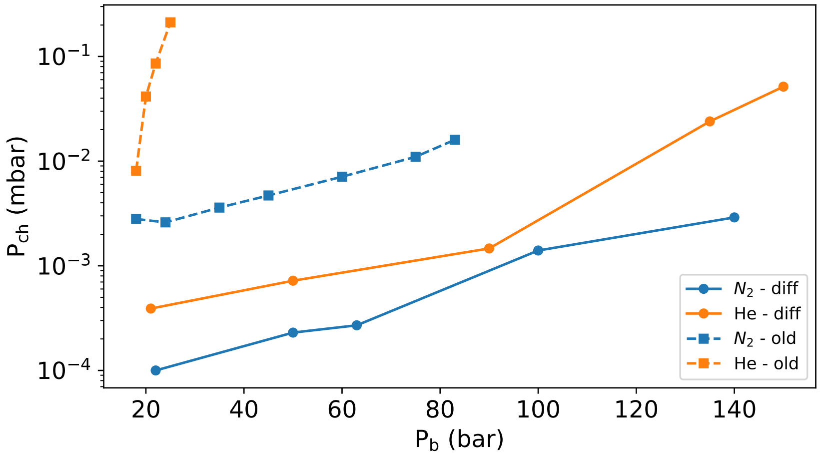

Figure 2.16 – Comparison of the pumping performances in the old configuration , and with the differential pumping system. The nozzle used has a throat with a 100 µm diameter, which is the largest used in our experiments .

through 100 µm throat nozzles possible while keeping the residual pressure inside the vacuum chamber below 10^{-2} mbar. Note that this system, due to space requirement of the mechanical pieces, makes it impossible to use the f′=50 mm off-axis parabola, and requires a parabola with at least f′=100 mm, which means larger focal spots.

2.5 Particle-in-cell simulations

2.5.1 General principle of PIC simulations

Particle-in-cell (PIC) [108] codes are widely used to model the physics of laser-plasma interaction and particularly laser-wakefield acceleration. In PIC codes, the plasma is modeled as a set of discrete charged particles that interact together through electromagnetic interactions. In practice, this consists in solving the equations of motion of the charged particles coupled with Maxwell's equations. The particles move in a continuous space while the field are interpolated on a grid. Additionally, the simulated particles do not represent a single electron as this would be too numerically expensive (at $n_e = 1 \times 10^{20}\,\mathrm{cm}^{-3}$, there are 10^8 electrons in a $1\,\mu\mathrm{m}^3$ volume) but many physical particles. Such numerical entities are called macroparticles. The PIC loop can then be summarized as follows:

— Interpolation: the fields are interpolated from their value of the grid, to the actual position of the macroparticles.

— Particle pusher: The equation of motion are integrated to retrieve the particle positions and momenta. Usually, this is performed using a leap-frog type Boris Pusher [109].

— Charge and current deposition: from the new positions of the charged particles, source terms of the Maxwell's equations are computed on the grid.

— Maxwell solver: using the source term from the previous steps, Maxwell equations are solved numerically to retrieve the new fields on the grid. The code can then loop back and interpolate these fields at the particle positions again.

2.5.2 Particularities of FBPIC: cylindrical geometry and spectral solver

The PIC code that is used to model the laser-plasma interaction in this manuscript is FBPIC (Fourier-Bessel Particle-in-cell) [110]. It uses a cylindrical geometry with azimuthal decomposition that allows to model 3D problems with a close-to-cylindrical symmetry with a quasi-2D computation cost.

Cylindrical grid with azimuthal decomposition

One of the main distinctive feature of FBPIC is that instead of using a 3D Cartesian grid, it uses a cylindrical geometry (r, θ, z) where the fields are decomposed as a Fourier series expansion in the azimuthal direction θ. This is the same method as used in the code Calder-Circ [111]. For a given field A:

$$A(r, \theta, z) = Re\left(\sum_{m=0}^{\infty} \tilde{A}^m(r, z)\exp(-im\theta)\right) \tag{2.16}$$

Where $\tilde{A}^m$ is the m$^{\mathrm{th}}$ Fourier coefficient. For a geometry close to the cylindrical symmetry, the first few modes will be sufficient to model the system. The complexity of the 3D simulation is thus reduced from N^3 to mN^2 where m is an integer typically between $m = 2$ and $m = 5$.

Spectral solver

In most PIC codes, the Maxwell's equations are solved using a finite-difference solver [112]. These solver can lead to numerical artifacts due to errors in the evaluation of differentials, leading to non physical dispersion of the laser even in vacuum, numerical Cherenkov radiation [113] and emittance growth [114].

But FBPIC uses a spectral solver [110, 115] in which the fields are solved in Fourier domain where derivatives can be computed analytically. This means that at each iteration, the code transforms the fields to spectral space, advances them in time, and transforms them back to real domain. Thanks to this algorithm, FBPIC is dispersion-free which is very important when simulating near-single cycle pulses, and mitigates numerical Cherenkov radiation and emittance growth.

Centering in time and space

The standard PIC algorithm uses staggered fields, meaning for instance that the electric field E is computed at integer time-step (n, n+1), while the magnetic field is computed at half-integer time-steps (n-1/2, n+1/2). This might lead to an overestimation of the force in situations where the amplitude of $\boldsymbol{E}$ and $\boldsymbol{v} \times \boldsymbol{B}$ are similar, which can be the case when a relativistic particle co-propagates with the laser. FBPIC defines all the fields (at the exception of the currents) at the same point in time and space, which allows to avoid such artifacts. This is of particular interest for section 5.1.4 where a similar situation is studied.

2.5.3 Modeling experimental laser data in simulations

In order to match more precisely experimental results, in some cases we will use the temporal and/or the spatial profile of the laser measured experimentally. To achieve this, the laser field is initialized at focus using a virtual antenna, which is a virtual 2D-array of oscillating macroparticles that self-consistently generate the fields matching the input focal spot and temporal profile. The pulse is then retro-propagated by simulating vacuum propagation up to the starting point of the simulation, assuming a flat spatial phase at focus. Finally, the obtained pulse is launched in the forward direction into the plasma. Note that this does not take into account the effect of a non-flat spatial phase of the laser spot, nor spatio-temporal couplings.

Typically, our simulations have a grid with a longitudinal resolution $\Delta z \sim \lambda_0/40$ and $\Delta r \sim 2 - 3\Delta z$ ($\lambda_0 = 800\,\mathrm{nm}$) and we use 4-5 azimuthal Fourier modes. The simulations are initialized with neutral atoms (nitrogen or helium), and their ionization is simulated using the ADK tunnel ionization model [43]. We use between 16 and 96 neutral macroparticles per cell, each of which can liberate 7 (nitrogen) or 2 (helium) electrons via ionization. The simulations are parallelized and were run on between 2 and 8 simultaneous graphic processors (GPU) for typically 3 to 5 hours per simulation. I carried out most of the simulations presented in this manuscript, apart from the simulations of section 4.1 on the effect of the FTL pulse duration and plasma density, and the 3D simulation on WarpX in section 5.2.2 that were performed by Igor Andriyash.

Chapter 3

Micrometric shocked gas targets

Sommaire

The gas targets play a fundamental role in laser-wakefield acceleration. Tailoring precisely the plasma profile can enable to: better control propagation effects such as self-focusing or ionization defocusing, trigger injection in a downramp [58, 116–118], optimize betatron radiation [119–121] or increase the energy of the electrons via rephasing in a density up-ramp [122–124]. Two main types of gas targets are used in LWFA: gas cells/capillary [16] and gas jets [101]. In experiments using a gas cell operating in steady flow regime it has been showed to benefit from an increased stability [125] but in our case we will prefer gas jets for two main reasons. Firstly, reaching sufficiently small profile widths of the order of ∼100 µm with a cell is a technical challenge. Additionally, gas cells tend to be damaged by the laser faster than gas nozzles, which is an issue when operating at 1 kHz.

The gradient injection scheme has been used in numerous experiments and has proven very efficient to increase beam quality and stability. It has been mainly implemented through laser-induced density transition [61, 126] and by inserting a thin blade in the outflow of a supersonic gas jet [62–64, 127] which results in the formation of a shock-front in the gas profile. The physics of supersonic gas jets impinged by a blade has been recently thoroughly described [128] and such design works well with millimetric-scale targets used in experiments with high-power lasers where the Rayleigh length is relatively long, and thus where distance and positioning constraints are not too stringent. But current high-repetition rate laser-plasma accelerators the targets are scaled down to micrometric dimensions, and the laser is focused at around 150 µm from the nozzle. With such small dimensions, inserting a knife-edge in the flow with good precision can prove difficult. Moreover, as LPA technology advances, questions of stability and reproducibility gain importance in the perspective of applications, and integrating the shock formation in the design of the nozzle would offer a more compact, robust and simple solution than the blade technique. This comes at the cost of the real-time tunability that is achieved with a motorized knife-edge that can be inserted at different positions in the jet.

In this chapter, we study supersonic shock-nozzles of micrometric-dimensions, relying on the formation of oblique shocks due to the sudden change of flow direction in the final section of the nozzle, with fluid simulations and experimental measurements. A symmetrically shocked design yielding a high on-axis density, with peaked profile [129] is studied through simulations, which are validated by an experimental measurement. We then propose and characterize a newly designed one-sided shocked (OSS) nozzle intended to provide the density downramp followed by a plateau, necessary to gradient injection.

3.1 Theory of supersonic gas flows and shock formation

3.1.1 1D isentropic flow

We consider the behavior of a compressible, one-dimensional flow in a varying area duct, under the following assumptions [107]:

- The flow is in steady-state (no time dependence)
- The flow is isentropic (no heat transfer or dissipation via friction): $\delta q = 0$, $ds = 0$
- The potential energy change is negligible: $dz = 0$
- No shaft work: $\delta w = 0$

Let us start by writing the first principle of thermodynamics stating the conservation of energy of an open system:

$$d(e + pv) = \delta q + \delta w \tag{3.1}$$

Where e is the total energy of the system: $e = u + v^2/2 + gz$, with u the internal energy, $v^2/2$ the kinetic energy (v is the velocity of the flow) and gz the potential energy. Every term is given per unit of mass. We introduce the enthalpy $h = u + pv$. The first principle becomes:

$$dh + \frac{dv^2}{2} + gdz = \delta q + \delta w \tag{3.2}$$

Under the assumptions above, the energy conservation equation can be simplified:

$$dh = -vdv \tag{3.3}$$

Then using the following property relation $Tds = dh - dp/\rho$ which simplifies for an isentropic flow ($ds = 0$):

$$dh = \frac{dp}{\rho} \tag{3.4}$$

Then combining 3.3 and 3.4 yields:

$$dv = -\frac{dp}{\rho v} \tag{3.5}$$

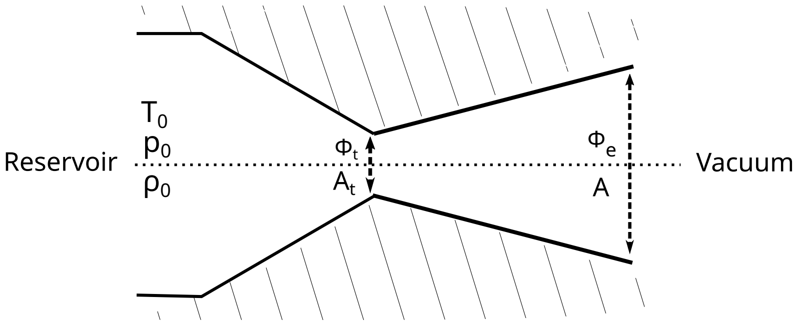

Figure 3.1 – Sketch of a "de Laval" nozzle producing a supersonic flow.

Let us now consider the continuity equation (mass conservation) for a steady, 1D flow:

$$\dot{m} = \rho A v = cst \tag{3.6}$$

$$\frac{d\rho}{\rho} + \frac{dA}{A} + \frac{dv}{v} = 0 \tag{3.7}$$

Where A is the area of the duct and v the velocity of the flow. Using 3.5 we show that:

$$\frac{dp}{\rho} = v^2 \left(\frac{d\rho}{\rho} + \frac{dA}{A} \right) \tag{3.8}$$

We introduce the sonic velocity:

$$a^2 = \left(\frac{\partial p}{\partial \rho} \right)_s = \frac{dp}{d\rho} \tag{3.9}$$

Using the sonic velocity in equation 3.8 yields:

$$\frac{d\rho}{\rho} = M^2 \left(\frac{d\rho}{\rho} + \frac{dA}{A} \right) \tag{3.10}$$

Where $M = v/a$ the Mach number of the flow. This allows us to express the density as a function of the mach number and the area change:

$$\frac{d\rho}{\rho} = \left(\frac{M^2}{1 - M^2} \right) \frac{dA}{A} \tag{3.11}$$

By substituting it in the continuity equation, we obtain the relation between the velocity variation and the area change:

$$\frac{dv}{v} = -\left(\frac{1}{1 - M^2} \right) \frac{dA}{A} \tag{3.12}$$

The equation 3.12 allows us to understand qualitatively the behavior of the flow depending on the duct geometry, and the Mach number:

- if M<0 (subsonic) and the area is increasing (diverging), the flow velocity decreases
- if M<0 (subsonic) and the area is decreasing (converging), the flow velocity increases
- if M>0 (supersonic) and the area is increasing (diverging), the flow velocity increases
- if M>0 (supersonic) and the area is decreasing (converging), the flow velocity decreases

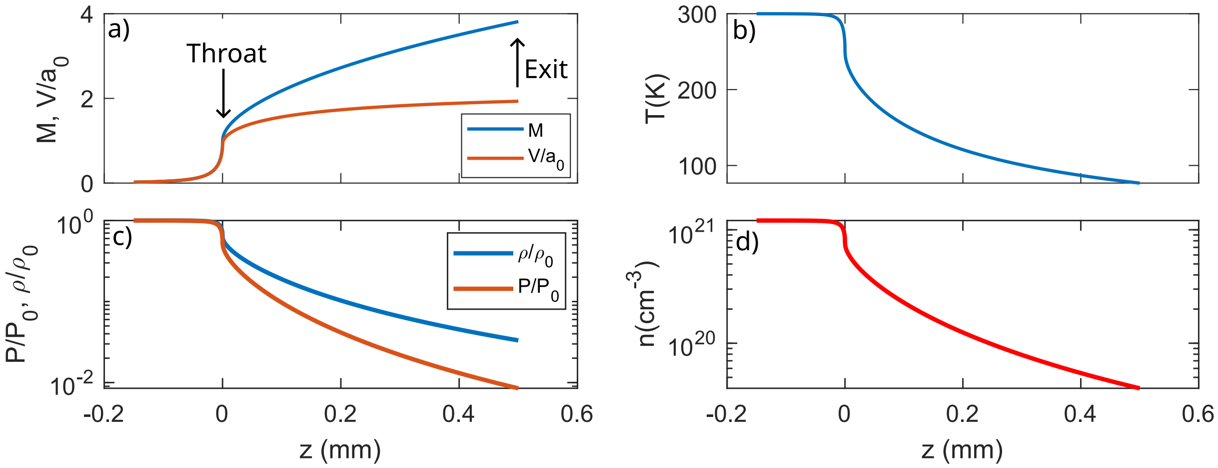

Figure 3.2 – Evolution of hydrodynamic parameters of a nitrogen flow inside a de Laval nozzle with a 50 µm throat, 150 µm exit diameter and a diverging section length of 500 µm, with a reservoir pressure $P_0 = 50$ bar. a) Mach number and flow velocity normalized to the sonic velocity in the reservoir $a_0 = \sqrt{\gamma RT}$, b) Gas temperature, c) Normalized pressure and mass density, d) Molecular gas density as a function of the position in the nozzle. The throat is positioned at $z = 0$ µm and the exit is at $z = 500$ µm.

So let us consider the situation of a subsonic flow inside a converging duct, its velocity will increase up to the point where it will reach a Mach number $M = 1$. If after reaching a sonic velocity, the duct starts diverging, then the flow velocity will become supersonic, and will continue to increase. This kind of converging-diverging geometry (see Fig. 3.1) capable to generate supersonic flows is called a “de Laval” nozzle.

When considering an ideal gas, the flow parameters, namely the temperature T, the pressure p and the density ρ, can be expressed, using the governing equations of the flow, according to the Mach number M and their initial value in the reservoir [107]. The coefficient γ is the specific heat ratio of the gas, which is 5/3 for monoatomic gases and 7/5 for diatomic gases. A_t is the cross-section area of the nozzle at the throat (M=1), and A the area at the interest point.

$$\frac{A_t}{A} = M\left[1+\frac{\gamma-1}{\gamma+1}(M^2-1)\right]^{-\frac{\gamma+1}{2(\gamma-1)}} \tag{3.13}$$

$$\frac{T}{T_0} = \left(1+\frac{\gamma-1}{2}M^2\right)^{-1} \tag{3.14}$$

$$\frac{p}{p_0} = \left(1+\frac{\gamma-1}{2}M^2\right)^{-\frac{\gamma}{\gamma-1}} \tag{3.15}$$

$$\frac{\rho}{\rho_0} = \left(1+\frac{\gamma-1}{2}M^2\right)^{-\frac{1}{\gamma-1}} \tag{3.16}$$

It appears that all the physical quantities are determined by the ratio between the area of the nozzle at the throat and the area at the considered point. Figure 3.2 shows the evolution of the hydrodynamic parameters of a nitrogen flow inside a de Laval nozzle computed using this isentropic model. We see than the flow indeed reaches a Mach number $M = 1$ at the throat, an then becomes supersonic in the diverging section. The final Mach number for a ratio of the exit diameter on the throat diameter $\phi_e/\phi_t = 3$ is $M = 3.8$. Figures 3.2a-b show that as the velocity of the flow increases, its temperature decreases: the nozzle converts the enthalpy of the gas into kinetic energy.

Due to their supersonic velocity, de Laval nozzles provide more collimated flows when expanding into vacuum, which results in steeper transverse density profiles [130] as well as a slower decrease in the density when moving away from the nozzle. Switching from subsonic to supersonic targets has been shown to significantly enhance the performances of the accelerator during the thesis of Dominykas Gustas [35, 131], mainly by mitigating detrimental effects of the plasma on the propagation of the laser in the jet up-ramp.

3.1.2 Oblique shocks

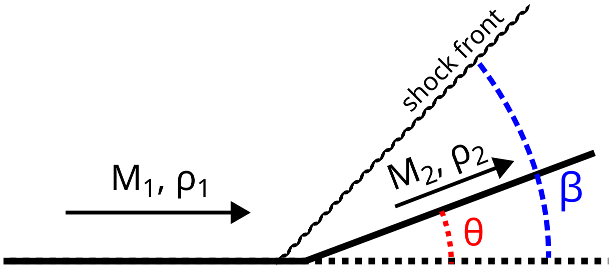

Figure 3.3 – Wedge-like configuration leading to an oblique shock. For a shock to occur, it is necessary that $M_1 > 0$. The deflection angle θ and the shock angle β are indicated.

A shock in a supersonic flow is characterized by a sudden reduction of the Mach number at a certain position, leading to the compression of the gas in the shocked region. This compression leads to higher density which can be interesting for gas target design. When a supersonic flow changes direction abruptly, such as when encountering a wedge with a moderate (we will see later what is moderate in this case) deflection angle θ, it generates an oblique shock-wave originating from the corner of the wedge and at an angle β to the original flow direction (see Fig. 3.3). The relation between the shock angle β, the deflection angle θ and the Mach number before the shock M_1 is given by the following equation [107, 132]:

$$\tan\theta = 2\cot\beta \frac{M_1^2 \sin^2\beta - 1}{M_1^2(\gamma + \cos 2\beta) + 2} \tag{3.17}$$

Equation 3.17 does not enable to explicitly express β according to θ and M_1, but we can determine it graphically. The solution of $\beta - \theta$ according to θ for different Mach numbers is displayed in Fig. 3.4b. For each deflection angle there are two solutions, one with a low shock angle, corresponding to a *weak shock* leading to a still supersonic Mach number after the shock $M_2 > 1$, and one with a higher shock angle, corresponding to the *strong shock* case, with a subsonic downstream flow. Even if no clear mathematical criterion is known, in practice, the *weak shock* case is almost always observed in experiments, as the *strong shock* requires a higher pressure downstream [133] obtained only in specific conditions. In our case where a supersonic flow expands into near-vacuum, the weak shock will thus occur.

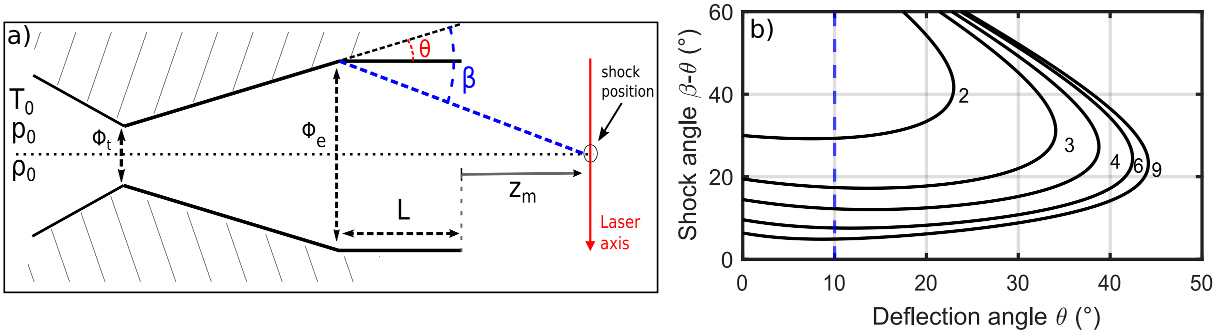

Figure 3.4 – a) Sketch of a nozzle leading to the formation of converging oblique shocks. b) Shock angle as a function of the deflection angle for different Mach numbers. The dashed blue line represents the angle of 10° used later in the design of our jets.

We propose to study the configuration sketched in Fig. 3.4a where a straight duct added at the end of the diverging section of a de Laval nozzle induces a shock-front of angle $\beta - \theta$ with the longitudinal axis. The shock-fronts then converge on-axis at a distance z_m from the nozzle exit determined by the shock angle and the length of the straight duct. This configuration yields a peaked gas profile with high density relatively far from the nozzle [129]. Equation 3.17 does not have any solution for deflection angles $\theta > \theta_{max}$ depending on the Mach number, in this case the shock solution is not an oblique shock but a detached bow-shock [107].

It is then possible to determine geometrically the on-axis position of the shock, thanks to the angle $\beta - \theta$:

$$z_m = \frac{\phi_e/2}{\tan(\beta - \theta)} - L \tag{3.18}$$

Where L is the length of the straight section at the end of the diverging section, and ϕ_e is the exit diameter of the nozzle (see Fig. 3.4a). Even though the oblique shock originates from the corner of the wedge, the on-axis shock position z_m is given with respect to the exit of the nozzle, (hence the subtraction of L) because this is the relevant quantity from an experimental point of view.

In order to have a shock position far from the nozzle and preserve its integrity, the shock angle should be kept small. As is clear from 3.4b, this can be obtained through a sufficiently high Mach number (> 3) at the end of the diverging section (determined by A_e/A_t) and selecting an adequate deflection angle for which $\beta - \theta$ is minimal. Although very useful to determine the above principles, this geometrical model does not give indications on the density obtained, nor on the effect of the length of the straight section. Numerical simulations are therefore needed to understand these characteristics. It is important to note that this simplified model (1D-isentropic flow expansion + geometric oblique shock) does not take into account the effects of the boundary layer, i.e the region near the wall where the flow velocity transitions from 0% to 90% of the center velocity and where the isentropic assumption is not valid. These boundary layers impose a velocity gradient between the walls and more inner parts of the flow. With this reduced velocity near the walls, one can expect the shock angle to be higher than predicted by the simplified model.

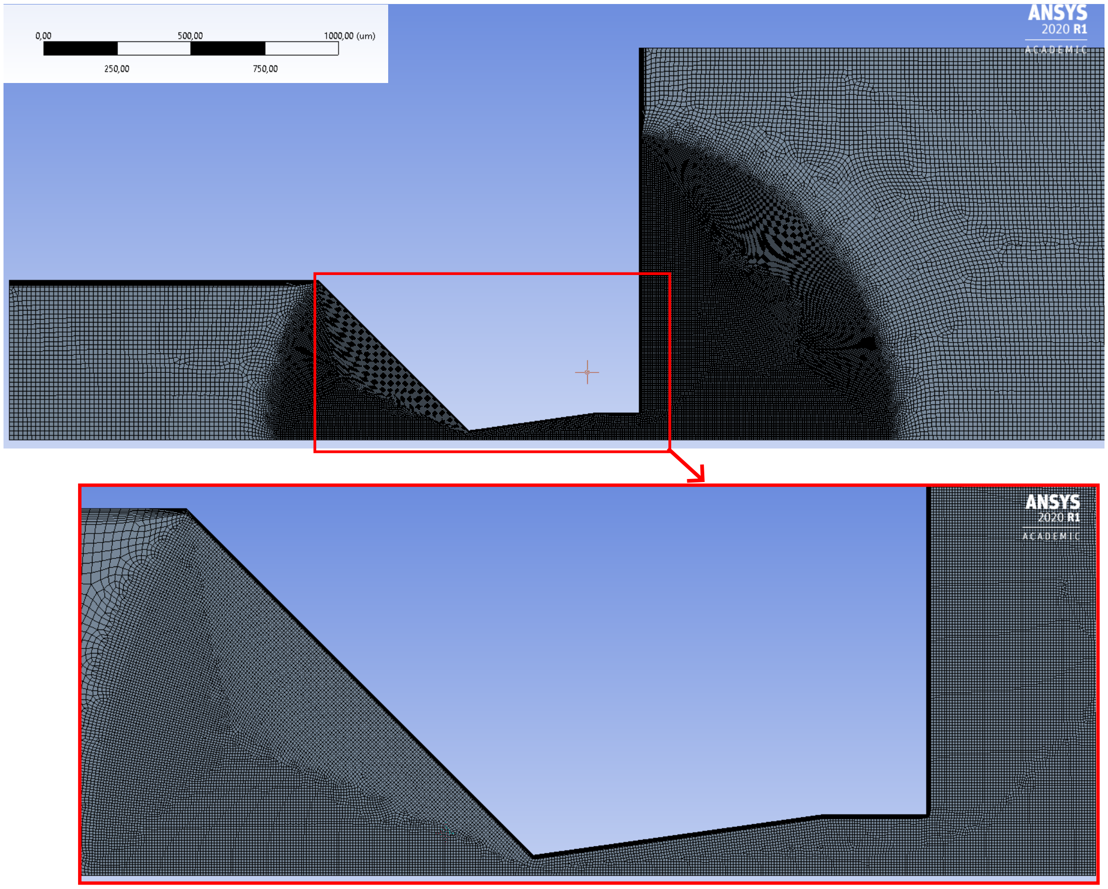

Figure 3.5 – 2D mesh for the axisymmetric CFD simulations of the symmetric shock nozzle with $\phi_t = 60\,\mu\text{m}$, $\phi_e = 180\,\mu\text{m}$ and a straight duct length $L = 100\,\mu\text{m}$

3.2 CFD simulations of symmetric shocked gas jets

The study of symmetric shock-jets can be performed in 2D-axisymmetric geometry. From this cost-efficient study, we will analyze with computational fluid simulations how the nozzle parameters impact the shock formation. This understanding can then be used in the context of the asymmetric shock-jet of section 3.3, which requires full-3D simulations.

3.2.1 Methods

The simulations are carried out with the CFD software ANSYS Fluent which solves the Navier-Stokes equations. The k-ω shear stress transport (k-ω SST) turbulence model [134, 135] is used. It is a robust and efficient model which uses the k-ω formulation near the boundary layers, and switches to the k-ϵ formulation in the free-stream. Simulations are performed using nitrogen N_2. The symmetric geometry of the nozzle allows to use a 2D-axisymmetic modeling to lower computing costs. The mesh is refined around regions of interest, and is composed of $\sim 10^5$ cells in the 2D case. A convergence study has been performed to ensure that further refining of the mesh does not significantly change the solution. Full-multigrid initialization (FMG) is used to obtain an initial guess of the solution thus allowing faster convergence. Figure 3.5 shows a typical mesh used to simulate a 2D-axisymmetric shock jet.

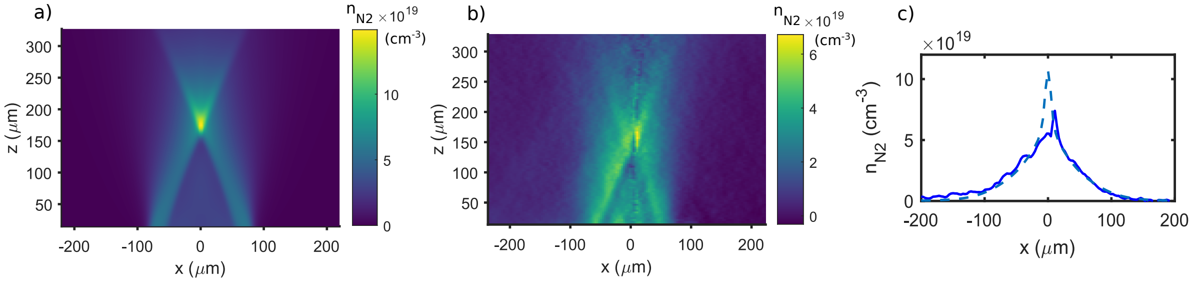

Figure 3.6 – a) Simulated and b) experimental nitrogen molecular density map of a symmetric shock nozzle with a backing pressure $P_{back} = 50\,\text{bar}$ c) Comparison of the simulated (dashed) and measured (solid) density profiles at $z = z_m$

3.2.2 Comparison between measurement and simulation

In order to validate our CFD simulations, we have performed measurements of the gas density profile of a symmetric shock-jet. Figure 3.6 shows the results of the measurement performed on a jet with $\phi_t = 60\,\mu\text{m}$, $\phi_e = 180\,\mu\text{m}$, and a 10° diverging section, with a straight duct length $\text{L} = 100\,\mu\text{m}$, and the comparison with the simulated profile. The isentropic model predicts a Mach number of 3.8 at the end of the diverging section, which would result in a 13° $\beta - \theta$ shock angle. The geometric model of section 3.1.2 predicts an on-axis shock position at $z_{m,th} = 289\,\mu\text{m}$.

The measurement indeed shows the convergence of shock structures on the jet axis, yielding a substantially high density and peaked profile. The simulation prediction of the position of the shock is $\text{z}_{\text{m,s}} = 176\,\mu\text{m}$ while the measured position is $\text{z}_{\text{m,m}} = 166\,\mu\text{m}$, which shows a fairly good agreement. These values are significantly lower than predicted by the geometrical model, indicating that the boundary layer plays an important role in the physics of micrometric jets. In the simulation, the center Mach number at the end of the diverging section is 3.6, and the flow velocity decreases near the walls. The simulated and measured gas density transverse profiles at the on-axis shock position are showed on Fig. 3.6c. Both profiles have similar widths, but in the experimental case, the peak density is significantly lower. This could be due to an insufficient resolution (phase resolution is $3.2\,\mu\text{m}$) combined with the high on-axis noise of the Abel inversion used to retrieve the density from the measured phase. Still, the good overall agreement between measurement and simulation validates the use of CFD simulations for the design and study of shocked gas jets.

3.2.3 Parametric study of symmetric shock nozzles

We numerically study the influence of two parameters, the length of the final straight duct L, and the diameter of the throat ϕ_t, on the position z_{max} where the shock structures meet on the axis thus forming a peaked density profile, and on the density n_{max} at this position. The exit diameter is fixed at $300\,\mu\text{m}$, the angle of the diverging section is fixed at 10°, the origin of the z axis is the exit of the nozzle

A numerical study of the effect of the straight duct length, in Fig. 3.7a is of particular interest, as no information on the matter is given by the theoretical model. In Fig. 3.7a, it appears that for $\text{L} < 100\,\mu\text{m}$ an increase in the length of the straight section leads to the shock being formed

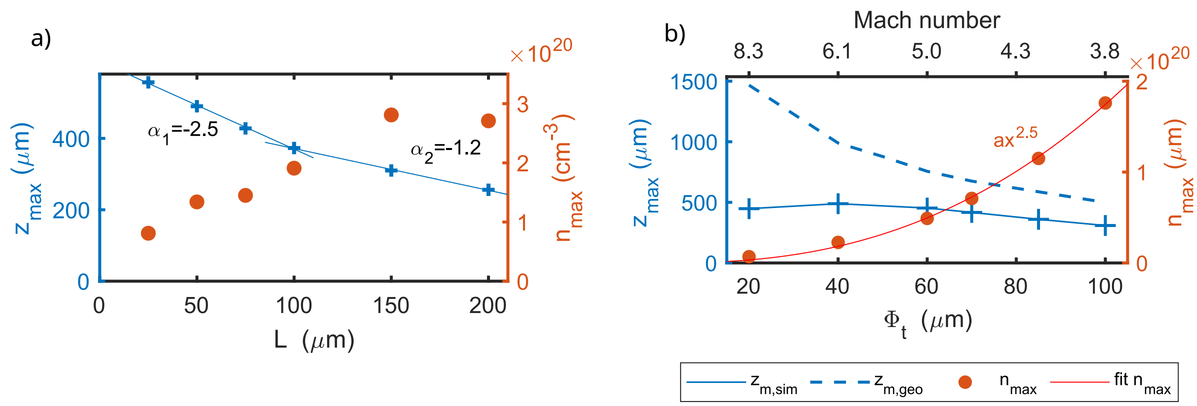

Figure 3.7 – a) Simulated on-axis shock position (blue cross) and linear fit for the two regimes, nitrogen molecular density at this position (orange dots), as a function of the length of the final straight duct L. α_1 and α_2 are the slopes of the linear fits. Throat diameter is fixed at $\phi_t = 100\,\mu\text{m}$. Simulations are performed in nitrogen with a backing pressure $P_{back} = 50\,\text{bar}$. b) Evolution of the on-axis shock position (blue cross) and of the maximum density at this point (orange dot) as a function of the throat diameter, and corresponding Mach number at the end of the diverging section. The blue dashed line represents the predictions of the geometrical model of section 3.1.2. The orange line is a power fit of the maximum density data. Simulations are performed in nitrogen with a backing pressure $P_{back} = 50\,\text{bar}$.

closer to the nozzle, with a slope of -2.5. For higher values of L, a further increase of the straight duct length has almost no significant effect on the position of the shock other than the nozzle's exit being brought closer to it due to the length increase. On the other hand, the maximum density increases with L, until it saturates at L=150 µm. These results show that a compromise on the final duct length has to be made to obtain high density sufficiently far away from the nozzle to prevent from damaging. In our configuration, values of L larger than 150 µm do not provide any benefit.

The influence of L on the shock is highlighted by Figure 3.8 which shows the flow velocity vectors and radial velocity amplitude for shock nozzles with a short ($L = 50\,\mu\text{m}$) and and long ($L = 150\,\mu\text{m}$) flat duct. Upon crossing an oblique shock, the flow velocity is slowed down in the direction perpendicular to the shock and velocity along the shock remains unaffected [107]. This tends to reduce the velocity in the radial direction to align the flow with the flat duct direction. But for short L, the zone imposing an horizontal flow is limited, and it rapidly recovers a behavior of expansion in vacuum, with increasing radial velocities. Because of this competing expansion, the loss of radial velocity across the shock is not as strong as if the duct was infinitely long, which leads to a smaller shock angle. For sufficiently long L (bottom) the zone for which the horizontal velocity is imposed is larger, meaning that the flow does not expands directly into vacuum right after the shock. The radial velocity is thus more strongly reduced, which leads to a higher shock angle. Because this radial velocity is smaller for longer L, the flow is more compressed at the shock and the density is higher than for shorter L.

Figure 3.7b shows the numerical evolution of those two same quantities, shock position and maximum density, as well as the prediction of the geometric model of section 3.1.2 for the shock position, as a function of the throat diameter, with the same geometry as before and a fixed value of L = 100 µm. Reducing the throat diameter while keeping the same exit diameter leads

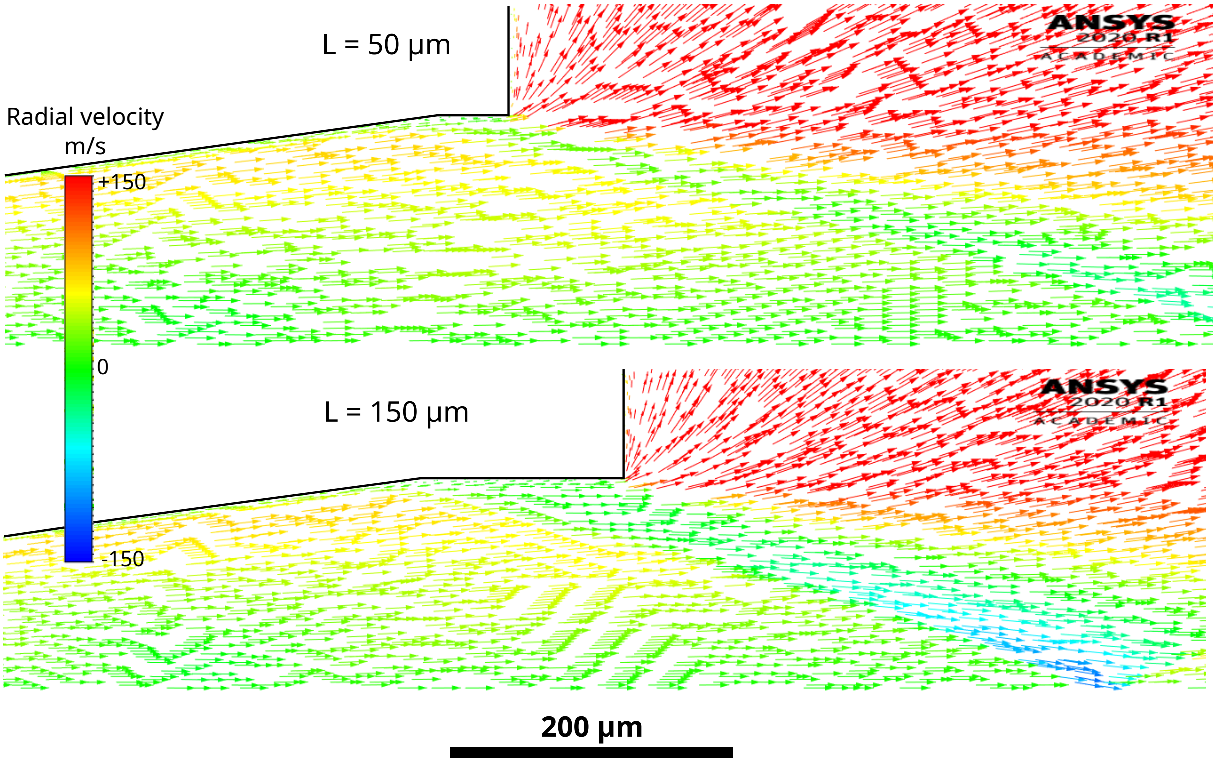

Figure 3.8 – Velocity vectors (arrows) and amplitude of the radial velocity (colors) in a shock nozzle for section length $L = 50\,\mu\text{m}$ (top) and $L = 150\,\mu\text{m}$ (bottom) in CFD simulations. The colormap is saturated at $v = +150\,\text{m/s}$.

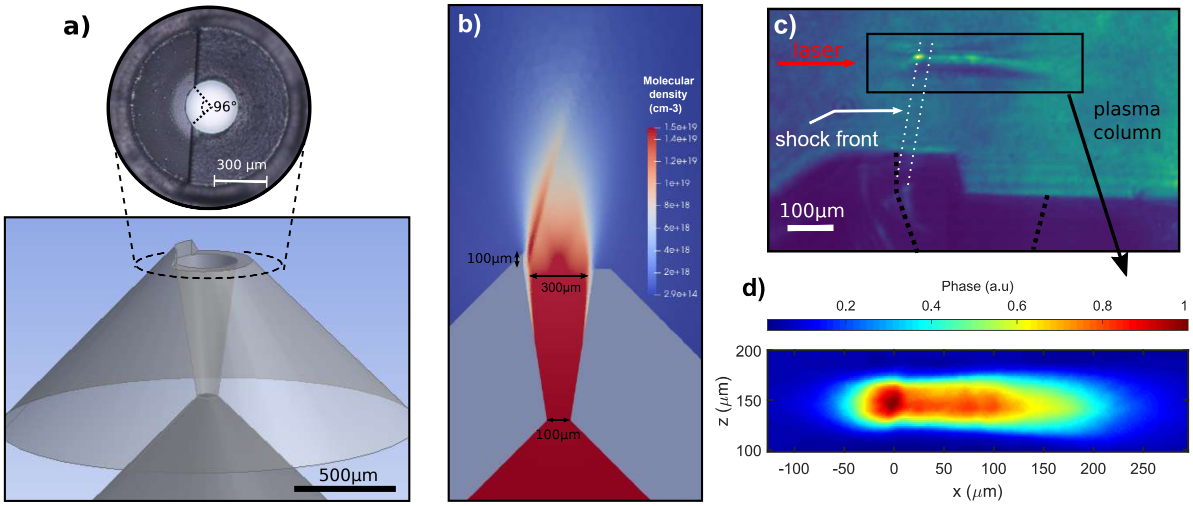

Figure 3.9 – a) 3D-model of a one-sided shock (OSS) nozzle, with a zoom on a top-view picture of the nozzle taken with an optical microscope. b) Slice of the nitrogen density map from 3D CFD Fluent simulation, with a backing pressure of 15 bar. c) Experimental shadowgraphic image of the plasma. The black dotted line suggests the inner walls of the nozzle, the white dotted lines highlight the shock front. d) Normalized phase map of the plasma channel obtained by quadriwave lateral shearing interferometry at $z = 150\,\mu\text{m}$ from the nozzle's exit

to an increase of the Mach number, as can be deduced from Eq. 3.13, which can be interesting in order to increase the distance of the density peak z_m. It appears that for diameters larger than 60 µm, the simple geometric model correctly predicts the tendency observed in the simulations of an increase in the shock position when the throat diameter ϕ_t decreases, despite an offset in the actual value. For smaller ϕ_t the flow is governed by boundary layers, which are not considered in the simple model, and the shock position saturates around $z_{max} = 500\,\mu\text{m}$ and even decreases for the smallest diameter considered. Moreover, the offset of the geometric model compared to the simulations for the higher ϕ_t values can be explained again by the effect of the boundary layer, which induces a lower Mach number than calculated with the 1D-isentropic model in the region near the walls, therefore increasing the shock angle. The maximum density increases with the throat diameter, but this process is largely governed by the evident rise of mass flow rate at the throat due to the larger cross section.

This parametric study shows that by modifying the length of the straight section and the throat diameter, it is possible to control the peak density and its distance from the nozzle. But both nozzle features have an opposite impact on the flow characteristics, therefore a compromise corresponding to the experimental requirement has to be found. With a backing pressure $P_{back} = 50\,\text{bar}$, nitrogen density up to $2.8 \times 10^{20}\,\text{cm}^{-3}$ at $z_m = 310\,\mu\text{m}$ is predicted with this design, which corresponds to a plasma density $n_e = 2.8 \times 10^{21}\,\text{cm}^{-3} = 1.6\,n_c$ at $\lambda_0 = 800\,\text{nm}$ after ionization of N_2 into N^{5+}. Symmetric shock nozzles therefore make it possible to reach near-critical to over-critical densities without the need to use a high-pressure compressor. Moreover, with a 150 bar backing pressure, which can be obtained directly at the exhaust of commercial gas bottles, a density even three times higher would be achievable.

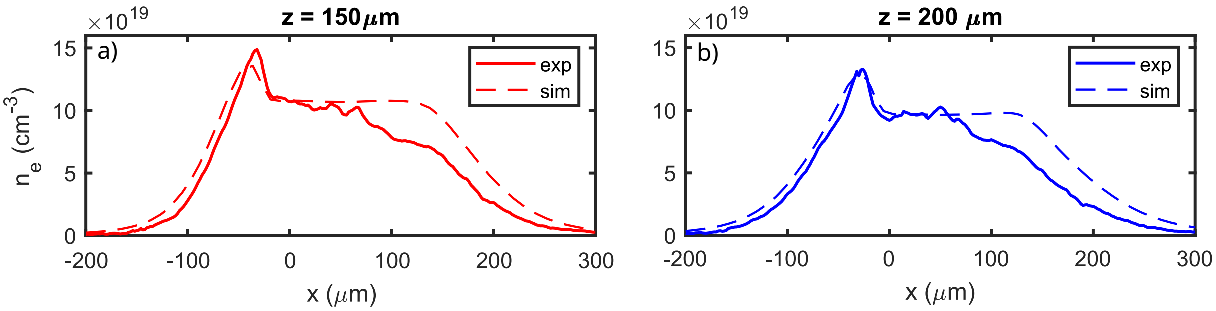

Figure 3.10 – Comparison of measured and simulated plasma profile obtained with a one-sided shock nozzle using nitrogen with a backing pressure of 15 bar at a distance of (a) 150 µm and (b) 200 µm.

3.3 One-sided shock nozzles

In this section, we present a design using an oblique shock only on one side of the nozzle, with an opening angle of 96° (see Fig. 3.9a) in order to tailor the gas profile for injection in the sharp density downward transition induced by the shock structure. This design is asymmetric, and therefore 2D-axisymmetric simulations can no longer be used. It is necessary to perform more numerically expensive full-3D CFD simulations.

The manufacture of such small nozzles with asymmetric features has been made possible by the collaboration with a team of the Center for Physical Science and Technology (FTMC, Lithuania) which developed the femtosecond laser-assisted selective etching (FLSE) technique [136, 137]. FLSE is achieved in two steps: (i) the shape of the inner channels of the nozzle are imprinted on a nozzle frame by a femtosecond laser pulse which damages the fused silica, (ii) the imprinted shape is chemically etched in a potassium hydroxide (KOH) solution for several hours, which affects selectively the laser-damaged parts. This can lead to surface roughness as low as ∼100 nm and average peak-to-valley distances around 500 nm [137].

Figure 3.9b shows the simulated density map obtained by using nitrogen with a backing pressure of 15 bar. The straight section here shown on the left side was designed to generate an additional shock propagating at an angle with respect to the jet axis. In the simulation, the shock angle is $\beta - \theta \sim 14^\circ$ which is in good agreement with the theory presented in Sec. 3.1.2 that predicts an angle of 13°. The slight difference can be explained by the effects of boundary layers that are not taken into account by the 1D-isentropic model. A shadowgraphic image of the plasma above the one-sided shock jet is displayed in Fig. 3.9c and the phase map measured with the quadri-wave lateral shearing interferometer (QWLSI) is showed in Fig. 3.9d. Figure 3.10 compares the density profile obtained in the simulations with the one retrieved from the measured phase map in a nitrogen plasma. Fluid simulations give us the N_2 molecular density, from which we retrieve the corresponding plasma density by assuming ionization up to N^{5+}. The simulation shows a very good agreement with the measured profile as well as with the absolute density value. At $z = 150\,\mu\text{m}$ the measured length of the density downward transition is 16 µm (18 µm in the simulation) for a density drop of 26% (21% in the simulation). At $z = 200\,\mu\text{m}$ the measured length of the density downward transition is 26 µm (27 µm in the simulation) for a density drop of 31% (24% in the simulation). This typical shock length corresponds to only a few plasma wavelengths in our high density regime ($\lambda_p \sim 3\,\mu\text{m}$ at $n_e = 1.4 \times 10^{20}\,\text{cm}^{-3}$) which is well suited to density gradient injection. It also appears that after $x = 75\,\mu m$ there is a decrease in the measured density that is not predicted by the simulation. It has been verified that this is not due to a decrease in intensity by scanning the relative position of the jet with respect to the laser focus. This could be explained by different factors such as defects in the inside geometry of the nozzle or a slight angle between the laser direction and the normal to the shock structure.

Conclusion

We have presented a CFD parametric study of the effect of different parameters on the behavior of oblique shock created by a straight section at the end of a supersonic nozzle. Through the modification of the straight duct length and throat diameter, it is possible to control the position and maximum density of the shocked region. We then presented a new design of shocked gas jet, with an oblique shock on only one side, therefore providing a downward density gradient at the beginning of a transverse path in the flow, that can be used for the gradient injection scheme. The knowledge about the behavior of oblique shock obtained through the 2D-axisymmetric simulations can be applied to the one-sided shock case, and provides us with the general laws to modify the characteristics of the density gradient. This new asymmetric design is particularly well suited to small targets, where inserting a knife-edge in the flow can be difficult. This new OSS target design is used in section 4.2 in order to increase the long-term stability of the accelerator.

Chapter 4

Towards applications: optimization and stabilization

Sommaire

Developing a high-repetition rate LWFA source for applications requires to accelerate electron beams with the best quality achievable. An ideal beam would have, depending on the application, a high (tunable) energy with a narrow distribution, a high charge, a low divergence, a high emittance, an ultra-short duration, or a combination of these. But this is not sufficient. In order to use a laser-plasma for application, obtaining this ideal beam should be a certainty every day, every shot, meaning the accelerator should be both stable and reliable. This chapter presents the efforts made in this direction, trying to enhance the accelerator performances and

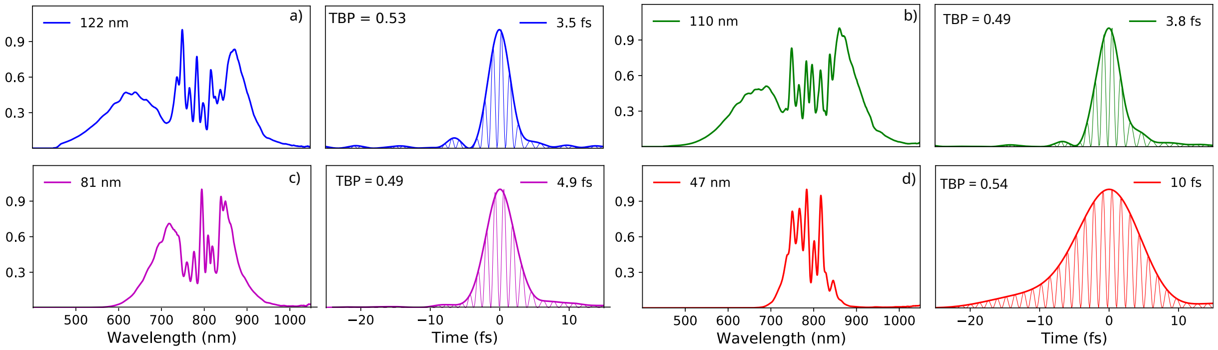

Figure 4.1 – Laser spectral and temporal intensity measured for different hollow core fiber pressures: P_{HCF} = 1100 mbar (blue), 1000 mbar (green), 700 mbar (magenta), 250 mbar (red). Legends provide the RMS spectral width σ (left), and FWHM duration τ_{fwhm} (right) for each P_{HCF} . The thin curves represent $|E|^2$, and the thick curves the envelope. All curves are normalized. FWHM time-bandwidth products (TBP) are also given for each case

stability. A study of the effect of the Fourier-transform limited pulse duration and plasma density is discussed in section 4.1, results on long-term stability using a one-sided shock (OSS) jet are presented in section 4.2. Then, we demonstrate the beneficial effect on the electron energy of using a low-Z gas such as helium in section 4.3, and finally we present the results of the first application experiment in radiobiology of our accelerator in section 4.4.

4.1 Effect of the FTL pulse duration and plasma density

Previous work on kilohertz laser-wakefield acceleration operated in three distinct regimes. First experiments used 20-30 fs pulses with few-mJ of energy per pulse in a low plasma density $n_e \sim 1 \times 10^{19}\,\text{cm}^{-3}$ and achieved acceleration of sub-relativistic, 100 keV electrons [23, 138]. Then, the acceleration of MeV electrons was demonstrated in two other regimes: one with 30 fs laser pulses of peak power of $P_0 \approx 300$ GW and high plasma density $n_e > 4 \times 10^{20}\,\text{cm}^{-3}$ [25], and another, corresponding to the results achieved on the experiment before my arrival, with laser pulses that were post-compressed to nearly single-cycle durations $\tau \sim 3.5$ - 5 fs, and reaching $P_0 \gtrsim 420$ GW, but operating at lower plasma density [26, 131]. Both regimes resulted in the acceleration of MeV electrons but the accelerated beams had very different characteristics. The longer pulses yielded diverging beams with continuous, thermal-like spectra, while peaked spectra at $E \sim 5$ MeV were achieved with sub-5 fs pulses in a lower density plasma. The scaling laws of the bubble regime tends to confirm the advantage of near-single cycle pulses when the laser energy is in the millijoule range, but as discussed earlier, the application of these scaling laws to near-single cycle pulses can have limitations due to additional phenomena driving the physics in this regime. For instance, slightly longer pulses could benefit from lower dispersion effects while still achieving relativistic intensities. Therefore, there is a need for an in-depth study of the effect of laser and plasma parameters in the range between the two documented regimes, in order to optimize the performance of kHz laser-plasma accelerators. The results presented here were published in [139].

By varying the helium pressure in the hollow-core fiber, our set-up enables the continuous tuning of the laser spectral bandwidth from $\sim$ 30 nm to $\sim$ 300 nm (see Sec. 2.1.2), delivering

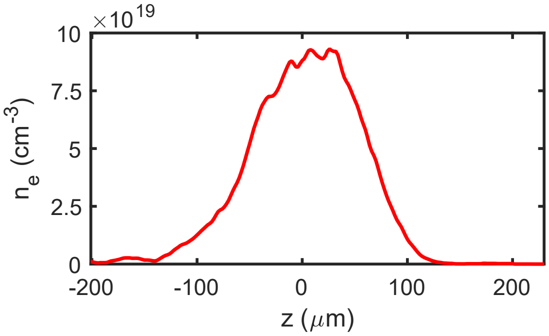

Figure 4.2 – Plasma density profile of the supersonic jet with a backing Pressure $P_{back} = 25\,\text{bar}$

laser pulses with near Fourier Transform Limited (FTL) durations ranging from 25 fs to 3.5 fs. This remarkable feature makes it possible to understand the role of the pulse duration without having to introduce a frequency chirp in the laser pulses. In a way, this amounts to comparing different lasers systems with different bandwidths in a single experiment. This study is limited by the fact that the energy of the laser cannot be increased so longer pulses will necessarily result in a lower laser intensity in vacuum.

4.1.1 Experimental set-up

The experiment that follows was conducted using our kilohertz laser system. The spectral width and the pulse temporal profile were measured in vacuum using the d-scan, and are showed in Figure 4.1. The residual frequency chirp of the laser pulses was minimized by fine-tuning the dispersion using a pair of silica prism. Downstream, the laser was focused on target by, a f/2 off-axis parabola to a 3×3 μm spot (FWHM). The energy on target is ≈ 2.5 mJ, and the maximum laser amplitude in vacuum achieved for 3.5 fs pulse was $a_0 \simeq 1.5$. Overall, the laser energy did not vary significantly, (2.5 mJ at 3.5 fs and 2.6 mJ at 10 fs) when changing the pressure in the hollow core fiber. We note that the data on the shortest case (3.5 fs) was collected one day before the other pulse durations.

For the LPA target we used a convergent-divergent nozzle with a 40 μm throat, 120 μm exit diameter which generated a supersonic flow of molecular nitrogen N_2. The gas profile was characterized using our quadri-wave lateral shearing interferometer. We measured a quasi-gaussian density profile $\propto \exp(-z^2/L_p^2)$ with $L_p = 65$ μm on the laser axis (150 μm from the nozzle). For backing pressures between 12 bar and 100 bar, the peak electron density varied from 4.2×10^{19} cm^{-3} to 3.5×10^{20} cm^{-3}. The density profile for a backing pressure $P_{back} = 25\,\text{bar}$ is showed in Figure 4.2.

4.1.2 Experimental results of the parametric study

The raw data for the electron beams and spectra is presented in 4.3. Electron beams were never observed for the case of 25 fs FTL duration so that this case is not represented. In all other cases, an electron beam was obtained while its charge and divergence could vary greatly depending on the experimental parameters. A global analysis of electron beam data is presented in 4.4a-d, where we plot the mean value, the charge (4.4a), the RMS divergence of the beam (4.4b) the average electron energy (4.4c) as a function of laser pulse FTL duration and electron plasma

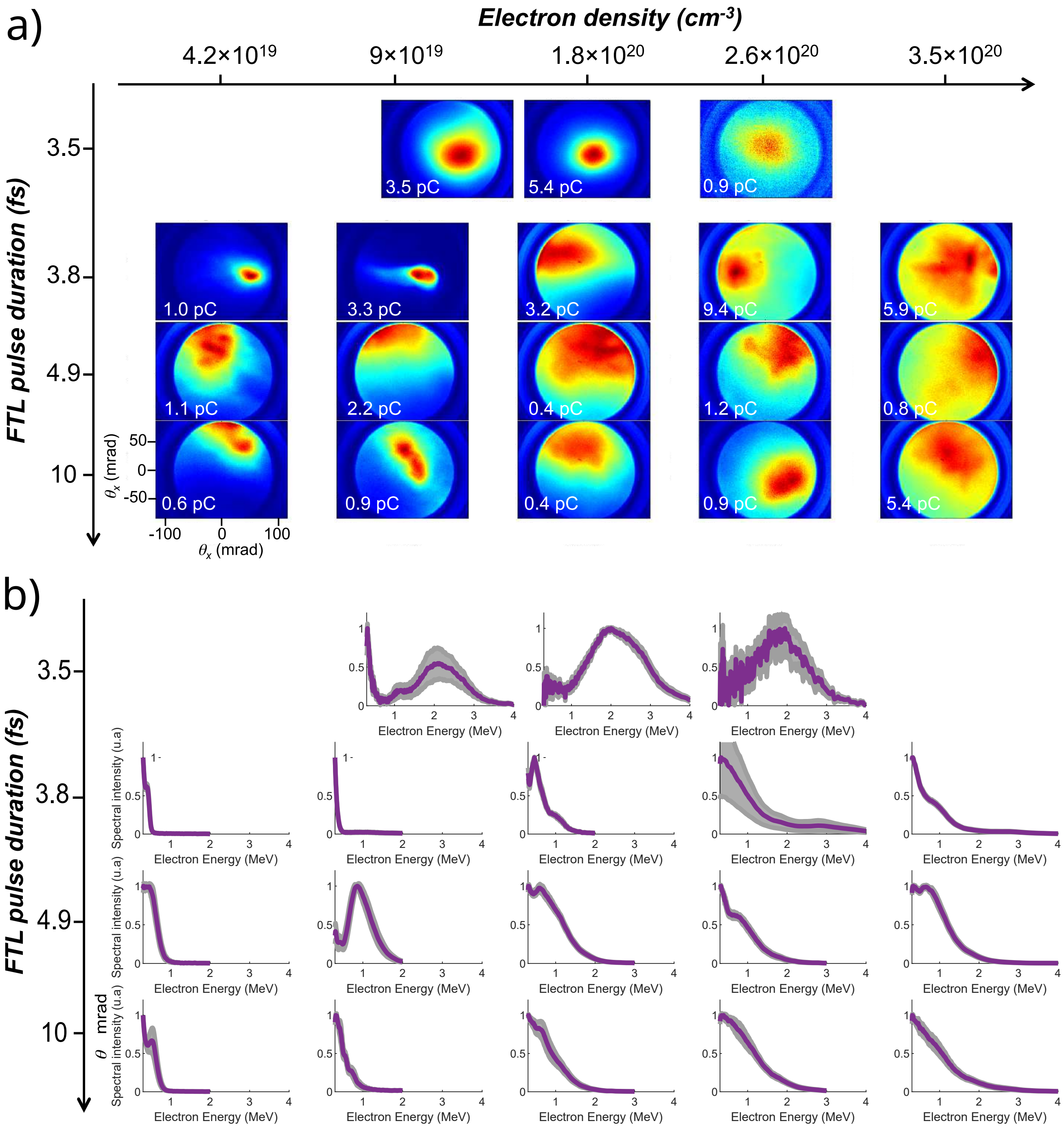

Figure 4.3 – Results of the parametric scan in FTL pulse duration and plasma density. a) Beam profiles and charge. Each beam image was obtained by averaging over 10 to 1000 laser shots, depending on the signal level. b) Normalized electron spectra. Each spectrum was obtained by averaging 10 measurements each accumulating between 100 to 1000 laser shots, depending on the signal level. The gray shaded areas correspond to the standard deviation on these 10 measurements.

density. Each point is averaged over 20 acquisitions, and thus represents an average over 200 shots minimum (high signal case) and 20000 shots maximum (for the low signal cases). The vertical error bars represent the standard deviation from the mean value estimated from the 20 acquisitions. To quantify the LPA performance, we define the quality factor, $f_q = \langle E \rangle \, Q / \sqrt{\sigma_x \sigma_y}$, shown in 4.4d. In this formula, Q is the total charge per shot, $\langle E \rangle$ the average energy of accelerated electrons, and σ_x, σ_y are the RMS angular divergences of the beam along x and y directions. Clearly, this quality factor favors electron beams with high energy, high charge and narrow divergence. The first clear result is that the highest quality factor is obtained for the shortest 3.5 fs pulses, at a specific resonant density. This is associated with with a collimated ~ 50 mrad FWHM beam with relatively high charge (5.4 pC/shot) and a spectra peaked at 2 MeV. Another case yielding a beam with a high quality factor is the 3.8 fs pulse at $n_e = 2.6 \times 10^{20}\,\mathrm{cm}^{-3}$, with a notably high charge (9.4 pC/shot). Most of this charge is part of a very divergent beam with a low-energy thermal-like spectrum, but this spectra also has a higher energy peak at $\sim$3 MeV that seems to correspond to a more collimated part of the beam.

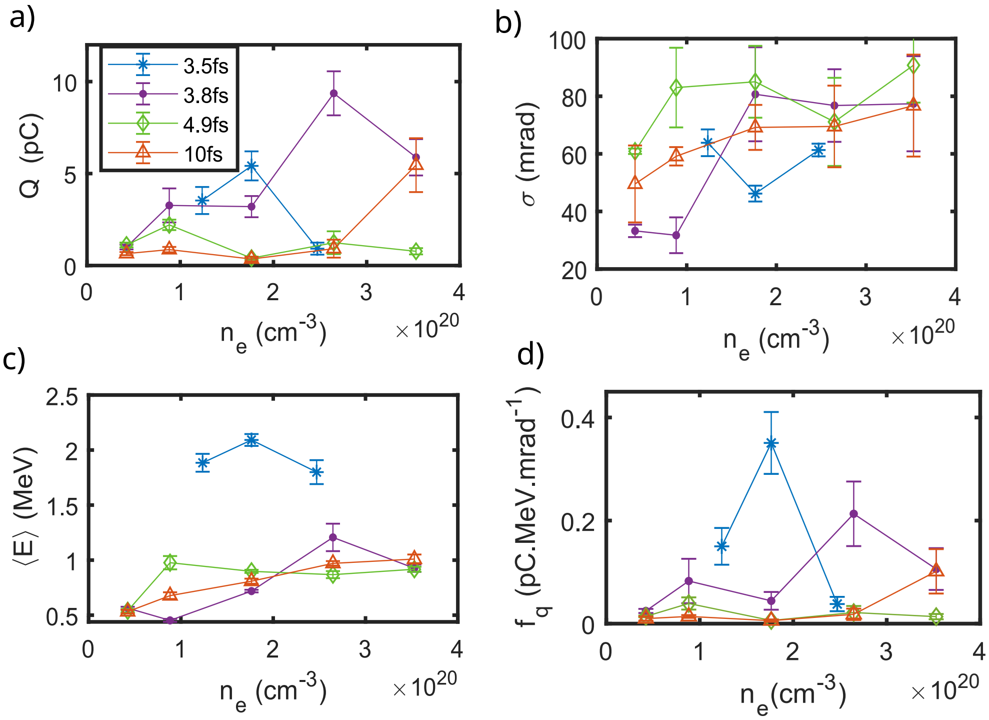

Figure 4.4 – a) Injected charge b) RMS beam divergence c) electron mean energy and c) Electron beam quality factor $f_q = \langle E \rangle \, Q / \sqrt{\sigma_x \sigma_y}$ for different pulse durations and plasma densities.

Let us now consider correlations between experimental parameters and LPA performance. In 4.5, we plot the same parameter space as in 4.4a, and show the measurements using red circles whose size represent the total beam charge. On the same graph, the conditions for relativistic self-focusing, and longitudinal matching of the laser pulse with the plasma are also represented. We recall these conditions:

$$P_0 \gtrsim 17\, n_c / n_p \text{ [GW] (a), and } c\tau \simeq c/\omega_p \text{ (b)}, \tag{4.1}$$

where $n_c = 1.1\, \lambda_0^{-2}\, 10^{21}\ \mathrm{cm}^{-3}$ is the plasma critical density for laser wavelength λ_0 (here in

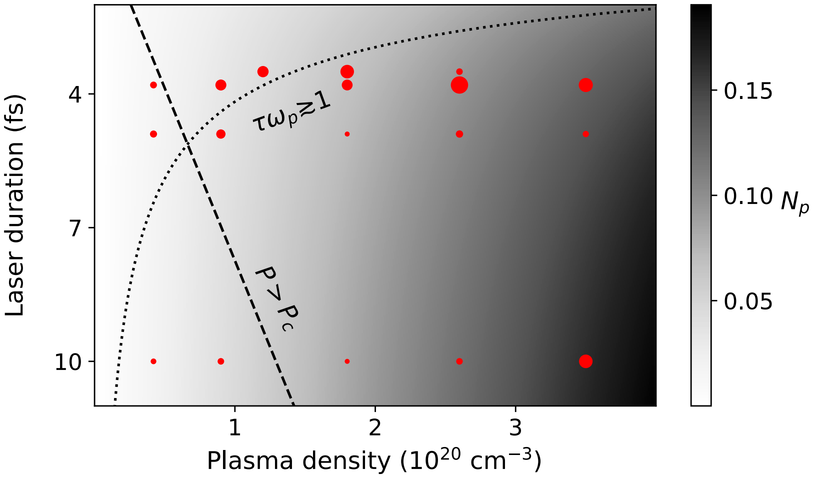

Figure 4.5 – Parameter space of the kHz LPA. Measurements are represented by red circles with sizes proportional to the beam charge. Dashed and dotted lines represent conditions in 4.1, and the gray colormap corresponds to the normalized plasma density $N_p = n_p/\gamma_\perp n_c$.

micrometers), and $\omega_p = c\sqrt{4\pi r_e n_p}$ is the plasma frequency with the plasma density n_p, and the classical electron radius r_e. Note that the pulse duration τ in Eq. (4.1b) is defined as the RMS of the intensity profile and corresponds to $\tau = \tau_{\text{fwhm}}/2.355$. For these estimates, it was assumed that the laser energy is 2 mJ and the focal spot size $R_{\text{fwhm}} = 3\ \mu$m.

In 4.5, we plot Eq. (4.1a) and Eq. (4.1b) with the dashed and dotted curves respectively. Firstly, one may note that below the relativistic self-focusing threshold, the accelerated charge is low, indicating that self-focusing is required to reach the high intensity required for stable self-injection. Most of the high-charge cases correspond to above-critical laser powers and pulse duration close to the plasma wave periods – cases of 3.5 fs and 3.8 fs laser pulses. Figure 4.4a shows that for the 3.8 fs pulse, as the plasma density grows, the injected charge increases, and so does the beam angular divergence. The charge increase can be explained by stronger self-focusing and also by the laser group velocity slowdown in the plasma, $v_g/c \simeq 1 - n_p/(2\gamma_\perp n_c)$, where $\gamma_\perp \simeq \sqrt{1 + a_0^2/2}$ is the relativistic factor of laser-driven electron fluid. This plasma wave slows down for the higher n_p, which facilitates electron trapping. Beam divergence is determined by the spread of electron transverse momenta acquired during the injection. Naturally, this initial divergence scales with the plasma focusing force growing as $F_\perp \propto n_p$.

The longer laser pulses (10 fs case) clearly do not fulfill the longitudinal resonance condition Eq. (4.1b), and its $a_0 \approx 1$ is too low to trigger self-injection. These longer pulses need to evolve in the plasma, via the self-modulation and relativistic self-focusing instabilities to efficiently excite a plasma wave. For the considered parameters, these processes are strongly nonlinear and can be quantified by the normalized plasma density, $N_p = n_p/\gamma_\perp n_c$, an equivalent to the similarity parameter in Ref. [140]. For higher Np, laser plasma interaction becomes more nonlinear, i.e. the laser shape and spectrum are strongly affected by the plasma instabilities such as relativistic self-focusing, self-modulation etc. In 4.5, N_p is plotted in gray, and we see that in the unmatched case (10 fs), efficient electron acceleration occurs preferentially when plasma parameter reaches $N_p \gtrsim 1/6$, which favors nonlinear plasma effects.

4.1.3 PIC Simulations

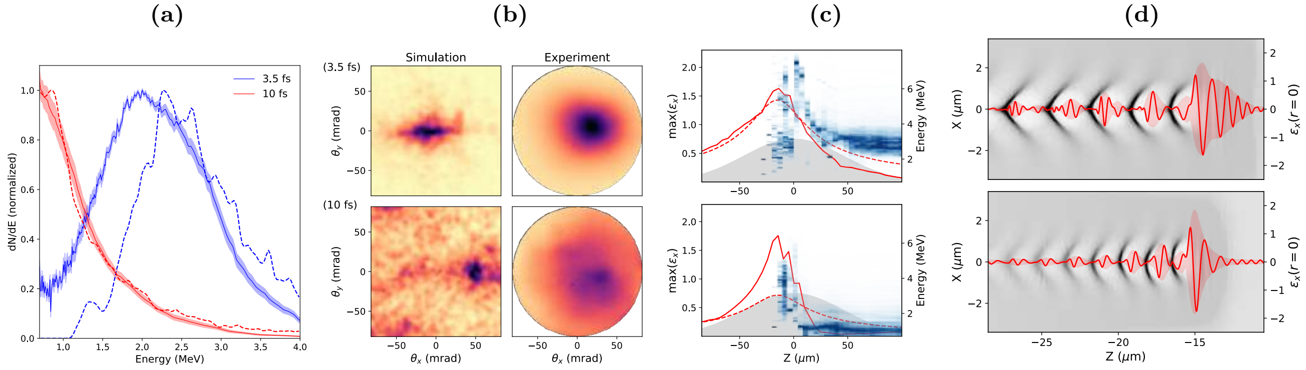

Figure 4.6 – Measured and modeled electron beams with 3.5 fs laser pulse and $n_p = 1.8 \times 10^{20}$ cm^{-3} (blue in (a), top in (b,c,d)), and with 10 fs pulse and $n_p = 3.5 \times 10^{20}$ cm^{-3} (red in (a), bottom in (b,c,d)). (a) Measured electron spectra (solid curves shaded with standard deviation) and modeled (dashed curves). (b) Measured (right) and simulated (left) angular electron distribution. (c) Simulated evolution of the peak laser field $\epsilon_x = eE_x/m_e c\omega_0$ (red curve) and the electron energy spectrum normalized at each time-step (blue scale); the dashed red curve is the in-vacuum laser propagation, and the gray area represents the plasma density profile in arbitrary units. (d) On-axis laser field (red curve), its temporal envelope (red filled area), and electron density normalized to $15n_p$ (gray scale) at the laser focal position, just before injection.

In order to understand the underlying physical processes specific to the two extreme regimes, we performed PIC simulations for the shortest (3.5 fs) and the longest (10 fs) laser pulses with their corresponding plasma densities $n_e = 1.8 \times 10^{20}$ cm^{-3} and 3.5×10^{20} cm^{-3}, respectively. These two cases correspond to (i) the resonant case, giving peaked electron energy and narrow divergence beams, and (ii) the self-modulated case, giving high charge and high divergence beams.

The interaction domain was discretized in a cylindrical grid with cell-sizes $\Delta z \times \Delta r = 21\,\text{nm} \times 40\,\text{nm}$. Five azimuthal Fourier modes were used. The plasma was initially modeled as a neutral nitrogen gas with 16 macro-particles per cell and with a density profile corresponding to measured experimental profile. The experimental laser temporal and spatial profiles were used following the method described in section 2.5.3. In the simulations, the laser energy was adapted to match the experimental results, giving 2 mJ for the 3.5 fs case, and 1.5 mJ for the 10 fs case. The laser energy in the long/high-density case had to be reduced more than in the matched case in order to reach accelerated charge at a similar level to what was obtained experimentally. The adjustment between the two cases could be explained by the pressure buildup in the chamber when using higher gas pressures which is not modeled by the simulation and has been shown to be detrimental to the performances of the accelerator [25].

In 4.6(a,b) we compare the spectral and angular electron distributions obtained in experiment to the simulation results. For the chosen parameters, the simulated beam features are in a good agreement with the experiment. We see that the shortest pulse provides a collimated electron beam with a peak in spectrum around $2 - 2.5$ MeV, while in the 10 fs case, the beam is rather divergent and has a thermal spectrum with an equivalent "temperature" $T_e \approx 700$ keV. In the experiment, the total charge was measured within a 75 mrad aperture, and was found to be

5.4 pC in both cases. In simulations, considering the same aperture, the beam charges are 4.6 pC (22 % from ionization injection) and 9 pC (16 % from ionization injection) in the 3.5 fs and 10 fs pulse cases respectively. However, in the latter case, the modeled beam divergence was ~ 200 mrad (fwhm) and the total charge reached 48 pC (mainly from the self-injection) in that larger aperture.

The dynamics of the electron spectra and laser peak field are depicted in 4.6(c). In the 3.5 fs case, the laser experiences moderate self-focusing and produces electron injection and acceleration, which brings electrons to high energies $\lesssim 8$ MeV. But when particles reach the front half of the bubble, the plasma field tends to decelerate them until the laser diffracts too much to drive a plasma wave when $a_0 \lesssim 0.5$, and leaves the electron spectrum with a peak around 2.5 MeV. In the second case (4.6(c) bottom), the laser gets strongly focused and modulated, $a_0 \gtrsim 1.7$, which triggers electron injection. Although self-focusing greatly enhances the laser field, the interaction length and the acceleration length are both strongly reduced because of strong pump depletion and strong defocusing. In this case, electron dephasing is also very fast (distance of few μm), so that electrons are continuously accelerated-decelerated, which produces a thermal electron spectrum around $\epsilon_w = 700$ keV. In both cases, the electrons originate mainly from self-injection even though a significant ($\sim$20%) part of the total charge can be attributed to ionization injection of K-shell electrons of nitrogen.

Laser self-modulation is essential to achieve laser-plasma acceleration for the longer pulses, $\omega_p \tau \gg 1$, which in our study occurs with a 10 fs pulse duration. In 4.6(d), we see that in both short and long cases, the pulse profile at its focal position acquires a peak located in the first bucket of the plasma wave. This "driver" peak is shaped by the plasma resonance, and its duration, measured with a Gaussian fit, matches exactly the condition Eq. (4.1b), giving $\tau_{\text{fwhm}} = 3.1$ fs and 2.1 fs for $n_e = 1.8 \times 10^{20}$ cm^{-3} and 3.5×10^{20} cm^{-3} respectively. Additionally, in both cases, the laser experiences strong redshift which facilitates trapping by reducing the laser group velocity, and thus the wake phase velocity. By looking at the evolution of the pulse energy during propagation, we confirm that the concept of the etching length L_{etch} presented in the scaling laws of the bubble regime in section 1.4 is not well adapted to our regime. Indeed, the equation 1.45 provides etching lengths of $L_{etch} \simeq 10\,\mu$m in the short case, and $L_{etch} \simeq 14\,\mu$m in the 10 fs case, while the pump depletion occurs on much larger scales in the simulations. For the short pulse and moderate density, half of the pump energy is depleted in $\sim 120\,\mu$m, while it occurs on a smaller distance of $50\,\mu$m in the long pulse case with high plasma density. Surprisingly, the physics of these two cases is thus relatively similar. The main difference is that in the high density case, the nonlinearities are more violent and the pump depletion and dephasing lengths are shorter, which greatly limits the acceleration length.

4.1.4 Conclusions

We have studied the performances of our accelerator in a large range of laser durations and plasma densities. This allowed us to verify that the regime yielding the best performances with collimated beams and peaked spectra is obtained with the shortest pulses and moderate plasma densities which roughly matches the parameters predicted by the bubble scaling laws. Another notable regime arising from this data is obtained when focusing longer ($\sim$10fs) pulses in a high density $n_e \sim 3 \times 10^{30}$ cm^{-3} plasma. These conditions lead to high charge divergent beams with a thermal energy distribution reaching a few MeVs. Simulations also seems to indicate that the acceleration regime attained in the experiment is not optimal yet as the electrons reach high energies ($\sim$ 8 MeV) in the plasma before being dephased and strongly slowed-down to 2.5 MeV. An improvement would be to reduce the extension of the plasma so that the electrons exit it when reaching their maximum energy, but the targets that we use are already close to the limit of what is feasible considering the safety distance from the laser focusing point to the target and the high densities that are needed. Another solution would be to reduce the effective size of the plasma after injection by focusing the laser near the end of the jet. But in nitrogen, the ionization defocusing associated with propagation in the high density high-Z gas would prevent the laser from reaching the high intensities necessary to drive a wake.

4.2 Long term stability using a one-sided shock jet

Using a laser-plasma accelerator for applications will require to achieve stable performances over extended and continuous periods of time, while providing consistently similar acceleration regimes from one day to another. Even though numerous articles reported on the accelerator stability on short timescales [15, 127, 141] comparing shot-to-shot variations on a few tens of shots. This question of long-term stability and reliability of the LPA was notably absent from the literature, most studies focusing on proof-of-principle experiments and the study of underlying physical processes occurring in laser-plasma interaction.

This was also one of the main issue of our high-repetition laser wakefield accelerator, because even if good quality beams, with high shot-to-shot stability [131] could be obtained, those regimes could not be sustained for more than a few minutes ($\sim$ 10 min) without the need to re-optimize the electron beam, by moving the position of the gas jet relatively to the focus, or slightly adjusting the other parameters. This indicates that the accelerator is extremely sensitive to slight variations in the experimental parameters which is not adequate to achieve long term stability. Moreover, the interesting regime of collimated, few (3-5) MeV beams with peaked spectra could proves difficult to obtain consistently from one day to another, while laser beam parameters were remaining seemingly similar. More generally, the accelerator day-to-day reproducibility was not sufficient to be able to carry out application experiments, as the typical electron beam one could obtain would significantly vary on different days.

However, the interest for the long-term stability of LPA is rising with initiatives such as the LUX beamline at DESY aiming at turning laser-wakefield accelerators into an actual machine, where they demonstrated a 24 h continuous operation of their accelerator driven by a 50 TW laser operating at 1 Hz corresponding to 100 000 shots with electron beams of energy around 300-400 MeV [142]. Those results were published just a month before the ones presented in this section [143].

4.2.1 Experimental set-up

Laser

The laser energy was higher for this experiment thanks to an upgrade, with a energy on target of 3.8 mJ. This allowed us to use a longer focal f'=100 mm off-axis parabola to focus the pulses, resulting in a 6.2 µm × 5.5 µm FWHM focal spot, which corresponds to a Rayleigh range of $z_R \sim 100\,\mu\text{m}$. These laser parameters yield a measured peak intensity in vacuum

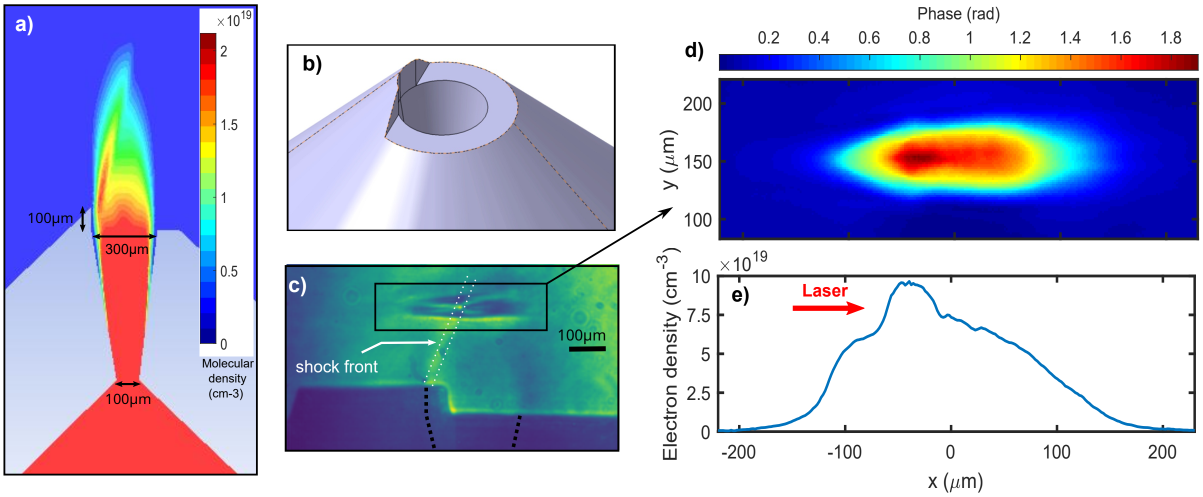

Figure 4.7 – a) Molecular density map from a 3D CFD simulation of an OSS jet performed with Fluent. Gas is N_2 and backing pressure P = 20 Bar. Colormap is capped at 2.1×10^{19} cm^{-3} for viewing purpose. b) 3D model of the One-Sided Shock nozzle. c) Shadowgraphic side view image of the plasma. Black dotted line suggests the inner walls of the nozzle, white dotted lines follow the shock front. d) Experimental phase from the plasma column measured with the wave-front sensor. The y-axis represents the distance from the nozzle exit, the x-axis is the laser propagation axis. e) Electronic density profile at 150 µm from the OSS nozzle's exit, retrieved by Abel inversion of the phase map. Laser propagation direction is from left to right (red arrow)

of $I = 2.0 \times 10^{18}$ W cm^{-2} and a normalized vector potential $a_0 \simeq 1.0$. Note that due to the energy upgrade, damages could appear periodically (after 2-3 days) on the mirror right after the HCF because of the increased fluence. Considering the long optical path from the exit of the fiber to the experiment itself, compensation for long-term thermal drifts proved crucial to the long-term stability of the LPA. We thus set up a slow beam pointing device operating at < 1 Hz just before the experiment, using the leakage through a mirror in the turning box just before the final focusing parabola. This ensured that the laser beam alignment on the gas jet stayed rigorously the same and that the focal spot quality was identical throughout the long acquisition run. Images of the focal spot were taken before and after the experiment, and displayed no significant evolution.

Gas jet

The implementation of the density transition injection scheme has been showed to facilitate trapping and enhance the stability of LWFA [58–62]. Indeed, it localizes the injection at the shock position, regardless of laser variations and non-linear effects, and lowers the density of the plasma necessary for electrons to be injected. Therefore, in order to enhance the stability of our accelerator, we use a one-sided shock nozzle manufactured in fused silica, as described in section 3.3 to trigger injection in the density downramp. It has a 100 µm throat and 300 µm exit hole diameter, with a 100 µm long flat section at the end. Figure 4.7a shows a map of the molecular density obtained by simulating a nitrogen flow through the OSS nozzle using the software FLUENT, with a backing pressure of 20 bar. The shock-front in gas density originating from the final straight section is clearly visible.

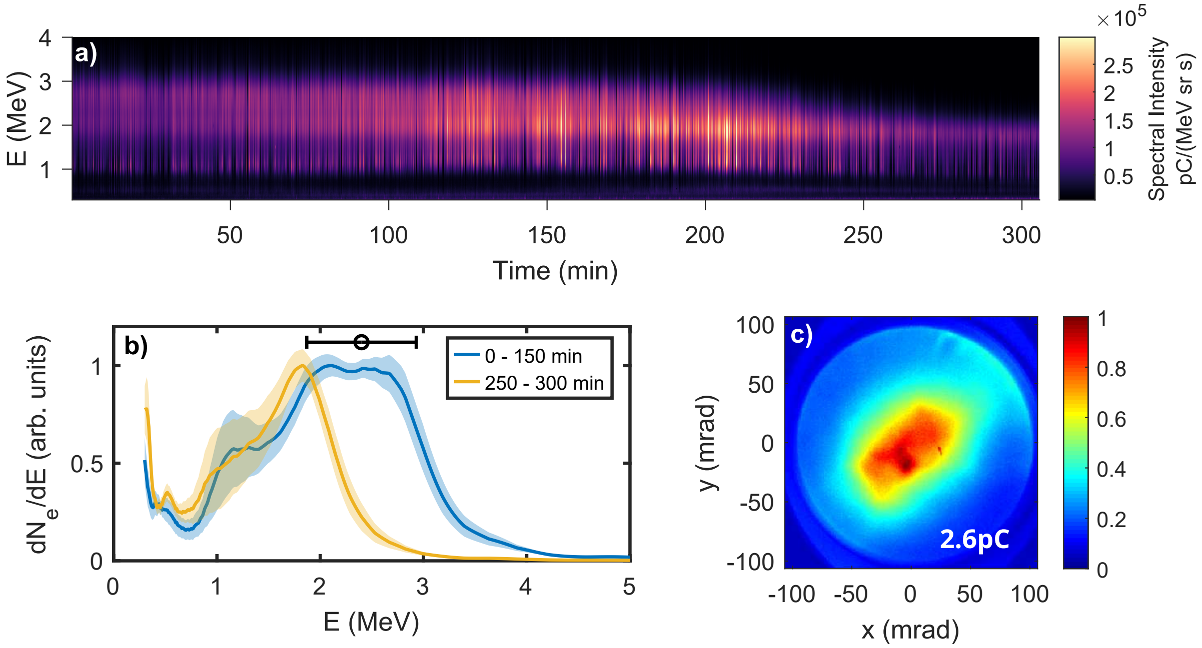

Figure 4.8 – a) Electron spectra measured continuously for 306 min. Each spectrum is averaged over 100 shots. b) Electron spectra averaged over 0-150 min (blue) and 250-300 min (orange), and their standard deviations (shaded area); the black error bar represents the spectrometer resolution at 2.4 MeV. c) Electron beam measured just before the start of the 5h spectrum monitoring. The total charge per shot is 2.6 pC ± 0.6 pC (std). The beam divergence is approximately 80 mrad FWHM.

The plasma density profile was characterized experimentally by creating a plasma column using the laser beam and measuring the phase shift with the SID4-HR, as described in section 2.4.2 for asymmetric jets. Figure 4.7e shows the measured electron density lineout at 150 µm from the nozzle exit, with a backing pressure of 22 bar. The peak density is $n_e = 9.7 \times 10^{19}\,\mathrm{cm}^{-3}$ and the density after the shock is $7.3 \times 10^{19}\,\mathrm{cm}^{-3}$, corresponding to a 25% density drop with a transition width of 15 µm. Finally, in this free flowing jet, the stability of the plasma density is determined by the precision of the pressure regulator, and is estimated to be better than 4%. The differential pumping system was not yet implemented for this experiment.

4.2.2 Experimental results

Stability over 5h of continuous operation

The beam profile and charge were measured right before the start of the electron spectrum monitoring. Statistics were performed from 20 acquisitions, each consisting of an accumulation over 10 shots, thus accounting for 200 shots in total. This initial measurement yielded a mean charge of 2.6 pC per shot with a 0.6 pC standard deviation, and a beam divergence of 80×75 mrad $\pm\, 8\times9$ mrad FWHM(see Fig. 4.8c). Electron beam pointing stability is 17×11 mrad RMS. This regime was obtained by setting the focal point of the laser at the position of the shock-front, strongly suggesting that the injection occurs indeed at the density transition. The electron spectrum was then monitored during 5 hours of complete hands-off operation of the kilohertz laser-plasma accelerator, i.e. with no other intervention than the beam pointing stabilization feedback loops in the laser chain. Results of this measurement are displayed in

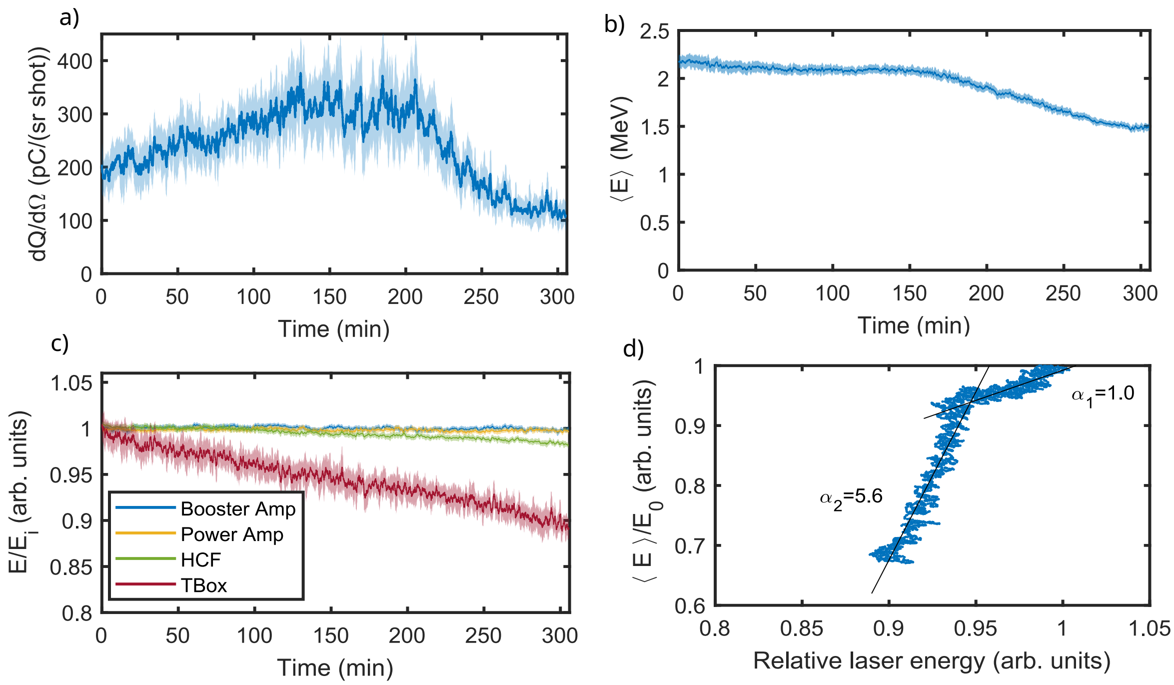

Figure 4.9 – a) Total charge per solid angle collected through the electron spectrometer pinhole. b) Mean electron beam energy versus time. c) Monitoring of the laser energy at four points in the laser chain. Each curve in this figure is averaged over a one minute moving window and shaded areas represent the corresponding standard deviation. d) Correlation between the electron mean energy and the relative laser energy right before the off-axis focusing parabola, and linear fits of the two different parts of the curve, with slopes α_1 and α_2.

Fig. 4.8a. Beams with peaked spectra and a large majority of electrons with energy exceeding 1 MeV were reliably produced throughout the whole 306 min of monitoring. Moreover, during the first 150 min, the spectrum remained very stable, with a peak energy of 2.5 MeV. After that, the high-energy part noticeably eroded with time, lowering the peak energy to 1.9 MeV. A comparison of the spectra during the first 150 min and the last 50 min is represented in Fig. 4.8b.

To complete these data and assess more thoroughly the question of stability, we plot the temporal evolution of the total charge per solid angle $dQ/d\Omega$ collected through the pinhole of the spectrometer (Fig. 4.9a), the mean energy of the electrons $\langle E \rangle$ (Fig. 4.9b), as well as the relative laser energy at different points of the laser chain (Fig. 4.9c). All curves are averaged over a 1 min moving window. The data show an increase in $dQ/d\Omega$ (Fig. 4.9a) during the first 130 min. This is likely due to a small angular drift of the electron beam on a long time scale, resulting in a higher electron signal through the electron spectrometer pinhole. Therefore, only the short term variation of the charge can be estimated with certainty from this measurement, giving typical fluctuation of about 50 pC/(sr shot) corresponding to 20% RMS.

Figure 4.9b confirms the observations made previously regarding the stability of the spectrum, and indeed, shows that the mean energy of the electrons is quite stable at $\langle E \rangle \simeq 2.1$ MeV during the first 150 min of monitoring, with short-term RMS variations of only 2-4% (shaded area in Fig. 4.9b). The decrease of the mean beam energy to $\langle E \rangle \simeq 1.5$ MeV toward the end

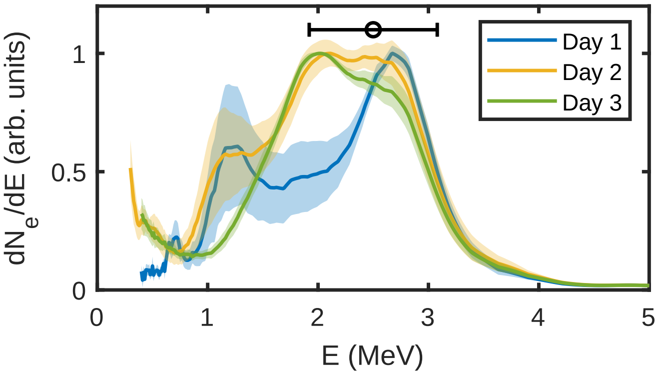

Figure 4.10 – Electron spectra obtained on three different days with the same one-sided shock nozzle. Spectra are the results of averaging over 2000 shots for day 1 and day 2, and 5000 shots for day 3. Day 1 and day 2 are 7 days apart, day 2 and day 3 are 6 days apart.

of the run can also be clearly observed. Note that during the run, the laser system was extremely stable, see Fig. 4.9c, except for the energy measured using the turning box diagnostic (red curve in Fig. 4.9c), which is the last measurement point before the focusing parabola and is, therefore, the most representative of the evolution of the laser energy on target. The energy measured at this point decreased steadily during the experiment and reached a 11% relative loss after 306 min. This progressive energy loss was due to the slow damage of a few chirped mirrors at the end of the compressor. Indeed, we see that the energy after the HCF slightly decreases during the run, indicating that the damage probably originates from the mirror right after the fiber, which created a hotspot in the beam profile that propagated the damage to the last chirped mirrors, where the laser approaches full compression. Interestingly, the evolution of the electron energy can be correlated to the evolution of the laser energy at this last measurement point. To display these correlations, Fig. 4.9d shows the normalized mean energy of the electrons plotted against the laser relative energy. Two different correlation regimes are clearly distinguishable: (i) the first 5% of laser energy loss leads to a $\sim$ 5% energy loss of the electrons suggesting a linear correlation. We then observe a threshold effect, (ii) as the next 5% drop of laser energy correlates with a $\sim$30% electron mean energy loss. Assuming a linear dependence in both regimes, the two parts of the correlation plot are linearly fitted, yielding a slope $\alpha_1 = 1.0$ in the first five percents of energy loss, and a slope $\alpha_2 = 5.6$ in the following five percents. This highlights the importance of laser energy stability: in our case, energy variations larger than 5% can cause significant modifications of the electron spectrum due to what seems like a threshold effect. Nevertheless, decent stability of the electron beam was achieved over the 300 min of continuous operation, with the first 150 min period displaying a remarkable stability correlated to the highest laser performance. This is a significant improvement compared to previous results of our experiment where this level of stability would not be achieved on times longer than 10 minutes. In addition, even though it led to a loss of performance, the decrease in laser energy highlights the robustness of the density downramp injection method, since this advance in long-term stability was achieved despite the significant variation of an important laser parameter.

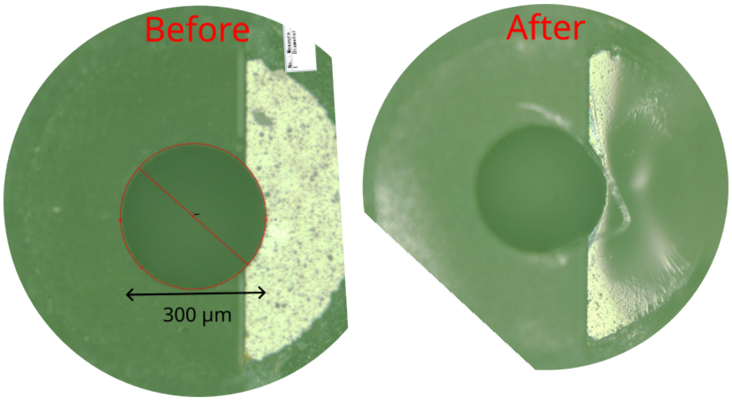

Figure 4.11 – Top view images of the OSS jet before and after being used for 30 - 50 × 10^6 shots, taken with an optical microscope.

Day-to-day repeatability

In order to determine the repeatability of the electron beam and to assess the sensitivity of the accelerator to small day-to-day variations of the laser parameters, the measurements were repeated on three different days, each separated by about a week. The same actual OSS nozzle was used for the three experimental runs and kept its integrity over time despite minor damages (see Fig. 4.11. Table 4.1 summarizes experimental conditions for each day, as well as the charge and mean electron energy corresponding to the electron spectra displayed in Fig. 4.10.

	Day 1	Day 2	Day 3
I (W.cm^{-2})	1.8×10^{18}	2.0×10^{18}	1.6×10^{18}
$n_{e,peak}$ (cm^{-3})	8.8×10^{19}	9.7×10^{19}	9.7×10^{19}
Q (pC/shot)	1.6±0.2	2.6±0.6	1.4±0.2
div. fwhm (mrad)	42±10	77±7	57±11
$\langle E \rangle$ (MeV)	2.29±0.13	2.11±0.06	2.19±0.04

Table 4.1 – Various experimental parameters and electron beam performance showing slight variations from day to day but overall fair reproducibility of the experiment. The values after the ± sign are RMS deviation.

These results show that the downward gradient injection method with one-sided shock nozzles increased significantly the reliability of the accelerator. Indeed, electron beams with similar charge and 2-3 MeV peaked spectrum were easily obtained even though the experimental parameters varied slightly from day to day. In particular, we see that experiments from day 2 and day 3, performed at the same plasma density, yield very similar electron spectra. Such level of reproducibility is decisive for a reliable use of the accelerator for applications. Moreover, the fused-silica nozzles showed a great resilience to damage, as the one used for this experiment provided reliable and reproducible results even after using it for about 30 - 50 × 10^6 shots.

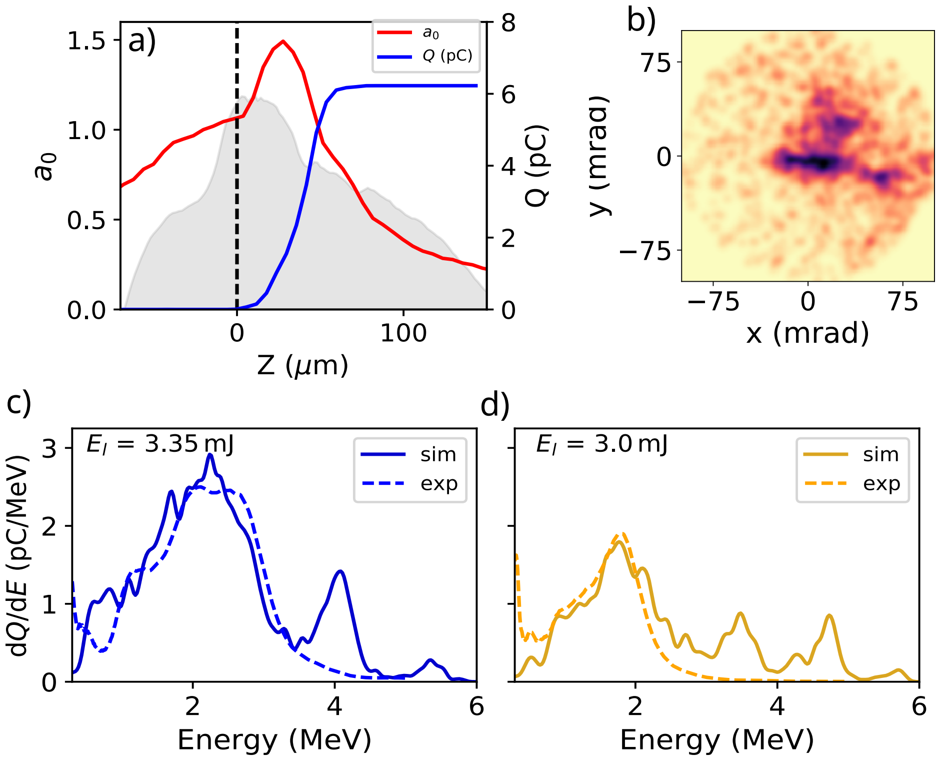

Figure 4.12 – a) Evolution of the peak normalized laser field $a_0 = eE_l/m_e c\omega_0$, electron charge of the beam (blue), and plasma density profile (gray) in arbitrary units with the laser propagation distance. b) Electron angular distribution. c) Electron spectrum from the simulations for an adjusted laser energy of 3.35 mJ (solid) chosen to best match the experimental spectrum at the beginning of the experiment (dashed). d) Electron spectrum from the simulations for an adjusted laser energy of 3.0 mJ (solid) corresponding to a 10% energy loss, and experimental spectrum at the end of the 5h run.

4.2.3 PIC simulations

Simulation setup and general results

To gain insight into the injection process and the role of the density transition, we now turn to particle-in-cell (PIC) simulations. The cylindrical simulation domain is discretized with a grid size $\Delta z = 26$ nm, $\Delta r = 2\Delta z$, 5 azimuthal Fourier modes, and 16 macro-particles of initially neutral nitrogen per cell. To reproduce the realistic laser pulse, we have used the intensity profile and the temporal field map recorded experimentally at the laser focus. The plasma density in the simulations is set to $n_e = 1.2 \times 10^{20}\,\mathrm{cm}^{-3}$. We study the dependence of the accelerated electron beam on the laser driver energy. To do so, 16 simulations were performed, varying E_l in the range 2.6-3.8 mJ.

Figure 4.12c-d represent the experimental and simulated spectra for laser energy corresponding to the beginning and the end of the experimental run. The energy in the corresponding simulations had to be slightly reduced to 3.35 mJ (instead of 3.8 mJ measured experimentally) and 3.0 mJ (maintaining the 10% drop associated with the damage in the chain) to match the experimental results. The simulations reproduce quite well the electron energy loss concomitant to a 10% decrease of the laser energy, even though some higher energy electrons (small peaks at $E > 3\,\text{MeV}$) were not detected in the experiment. The charge in the simulations is 6.2 pC for the 3.35 mJ case and 3.3 pC with the 3.0 mJ pulse.

In Fig. 4.12a, blue and red curves show the dynamics of electron injection and laser peak field as it propagates in the plasma (gray area). It shows that electrons are injected as the laser propagates through the density down-ramp confirming the importance of the density transition for triggering electron injection. Note that the laser also undergoes self-focusing as it propagates in the shocked region which increases the laser intensity and enhances electron injection at the adequate position because co-located with the density downramp. Finally, a series of simulations at different laser focus positions, $z_{\text{foc}} \in (0\,,40)\,\mu$m, was performed, showing that injection always occurs in the vicinity of the shock and in the density down-ramp. This suggests that the density transition region stabilizes the injection process by localizing it to the shocked region. Electrons from ionization injection represent only 5% of the total charge in the 3.35 mJ case, and lead to a small peak around 7.5 MeV in the spectrum. This peak was not detected during the experiment and is not displayed in Fig. 4.12c for the sake of clarity.

Injection mechanism and laser energy dependence

Let us now take a closer look at the injection mechanism, and its dependence to the laser driver energy. Firstly, the plasma wavelength at $n_e \sim 10^{20}\,\text{cm}^{-3}$ is $\lambda_p \sim 3.2\,\mu\text{m}$ which is significantly lower than the density transition typical length of 15 µm. It thus corresponds to the long gradient case described in section 1.5.3. In Fig. 4.13a-b, we represent, for two laser energies, the plasma density at the end of the downramp, the injected electrons in phase space and the on-axis E_z field. In both cases, L-shell electrons are trapped in several buckets, starting quite far behind the laser pulse, respectively from the 4^{th} and the 5^{th} bucket. This behavior is found in all the simulated cases: it is found that the first bucket in which electrons are injected moves backward when reducing the energy. It goes from the 3^{rd} bucket at $E_l = 3.8\,\text{mJ}$ to the 7^{th} bucket at $E_l = 2.6\,\text{mJ}$.

This can be explained by the mechanism of injection in a long downward density gradient. We recall the evolution of the wake phase velocity in a downward density transition [59]:

$$v_p = c\frac{1}{1+(z-ct)\frac{1}{k_p}\frac{dk_p}{dz}}\,, \tag{4.2}$$

With $k_p(z) = \sqrt{4\pi r_e n_e(z)}$ the local plasma wave number where r_e is the classical electron radius. According to Eq. 4.2 the wake phase velocity decreases with the laser co-moving coordinate $(\text{z}-\text{ct})$. Therefore, the wake phase velocity is smaller in buckets that are further away from the laser pulse and trapping of slower electrons is facilitated in these buckets. A similar effect has been observed experimentally in [138], when a laser was focused at the exit ramp of a subsonic jet. When lowering the laser energy, the amplitude of the wake decreases (see Fig 4.13c) and the first bucket where the wavebraking condition is satisfied moves further behind, leading to the behavior of the injection moving back observed in Fig 4.13a,b. To support this analysis, we plot the mean position of injection in the co-moving frame, according to the laser initial energy plotted in Fig 4.13c, where the mean position of injection $\langle z-ct\rangle_{inj}$ goes from $-19\,\mu\text{m}$ at 3.8 mJ to $-28\,\mu\text{m}$ at 2.6 mJ. This position is estimated on each step by taking

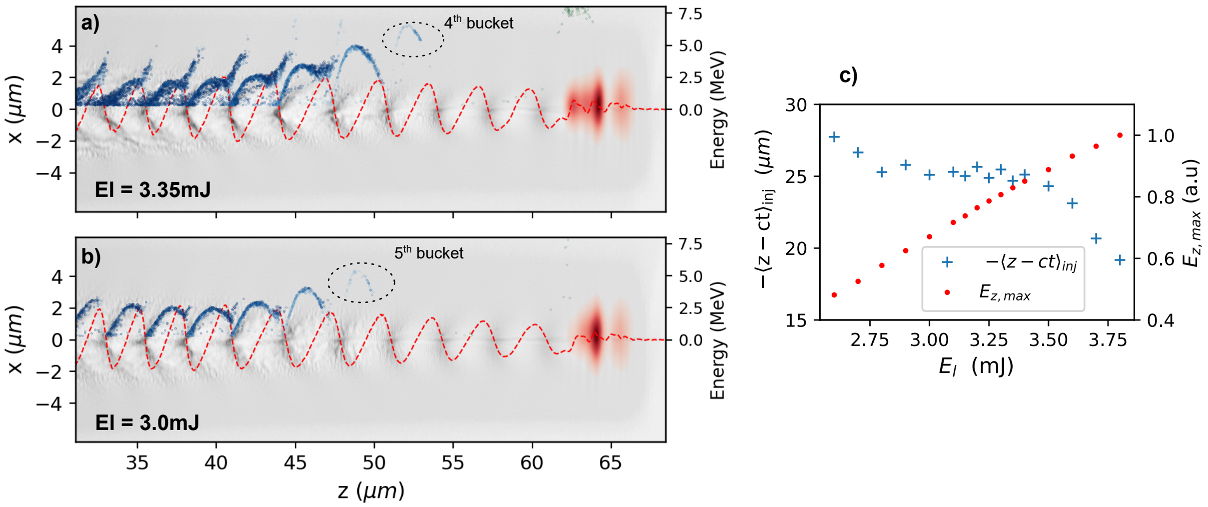

Figure 4.13 – Electron density (gray scale) in $z-x$ plane, and in phase space $z-\epsilon_z$, where ϵ_z is the energy neglecting the contribution of momentum along x and y, for L-shell and K-shell electrons (blue and green respectively), longitudinal electric field (E_z) (red dashed curve), and laser envelope (red shaded area) for the a) E_l =3.35 mJ case and b) E_l =3.0 mJ case. c) Mean position of injection behind the laser pulse and maximum longitudinal electric field (normalized to the value for $\mathrm{E_l} = 3.8$ mJ) according to the laser driver energy

the average longitudinal position of newly injected electrons. This behavior is interesting because it allows the wake to 'compensate' the loss of laser energy by injecting in plasma buckets further back, where the injection is facilitated. In a way, this mechanism can adapt to modest variations of energy to keep a steady injection, which can partly explain its improved stability.

It is clear from Fig. 4.13a,b and the typical parabolic shape of the electrons in phase space that electrons energy is limited by dephasing. As the phase velocity v_p decreases with the laser co-moving coordinate in the density transition region, so does the associated Lorentz factor $\gamma_p = (1 - v_p^2/c^2)^{-1/2}$, and so does the dephasing length $L_{deph} \propto \lambda_p \gamma_p^2$. The electrons reach faster the decelerating field of the plasma wave which leads to smaller energies further behind the laser. This can be clearly observed in both panels a) and b) of Fig. 4.13 where the maximum energy of each parabola in phase space is gradually smaller than the one before. The decrease in electron energy with the laser energy can therefore be explained by the backward shift of the injection position observed in Fig. 4.13c, leading to a globally smaller dephasing length.

Comparison with a supersonic profile

In Fig. 4.14 we compare the accelerated charge according to the input laser energy in the simulations, between both shocked and supersonic gas profiles with otherwise the exact same set of parameters (the laser is focused at the maximum of the gaussian plasma profile in the supersonic case). This shows that for the considered parameters, the shocked jet yields a significantly higher charge for all the energies (6.2 pC vs 0.8 pC at $E_l = 3.35\,mJ$) due to the eased injection in the density transition region. Moreover, the normalized curves highlight quite well the enhanced stability obtained with the OSS jet. Indeed, while for the supersonic case a slight decrease of the driver energy translates immediately into a loss of injected charge, the OSS jet benefits from a sort of 'stability plateau', where the injected charge is only weakly correlated to the pulse energy which can be attributed to the compensation mechanism mentioned earlier.

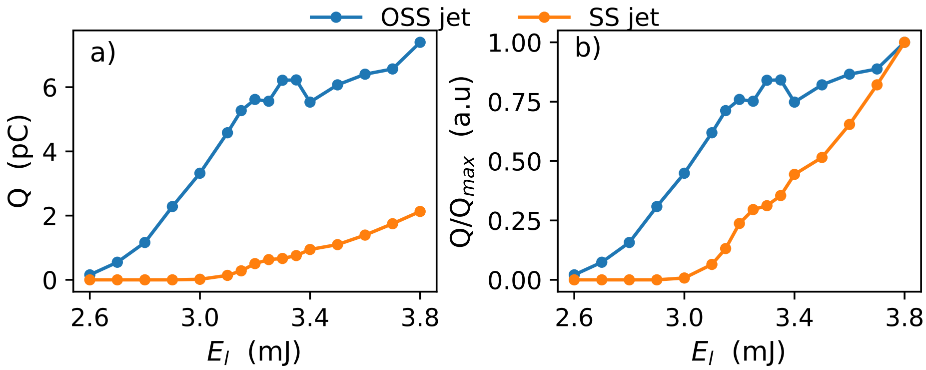

Figure 4.14 – a) Absolute accelerated charge in simulations and b) The same curves normalized to the charge obtained at $E_l = 3.8\,\mathrm{mJ}$ to show the superior stability of the OSS jet against laser energy fluctuations.

4.2.4 Conclusions, limitations and improvements

Using a new one sided shock nozzle, we have achieved stable, continuous hands-off operation of our LPA for 5 hours, accumulating more than 18×10^6 consecutive shots, with pC charge and few-MeV electrons. Additionally, a good day-to-day repeatability was demonstrated with similar acceleration regimes consistently obtained on different days. This level of performance makes possible to consider to use our accelerator to perform application experiments such as low-energy radiobiology experiments with significant irradiation dose. Concerning application to electron diffraction, the energy spread of 60% is still too large as such experiments typically require energy spreads around the percent level. Nevertheless, this requirement could be met by using a narrow energy filter, coupled with an electron beam line such as the one suggested in [144] to improve the emittance. Finally, PIC simulations confirmed the role of the density transition in the localization of electron injection but showed this injection occurs in many buckets quite far behind the laser, which is not optimal as it produces longer electron bunches, with wide energy distribution and diverging beams. This suggests that sharper gradients and higher laser intensities should permit to concentrate the charge in the first bucket, thereby producing few femtosecond bunches.

4.3 Increasing the electron energy with helium

Up until now, the experiment was restricted to using nitrogen as a gas to create the plasma, because a single molecule provides 10 electrons, which reduces the molecular density necessary while providing a better pumping efficiency. But the propagation of the laser in a nitrogen plasma is strongly impacted by ionization defocusing which reduces the effective intensity at focus and therefore negatively impacts the performances of our LPA. In a first instance, we tried to use a pulsed valve, which would open a limited time (10-100 ms) every second to limit the accumulation of helium in the chamber, but the pressures necessary to reach densities around

10^{20} cm^{-3} with our micrometric nozzles are higher than the maximal operating pressure of the valve (86 bar). The valve proved unreliable in these conditions and was deteriorating over time. Additionally, this method necessarily means reducing the effective repetition rate of the accelerator, which is not satisfactory. Finally, the differential pumping system (DPS) described in section 2.4 enabled the use of continuous flows of high pressure helium that reach densities sufficient to accelerate electrons. This section presents the results obtained with our laser-wakefield accelerator using a helium gas flow as a target, which yielded significantly higher electron energy than nitrogen.

4.3.1 Experimental set-up

The laser energy on target was comprised between 3.0 and 3.3 mJ depending on the experimental day. Unless specified otherwise, the differential pumping system was always implemented, which required to use the f'=100 mm off-axis parabola to focus the pulses. Typical focal spots are 5.5 × 5.5 µm FWHM, and the pulse duration is 4.0 fs, resulting in an intensity in vacuum between 1.5×10^{18} and 2×10^{18} W cm^{-2}.

We use a fused silica one-sided shock nozzle with a 60 µm throat and 180 µm exit hole diameter, and a 60 µm long flat section on one side at the end. Indeed, those targets enable us to obtain more easily and consistently relativistic electron beams. The plasma density profile was characterized experimentally by creating a plasma column using the laser beam and measuring the phase shift with the SID4-HR. Typical density profiles at 150 µm from the exit of the nozzle show a 20% downward density transition in the hydrodynamic shock of typical width 9 µm. For a backing pressure $P_{back} = 30$ bar of nitrogen, the peak plasma density is $n_e = 1.8 \times 10^{20}$ cm^{-3}, and for a backing pressure $P_{back} = 100$ bar of helium, the peak plasma density is $n_e = 1.4 \times 10^{20}$ cm^{-3}, and scales linearly with the backing pressure.

4.3.2 Acceleration experiment in helium

Comparison of nitrogen and helium

In order to measure the gain of performances associated with the use of helium, we start by comparing typical electron beams obtained in both cases. We also compare to the case of nitrogen with no differential pumping to see if there are differences. For the DPS case, the magnetic field strength of the spectrometer has been increased from 58 mT to 97 mT to increase to resolution at higher energies.

Figure 4.15 shows the electron beam data for nitrogen with and without differential pumping and for helium gas. It clearly indicates that the differential pumping system (DPS) significantly enhances the accelerator performances, even when solely considering nitrogen gas. Indeed, without the DPS, the measured electron beam in nitrogen has a larger divergence (~ 80 mrad) and lower energy with a thermal-like continuous spectrum. When switching to differential pumping we obtain, still in nitrogen, smaller beams (~ 50 mrad) with a peaked spectra at 3.3 MeV. The injected charge remains similar at around 1.7-1.8 ± 0.3 pC. We note that, we have obtained electron beam with peaked spectra at 2-3 MeV in nitrogen without differential pumping before (see previous section for instance). But during this experimental campaign, with the nozzle used here and the available laser performances, such spectra could not be achieved without the DPS on several experiment days. Switching to differential pumping immediately

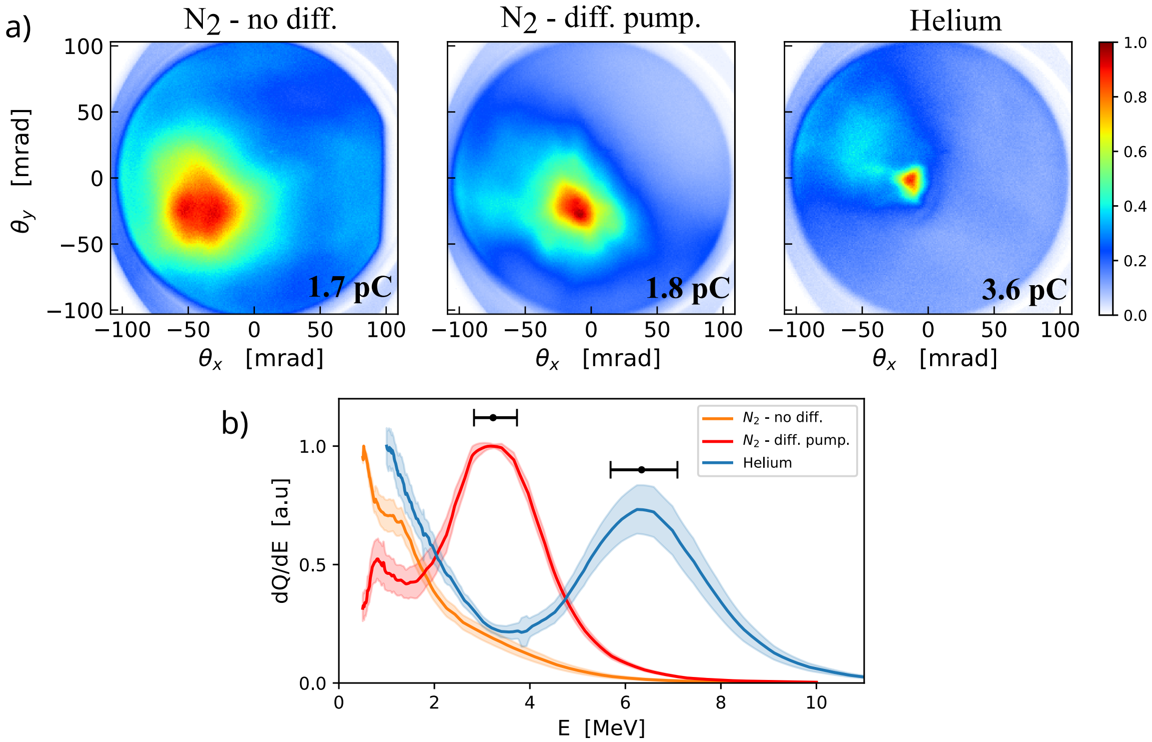

Figure 4.15 – a) Typical electron beams obtained for nitrogen and no differential pumping (left), nitrogen with differential pumping (center), and helium with differential pumping (right). The average charge per shot is showed at the bottom left. From left to right, the beam images corresponds to respectively 30, 50, and 10 shots. b) Spectra associated with the three previous cases. The shaded area correspond to the standard deviation. The black errorbars shows the resolution of the spectrometer at the considered energy. The spectra are averaged on 10 measurements each of which accumulating between 300 and 1000 shots. The peak plasma density is $n_e = 1.2 \times 10^{20}\,\mathrm{cm}^{-3}$ in nitrogen and $n_e = 1.1 \times 10^{20}\,\mathrm{cm}^{-3}$ in helium.

increased the energy of the electrons obtained in nitrogen. Additionally, by using differential pumping, we achieved electrons with peaked spectra at even higher energy of ∼5 MeV, which had not been reached until now during my thesis. This spectra was not used for the comparison because the experimental conditions were different (different nozzle, plasma density). Finally, using helium with a similar plasma density yields a higher beamcharge (3.6±1 pC) with a beam divergence that can be as low as 18 mrad FWHM, and a higher energy with a spectrum peaked at 6.4 MeV. Note that the showed beam profiles are selected to display a good beam for each case, but it can vary a lot from one measurement to the other.

These results highlight the double success of the differential pumping. Indeed, as anticipated, we achieve much better acceleration performances in helium, with notably the energy of the electrons increased by a factor of two, due to the mitigation of ionization defocusing associated with the numerous ionization levels of nitrogen. But, we also observe a significant increase of the performances in nitrogen when using the DPS because it keeps the residual pressure in the vacuum chamber at a lower level, thus limiting detrimental effects on the laser propagation.

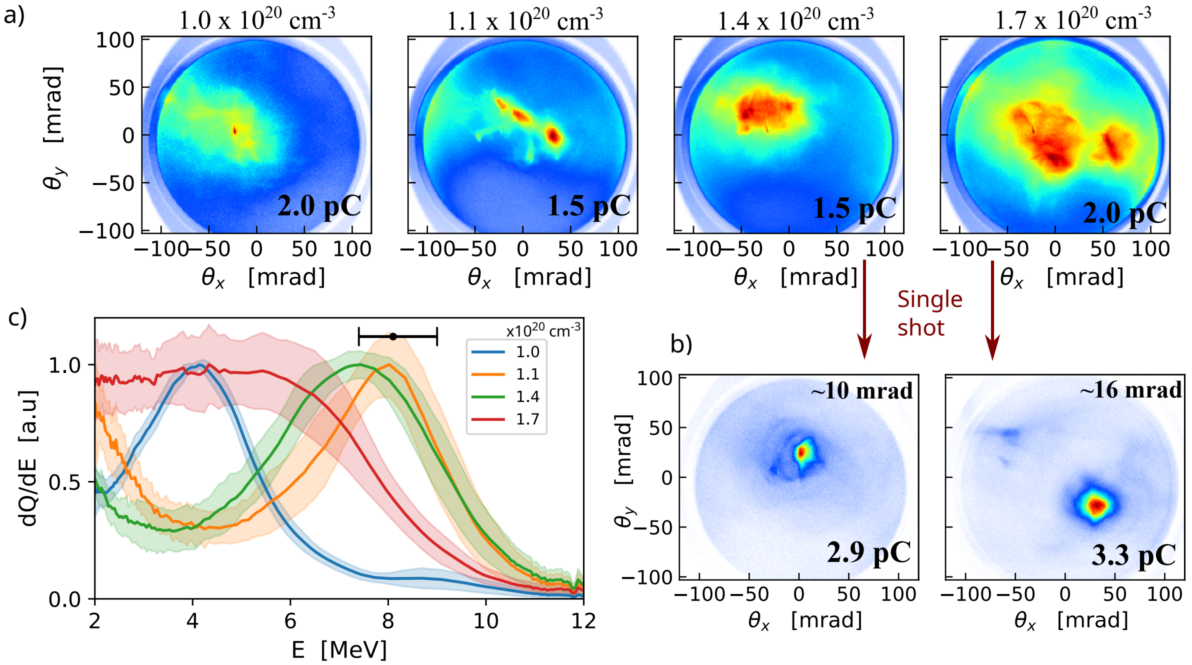

Figure 4.16 – a) Electron beam profiles accelerated for various electron densities of the helium plasma. From left to right, the beam images are accumulated on respectively, 8, 30, 50, 30 consecutive shots. The average charge per shot is showed in the bottom right corner. b) Single shot beam images associated with plasma densities $n_e = 1.4 \times 10^{20}\,\mathrm{cm}^{-3}$ (left) and $n_e = 1.7 \times 10^{20}\,\mathrm{cm}^{-3}$ (right). The beam charge and FWHM divergence are given. c) Electron spectra for different plasma densities, averaged on 10 measurements each accumulating between 300 and 800 consecutive shots. The shaded area corresponds to the standard deviation on the 10 measurements.

Results in helium at various plasma densities

The resolution of the spectrometer with a magnetic field of 97 mT proved rapidly insufficient for energies higher than 6 MeV. It was thus difficult to optimize the electron spectra beyond this energy. For this reason we increased again the magnetic field intensity up to 117 mT which provides a 20% resolution at 8 MeV. Using this enhanced spectrometer, we managed to optimize the energy by adjusting the jet position, chirp and plasma densities, and reached electron energy of 8 MeV with a peaked spectrum of width $\delta E/E \sim 40\%$ at $n_e = 1.1 \times 10^{20}\,\mathrm{cm}^{-3}$ (see Fig. 4.16). For all the plasma densities, the average charge per shot is between 1.5 and 2 pC, and the beam divergence integrated on many shots seems to grow with the density. But if wee look more closely at the beam distribution, we observe that these relatively large beams are in fact composed of several (many) 'impacts' corresponding to a smaller beam whose pointing varies on different shots. This is supported by the single shot images of the two highest density cases in the panel (b) where we remark that the actual single shot beam divergence can be as low as 10 mrad and 16 mrad. Obtaining clear single shot images of beams with was made possible by the higher signal yielded by the use of a YAG crystal instead of the previously used FOS (see Sec 2.3.1).

A statistical analysis can be performed on the two series of single shot beams obtained with $n_e = 1.4 \times 10^{20}\,\mathrm{cm}^{-3}$ and $n_e = 1.7 \times 10^{20}\,\mathrm{cm}^{-3}$. The beams are showed in Fig. 4.17, and are not consecutive, and approximately separated by 1 second each. An electron beam is present for 33/49 and 31/49 shots, by setting a presence criterion to a detected charge of 1 pC, while around 20/49 shots correspond to small collimated beams. The mean charge in the two cases is 1.5 ± 0.8 pC and 1.9 ± 1.5 pC, the uncertainty corresponds to the standard deviation. The typical pointing variations are around 40×25 mrad RMS (x,y). The laser is polarized in the y direction in which the pointing fluctuations are the smallest, which indicates they are probably not due to CEP variations (see Sec. 5.2).

Two main reasons can contribute to this strong shot-to-shot instability of the beam pointing: (i) for the DPS to be implemented, the pump and the optical table supporting the target have to be mechanically linked. It could induce mechanical noise and vibrations that would reduce the stability, (ii) the shock nozzle creates a gas profile with important transverse variations of density, and propagation in a transverse density gradient has been showed to induce laser and electron beam steering and instability [145, 146].

For the lowest plasma density, the electron spectra is peaked but at a lower energy (4 MeV). The optimal energy is achieved for moderate plasma densities $n_e = 1.1 - 1.4 \times 10^{20}\,\mathrm{cm}^{-3}$, and a further increase in density yields a continuous, flat spectra with a lower energy starting to decrease around 6 MeV. Indeed, at first an increase of density will lead to stronger self-focusing and stronger accelerating gradients thus higher energy. But if the density is further increased, more electrons will be injected and beam loading effects will reduce the accelerating gradient. Additionally, the laser will be more strongly redshifted, and the dephasing length will be reduced, leading to lower electron energies.

1.4×10^{20} cm^{-3}

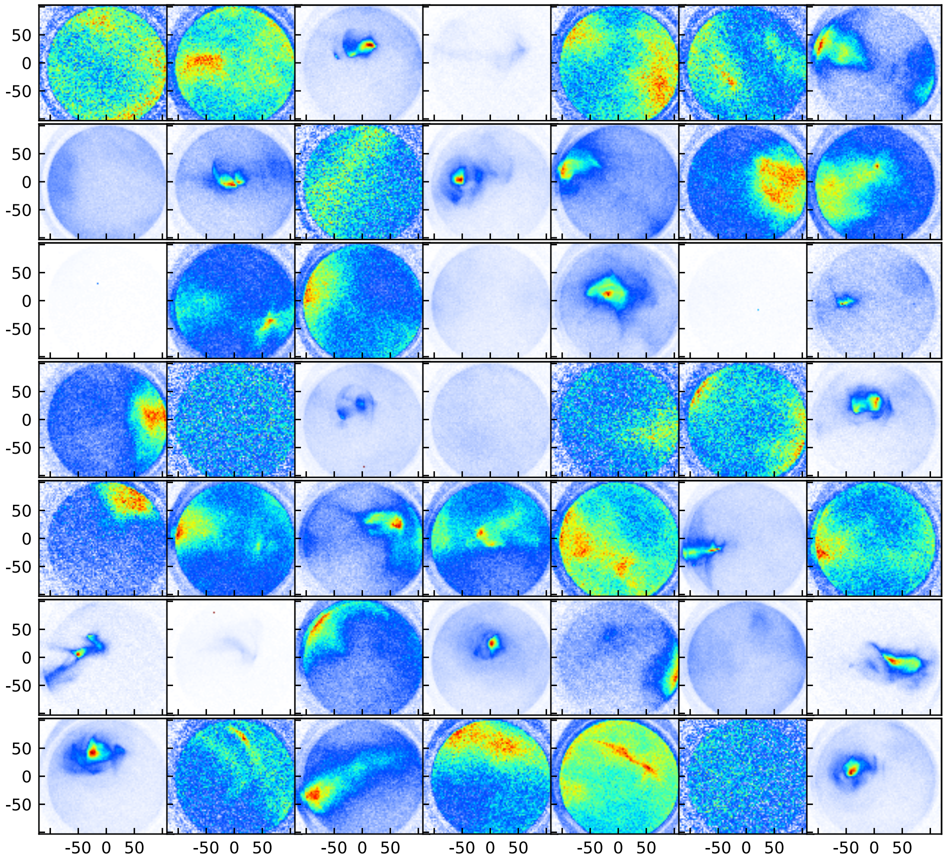

1.7×10^{20} cm^{-3}

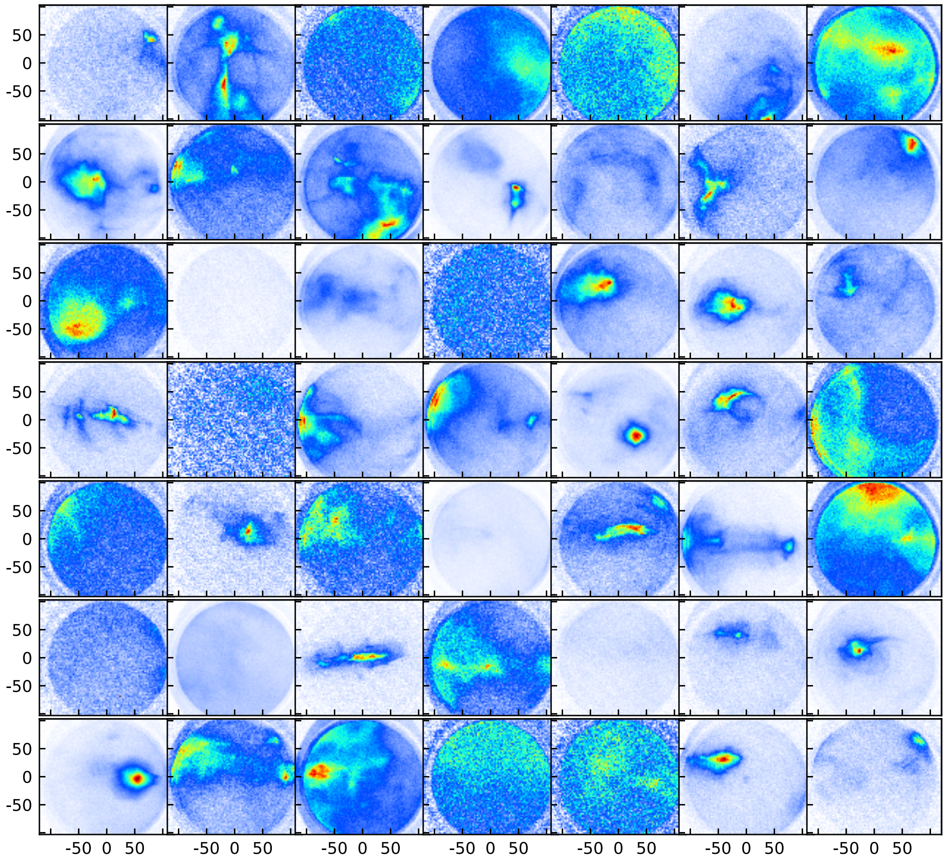

Figure 4.17 – Single shot beams for two different plasma densities using a OSS jet.

Supersonic gas profile

After demonstrating this significant energy gain in helium using one-sided shock nozzles, we wanted to compare these results to acceleration in a supersonic jet yielding a gaussian-like gas and plasma profile. But a design flaw on the batch of fused silica supersonic nozzles for this experiment was preventing us from using them with high pressure (the main drawback of these fused silica nozzle is their mechanical fragility). So we resorted to using a OSS nozzle that was turned 90° from its usual position, so that the laser does not enter the shock region and propagates in a supersonic-like gas profile (see Fig. 4.18). This is not entirely satisfactory as there remains an uncertainty on the actual plasma profile depending on the transverse position of the jet but it proved to be a good substitution method.

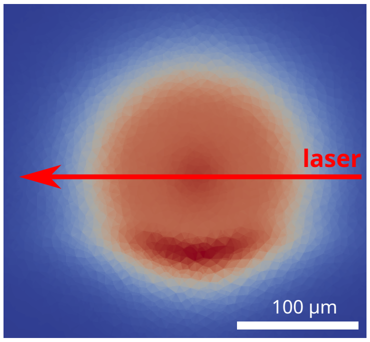

Figure 4.18 – Illustration of the supersonic-like geometry using a OSS jet turned at 90°. The image is a xy slice of the density taken at 150 μm from the nozzle exit from a FLUENT simulation.

Figure 4.19 shows a typical beam obtained in the supersonic-like profile in helium, and the associated energy spectrum, for a peak plasma density $n_e = 1.2 \times 10^{20}\,\mathrm{cm}^{-3}$. The accelerated beam is similar to what was obtained with the density gradient. The beams accumulated on 20 shots shows multiple 'impacts' of smaller beams, indicating there is still significant beam pointing fluctuations. The energy is peaked at 6.5 MeV with a wider spectrum of width $\delta E/E \sim 67\%$. The average charge per shot is 3.0 ± 0.6 pC which is higher than in the OSS case.

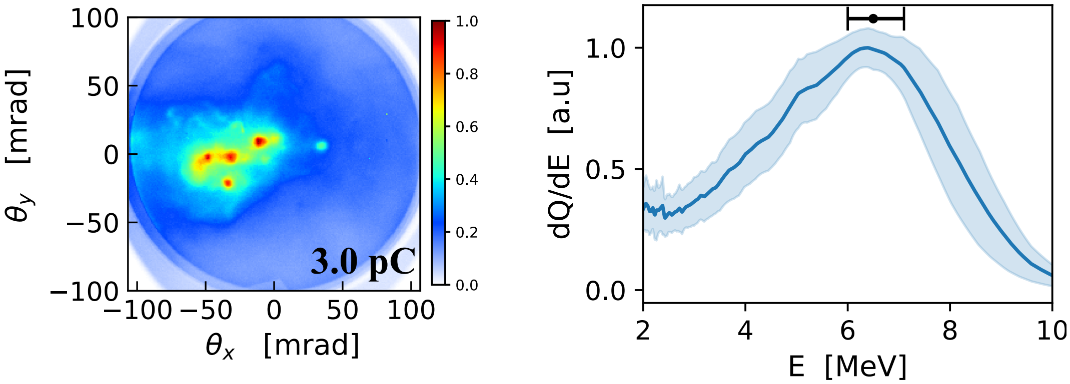

Figure 4.19 – Electron beam profile accumulated on 20 consecutive shots, and average charge per shot (left). Electron spectra obtained by averaging 20 measurement each accumulating 200 consecutive shots. The shaded area is the standard deviation (right). The peak plasma density is $n_e = 1.2 \times 10^{20}\,\mathrm{cm}^{-3}$.

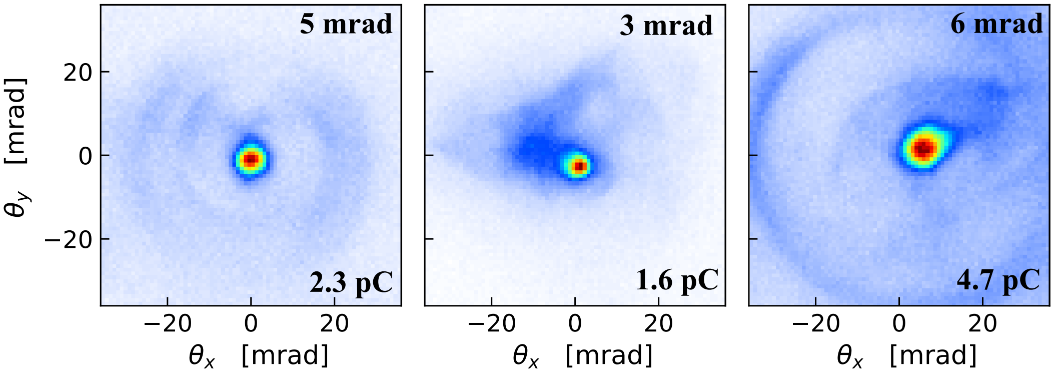

Figure 4.20 – Zoomed images on 3 specific low-divergence electron beams obtain with the supersonic-like profile.

We took again a series of 100 single-shot beam images in order to have information on each actual accelerated beam, and not only on integrated data. Figure 4.21 shows 48 images randomly selected from this scan. Two things can be quickly observed from this figure. Firstly, The accelerated beams can be extremely small, with a beam divergence as low as 3 mrad FWHM. The shot-to-shot stability is also much better, with a small-divergence beam being present in $\sim 80\%$ of shots. The beam pointing variations are 25×15 mrad RMS (x,y), which is significantly lower than in the previous scans, but still quite unstable. We note than once again, the beam is more unstable in the horizontal direction (x) which could be explained by the fact that the transverse (x) density gradient in the gas jet are more important than in the jet axis direction (y).

Figure 4.20 shows expanded images of three specific shots from this scan with particularly low divergence. In the left and right beams, we observe ring-shape structure with a divergence full-angle between 30 mrad and 70 mrad. Beams with rings in LWFA have been observed previously [147, 148], and also during the previous thesis on the experiment by Dominykas Gustas [35]. These rings are attributed to electrons from the second (and possibly further back) plasma bucket, that get trapped in a cavity pocket on the sides of the front bubble due to beamloading effects of the electron beam [147].

Even though this behavior of increased shot-to-shot stability was also obtained not only at this specific density, but also at other neighboring densities, concluding on whether it is indeed due to the difference in plasma profile, or simply to the day-to-day variability is not evident. Still, the consistently higher pointing fluctuations in the (x) direction (while the laser is polarized along y) suggest that the transverse density gradients in the target (which are stronger in a shocked profile) are a source of instability. A possible solution to benefit from the shock increased long-term reliability while not inducing a stronger shot-to-shot fluctuations could be to use an elongated target in the transverse direction. The shock front would thus be flat and the transverse gradients mitigated.

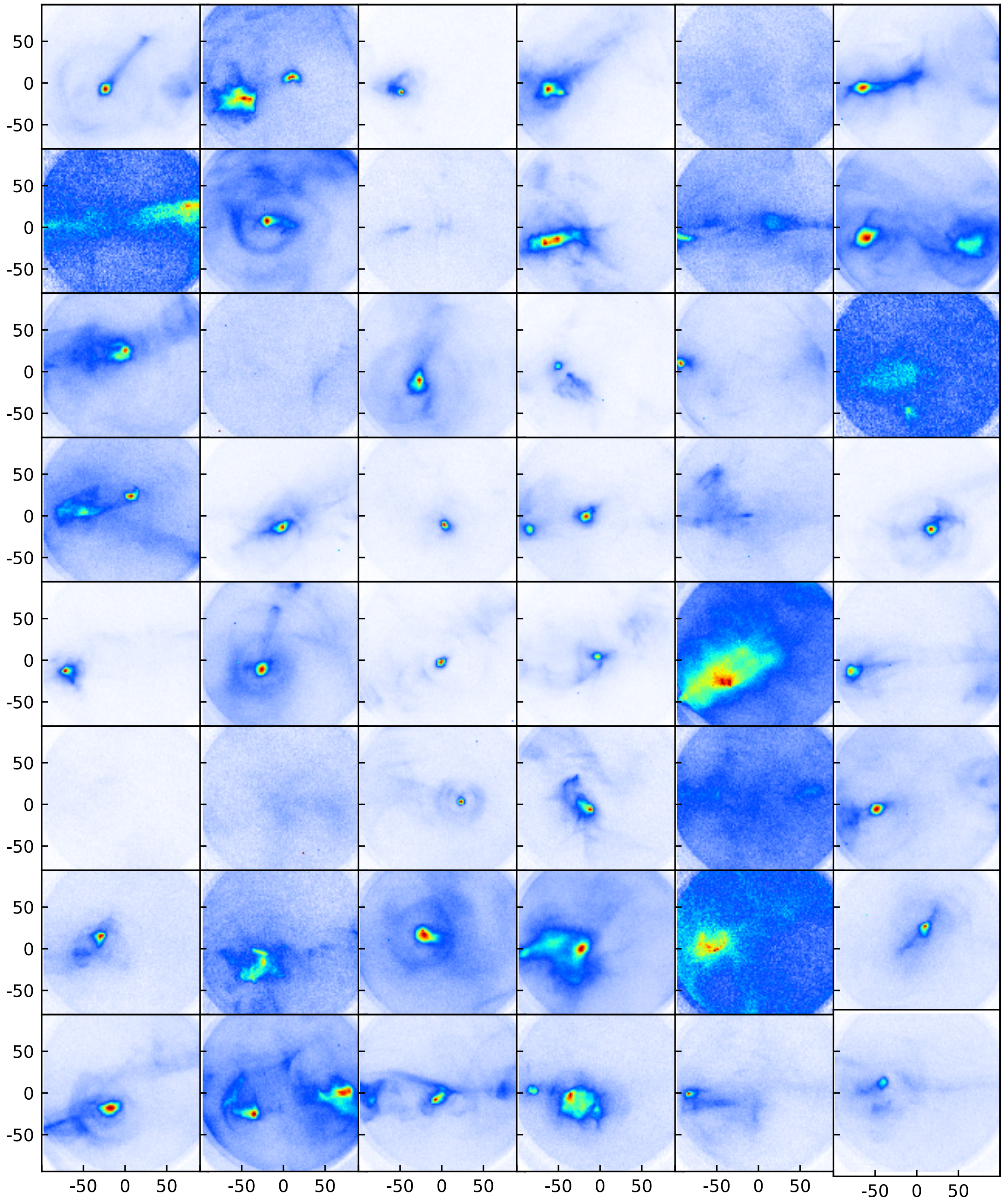

Figure 4.21 – Set of 48 single shot beams corresponding to the regime of Fig. 4.19 randomly selected among a 100 measurements series.

4.3.3 Ionization injection in a helium/high-Z gas mixture

When carrying out acceleration experiments in pure nitrogen, ionization injection is theoretically possible, but we have seen in previous sections that it remained minor compared to self-injection because the laser intensity was insufficient to efficiently ionize the K-shell levels of nitrogen. But now that the use of helium as the main gas in our experiment is possible, a mixture composed mainly of helium (99%) with a residual concentration (1%) of high-Z gas can be used. This could allow, with the help of self-focusing, for the laser to reach higher intensities by mitigating ionization defocusing effects, and therefore trigger ionization injection of electrons from higher levels of nitrogen, that require an intensity $\sim 10^{19}\,\mathrm{W.cm^{-2}}$ to reach the barrier-suppression regime (see Table 4.2). A mixture of helium and argon is also experimented. Argon has several ionization levels with a threshold intensity between $1-5\times10^{18}\,\mathrm{W\,cm^{-2}}$ (see Table 4.2) and therefore ensures ionization injection to occur. Both cases were measured the same day, with similar laser parameters as above, yielding a peak vacuum intensity $I = 1.6\times10^{18}\,\mathrm{W\,cm^{-2}}$. A supersonic-like gas profile is achieved by turning a OSS jet by 90°.

		1^+	2^+	3^+	4^+	5^+	6^+
N_2	E_i (eV)	14.5	29.6	47.4	77.5	97.9	552.1
	I_{bs} ($\mathrm{W\,cm^{-2}}$)	1.7×10^{14}	7.7×10^{14}	2.3×10^{15}	9.0×10^{15}	1.5×10^{16}	**1.0×10^{19}**
		7^+					
	E_i (eV)	667.0					
	I_{bs} ($\mathrm{W\,cm^{-2}}$)	**1.6×10^{19}**					
		1^+	2^+	3^+	4^+	5^+	6^+
Ar	E_i (eV)	15.8	27.6	40.7	59.8	75.0	91.0
	I_{bs} ($\mathrm{W\,cm^{-2}}$)	2.5×10^{14}	5.8×10^{14}	1.2×10^{15}	3.2×10^{15}	5.1×10^{15}	7.6×10^{15}
		7^+	8^+	9^+	10^+	11^+	12^+
	E_i (eV)	124.3	143.5	422.5	478.7	539.0	618.3
	I_{bs} ($\mathrm{W\,cm^{-2}}$)	1.9×10^{16}	2.7×10^{16}	**1.6×10^{18}**	**2.1×10^{18}**	**2.8×10^{18}**	**4.1×10^{18}**

Table 4.2 – Ionization energies and corresponding barrier-suppression intensities for nitrogen and argon. Intensities potentially relevant for ionization injection are shown in bold. The ionization energies are from [44].

Helium - nitrogen mixture

Figure 4.22 shows the results for a typical electron beam obtained in a mixture of 99% helium and 1% nitrogen. The electron beam shows a similar behavior than in previous experiments in pure helium, with a large electron beam distribution when accumulated on 20 shots, that looks like a smaller beam whose pointing varies significantly shot-to-shot. Single shot data (Fig. 4.22) tends confirms this, as the average divergence of beams accumulated on 20 shots is ~75 mrad FWHM, while single shot beams are much smaller with an average divergence of ~ 40 mrad FWHM with large pointing fluctuations of 26×20 mrad. The electron energy is a lower than in previous experiments, but this is consistent with a higher average injected charge of 4.5±0.7 pC, suggesting stronger beamloading effects.

This data does not shows any typical evidence of ionization injection such as an elongated beam in the polarization direction (y) or an enhanced stability (see Sec. 1.5.4), while yielding

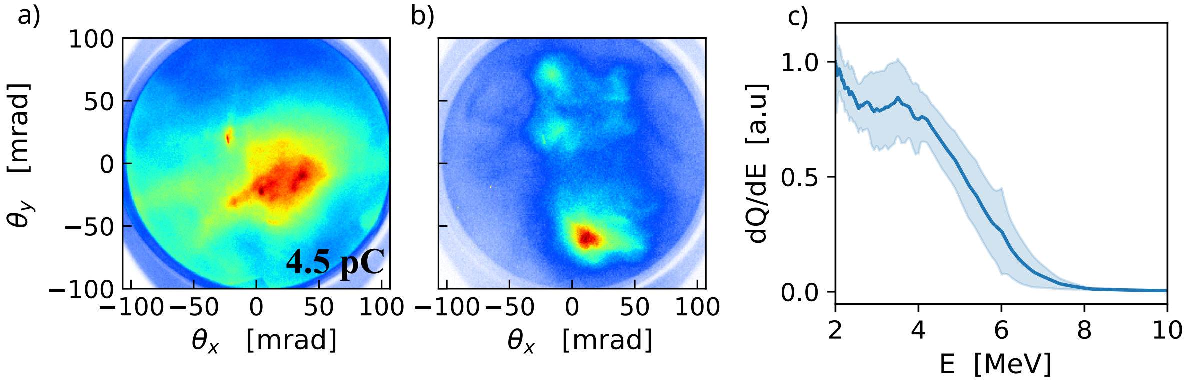

Figure 4.22 – *Experimental results in He/N$_2$ mixture, with* $n_e = 1.34 \times 10^{20}\,\mathrm{cm}^{-3}$. a) Electron beam profile accumulated on 20 consecutive shots. The average charge per shot is 4.5 ± 0.7 pC. b) Electron beam profile a single shot. c) Electron spectra obtained by averaging 20 measurements each accumulating 300 consecutive shots.

electron beams similar to what was observed in pure helium. This tends to indicate that we do not reach sufficient intensity ($I \sim 10^{19}\mathrm{W.cm}^{-2}$) through self-focusing to trigger massive ionization injection, and that self-injection remains the predominant mechanism. This was also the case for the other plasma densities scanned using this mixture.

Helium - argon mixture

Using argon instead of nitrogen in our mixture should ensure us to achieve ionization injection, as the barrier-suppression threshold for the ionization of Ar^{8+} into Ar^{9+} is $I_{bs} = 1.6 \times 10^{18}\,\mathrm{W\,cm}^{-2}$. Figure 4.23 shows the results for a typical electron beam obtained in a mixture of 99% helium and 1% argon. This time the regime is clearly different than previous results. The electron beam accumulated on 10 consecutive shots is relatively well collimated and elongated in the laser polarization direction, with a divergence of $32\times39 \pm 5\,\mathrm{mrad}$. As showed in Figure 4.23b, single-shot beams have shape similar to integrated measurements, with an average divergence of $23\times34 \pm 10\,\mathrm{mrad}$. Indeed, the beam pointing is much more stable than in previous cases, with fluctuations of $2 \times 5\,\mathrm{mrad}$ RMS. This clearly indicates that electrons are injected via ionization injection. Indeed, the elongated beam in the (y) direction is the result of the residual transverse momentum in the polarization direction associated with ionization, and the increased pointing stability comes from the fact that electrons are injected on-axis. A series of 54 single shot beams (taken at a slightly higher plasma density, because only few single shot beams were taken in the case of Fig. 4.23) is showed in Fig.4.24 and highlights the increased shot-to-shot stability, with a beam detected on every shot.

The energy spectrum is also quite different from previous cases. Here, it is composed of a relatively narrow ($\delta E/E \sim 30\%$) peak at 3.4 MeV, and a lower amplitude high energy tail between 4 and 6 MeV. This regime could be of interest for electron diffraction experiments, where electron beams with an energy from 3 to 5 MeV with a narrow distribution would be required [144, 149]. Indeed, the good shot-to-shot pointing stability and relatively low-divergence combined with a charge of a few pC per shots makes this injection method quite reliable for application experiments. We also note that by varying the plasma density and the initial chirp of the pulse,

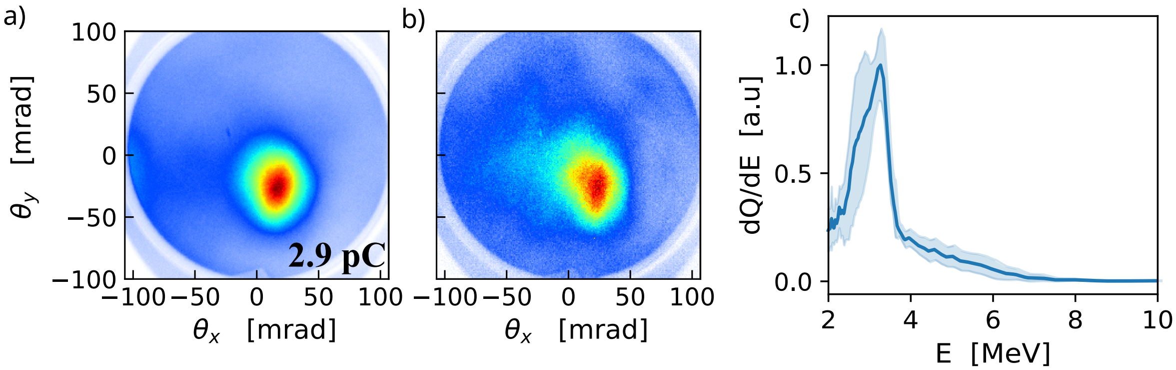

Figure 4.23 – *Experimental results in a He/Ar mixture, with* $n_e = 1.26 \times 10^{20}\,\mathrm{cm}^{-3}$. a) Electron beam profile accumulated on 10 consecutive shots. The average charge per shot is 2.9 ± 0.4 pC. b) Electron beam profile a single shot. c) Electron spectra obtained by averaging 20 measurements each accumulating 300 consecutive shots.

the energy of the peak can be tuned between 2.5 and 4 MeV. The issue of using argon as a ionization injection gas is that due to self-focusing, the zone for which the laser intensity will be higher than the threshold can be quite large, meaning electron are injected on an extended period. This might result in electron beams with longer durations and therefore in a poorer temporal resolution in such diffraction experiments.

4.3.4 Conclusion on experiments in helium

By implementing a differential pumping system, and using helium instead of nitrogen in our gas target, we managed to significantly increase, accelerated in our experiment. We are now able to generate collimated few-mrad beams at 8 MeV with a charge of several picocoulombs per shot. In this regime, the shot-to-shot stability of the beam remains the main issue to solve. Indeed, the pointing fluctuations are important ($\sim$ 20-30 mrad RMS) which results in large beams when integrated on tens of shots, and a beam is not detected on every shot. A possible explanation for this strong pointing instability could lie in the important transverse density gradients associated with our micrometric targets that would steer the laser and/or electron beam away from the center. This could be mitigated by using nozzles with a slit shape, wide in the transverse direction so that the density distribution does not evolve significantly on the plasma channel radius, and narrow in the longitudinal direction in order to match the typical acceleration length of a few tens of microns.

Using a mixture of helium and nitrogen, we observed no evidence of ionization injection, indicating that the intensity remains below the threshold of ionization of k-shell electrons of N_2. But by switching to a mixture of helium and argon, ionization injection was confidently achieved, yielding particularly stable beams of $\sim$ 30 mrad divergence with energies around 3 MeV that could be of interest for electron diffraction experiments.

Finally, even though ionization defocusing is strongly reduced in helium compared to nitrogen, helium still has two ionization levels, the highest corresponding to a laser intensity of $I_{sb} = 8.8 \times 10^{15}\,\mathrm{W\,cm^{-2}}$. Therefore it still contributes in reducing the laser intensity via defocusing, especially considering the high densities used in our experiment. Using hydrogen,

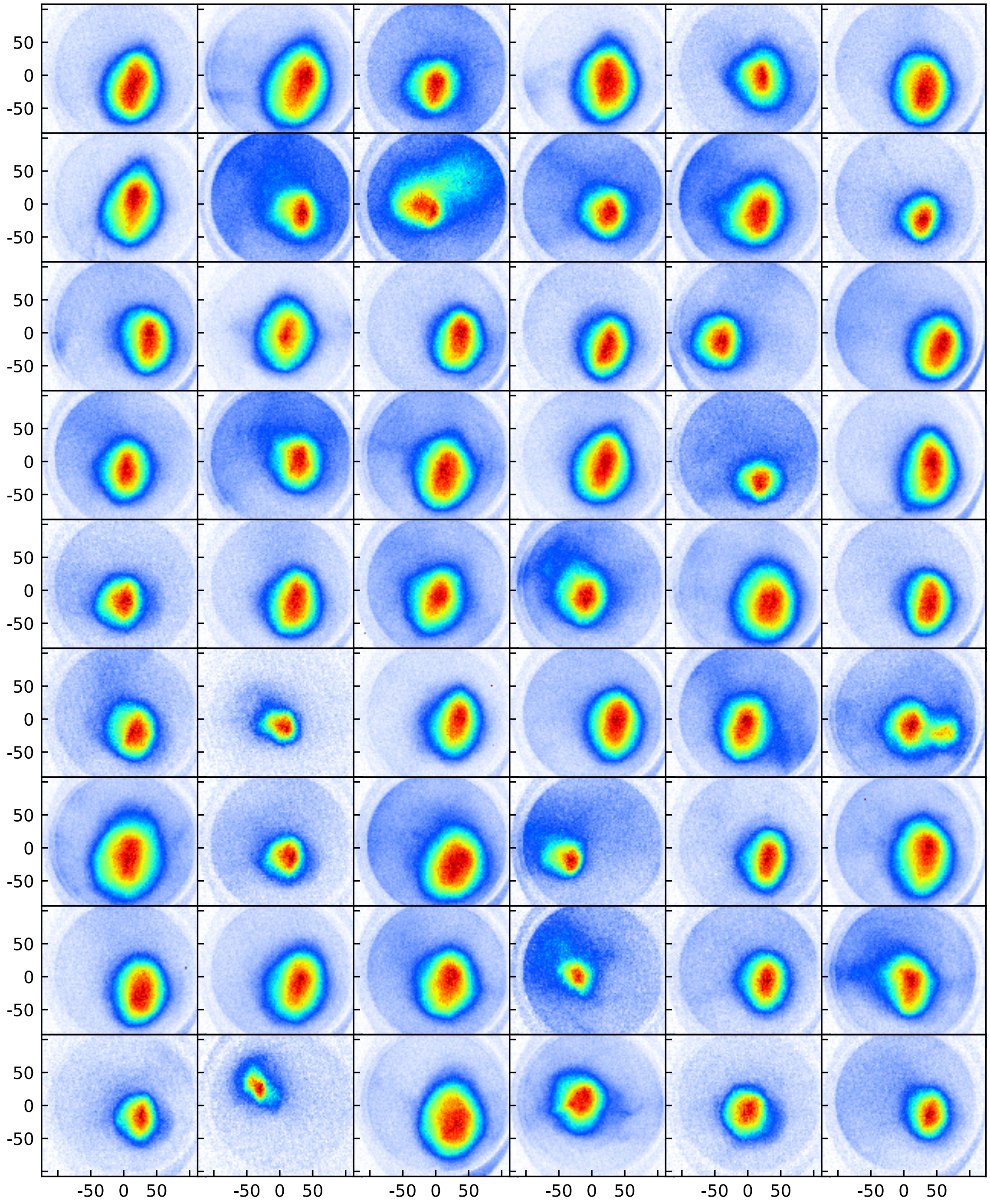

Figure 4.24 – Set of 54 single shot beams obtained using a helium-argon mixture with $n_e = 1.38 \times 10^{20}$ cm^{-3}.

which has a single ionization level at $I_{sb} = 1.4 \times 10^{14}\,\mathrm{W\,cm^{-2}}$, instead would make ionization defocusing almost completely nonexistent. This was recently demonstrated in an experiment using a kilohertz laser with similar parameters than ours, where electron beams were accelerated to 15 MeV using a hydrogen plasma at a reduced averaged repetition rate of 0.5 Hz [150]. Using high-pressure continuous flows of hydrogen is not so straightforward as it is a highly explosive gas in a wide range of concentration with air (4% to 75%). A specific gas line ensuring no hydrogen can be rejected inside the room, as well as additional safety equipment (H_2 detectors, nitrogen purge, shutdown valves) and procedures have been implemented, so that experiments using continuous flows of hydrogen should be carried out in a very near future.

4.4 Application experiment in radiobiology

Thanks to the improvements in long term stability and reliability of the accelerator provided by the use of the one-sided shock nozzles, we were able to carry out our first application experiment in radiobiology on our accelerator. This experiment was carried out in collaboration with Alessandro Flacco's team at LOA, the Gustave Roussy institute (Villejuif, France) and the Laboratory of Subatomic Physics and Cosmology (LPSC) of Grenoble (France), in the framework of Marco Cavallone's thesis [151]. The details of the radiobiology results are discussed in his thesis as well as in a paper that followed this experiment [152]. My contribution to this experiment was mainly to operate the accelerator in a regime that provided high dose rate, stable beams, and analyze data relative to the electron beams. The biological samples were prepared and analyzed by Emilie Bayart from Gustave Roussy institute/LOA. Marco Cavallonne performed the dosimetric and biological analysis. The goal of this section, apart from summarizing briefly these results, is rather to give an overview of the operation of a kilohertz accelerator and management of the source in an application experiment.

4.4.1 Context

Radiotherapy is, along with surgery and chemotherapy, one of the main form of treatment for cancer. It uses ionization radiation to kill malignant cells. These radiations damage the cancer cells DNA which leads to their death. But ionizing radiations affect healthy tissues as well and can lead to nefarious side effects on the patient. So a fundamental aspect of radiation therapy is the selectivity of the treatment, meaning the capacity of damaging the cancerous cells while leaving unharmed the surrounding healthy tissues. This is notably achieved by shaping and focusing several radiation beams aimed from different angles that intersect at the position of the tumor. That way, a significantly larger radiation dose is deposited in the crossing region on the tumor than in the surrounding cells. Other parameters can come to play in the optimization of the selectivity of the treatment, such as the type of radiation or amount of dose delivered. The effect of the temporal distribution of the delivery on the selectivity have recently gained in interest and remain to be investigated in details. Indeed, the positive effect of the dose fractionation of a treatment in several sessions on different days with rest period in between to let the DNA self-repair mechanisms take effect is well known and standard procedure [153] in clinical treatments. But other temporal effects such as dose rate or shorter timescale fractionation of the delivery still require extensive study.

In 2014, Favaudon *et al.* [154] irradiated mice using a linear accelerator, delivering the prescribed dose in a short time (<500 ms) with a high dose rate (>40 Gy/s), instead of the conventional clinical procedure of delivering it continuously over a few minutes at lower dose rate. They observed that this procedure largely increases the selectivity of the treatment. Indeed, at equivalent doses, the effect on the death of cancerous cells would be similar for the two procedures, while the side effects on healthy tissues, measured here by the level of fibrosis was strongly diminished. This new protocol is called FLASH radiotherapy, and has been experimented on the first human patient in 2019 [155].

The explanation of the FLASH effect remains an active research subject, but potential hypothesis have been proposed. Oxygen plays an important role in radiotoxicity, via the production of reactive oxygen species such as hydroxyl radicals by radiolysis of water that can damage DNA [156]. It has been suggested that the FLASH effect originates from the fact that delivering the dose in a short period of time quickly depletes the oxygen and saturates the quantity of oxygen radicals produced, while for conventional irradiation on longer periods, oxygen has the time to be renewed leading in the production of a higher number of harmful radicals [157]. The differentiated effect on cancerous cells, could come from the fact that tumors are less oxygenated, and therefore their radiotoxicity is less driven by indirect DNA damages of oxygen radicals. Another hypothesis considers the impact on the immune response [158, 159]. In FLASH protocol, only a small fraction of circulating T-Lymphocytes (immune system cells that participate to limit the proliferation of cancerous cells) are damaged during the short period of irradiation, while in the conventional protocol, a more important part of these cells are damaged during the extended irradiation time.

This clearly shows the importance of studying the effects of temporal dose distribution in radiation therapy. Laser-plasma accelerator are good candidates to provide short pulses, high dose rate radiation bursts to probe the mechanisms behind the FLASH effects, and eventually investigate the effects of even shorter, fs-ps radiation pulses. A high-repetition rate LPA will provide high average dose rate (∼Gy/s) compared to J-class systems such as Salle Jaune (∼Gy/min) and permit to reduce dose fluctuations on the second scale by averaging on a large number of consecutive shots. This experiment is a preliminary study on the feasibility of radiobiology experiments using our kHz laser-wakefield accelerator, and an assessment of the dosimetric performances of the system.

4.4.2 Experimental set-up and source characterization

General set-up

The general set-up of the experiment is showed in Figure 4.25. The 3.0 mJ, 4.0 fs laser pulses are focused by a f′=50 mm off-axis parabola onto a pure nitrogen gas jet, to a ∼3 µm focal spot, reaching a peak intensity in vacuum $I \sim 6 \times 10^{18}\,\mathrm{W\,cm^{-2}}$. A 50 µm throat, 150 µm exit hole diameter one-sided shock nozzle is used to facilitate electron trapping in the density transition, and this experiment was carried our prior to the installation of the differential pumping system. Electrons are accelerated along the laser axis, and their spectral and spatial distribution are measured with the magnetic spectrometer and phosphor screen. Then, the beam characterization setup can be moved out of the way of the electrons, so that they can go through a 100 µm thick Mylar window and irradiate cancer cells samples placed in a plastic holder inside

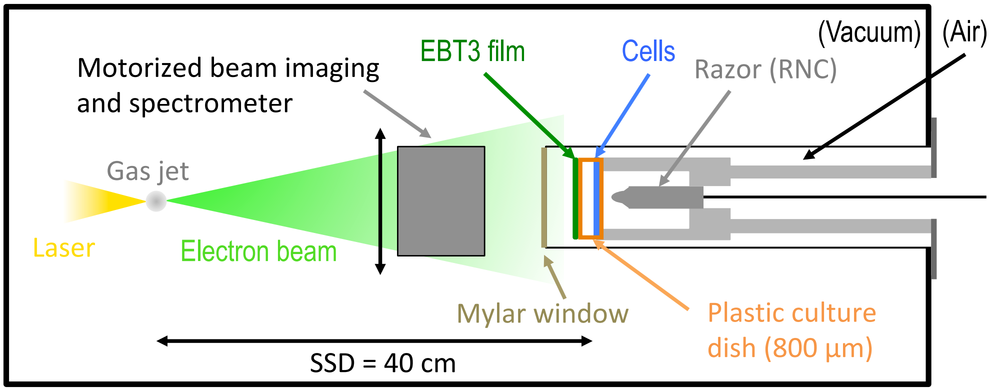

Figure 4.25 – Experimental set-up of the radiobiology experiment. From [151, 152].

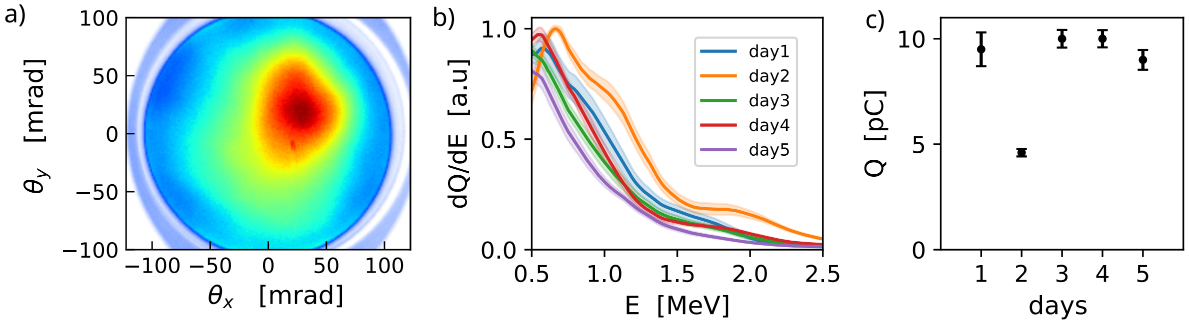

Figure 4.26 – a) Typical electron beam distribution used for irradiation experiments accumulated on 100 consecutive shots. b) Electron energy spectra on 5 different days of irradiation. c) Electron beam charge per shot measured on each day. The beam charge is obtained by taking the average of 15 measurements, each integrating 100 consecutive shots. The errorbars show the standard deviation on the 10 measurements.

an inverted tube kept in air. A radiochromic EBT3 film is placed on the front side of the plastic holder for dosimetry, and an ionization chamber Razor Nano Chamber (RNC) was placed behind the sample for on-line dosimetry monitoring. A fast, programmable shutter with an opening and closing time of $\sim 10\,\text{ms}$ is used to control the irradiation of the samples.

Beam parameters

For simplicity, no beam optics were used to shape the electron beam. In order to study the effect of the dose delivered on the cells, it is important that its spatial distribution remain homogeneous on the 1cm diameter sample. Therefore, we want to obtain a large, diverging beam so that the sample can be entirely covered by its center. Additionally, to maximize the dose deposited, we want to achieve the highest charge possible. We have seen in section 4.1 that using a high plasma density leads to high charge, diverging beams with thermal-like spectra. We use a high backing pressure of nitrogen $P_{back} = 70\,\text{bar}$ that yields a peak density $n_e = 3.2 \times 10^{20}\,\text{cm}^{-3}$, and a plateau at $n_e = 2.6 \times 10^{20}\,\text{cm}^{-3}$ after the shock. On day 2, a slightly lower peak density $n_e = 3.0 \times 10^{20}\,\text{cm}^{-3}$ was used. This resulted in beams with typical divergence between

80 and 140 mrad, a charge of 10 pC/shot (except on day 2 with 5 pC/shot) and a thermal-like spectra with most of the electrons below 1.5 MeV. On day 2, because of the lower plasma density, the charge was lower and the energies higher. When integrated on 100 consecutive shots, the charge standard deviation on each measurement is about 5%, which ensures a good stability of the dose. Apart from day 2 which was in slightly different operating conditions, the electron energy spectra are extremely close from one day to another, which is particularly important considering the low energy of the electrons. Indeed, electrons <1 MeV will be significantly stopped by the media crossed before reaching the cells (Mylar window, radiochromic film, plastic holder) suggesting that de deposited dose will depends on the energy spectrum.

Additionally, we observed some thermal effects associated with the opening and closing of the shutter. Indeed, due to space constraints, it was placed relatively far from the target, with 4 mirrors and a few meters of propagation left after. We observed that the beam parameters could vary depending on the opening time of the shutter. For instance, if the beam was optimized with the shutter open for an extended (few minutes) period, the electron beam obtained after closing the shutter for some time, would be sub-optimal until ∼30s of opening, after which the beam would re-converge towards its initial value. This clearly indicates that when the beam is blocked before the last mirror, the change in temperature due to the absence of deposited energy slightly modifies the pointing which impacts the performance. After some time of opening, the temperature converge to a stable regime and the electron parameters stop evolving.

Dosimetry

The dose on target was estimated using EBT3 radiochromic films, which have been calibrated at the Elekta Synergy linear accelerator of the University Hospital of Lausanne (CHUV, Switzerland). But solely using a film placed in front of the plastic cell holder would not be entirely accurate, as electrons would still cross 800 µm of plastic after. So before each irradiation series, the front EBT3 film was cross calibrated by placing another film inside the holder, where the cells should normally be. That way we can determine the factor linking the dose measured by the film in the front, to the actual dose received by the cancer cells. This factor was around 0.7 for all the irradiation series.

Figure 4.27 shows the mean dose rate at the front, and the corresponding dose on the cells obtained for 10 different series obtained on the 4 days where beams with 10 pC were achieved. We see that we are able to achieve dose rates between 0.7 and 0.9 Gy/s on sample, with an 8% standard deviation on different series. This mean dose rate is significantly higher than the typical doses rates of J-class lasers operating at 10 Hz reported in the literature of ∼Gy/min [160–165].

Moreover, the thermal effects mentioned earlier impacted the dose delivery, especially in fractionated series (see results) where the dose tended to vary depending on the opening time of the shutter, and rest time between the shots. This does not impact our capacity to know the dose on each irradiation, as it is measured for each sample, but can prove problematic when a specific dose determined beforehand has to be deposited.

For the spatial distribution of the dose, centering the electron beam on the sample was a key problem in the experiment. Indeed, the direction of the beam pointing is extremely sensitive to

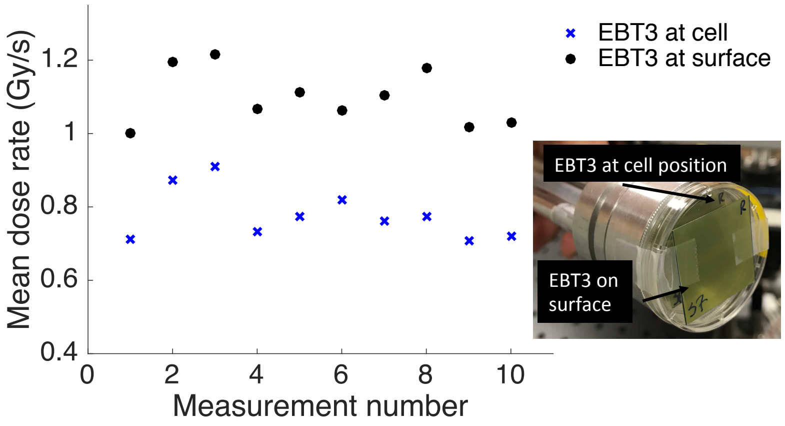

Figure 4.27 – Dose rate measured at the surface of the plastic holder and at the cell position with the double film arrangement shown in the insert. From [152].

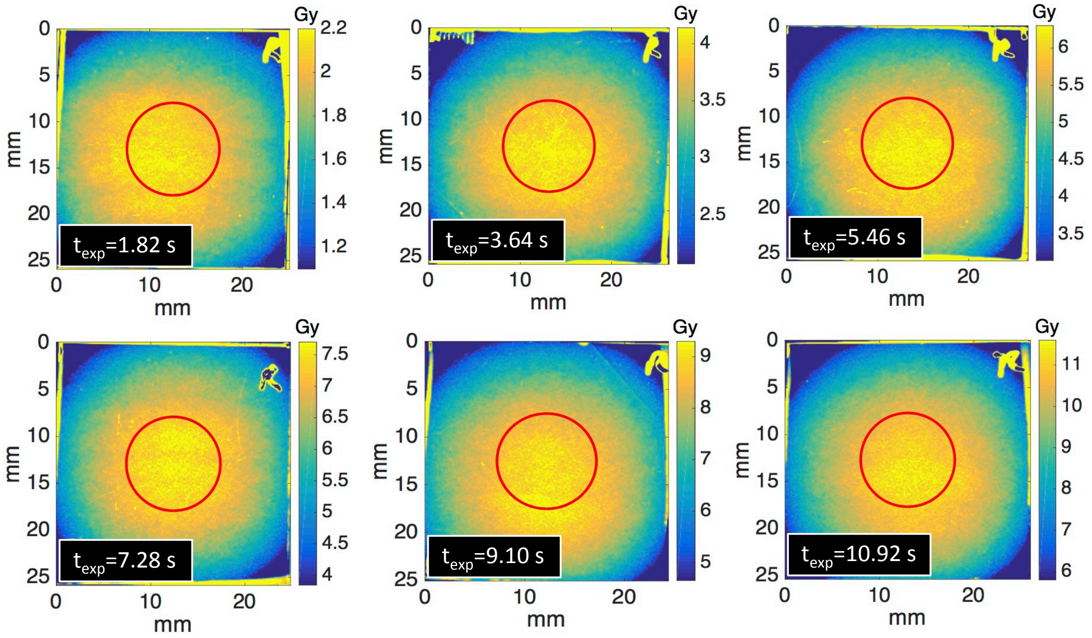

Figure 4.28 – Dose distribution measured with the radiochromic film placed in front the the cell holder, for six consecutive irradiations with varying irradiation time. The red circle corresponds to the 1 cm ROI where the cell where studied. The minimum of the colormap is at half the maximum dose. From [152].

many experimental parameters such as density, chirp, or slight variation of the jet position (a few microns transverse shift of the jet can lead to several tens mrad shift of the beam pointing). A possible reason for the unpredictability of the beam pointing is, as for its instability, transverse density gradients that would steer the beam in a specific direction. In order to place the electron beam at the position of the sample, we translate the position of the near field of the laser with two motorized mirrors, which changes the position on the parabola without modifying the incidence angle. Figure 4.28 shows the dose distribution measured with EBT3 film place in front of the cell holder, for six consecutive irradiations with incremental shutter opening time. When centered on the sample, a relatively homogeneous dose could be achieved on the 1 cm region of interest (red circle), with peak-to-valley variation of the dose around 7% in that zone.

Biological samples

We performed an *in vitro* study of the radiological response of human colorectal cancer cells HCT116. Two different lines of these cells were used: the wild type (HCT116 WT) and a mutated version with increased radioresistance (HCT116 p53$^{-/-}$). We also irradiated the cells deposited in two different spatial configurations. A monolayer configuration, where cells are grown in 2D on the surface of the dishes, and a spheroid configuration, were cells are grown in a 3D geometry with typical thickness of 300 µm. This spheroid configuration is supposed to model more closely the response of an actual tumor, and is more resistant to irradiation than monolayer.

4.4.3 Experimental results

During this experiment, we performed two types of study on the irradiation of biological samples. Firstly, we carried out survival assay of the cells, which consists in measuring the evolution of the surviving fraction of irradiated cells depending on the delivered dose. This is of limited biological interest, because those curves are well known and tabulated. But this is ideal to perform a proof-of-principle experiment, as we can verify that we were able to deliver a controlled dose to the biological samples and that their behavior matches the expectations. The second type of study we performed was fractionation assay, where the dose is delivered in 5 fractions separated by a variable delay (between 30s and 5s). Indeed, it has been observed in previous experiments using laser-accelerated protons that the surviving fraction of HCT116 cells at constant dose depended on the time between the fragments of the dose, but it still required further investigation [166].

Survival assay

The curves of the survival fraction on the HCT116 cells as a function of the dose are showed in figure 4.29. In all cases, the dose is delivered during a single continuous fraction by varying the irradiation time. The solid curves fit the data to a 'Linear-Quadratic model' where the cell surviving fraction is given by a function of the form [167, 168]:

$$S = \exp(-\alpha D - \beta D^2) \tag{4.3}$$

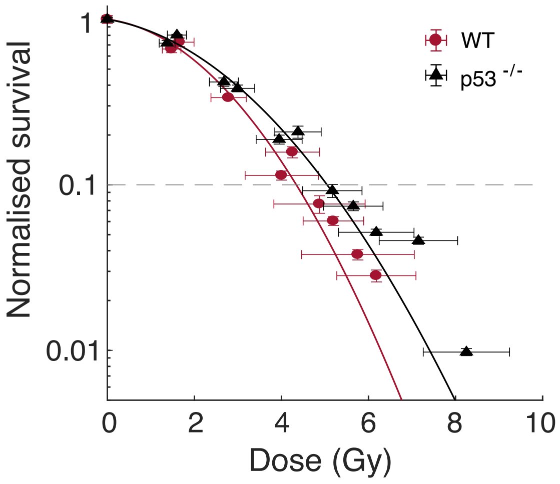

Figure 4.29 – Surviving fraction of monolayer HCT116 WT and p53$^{-/-}$ cells as a function of the deposited dose. Continuous curves are fit the data to the linear-quadratic model. From [152].

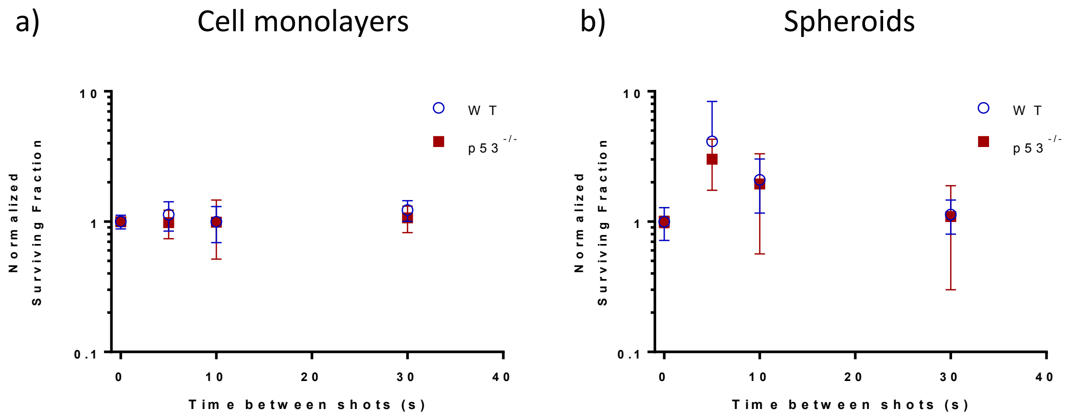

Figure 4.30 – Cell survival normalized to the value of the continuous irradiation for a) monolayer cells and b) spheroid cells. Each point is averaged on three sets of measurements taken on different days. The errorbars represent the standard deviation on the 3 sets of data. From [151]

Where α and β are radiosensitivity parameters, and D the delivered dose. The experimental points are well fitted by a linear-quadratic model, which confirms that we are able to deliver stable and controlled doses to the samples. Our curves reproduce the typical shoulder shape expected for irradiation by low-energy transfer sources such as electrons or photons [169]. A point of comparison to other irradiation experiment is the D_{10} value, which is the dose corresponding to a 10% surviving fraction. In our experiment, $D_{10} = 4.3 \pm 0.5\,\text{Gy}$ for the wild type cells and $D_{10} = 5.1 \pm 0.5\,\text{Gy}$ for the p53$^{-/-}$ cells. This matches the results from Pommarel *et al.* [170] with 662 keV photons, where they measured $D_{10} = 3.8 \pm 0.4\,\text{Gy}$ for the wild type cells and $D_{10} = 5.0 \pm 0.4\,\text{Gy}$ for the p53$^{-/-}$ cells. This result demonstrates our capacity to deliver a controlled and stable dose to biological samples with our laser-wakefield accelerator.

Fractionation of the dose

We now investigate the role of the fractionation of the dose in the radiological response of the cells. For both cell lines, in both monolayer and spheroid cases, a total dose of $\sim$ 6.5 Gy was delivered in 5 fractions with a delay between bursts that was varied between 30s, 10s, 5s, and continuous irradiation. Figure 4.30 shows the results of the fractionation assay. For monolayers, no temporal effect is observed, while for a spheroid irradiation, a delay of 5s and 10s between bursts lead to significantly higher surviving fraction. But, the absence of effect in the monolayer case could be associated to a too strong irradiation. Ideed, with a 6.5 Gy dose, the surviving fraction of cells is only 0.05, which could be too low for the effect to appears. The spheroids are more radio-resistant, and 6.5 Gy corresponds to a surviving fraction of 0.1. This excessive delivered dose is due to the fact that the EBT3 film was calibrated afterwards, meaning we underestimated the actual dose during the experiment. While the spheroid points at 5s and 10s tends to indicate the presence of a temporal dependence of dose fractionation, the errorbars remains of the same order as the effect, so definitive conclusions cannot be drawn. Still this is promising and calls for further study on this matter.

4.4.4 Conclusions on the radiobiology experiment

Biological conclusions

In this experiment we were able to reproduce typical surviving curves for HCT116 cells thus validating our dose deposition and estimation methods. Then, a temporal effect of fractionation of the dose was observed on spheroid cells. Although associated with large measurement errors, these results are encouraging, and further experiments should be carried out.

Laser-plasma source for radiobiology

Thanks to the newly enhanced reliability of our kHz laser-wakefield accelerator, we have been able to carry out our first application experiment. Although some points require improvement, our capacity to deliver a controlled and stable dose to biological samples has been demonstrated. For further application experiments, the following points should be addressed:

- The evolution of the performances depending on the opening time of the shutter. This should be solved by placing the shutter just before the off-axis parabola, to limit thermal effects on previous mirrors. Ideally, it would even be placed after the parabola, but the space constraints imposed by the short focal length make this impossible.
- The control and predictability of the beam pointing. Application experiments require to be able to control and predict precisely the position of the electron beam to send it on samples to irradiate. To enhance this, we propose to use a slit nozzle geometry, as discussed earlier, to limit the steering effect on the laser and electron beam associated with transverse density gradients.
- Better control of the dose via higher electron energy. To maximize the charge, and thus the dose, we operated the accelerator with high plasma densities, which results in a low energy, thermal-like spectrum. The electron with energies <1-2 MeV will interact with and be absorbed by the materials crossed before reaching the biological sample. This leads to a important sensitivity of dose to fluctuations of the energy spectrum, and require frequent calibrations between the doses measured on the front of the holder, and at

the position of the cells. To solve this issue, a better regime of operation would be to accelerate electrons to energies around 2-4 MeV, while keeping a high charge around 10 pC, which requires further optimization of the accelerator.

Conclusions

In this chapter, we have determined an optimal regime of our laser-wakefield accelerator that uses short (sub-4 fs) laser pulses and moderate ($\sim 1-2\times10^{20}\,\mathrm{cm}^{-3}$) plasma densities, provides collimated electron beams with peaked energy spectra at a few MeVs. We also showed that using longer ($\sim$ 10 fs) pulses with few-mJ energy requires to increase the plasma density in order to compress the pulse spatially and temporally to reach high intensities. But this comes at a cost of lower energy, diverging beams with continuous spectra.

Then, by using a newly designed one-sided shock jet allowing us to achieve injection in the density transition, we largely enhanced the long term stability and reliability of the accelerator, with notably a record of 18 millions consecutive shots in an autonomous, 5h-long run. This is a major step towards the use of high-repetition rate LPA for applications. Following this advance, we performed our first application experiment in radiobiology, that demonstrated our capacity to deliver stable and repeatable dose to biological samples.

Finally, by implementing a differential pumping system that allowed us to use helium gas in our experiment, we managed to double the energy of the accelerated electrons, and single-shot beams that are extremely well collimated, with a divergence reaching a few milliradians, for a charge of a few picocoulombs. The use of hydrogen gas in the near future let us envisage even higher energies (>10 MeV), and the possible use of our source to generate X-rays via betatron radiation or inverse Compton scattering.

Still, strong shot-to-shot fluctuations of the pointing were observed in this regime, and could be attributed to the strong transverse density gradients of our micrometric targets. Slit-shaped nozzles have been designed and could be manufactured and used in future experiments to mitigate these transverse gradients. The possible impact of hydrodynamic turbulence in the high pressure supersonic helium flow and shocks should also be investigated.

Ionization injection in a helium-argon mixture was also achieved, and produced very stable beams with a few pC/few MeV regime, that could be of interest for some applications such as electron diffraction.

Chapter 5

Carrier-Envelope Phase effects in laser-wakefield acceleration

Sommaire

Observing carrier-envelope phase effects on the accelerated electron beam in laser-wakefield acceleration represents a challenge from both a conceptual and technical point of view. The main difficulty arising from the physical processes has been discussed in Section 1.7 and lies in the fact that in laser-wakefield acceleration, the laser propagates in an underdense plasma where the dispersion induces a slippage of the CEP on the length scale $L_{2\pi}$. Thus, the interaction does not necessarily occur at a specific CEP value, and the potential effects associated with each of these values average out. So, in order to observe these effects, the processes affected by the carrier-envelope phase (e.g. injection) must occur on a distance inferior, or of the order of $L_{2\pi}$ which is particularly small ($\sim 10\,\mu\mathrm{m}$) in our experiment where we use high plasma densities resonant with the near-single cycle pulses. The technical difficulty resides in the stabilization of the CEP of a complex high power laser system (described briefly in Sec. 2.1.5, and in more details in Marie Ouillé's thesis [86]) , and in the high level of precise control of every other aspects of the experiments that is necessary in order to isolate fine effects associated with CEP changes. In this context, the high-repetition rate is of paramount importance because it allows to accumulate a large quantity of data from which statistical analysis can bring out CEP-dependent variations while averaging out unrelated random noise in the beam parameters, and reducing CEP variations. Previous experiments during the thesis of Domynikas Gustas [171, 172] resulted in preliminary results in which changing the CEP seemed to impact the electron beam energy, but these results could not be reproduced on several loops as the electron energy was drifting in time and the effects were washed away, motivating the more in-depth follow up study of CEP effects presented in this thesis.

5.1 CEP effects in nitrogen

Our first experiments aiming at demonstrating carrier-envelope phase effects in LWFA were carried prior to the installation of the differential pumping system described in Section 2.4.3, and were therefore restricted to the use of nitrogen gas. In nitrogen, ionization injection can occur, and therefore both mechanisms potentially leading to a dependence in CEP described in Section 1.7 (the oscillating transverse asymmetry of the plasma wave, and the shift of the initial conditions due to ionization injection) could be responsible for an observed effect. This means that PIC simulations will be necessary in order to understand the precise physical cause of any observed CEP-effect in nitrogen. The results presented in this section were published in two journal articles [173, 174]

5.1.1 Experiment in N_2

As described in Section 2.1.5, the Salle Noire 2.0 laser system allows to control and stabilize the CEP through two separate feedback loops, with a typical RMS stability between 300 mrad and 600 mrad. The typical distribution of CEP values during a loop between 0 and 2π is showed in Figure 5.1. It also highlights the advantage of averaging the data on a large number of shots N, as it largely decreases the variability (by a factor $\sqrt{N}$) of the CEP and therefore the uncertainty of the measurement.

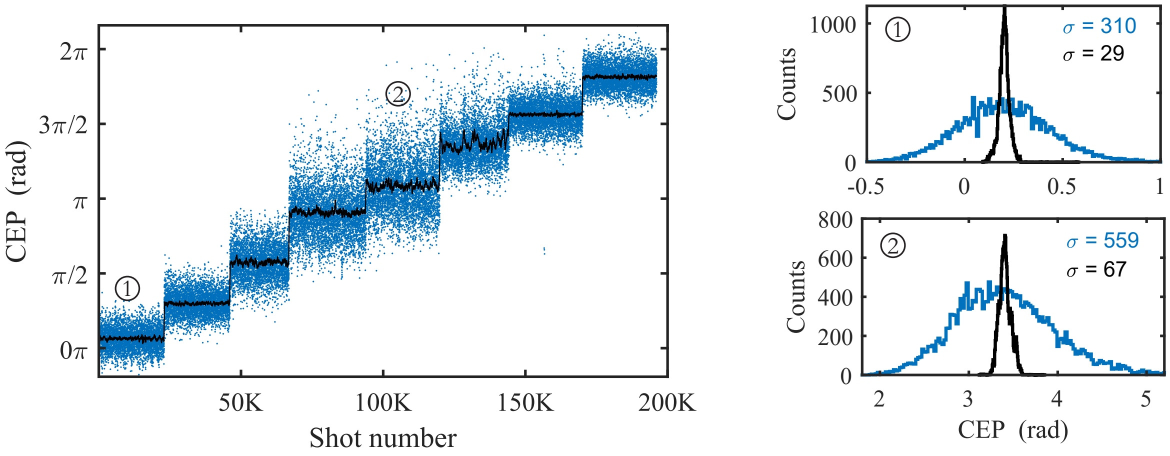

Figure 5.1 – left: Single-shot measurements (blue) and average over 200. Right: Histogram of the CEP values in the single-shot (blue) and averaged (black) cases, for targets values of 0 and π. shots (black) of the CEP.

The experiments were performed using our kilohertz laser with a final on-target energy of 2.5 mJ per pulse and a duration of 4.0 fs, focused by an f/2 off-axis parabola (f=50 mm) to a 2.7 × 2.8 µm focal spot, reaching a vacuum peak intensity of $I = 5 \times 10^{18}\,\mathrm{W\,cm^{-2}}$. A supersonic nitrogen gas jet, with a 60 µm throat and 180 µm exit diameter is used. Supersonic gas jets were chosen over one-sided shock jets because it was observed in simulations that gradient injection leads to significantly reduced effects of the carrier-envelope phase on the accelerated beam [78]. During the experiments, the CEP is varied by increments of $\pi/4$, and the electron beam parameters are measured for each CEP value. We repeat the CEP loop two or three times to ensure that the variations are repeatable with CEP and not associated with slow drifts of the accelerator. Figure 5.2 schematises the principle of the experiment.

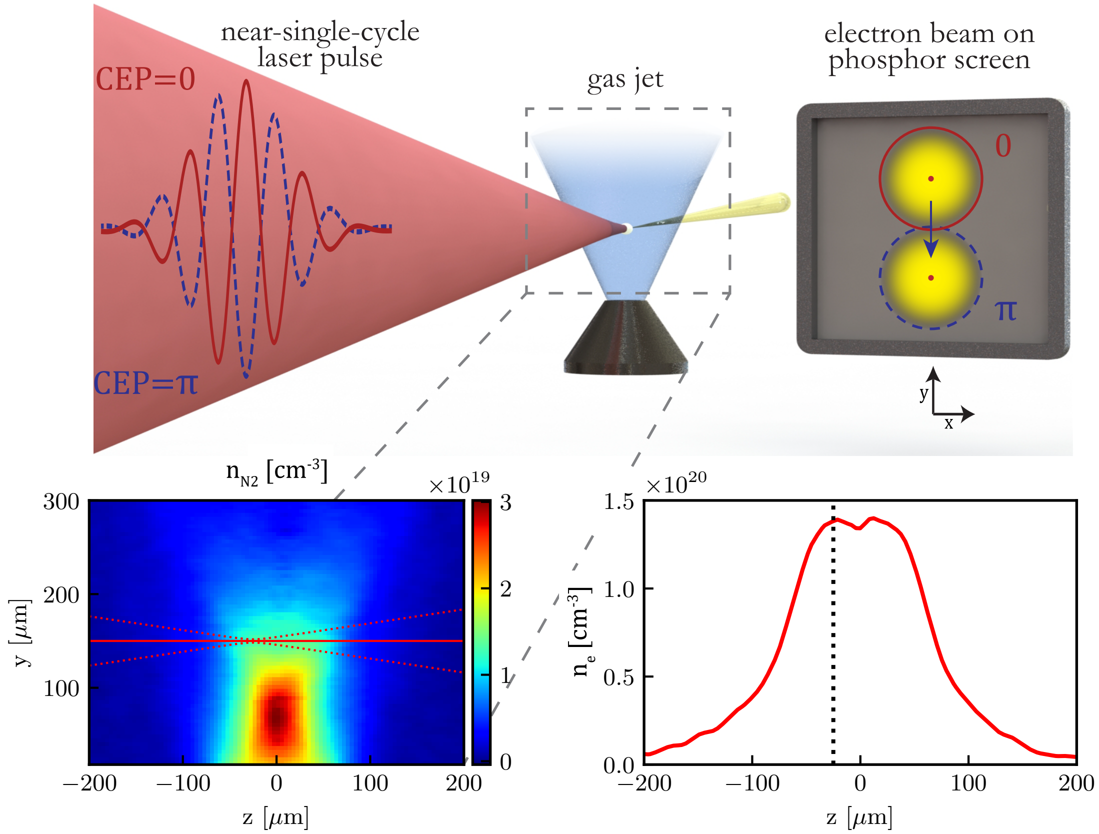

Figure 5.2 – Upper: Principle of the experiment. Lower: 2D map of the gas density, retrieved from the phase map of an interferometry measurement (left). The height of the laser beam is indicated in red (150 µm from the jet exit) for a backing pressure P_{back} = 15 bar. A lineout at this position of the plasma density (assuming full ionization of nitrogen up to N^{5+}) is shown on the right. The dotted black line indicates the laser focal position

Figure 5.3 presents data from a CEP scan between 0 and 2π repeated on three loops, at a plasma density at $n_e = 1.4 \times 10^{20}\,\mathrm{cm^{-3}}$ corresponding to a backing pressure $P_{back} = 13$ bar. The panels a) and b) show a clear dependence of the electron beam pointing in the polarization plane to the CEP, as it repeatedly oscillates during the three loops, with a significant amplitude of about 15 mrad ($\sim$ 30% of the beam divergence which is 50 mrad). In the perpendicular direction, the pointing does not vary with CEP, which is expected as single-cycle pulses induce no asymmetry in this plane. These pointing fluctuations can be an important source of instability of the electron beam. Indeed, we can estimate the maximum sensitivity of the beam pointing to the CEP by measuring the maximum slope of the pointing oscillations: $d\theta_y/d\phi = 20\,\mathrm{mrad/rad}$, meaning it would be necessary to stabilize the CEP to 50 mrad rms in order to keep the pointing variations under 1 mrad (not considering other sources of pointing jitter). This highlights the importance of CEP-control in the perspective of the development of a stable laser-wakefield accelerator driven by (near)-single cycle pulses.

The accelerated charge is showed in Fig. 5.3c and is in the picocoulomb range. By performing a moving average on 2π to remove the non-periodic slow variations, we bring out a slight charge modulation of the order of 8% depending on the CEP (see Fig. 5.3d), but this behavior is not as clear as the one observed on beam pointing because it is dominated by charge variation uncorrelated to CEP. The electron mean energy is around 1.9 MeV, and the normalized electron spectra as a function of the laser CEP is plotted in Fig. 5.3e. They show that the measured energy of the electron oscillates moderately with CEP, with variations of 5% of the mean energy. But this effect might be caused by a difference in the sampling of the beam in the spectrometer due to the beam pointing changing with CEP. As can be seen in Fig. 5.3b, the pinhole of the spectrometer represented by the small white circle samples different parts of the beam depending on the CEP. So if the energy distribution is not spatially uniform, this might lead to fluctuations of the measured energy even if the global beam energy remains constant. To further clarify this issue, we plot the non-normalized spectra, the mean energy of the electron and a drawing of the geometry of the spectrometer in Figure 5.4. It shows a significant dependence of the charge going through the spectrometer with the CEP, associated with different positions of the beam relative to the pinhole. The values for which the sampled charge is higher, corresponding to a more centered beam, also yield the highest energies. This indicates that the movements of the beam relatively to the spectrometer is at least partly responsible for the measured energy dependence.

5.1.2 Polarization control

The main observed effect of CEP in the previous section is the oscillation of the electron beam pointing in the vertical direction, which corresponds to the polarization direction. In a following experimental campaign, we aimed at adding another lever of fine control on the electron beam by controlling the polarization direction, which would also allow to verify that the beam oscillation plane indeed follows it. In this experimental run, we operate the LPA in slightly modified conditions compared to the previous section: we now use a f/4 off-axis parabola (f=100 mm) that focuses the laser to a larger 5 µm spot. The laser energy on target is 2.6 mJ, and the pulse duration is 4.0 fs, yielding a peak vacuum intensity $\mathrm{I} = 1.9 \times 10^{18}\,\mathrm{W\,cm^{-2}}$. The peak plasma density of the supersonic profile is $n_e = 8.3 \times 10^{19}\,\mathrm{cm^{-3}}$. We insert a zero-order broadband half-waveplate installed on a motorized rotation stage in the laser beam in order to control the direction of the linear polarization direction. To characterize the laser polarization depending on the waveplate rotation, we use a polarizing beamsplitting cube and a powermeter. The Table 5.1 summarizes these measurements. The energy is inferior to the total laser energy because the beam was irised to match the size of the 1" cube.

It appears that, while an almost perfectly vertical polarization is achieved, with only a sub-percent ellipticity, the horizontal polarization is not purely linear and an ellipticity of 10% remains. This residual ellipticity can be explained by the fact that the laser spectrum is extremely

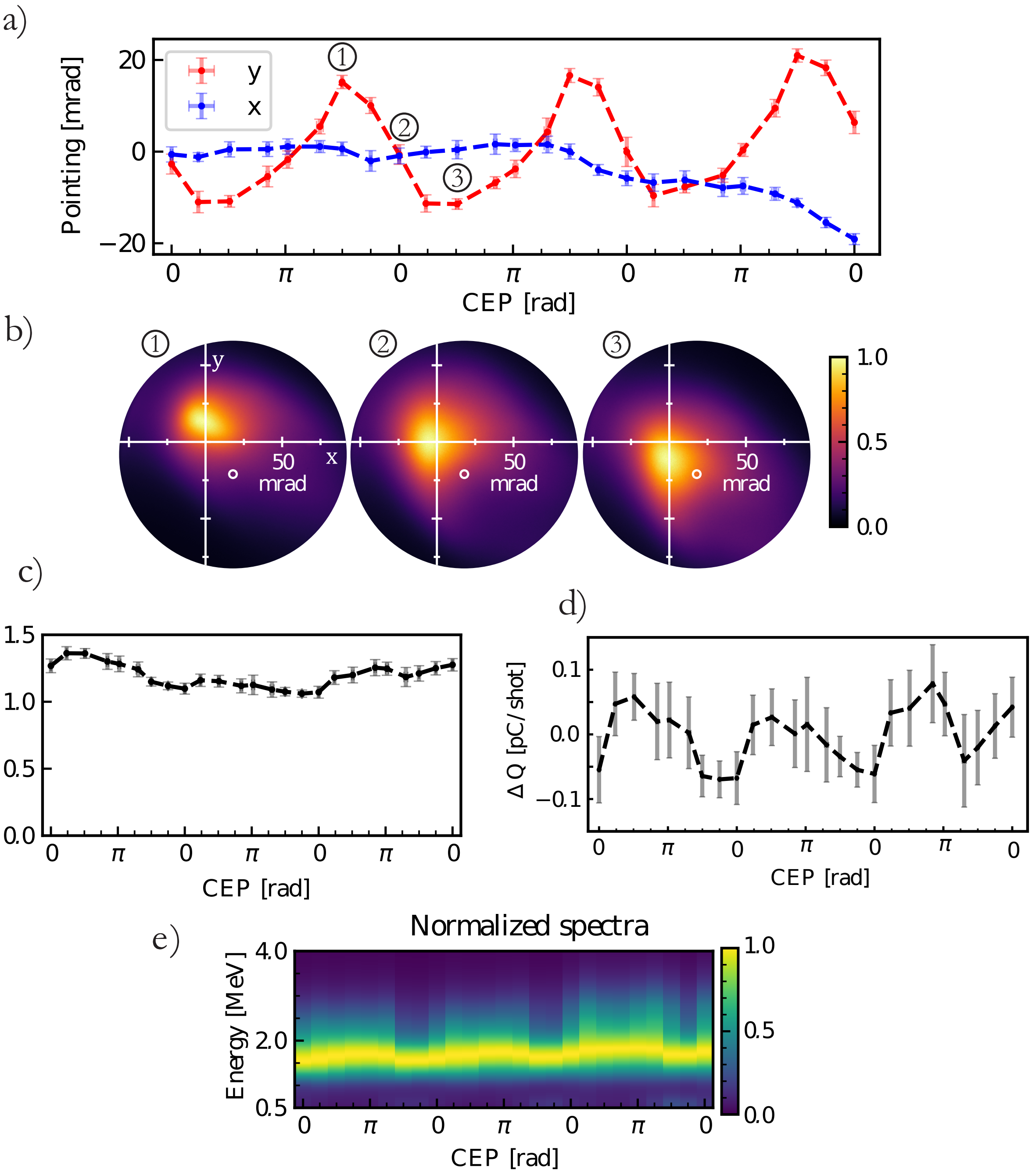

Figure 5.3 – Experimental results obtained at $n_e = 1.4 \times 10^{20}\,\mathrm{cm}^{-3}$ when varying the CEP. a) Electron beam pointing in the laser polarization direction (y,red) and in the perpendicular direction (x,blue). b) Electron beam profiles acquired by accumulating 200 consecutive shots, for three different laser CEP corresponding to (1) high, (2) central, (3) low beam pointing. The small white circle corresponds to the position of the sampling pinhole of the spectrometer. c) Electron beam charge as a function of CEP. d) Charge variations as a function of CEP. The slow non-periodic fluctuations are removed by performing a moving average on 2π. e) Normalized electron spectra as a function of CEP. Pointing, charge and spectra data are averaged on 20 measurement of 200 consecutive shots (4000 shots per point in total). The errorbars are obtained by estimating the standard deviation on these 20 measurements.

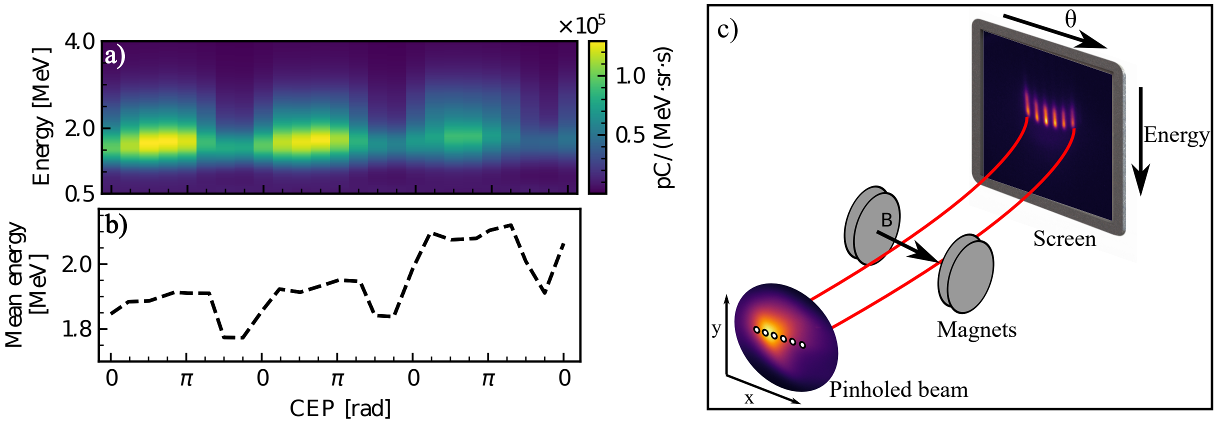

Figure 5.4 – a) Electron energy spectra without normalization and b) mean energy of the electrons as a function of the laser CEP. c) Geometry of the spectrometer.

Polar. direction	E_x **(**μJ**)**	E_y **(**μJ**)**	ϵ
Vertical	5	730	0.7%
Horizontal	675	65	10%

Table 5.1 – Polarization measurement for the two position of the waveplate yielding mostly horizontal and mostly vertical polarization. The ellipticity ϵ is the ratio of the energy in the main direction on the energy in the perpendicular direction

large, ranging from 500 nm to 1000 nm (see Sec.2.1.2), which is too wide even for a broadband waveplate, resulting in a final polarization which is not perfectly linear. The vertical polarization is almost not impacted because in this case, the incident laser polarization is along a neutral axis of the waveplate.

As shown in Fig. 5.5 The beam oscillates in the laser polarization direction, with an amplitude of around 5 mrad, while it does not move in the perpendicular direction. When the polarization of the laser is rotated by 90°, so is the direction of oscillations of the beam pointing (see Fig. 5.5). This indicates we can achieve fine control of the beam pointing in all the directions. Additionally, Fig. 5.5b,d show a significant difference in divergence between the two cases (43 mrad vs 68 mrad FWHM), which can be explained by the fact that the beam was optimized by adjusting experimental parameters such as chirp and position of the focus for the horizontal polarization direction, which were then kept constant when shifting to vertical polarization while some residual dispersion of the pulse could be induced by the rotated waveplate.

This new case gives us additional insight on two aspects that still required further study: the dependence of the beam charge and the energy to the CEP. Indeed, as showed in Figure 5.6, clear variations of the charge correlated with the CEP are observed in the horizontal case, with variations up to 30%. The vertical case shows similar dependence of the charge, but uncorrelated variations make it less obvious. Moreover, the horizontal laser polarization enables the use of a series of pinholes on a horizontal line, allowing us to obtain information on the electron spectra independently of the CEP-dependent beam pointing by averaging the spectra on the whole sampling line. This is not possible to do vertically because the magnets would disperse the electrons in the same direction. With this new geometry, Fig. 5.6 shows no clear effect, at

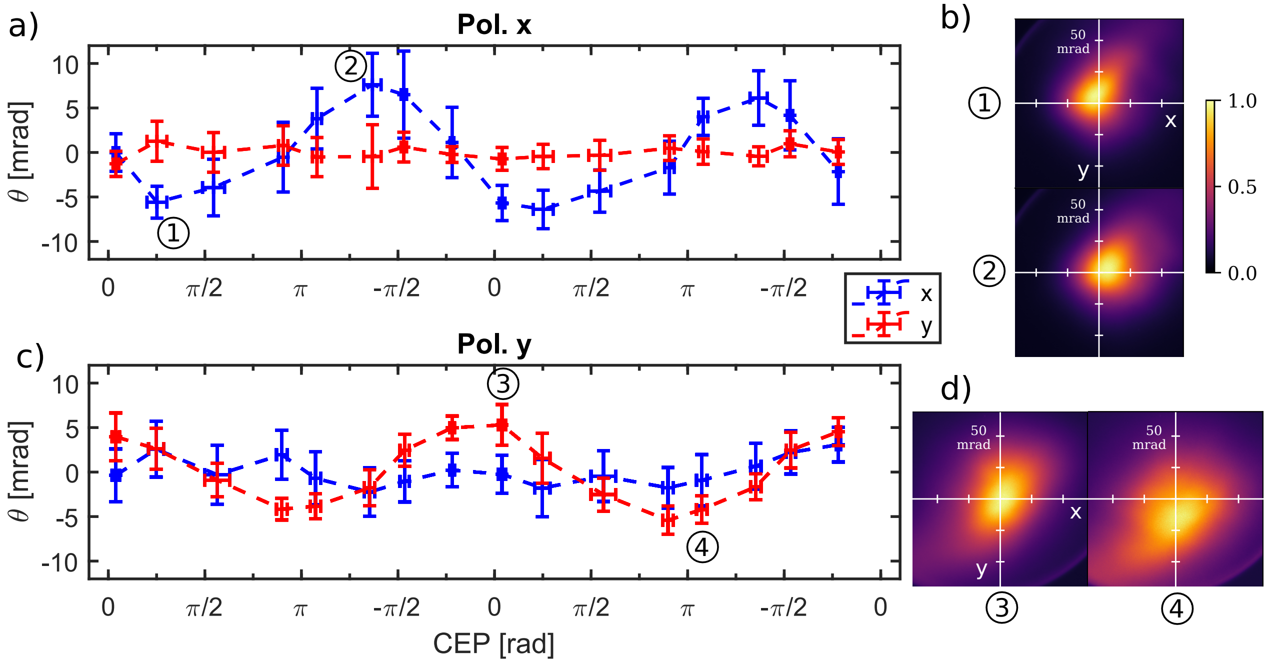

Figure 5.5 – CEP effects on the electron beam depending on the laser polarization with N_2. a) Electron beam pointing in both x (blue) and y (red) directions for a horizontal laser polarization (along x). Each point corresponds to 2000 shots.b) Images of the beams accumulated on 100 shots corresponding to CEPs of $\pi/4$ and $-3\pi/4$ in the horizontal case. c) Electron beam pointing in both x and y directions for a vertical laser polarization (along y). The pointing errorbars correspond to the standard deviation on 20 measurements. The CEP errorbars correspond to the standard deviation of the CEP averaged on 100 consecutive shots. d) Images of the beams corresponding to CEPs of 0 and π in the vertical case.

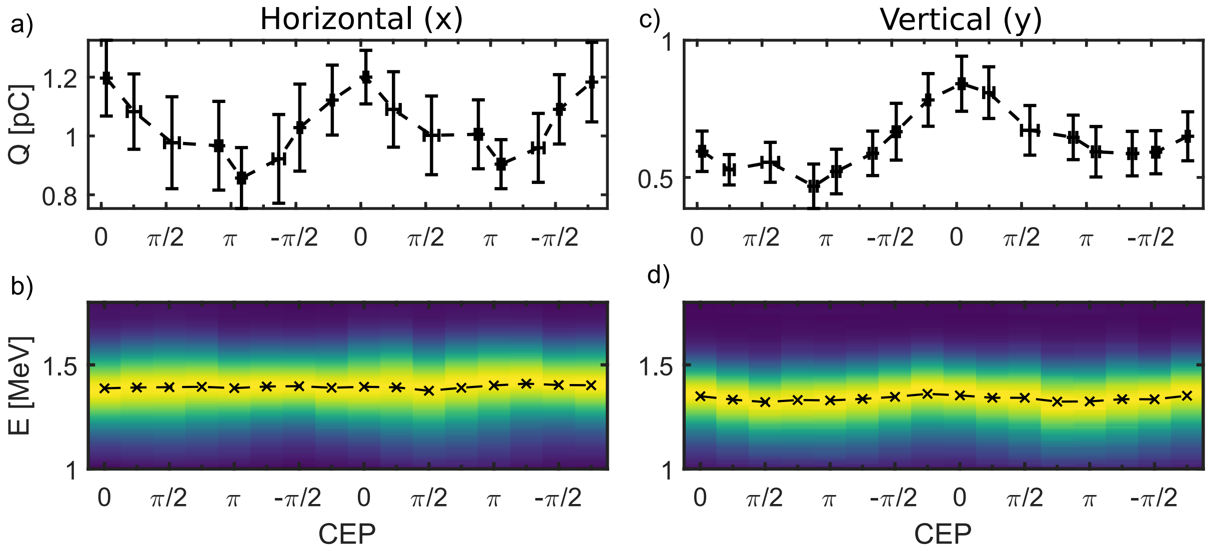

Figure 5.6 – a) Electron beam charge Q and b) electron spectra plotted against CEP for the horizontal polarization case in N_2. c) Electron beam charge Q and d) electron spectra plotted against CEP for the vertical polarization case in N_2. The black crosses correspond to the mean energy. Each point corresponds to 2000 shots

least in this case, of the laser CEP on the energy spectrum, while the vertical polarization (beam moving perpendicular to the pinhole line) case exhibits similar oscillation of the energy as observed in the previous section. This clearly points towards the explanation that the observed energy dependence to CEP was mainly due to the different sampling of the beam, and that CEP does not impact significantly the energy of the electrons in this case.

The fact that the charge is strongly impacted, but not the energy of the electrons indicates that the carrier-envelope phase mainly plays a role in injection, and not really in the subsequent acceleration mechanism.

5.1.3 PIC simulations

As mentioned earlier, the observation of a dependence of the accelerated beam to the carrier-envelope phase in nitrogen does not allow to determine *a priori* if those effects are due to ionization injection, the transverse asymmetry of the plasma wave or a combination of both. In order to understand in details what are the mechanisms behind the observed dependence of the accelerated electron beam to the CEP, we perform particle-in-cell simulations with the code FBPIC. The mesh used for simulations is $\Delta z = \lambda_0/60$ and $\Delta r = 5\Delta z$. Five azimuthal Fourier modes were used to properly capture the asymmetries associated with the plasma response to near-single cycle pulses. The simulations were initialized with pure neutral nitrogen, and ionization was calculated with the ADK model of tunnel ionization [43]. Atomic nitrogen was initialized using 96 macroparticles per r-z cell, and each such macroparticle could produce up to 7 macroparticles of electron species via ionization. Idealized Gaussian temporal and spatial laser profiles were used in order to focus on clarifying the underlying physical process associated with CEP without including additional complexity arising from imperfections of the laser. The waist and pulse duration we chosen to matching the experiment, and a pulse energy of 2.3 mJ, corresponding to $a_0 = 1.6$. Dispersion in the plasma was pre-compensated by adding a 5 fs^2 positive chirp. For the simulated plasma profile, we used a combination of two supergaussian functions to fit the experimentally measured profile, with a peak density of $1.8 \times 10^{20}\mathrm{cm}^{-3}$. The laser focus position was placed 25 μm upstream of the center of the profile. Typical simulated electron beams have a charge around 2.7 pC with a mean energy of 4.3 MeV.

The simulations parameters were chosen to be close to the experimental ones, and then varied around these positions (mainly pulse energy and plasma density) by performing many simulations in order to converge to electron beam parameters as close as possible to the experiment. In our regime, the interaction is extremely sensitive to slight changes of these parameters, and matching exactly the charge and energy of the experiment has proven difficult. Indeed, the experimental beam had both a relatively low energy (2 MeV) and moderate charge (<1.5 pC). In the simulations, when lowering either the laser energy or the plasma density, a low charge could be achieved, but in this case the electron were accelerated to excessive energies (>5 MeV) because of the absence of beam-loading effects perturbing the accelerating structure. When decreased even further, injection was not occurring. Achieving a moderate energy around 2 MeV in the simulations was possible by increasing either the laser energy and the plasma density, because in this situation a massive amount of electrons were injection, inducing a strong beam loading effect limiting the accelerating field, but in this case charges of around 15 pC were obtained. This difficulty to reproduce exactly the beam parameters could be explained by the different experimental aspects not taken into account in the simulations. First, the simulation is run with an idealized laser pulse with Gaussian temporal and spatial profiles, which ignores the laser imperfections and asymmetries and spatio-temporal couplings. Additionally, because of the continuously flowing gas jet, there can be some nitrogen pressure buildup in the chamber that has been showed to be detrimental to the accelerator performances due to ionization defocusing of the laser [25].

Injection triggered by bubble transverse oscillation

By looking at the injected charge distribution between L-shell (self-injection) and K-shell (from ionization injection) in Figure 5.7, it appears that the charge originates almost exclusively from self-injection (95%). We remind the expression of the laser intensity as a function of the normalized potential and the central wavelength:

$$I = \left(\frac{a_0}{\lambda \times 0.85}\right)^2 \times 10^{18}\,\mathrm{W\,cm^{-2}} \tag{5.1}$$

Even though the laser normalized potential reaches $a_0 = 2.4$ through self-focusing, which would correspond to an laser intensity of $1.2 \times 10^{19}\,\mathrm{W\,cm^{-2}}$ with a laser wavelength $\lambda_0 = 0.8\,\mu\mathrm{m}$ and be sufficient to massively ionize N^{5+} in N^{6+} ($I_{bs} \sim 10^{19}\,\mathrm{W\,cm^{-2}}$) triggering ionization injection, the laser has been strongly redshifted by its interaction with the plasma, and its central wavelength is $\lambda = 1.25\,\mu\mathrm{m}$ at peak a_0, yielding a maximum laser intensity $I_{peak} = 5 \times 10^{18}\,\mathrm{W\,cm^{-2}}$. Ionization injection thus occurs only through tunnel ionization of N^{5+} and remains marginal (<5%) compared to self-injection. We can therefore exclude ionization injection as a source for the observed CEP-dependence in the experimental results presented in the previous section.

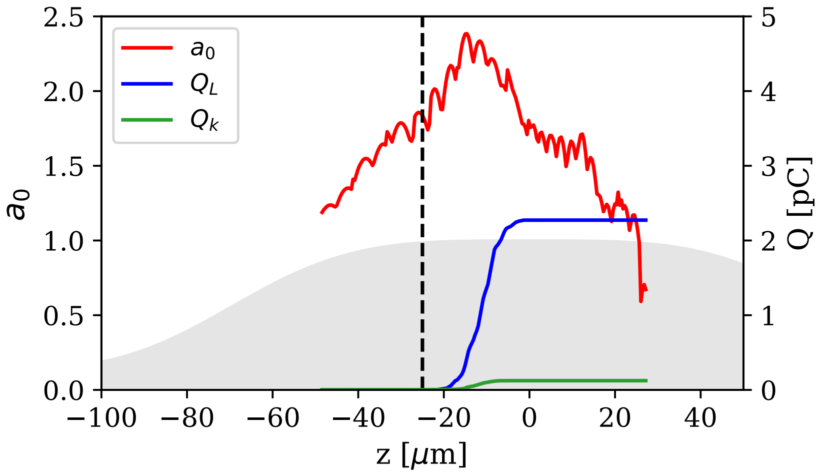

Figure 5.7 – Normalized laser potential (red), injected charge from L-shell (blue) and K-shell (green) electrons as a function of the propagation distance in the simulation. The plasma density profile is plotted as a gray shaded area. The initial laser CEP is π.

Figure 5.8 shows the asymmetry of the plasma response to the near-single cycle pulse in the polarization plane, where the bubble is pushed upward, while it remains perfectly symmetric

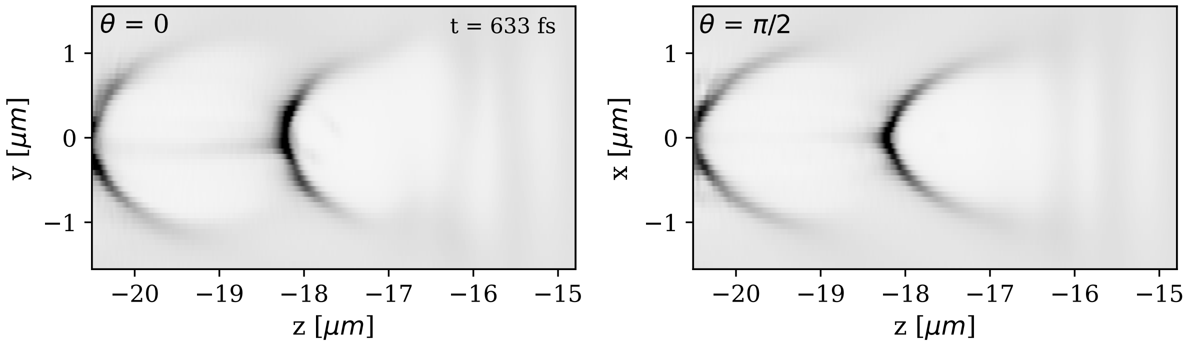

Figure 5.8 – Slices of the wakefield in the polarization plane ($\theta = 0$) and in the perpendicular plane ($\theta = \pi/2$) at simulation time t=633 fs. The plasma density is showed in gray. The colormap is saturated at $0.7n_c$

in the perpendicular plane. So in the following, we will focus on the dynamics in the polarization plane, where the phenomena specific to near-single cycle pulses occur. Figure 5.9a shows a first injection event that occurs off-axis in the asymmetric wakefield, in the laser polarization plane. As the CEP slips by π, a second injection event occurs on the other side of the wakefield (panel b). These two electron bunches are injected with opposite initial transverse momenta and they end up with an opposite pointing when they exit the plasma [Fig 5.9e]. More generally, it appears the evolving CEP-dependent asymmetry of the plasma wave is responsible for off-axis injection of several electrons sub-bunches. To study it in more details, we characterize this asymmetry with two quantities, the transverse centroid of the bubble normalized to the laser waist: $\Gamma_y = \frac{\int n_e y dy}{\int n_e dy} \times \frac{1}{w_0}$ and the difference in the mean longitudinal position of the density peak between the $y > 0$ and $y < 0$ parts: $\Delta z = z_m(y > 0) - z_m(y < 0)$, with $z_m = \frac{\int n_e z dz}{\int n_e dz}$ considering only densities higher than $0.1n_c$. This longitudinal asymmetry is illustrated by Fig. 5.9d. As shown in Fig. 5.9c, the asymmetry of the wake oscillates during the propagation in the plasma due to the shifting CEP. It appears that Δz is dephased by $\pi/2$ with respect to Γ_y, meaning that the bubble is not only moving upwards and downwards as described in the analytical work of Kim *et al.* [175], but it also rotates around its center, i.e. it is moving forward and backward alternately for positive and negative y, as schematically represented in Fig.5.9d.

By comparing the charge injection rate to the quantities characterizing the asymmetry in Fig. 5.9c, it appears that electrons are injected when the bubble is moving backward on one side, with the injection peaks occurring when Δz changes sign, corresponding to its maximum local slow down, but also to an extremum of the transverse asymmetry. This is analogous to the injection in a density gradient where the bubble moves backwards and traps electrons [58, 116]. Because the bubble is moving backwards only on one side at a time, electrons are injected off-axis on an alternating y-side depending on the CEP. When the electrons are injected from the bottom, they have a non-zero positive transverse momentum and therefore end up pointing mainly upward after a single betatron oscillation at the end of the simulation. Conversely, electrons end up pointing downwards when injected from the top. In the direction perpendicular to the polarization, the plasma wave remains perfectly symmetric, electrons are injected on-axis and therefore the beam is centered in this direction. Moreover, during its interaction with the plasma, the laser is strongly redshifted up to a wavelength of 1.4 μm (see Fig 5.9c),

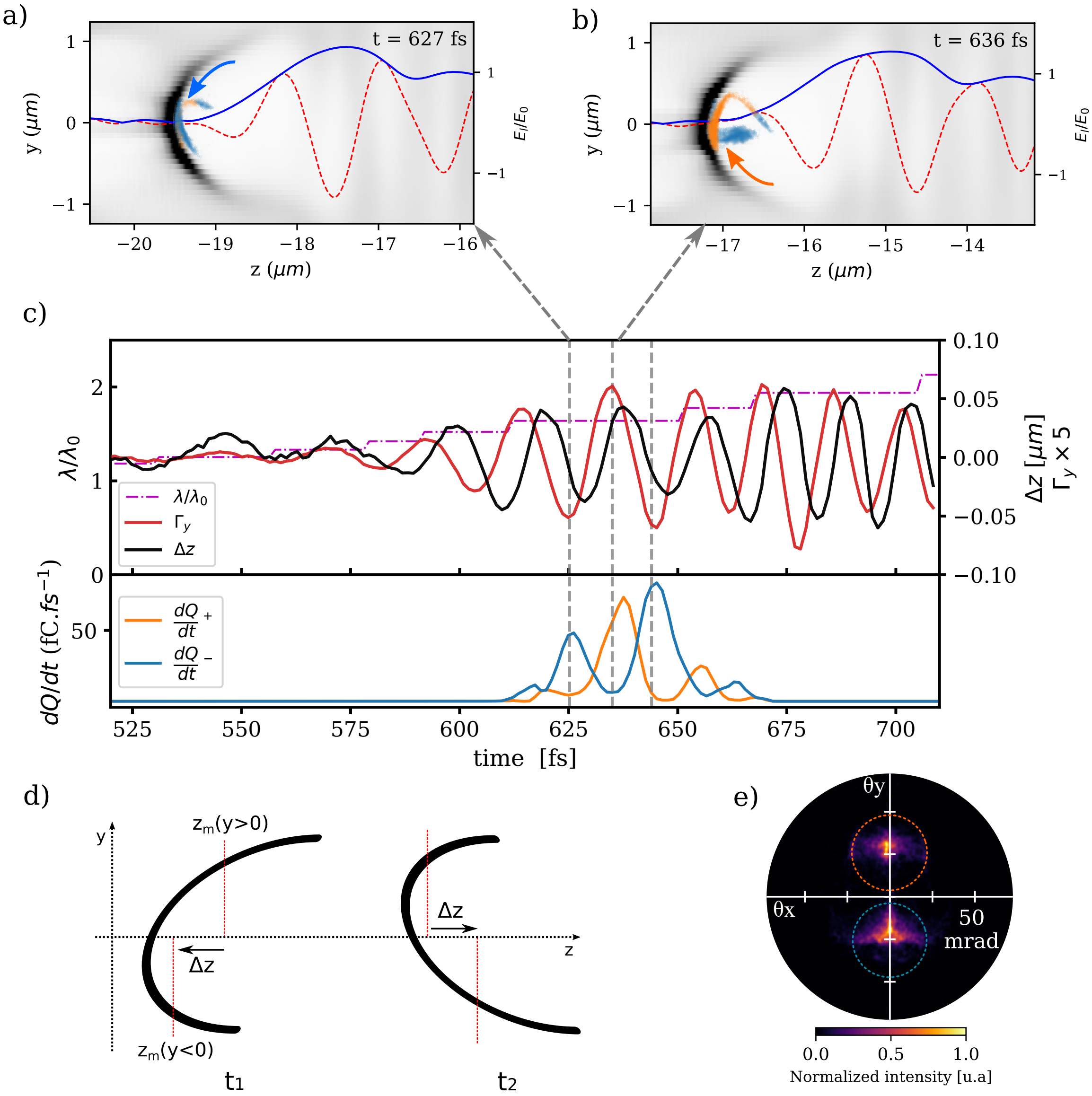

Figure 5.9 – Particle-in-cell simulation of a LPA driven by a 4.0 fs in N_2. a)-b) Snapshots of the wakefield, for an initial CEP of π, at two different times, showing the injection of two separate bunches. Electron density in the (z-y)-plane is shown in gray, and injected electrons are displayed in orange (blue) when their pointing is positive (negative) at the end of the simulation. The normalized laser electric field $E_l/E_0 = E_l/(m_e c\omega_0/e)$ (red dashed line) and its envelope (blue solid line) are also shown. The arrows show the typical trajectories prior to injection for each case. c) Wakefield transverse (Γ_y,red) and longitudinal (Δz, black) oscillation in the polarization plane, peak wavelength of the laser normalized by the initial wavelength (magenta), and charge injection rate for the two electron populations shown in a),b) with corresponding colors, as a function of the simulation time for an initial CEP of π. The gray dashed lines highlight the three main injection events. d) Schematic description of the longitudinal bubble asymmetry for two times t_1 and t_2 corresponding to $\Delta z < 0$ and $\Delta z > 0$. The change of asymmetry from t1 to t2 would lead to injection of electrons from the upper part of the bubble. e) Simulated electron beam for an initial CEP of π.

which reduces the CEP oscillation period, increases the amplitude of the asymmetry through the scaling $\Gamma_y \propto a_0^3 \lambda_0^4$ [28] and facilitates electron trapping by lowering the wake phase velocity

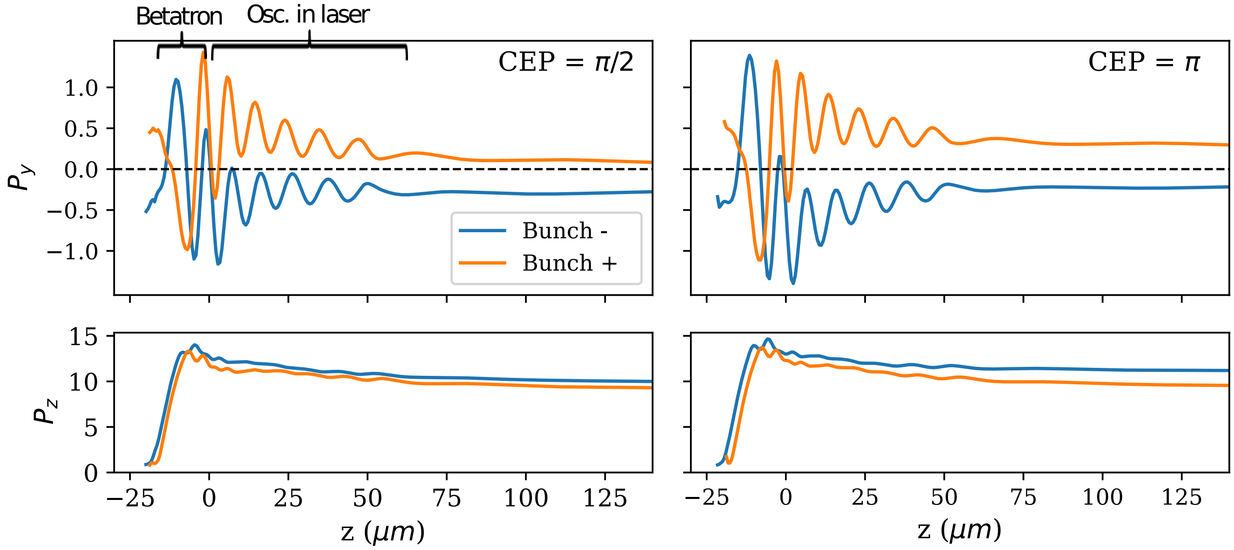

Figure 5.10 – Transverse (top) and longitudinal momentum (bottom) of two different sub-bunches with opposite beam pointing as a function of the propagation distance in the simulation for two different initial CEPs. Momenta are normalized to $m_e c$

($v_\phi = v_{g,las} \simeq c[1 - \lambda_0^2/2\lambda_p^2]$) [36, 70].

Sub-bunches tracking and properties

We have seen that the transverse oscillations of the wakefield trigger the periodic injection of several (three main here) sub-bunches. We track two of these bunches, injected at opposed transverse momenta, during their propagation in order to gain a deeper insight of their dynamics, and a better understanding of the causes leading to a different beam pointing when changing the initial laser CEP. We will call 'bunch +' an electron sub-bunch injected with a positive transverse momentum in the polarization direction ($P_y > 0$) from the bottom of the bubble ($y < 0$) and 'bunch -' an electron sub-bunch injected with a negative transverse momentum in the polarization direction ($P_y < 0$) from the top of the bubble ($y > 0$).

The transverse and longitudinal momenta of the two sub-bunches are plotted in Figure 5.10 for two different initial CEP. It shows that the bunches are indeed injected with a non-zero transverse momentum in the polarization direction ($P_y \sim \pm 0.5\, m_e c$) and that their initial momentum determines the sign of the bunches pointing at the end of the simulation. After their injection, the electrons perform a betatron oscillation before escaping the plasma bubble and catching up with the laser electric field. Subsequently they oscillate in the laser field several times before it diffracts too much to have a significant effect anymore. When changing the laser CEP, the exact time of injection is slightly shifted, therefore the bunches will have slightly modified initial conditions in this complex dynamics, leading to a different pointing of the sub-bunches. For instance, in Figure 5.10, the 'Bunch +' ends up with a significantly increased transverse momentum at the end of the simulation for a CEP of π than $\pi/2$. This leads to differences in the global beam pointing for the two cases: $\theta(\pi/2) = -9$ mrad and $\theta(\pi) = 0$ mrad. Note that the relative charge in 'bunches +/-' also plays a role in the final beam pointing: if more electrons are injected in the 'bunches +', it contributes to a positive beam pointing and conversely.

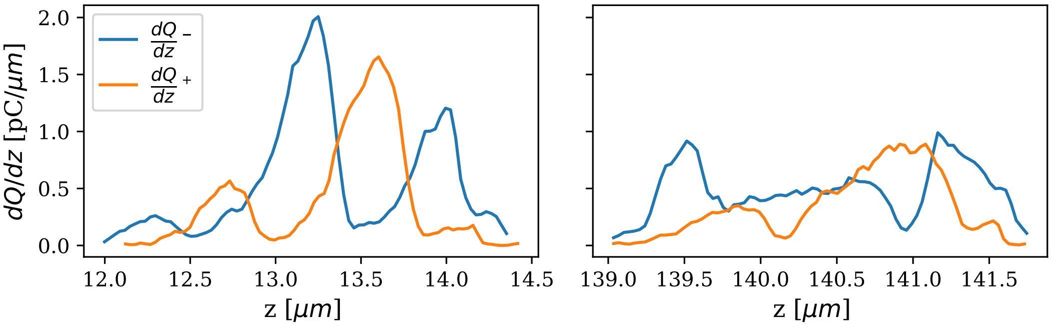

Figure 5.11 – Distribution of the charge of injected electrons differentiated according to their final pointing, as a function of the position just after injection (left) and at the end of the simulation (right). Laser initial CEP is π.

Additionally, the oscillations of the electrons solely in the laser electric field uncover an unexpected behavior: the transverse momentum of each bunch gradually decreases while oscillating in the laser, reducing their final divergence. This is surprising, because it is the exact opposite of what one could naively predict from the effect of the ponderomotive force, where the electrons would be expelled from the higher intensity zones and therefore gain transverse momentum. This phenomenon is explained in section 5.1.4, and originates in a combined effect of the longitudinal electric field of the focused laser, and the $v_z \times B_x$ force of the laser on the electrons.

Longitudinally, the electrons are accelerated on a very short distance (12 µm) and then exit the wakefield and keep a steady momentum, though with a slight decrease. They end up with similar u_z at the end of the simulation.

The sub-bunches have particularly interesting properties associated with their injection process. Each injection event is very localized in time, which translates in extremely short bunch duration, as short as 0.9 fs just after injection (see Fig. 5.11). Due to their energy spread and their moderate energy, the bunches tends to stretch during propagation, but this effect would be limited with more relativistic electrons.

Finally, each bunch also has extremely low emittance, due to the low spread in transverse momentum at injection (electrons are injected with a non-zero, but narrow distribution in P_y). Figure 5.12 shows that the normalized emittance in y of the third bunch is as low as 10 nm not long after injection. The subsequent propagation in the laser leads to emittance growth, and at the end of the simulation, the emittances in x and y are $\epsilon_x = 60\,nm$ and $\epsilon_y = 50\,nm$. Note that using a more realistic laser pulse, with non-gaussian features and imperfections would probably lead to wider distributions in P_x and P_y and therefore higher emittances.

CEP scan in simulations and comparison to the experiment

We now carry out the same simulation by varying the initial CEP between $-\pi$ and $+\pi$ by increments of $\pi/4$ in order to verify if the mechanisms observed in the simulations leads to the behavior measured experimentally when varying the CEP. The results of this scan are represented in Figure 5.13, and the panel (a) shows a clear oscillation of the beam pointing with the

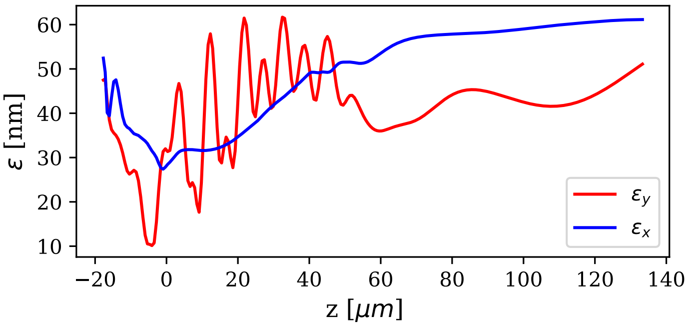

Figure 5.12 – Normalized emittance of the third bunch in both x and y directions, as a function of the propagation distance. Initial laser CEP is π.

initial CEP in the polarization plane, with an amplitude of 9 mrad comparable to the 15 mrad observed experimentally in Figure 5.3. The beam pointing in the perpendicular direction remains centered regardless of the CEP value. Note that because the absolute CEP value is unknown in the experiment, the offset value was chosen to match the phase of the oscillation in the simulations. By adding a pointing jitter of 15 mrad which corresponds to the level of the variations from sources other than CEP observed experimentally and averaging on 200 shots, the two sub-beams merge into a larger divergence single beam, similar to what is observed experimentally. In some cases (i.e. CEP = 0) a structure with two peaks in the beam still remains, which was not the case in the experiment, this could be explained by a combination of two factors: first, in the simulations we use an idealized laser, but we can expect that the pointing distribution of each sub-bunch will be more widespread due to imperfections in the plasma wave, therefore reducing the separation between the 'bunch +' and 'bunch -'. Additionally, space charge effects during propagation of the electron beam from the source to the detector could lead to the merging of these two initially separated sub-beams. Indeed, simulations with the General Particle Tracer code [176] show that for a micrometric, 1 pC bunch at 2 MeV, space charge increases the divergence to tens of mrad FWHM, depending on the exact initial conditions.

Figure 5.13b shows that the mean energy of the electrons varies by 3%, indicating that even though the energy dependence observed experimentally was probably mostly due to a measurement artifact, a slight effect of the CEP on the spectrum might still be present. The charge varies by up to 8% in the simulations due to a slightly shifted position of injection, consistent with the data of Fig. 5.3. The cases where the injection happens slightly ($\sim$ 1-2 μm) later yield a higher charge because conditions are more favorable through a stronger redshift and self-focusing. Still, this slight evolution cannot account for the large 30% charge variations observed in Section 5.1.2. An additional potential source for this observation is studied in section 5.2.3 through the asymmetry of the experimental laser spot.

Our simulation scan reproduces quite well the main feature associated with the carrier-envelope phase in the experiment, which is a clear oscillation of the beam pointing in the polarization plane. They also tends to show that the energy of the electrons is only weakly impacted, and that even though this idealized case can account for part of the charge variations observed experimentally, another factor probably plays a role in inducing large changes in the injected

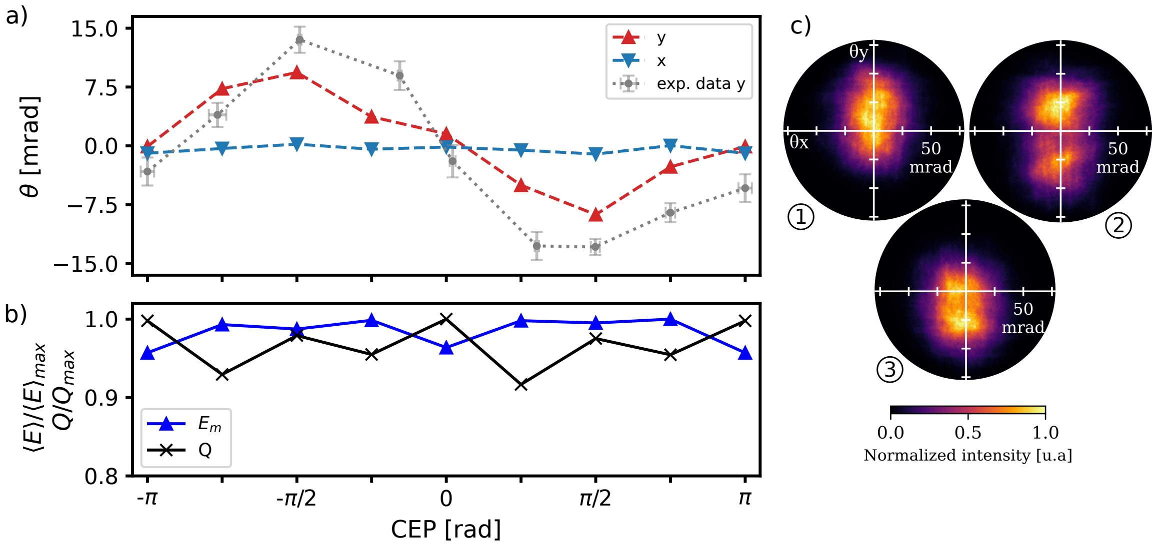

Figure 5.13 – a) Electron beam pointing in the simulations in the polarization direction (y, red) and in the perpendicular direction (x, cyan) as a function of the laser initial CEP. The experimental data of Fig. 5.3 in the y direction are shown in gray. b) Electron mean energy (blue) and beam charge (black) normalized to the maximum value, as a function of the CEP. c) Simulated electron beams for initial CEP values of $-\frac{\pi}{2}$, 0, $+\frac{\pi}{2}$, which produce a high, centered and low beam, respectively. The experimental beam pointing jitter is simulated by averaging 200 simulated shots with randomly generated beam pointing variations following a normal distribution with a 15 mrad standard deviation (shot-to-shot) in both x and y.

charge associated with CEP.

5.1.4 Counter-ponderomotive effect *via* $\mathbf{v} \times \mathbf{B}$ drift

In the previous section, we have observed a surprising effect in the PIC simulations of a 4 fs pulse with $a_0 = 1.6$ propagating in a plasma with a density $n_e = 1.8 \times 10^{20}\,\mathrm{cm}^{-3}$: the accelerated electrons that catch up with the laser and oscillate in its electric field tend to lose an important part of their initial transverse momentum in the polarization direction, while one would expect it to increase due to the ponderomotive force. A possibility could be that the electrons end up at a transverse position opposed to their transverse momentum when propagating into the laser (i.e on the y>0 side with $u_y < 0$), and in this case ponderomotive force could indeed lead to a decrease in the transverse momentum which would be oriented toward the laser intensity gradient. But looking at the trajectories of the electrons in the simulations, we see that it is not the case here: after performing a betatron oscillation, the bunches with a positive transverse momentum end up on the (y>0) side and conversely for the negative momentum. In this configuration, the ponderomotive force would increase the momentum, not decrease it. We performed a PIC simulation in conditions similar to previous sections, but with an artificially injected rectangular test beam supposed to model off-axis injection (polarization along y). The electrons injected from the top (y>0) have a negative initial transverse momentum, and conversely while u_{y0} is set at zero for electrons injected near the axis (see Fig. 5.14a). Because the plasma density is high and the laser strongly redshifted, its propagation velocity is reduced and electrons quickly catch-up with the pulse and end-up co-propagating with it. Similarly to what was observed previously, we see in Figure 5.14b that the transverse momenta of the two bunches injected off-axis decreases indeed after oscillations in the laser electric field, while electrons injected on-axis end up with a near-zero momentum. The situation is schematized in Figure 5.14c, where the electrons are slowed down transversely despite the opposite action of the ponderomotive force. Therefore another effect must be at play.

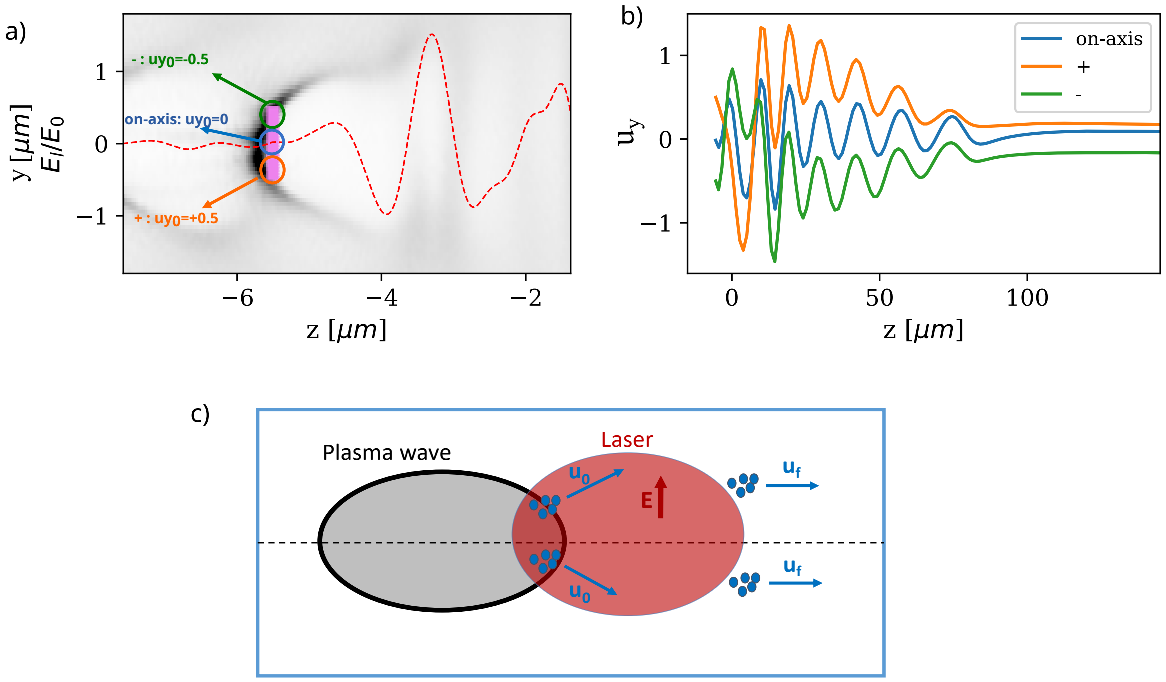

Figure 5.14 – a) PIC simulation at the moment of injection of the rectangular test beam (violet). Top electrons (green) are injected with an initial normalized transverse momentum $u_{y0} = -0.5$, bottom electrons (orange) with $u_{y0} = +0.5$ and electrons injected on-axis (blue) with $u_{y0} = 0$. The laser is polarized along the y axis. b) Tracking of the transverse momentum of the three electron populations during their propagation, highlighting the decrease of transverse momentum after propagation in the laser field. c) Schematic illustration of the geometry of the problem.

This phenomenon seems purely associated with the propagation of electrons in the laser field, because it appears after the electrons have escaped the plasma bubble. We can therefore study it through test-particle simulations where the effect of the plasma will be modeled simply as a reduced group velocity and redshifted central wavelength of the laser. We will use a `test-particle code` which solves the equations of motion for particles in an analytical laser field.

Description of a tightly-focused pulse

A usual description of a gaussian laser pulse relies on simplifying the Helmholtz Equation through the paraxial approximation [177] assuming the wavevectors $\mathbf{k}$ of the pulse are nearly tangential to the optical axis which corresponds to a weak focusing. In this approximation the electric and magnetic fields are purely transverse. But when the laser is tightly focused, with $w_0 \sim \lambda$, such as in our case, this paraxial approximation becomes invalid. It is possible to correct the paraxial expressions by expanding Maxwell's equations near the paraxial solution as a power series of the parameter $\epsilon = 1/kw_0$ [178, 179] and obtain at the first order for a laser linearly polarized along (y):

$$E_x = 0 \tag{5.2}$$

$$E_y = E_0 \frac{w_0}{w} \exp\left(-\frac{r^2}{w^2}\right) \sin\phi_G \tag{5.3}$$

$$E_z = 2E_0 \epsilon \frac{w_0 y}{w^2} \exp\left(-\frac{r^2}{w^2}\right) \cos\phi_G^{(1)} \tag{5.4}$$

$$B_x = -\frac{E_y}{c} \tag{5.5}$$

$$B_y = 0 \tag{5.6}$$

$$B_z = 2\frac{E_0}{c} \epsilon \frac{w_0 x}{w^2} \exp\left(-\frac{r^2}{w^2}\right) \cos\phi_G^{(1)} \tag{5.7}$$

with:

$$\phi_G = \omega_0 t - kz + \tan^{-1}(\frac{z}{z_R}) - \frac{kr^2}{2R(z)} - \phi_0 \quad ; \quad \phi_G^{(1)} = \phi_G + \tan^{-1}(\frac{z}{z_R})$$

Where $w = w_0\sqrt{1 + z^2/z_R^2}$ and $R(z) = z(1 + z_R^2/z^2)$, and ϕ_0 is the CEP of the pulse. It appears that, contrary to the paraxial case, the fields of a tightly focused laser have non-zero longitudinal components E_z and B_z. We will see that this longitudinal electric field plays an important role in the counter-intuitive evolution of the transverse momentum of the electrons in the laser. For enhanced accuracy, we use an expansion of the fields up to the fourth order in the test-particle code.

Test-particle simulations

We perform test-particle simulations trying to reproduce a simplified situation that is similar to the PIC simulations conditions. Test-particle simulations, in addition to being fast to compute, allow us to study the impact of the co-propagation of the electron beam with the laser pulse, without the added complexity of the plasma fields. The laser pulse is linearly polarized along the y axis, with a waist $\omega_0 = 3\,\mu\text{m}$, a pulse duration $\tau = 4.5\,fs$ and a normalized potential $a_0 = 2$ with a wavelength $\lambda_0 = 1.2\,\mu\text{m}$. The laser group velocity is set at $0.89c$ which would correspond to a plasma density $n_e = 1.6 \times 10^{20}\,\text{cm}^{-3}$. Simulations are performed with 100 particles initialized with a $0.1\,\mu\text{m}$ length distribution and no transverse width, a longitudinal momentum $u_z = 6$ (2.6 MeV) and no transverse momentum. Three cases are studied: (0) the particles are placed on-axis, (+) at a transverse position $y = +1.5\,\mu\text{m}$ and (-) at a transverse position $y = -1.5\,\mu\text{m}$. In all cases the electrons are initialized in $x = 0$, and at a position in z behind the laser so that they catch-up with the laser quickly after the start of the simulation. Two additional cases where the electrons are placed off-axis in the x direction (perpendicular to the laser polarization) are also considered to highlight the difference with the usual ponderomotive behavior.

Figure 5.15 shows the trajectories of the electrons in the electric field. It appears that when crossing the laser, they perform small oscillations in it, and end up with a non-zero transverse

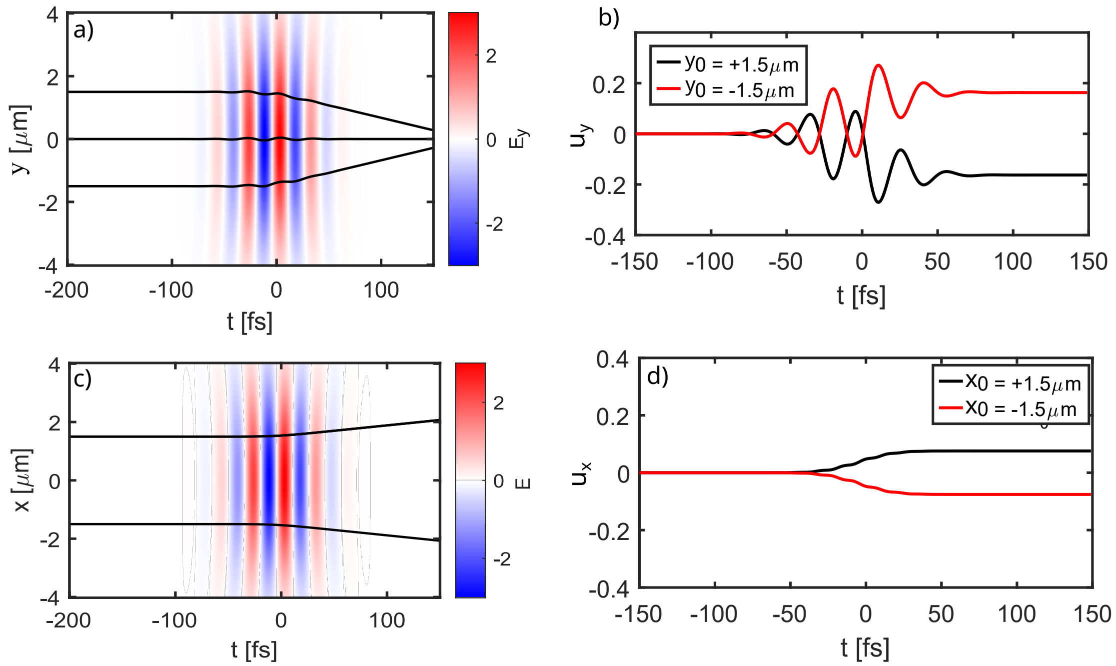

Figure 5.15 – a) Electron trajectories in y (black) in the laser electric field along plotted against the time of the simulation. b) Evolution of the electron transverse momentum in y for two initial off-axis transverse positions. c) Electron trajectories in x (black) in the laser electric field along plotted against the time of the simulation. b) Evolution of the electron transverse momentum in x for two initial off-axis transverse positions. The laser polarization is along y.

momentum in u_y which tends to bring them closer to the axis. Electrons injected on-axis are not impacted. The electrons that are off-axis in the x direction 5.15c,d display the expected ponderomotive behavior, as they gain a transverse momentum u_x that tends to push them away from the high intensity zones.

Even though this configuration is slightly different from the PIC simulations, where the initial transverse momentum was non-zero, this seems to reproduce quite well the phenomenon observed. This geometry was preferred for the study to highlight that it is indeed the position in the electric field that is associated to the gain in transverse momentum. We then verified that starting from electrons with a non-zero momentum lead indeed to a reduction of the momentum in the polarization direction.

The process leading to this gain of transverse momentum in the direction opposed to the ponderomotive force can be broken down in two separate steps, described in Figure 5.16. As mentioned earlier, the electric field of the tightly focused laser has not only a transverse component E_y but also a longitudinal one with $\max|E_z| \simeq 0.05 \max|E_y|$. As showed in Fig.5.16c, the longitudinal momentum of the electrons is modulated during the propagation in the laser by the Lorentz force $\dfrac{\mathrm{d}u_z}{\mathrm{d}t} = -e(E_z - v_y B_x)$. Here, this force is almost purely driven by the longitudinal electric field E_z. This modulation of u_z corresponds to a modulation of the velocity between $0.983c$ and $0.989c$. Additionally, E_z is anti-symmetric with respect to the axis, and so is the longitudinal modulation, therefore, when the velocity of the particles initialized with $y_0 > 0$ is maximum, it is minimum for electrons with $y_0 < 0$ (see Fig.5.16c). The magnetic field B_x is symmetric along the axis and therefore is the same for both populations. We remind the Lorentz force in the y direction: $\frac{\mathrm{d}u_y}{\mathrm{d}t} = -e(E_y + v_z B_x)$. It is plotted for both (+) and (-) in Figure 5.16d along with the magnetic field B_x. The drift in u_y can be understood qualitatively by considering the two times (1) and (2) of Figure 5.16d for the two cases (+) and (-), where wee see that the transverse force in (y) in the case (-) is shifted towards the top compared to the (+) case:

- In the (+) case, v_z is maximum when B_x is negative and therefore when $v_z B_x$ is negatively oriented (1), and minimum when B_x is positive (2) and thus when $v_z B_x$ is positively oriented. Therefore the two magnetic Lorentz forces do not compensate perfectly, and a drift towards $y < 0$ appears during the oscillations.
- In the (-) case, conversely, v_z is maximum when B_x is positive (2) and therefore when $v_z B_x$ is positively oriented, and minimum when B_x is negative (1) and thus when $v_z B_x$ is negatively oriented. Therefore a drift towards $y > 0$ appears during the oscillations.

Moreover, when integrating the force in (y) along the propagation, the final momentum of the electrons is obtained in both case.

This phenomenon will be observed only for moderately relativistic electrons ($u_z < 10$) for which changes in the longitudinal momentum induces significant variations in the velocity. Additionally, we can check if the CEP has an impact on the momentum acquired by the electrons through the laser. Figure 5.17 shows that the final transverse momentum is the same regardless of the laser CEP, which is not surprising, because changing the CEP does not modify the relative phase between the two fields responsible for the drift E_z and B_x, and the motion is integrate in time over the force. But note that the transverse momentum gain depends of the position in y, which can depend on CEP through the injection process.

We also note that this study focuses on a simplified case where the laser parameters remain constant through propagation, which is not the case in the PIC simulations, where the wavelength can depend on the position in the laser pulse, and the group velocity can vary during propagation, increasing towards c with the decreasing plasma density. Still, with the the test-particle simulations we were able to reproduce and shed light on this unexpected behavior.

Effect on an electron beam

We now look at the effect of this force on an electron beam with a gaussian distribution of transverse momentum. The longitudinal momentum is still $u_z = 6$, but now we simulate a beam of 50000 electrons with a initial gaussian spatial distribution of width $\sigma_{xy} = 0.2\,\mu\mathrm{m}$ and $\sigma_z = 3\,\mu\mathrm{m}$ in length. The beam has a gaussian distribution of momentum with transverse width of $\sigma_{ux}, \sigma_{uy} = 0.2$ and spread $\sigma_{uz} = 0.1$.

Figure 5.18 shows the evolution of the beam after the interaction with the laser. The counter-ponderomotive effect described previously reduces the beam divergence in the laser polarization direction. Indeed, electrons with initial positive transverse momentum end up on the positive y side, and therefore gain a negative momentum which reduces their divergence. In the perpendicular direction, the beam is scattered by the ponderomotive force and the beam divergence is increased. But now, if we look at the effect of a circularly polarized laser (a_0 = 2

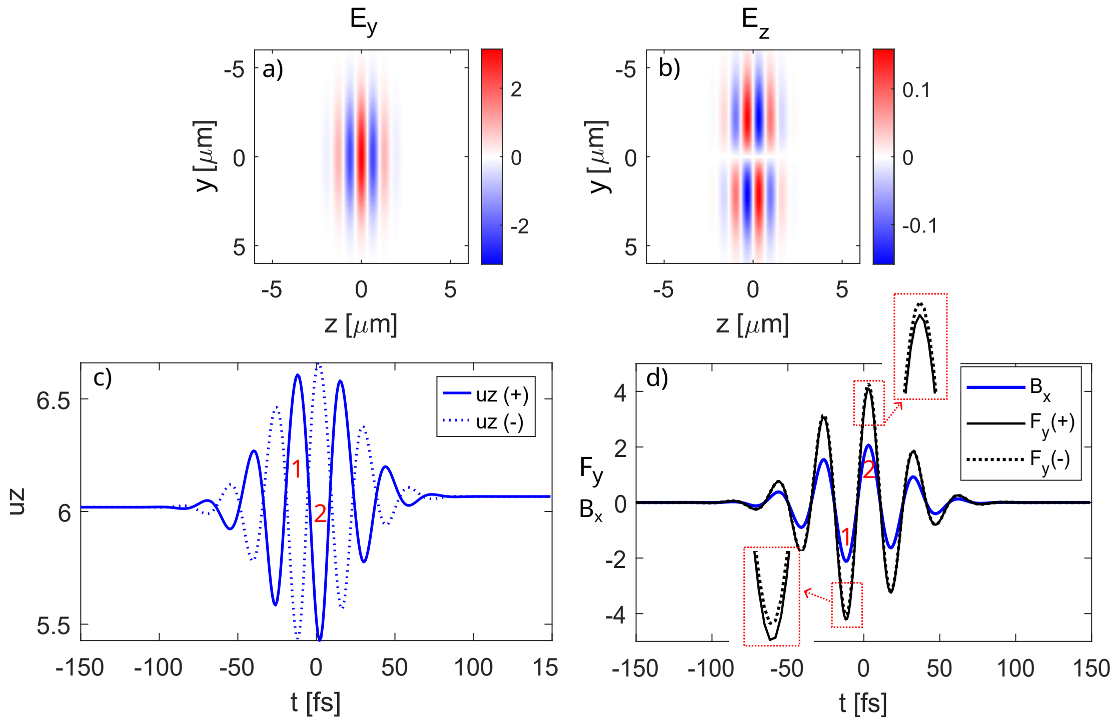

Figure 5.16 – *Test particle simulations.* a) Transverse and b) longitudinal electric field of the laser at focus. c) Longitudinal momentum of the electrons for the (+) case (solid) and for the (-) case (dotted). The oscillations are mainly due to the non-zero, anti-symmetric E_z field associated with the tightly focused pulse. d) Transverse force in y: $F_y = -E_y - v_z B_x$ for the (+) and (-) cases (black), as well as the magnetic field B_x (blue).

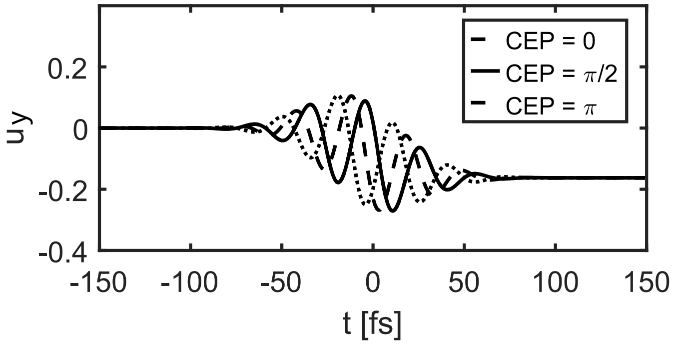

Figure 5.17 – *Test-particle simulations*. Transverse momentum in y of the electrons in the simulation for three different initial laser CEP.

too), the contraction of the beam occurs alternatively in each direction, in competition with the ponderomotive force, and the result is a beam with reduced divergence in both directions. At first glance, this phenomenon could be interesting as a tool to reduce the beam divergence, but apart from the very constraining conditions of its occurrence, Figure 5.18 also demonstrates that the interaction with the laser leads to an emittance growth, and therefore degrades the

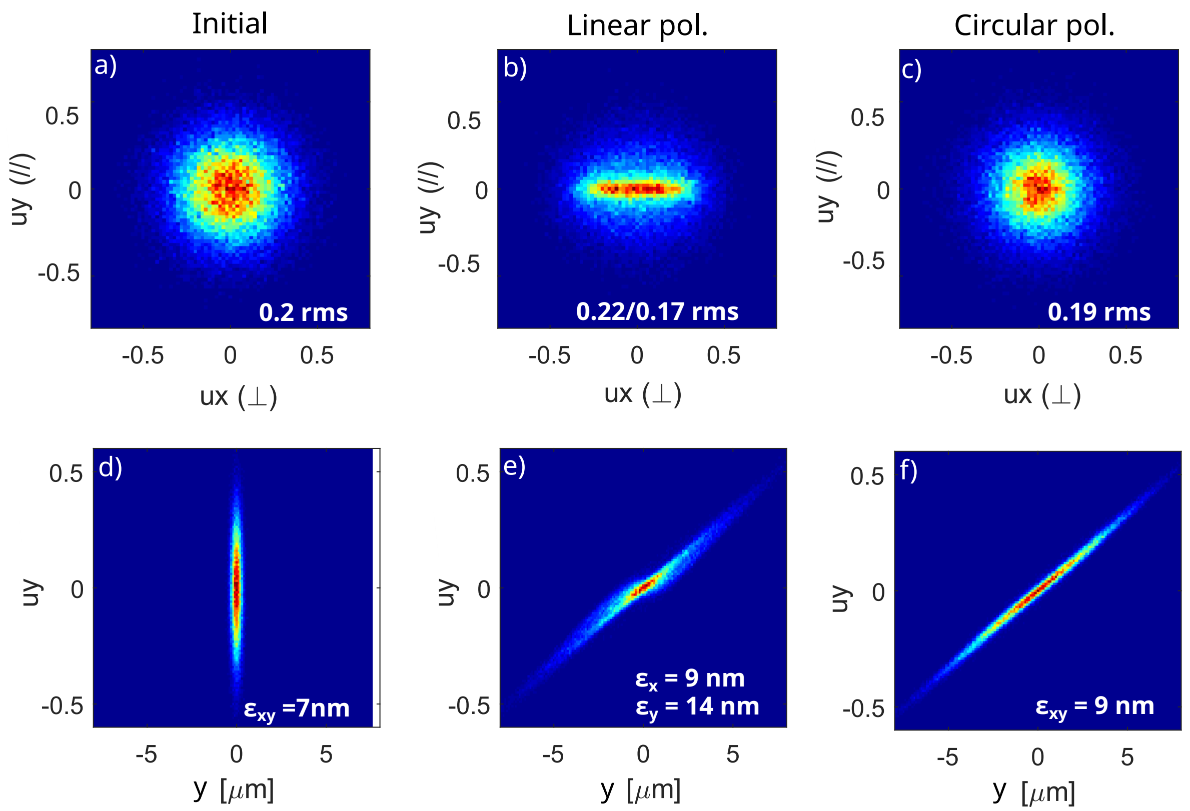

Figure 5.18 – *Test-particle simulations.* Distribution of transverse momenta of the electron beam a) before the interaction b) after crossing a linearly (y) polarized laser and c) after crossing a circularly polarized laser. d),e),f) show the electrons in (u_y-y) phase-space and their associated normalized emittances.

overall quality of the beam. Indeed, the normalized emittance is expressed as follow:

$$\epsilon_{n,y} = \sqrt{\langle y^2 \rangle \langle u_y^2 \rangle \; - \; \underbrace{\langle y \cdot u_y \rangle^2}_{\text{correlation term}}} \tag{5.8}$$

The first term corresponds to the spread in position and momentum, and the second, which is subtracted, corresponds to the correlation between position and momentum. The propagation of the beam in the laser field, by reducing the momentum of the electrons that are away from the axis, breaks the correlation and therefore increases the emittance.

To conclude this parenthesis, using test-particle simulations we have uncovered an unexpected effect that makes mildly relativistic electrons placed off-axis in the polarization direction gain momentum that bring them closer to the axis when overtaking the slower laser pulse. This phenomenon, opposed to the ponderomotive force, is due to the combined effect of the longitudinal electric field E_z modulating the velocity of the electrons and inducing a drift in the $v_z \times B_x$ force. But this requires very specific conditions to occur because if the electron energy is too low, they wont be able to overtake the laser, but if it is too high, their velocity will not change significantly. Moreover, the laser has to be slowed down sufficiently through strong redshift and high plasma density to be overtaken by the electrons before it diffracts away.

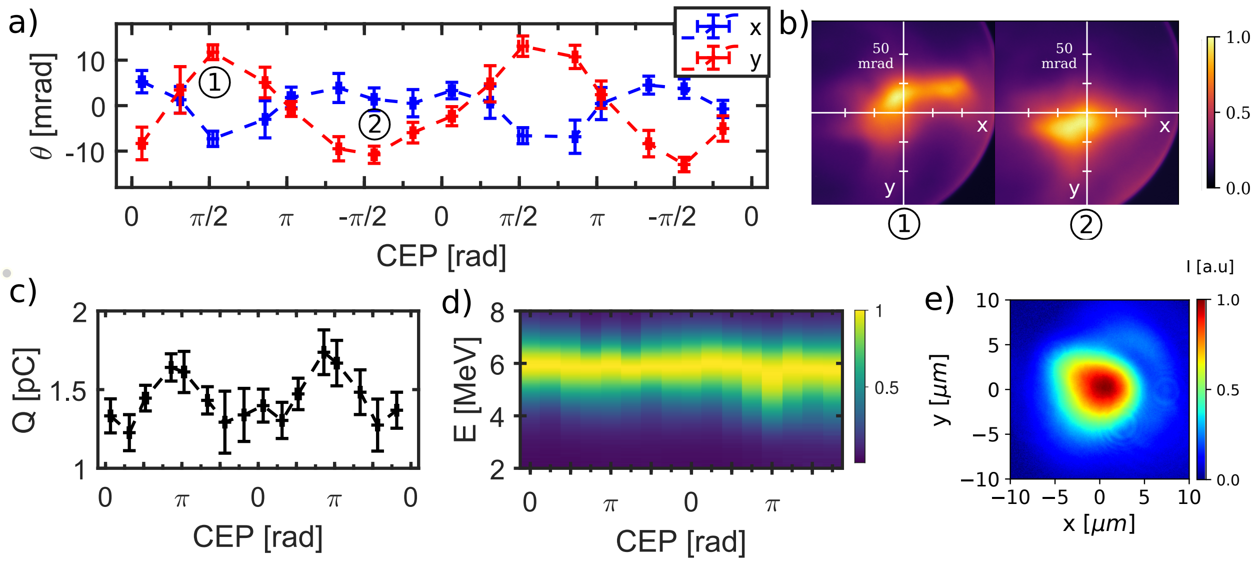

Figure 5.19 – CEP effects on the electron beam in helium with $P_{back} = 85$ bar, corresponding to a plasma density $n_e = 1.0 \times 10^{20}\,\mathrm{cm}^{-3}$ a) Electron beam pointing in both x (blue) and y (red) directions (laser polarization along y) plotted against CEP. b) Images of the beams corresponding to CEPs of $\pi/2$ and $-\pi/2$. c) Electron beam charge Q against the laser CEP d) Electron spectra against CEP. e) Laser focal spot in vacuum. The beam pointing, charge and spectra are estimated by averaging 20 measurements, each accumulating 100 consecutive shots. The errorbars correspond to the standard deviation on the 20 measurements.

5.2 CEP effects in Helium

Previous experimental results on CEP effects in N_2 relied on PIC simulations in order to determine the origin of the beam parameters variations, and exclude ionization injection as a leading mechanism. Additionally, these effects were observed in a regime were electrons were accelerated to moderate 1-2 MeV energies, quite far from the optimal operating mode of the accelerator. The implementation of the differential pumping system described in Section 2.4.3 enabled the use of a continuous flow of high pressure helium gas in the experiments, allowing us to verify if the effects observed in N_2 are also measured in a gas where ionization injection is impossible, therefore confirming that the interpretation from the simulations is correct. The results presented in this section were published in [174].

5.2.1 Experiments in He

The experiments are conducted in conditions similar to the previous section, but with an f/4 (f = 100 mm) off-axis parabola (the longer focal length is necessary for the differential pumping). The kilohertz laser with a final on-target energy of now 3.0 mJ per pulse and a duration of 4.0 fs, is focused to a 5 μm focal spot, reaching a vacuum peak intensity of $I = 1.9 \times 10^{18}\,\mathrm{W\,cm^{-2}}$. A supersonic helium gas jet, with a 60 μm throat and 180 μm exit diameter is used. During the experiments, the CEP is varied by increments of $\pi/4$, and the electron beam parameters are measured for each CEP value. We repeat the CEP loop two times. In order to achieve optimal performances, the waveplate was not used here, and therefore the laser polarization is vertical (y axis).

Figure 5.19 shows the experimental results of two CEP loops using helium with a backing pressure $P_{back} = 85\,\mathrm{bar}$ corresponding to a plasma density $n_e = 1.0 \times 10^{20}\,\mathrm{cm}^{-3}$. As anticipated, the electrons are accelerated to energies significantly higher than in N_2, with spectra peaked around 6 MeV (see Fig. 5.19d). The beam parameters exhibit a CEP-dependence that is similar to what was obtained in nitrogen, with the beam pointing oscillating in the polarization direction (y) with a large amplitude of 11 mrad, as shown in Fig. 5.19. A surprising observation is that, the beam pointing in the perpendicular direction also varies periodically with the CEP, but with a smaller amplitude (∼5 mrad). We also observe the horizontal appearance and disappearance of a smaller electron beam depending on the CEP value (on the left in Fig.5.19b①). This is surprising because theoretically the plasma asymmetry, and therefore the CEP-dependence, should only occur in the plane of polarization [28]. We explain this unexpected behavior by a coupling between the asymmetry in the polarization plane, and an asymmetry in the perpendicular plane due to an asymmetric focal spot, as can be seen in Fig. 5.19e. This is studied in more details with PIC simulations in section 5.2.3. Additionally, the beam charge varies by up to 30%, between 1.2 pC and 1.7 pC, due to CEP changes, while the energy spectrum remains unaffected (see Fig. 5.19c,d). These results confirm the explanation of the observed CEP effects being due to the off-axis injection of electrons caused by the bubble asymmetry, as ionization injection cannot occur at all in helium.

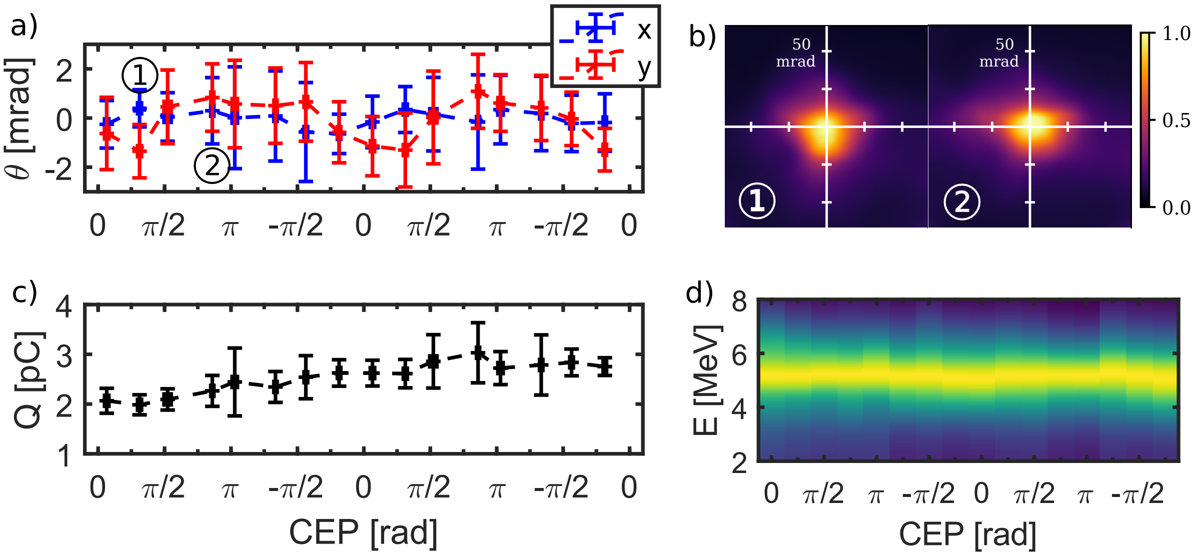

Figure 5.20 – Experimental results in helium with $P_{back} = 110$ bar, corresponding to a plasma density $n_e = 1.3 \times 10^{20}\,\mathrm{cm}^{-3}$. a) Electron beam pointing θ plotted against CEP. a) Beam profiles for two different CEP of $\pi/4$ and $3\pi/4$. Typical divergence is 40 mrad FWHM. c) Electron beam charge plotted against CEP. d) Spectra of the electrons plotted against CEP.

Now we increase the plasma density to $n_e = 1.3 \times 10^{20}\,\mathrm{cm}^{-3}$ by setting the backing pressure to $P_{back} = 110$ bar. Figure 5.20 shows the electron beam data for this density. It results in much smaller pointing variations of 1 mrad amplitude, while charge appears this time uncorrelated to CEP changes. This higher density case yields more charge per shot than the previous one, with charge slowly evolving from 2 pC/shot to 3 pC/shot during the scan, seemingly uncorrelated to CEP. The energy of the electrons is slightly lower, with a spectrum peaked at 5 MeV. Overall, it seems that an increased plasma density reduces the effects of carrier-envelope phase on the final electron beam. This is also reflected in the smaller electron beam distribution (~ 40 mrad fwhm). Indeed, if the injection process is less reliant on off-axis injection associated with CEP, electrons will be injected generally closer to the axis, leading to a smaller divergence. This can be explained by two factors. Firstly, increasing the plasma density also increases the dispersion in the plasma and therefore results in a smaller CEP slippage length $L_{2\pi}$. Moreover, a higher density leads to stronger self-focusing of the laser driving a higher amplitude plasma wave in which the time window where injection is possible is larger. So injection is less localized, resulting in an averaging of the effects of the CEP. Additionally, the increased amplitude of the plasma wave facilitates self-injection, making the trapping process less dependent on bubble oscillations (thus on CEP) to occur.

5.2.2 PIC simulations with an ideal gaussian laser pulse

Even though PIC simulations are not required to determine whether the CEP effects can be attributed to off-axis injection, or ionization injection because the latter cannot occur in pure helium, they can still be useful to check how the interaction in helium compares to the nitrogen case. Moreover, we will take advantage of these simulations to add an artificial test electron beam on axis to verify the importance of the initial off-axis position of the injected electrons in the final beam pointing and thus confirm that the pointing variations are mostly associated with the off-axis injection. The simulations of this section will again be performed using an idealized gaussian laser pulse, and they will serve as a basis for comparison when using an asymmetric laser spot in the next section.

In the simulations the mesh is $\Delta z = \lambda_0/48$, $\Delta r = 3\Delta z$, and five azimuthal Fourier modes are used. The simulation is initialized with neutral helium and ionization is computed with the Ammosov-Delone-Krainov model of tunnel ionization [43]. Helium is initialized with 256 neutral macro-particles per r-z cell, and each helium atom can produce 2 electrons after complete ionization. The plasma profile is a super-gaussian matching experimental measurements, with a peak plasma density $n_e = 1.35 \times 10^{20}\,\mathrm{cm}^{-3}$. The laser focus is positioned 10 µm before the peak density, and a positive chirp of $10\,\mathrm{fs}^2$ is used to pre-compensate the dispersion due to the propagation in the plasma. The energy per pulse is 2.8 mJ ($a_0 = 0.9$), which was slightly adjusted to better match experimental results. The laser is linearly polarized in the vertical (y) direction. The accelerated electron beam in our simulations has a charge of 3 pC, and an energy spectrum peaked around 7 MeV, matching quite well the experimental results.

These simulations show that the global interaction is quite similar to the nitrogen case, with a periodic off-axis injection triggered by the CEP-locked oscillations of the plasma bubble. Figure 5.22 shows the details of this interaction compared for two different initial CEPs. The quantities Δz and Γ_y are the same as defined in Section 5.1.3. Electrons are injected when the bubble is moving backward on one side, with the injection peaks occurring when Δz changes sign, corresponding to its maximum local slow down, but also to an extremum of the transverse asymmetry, as was observed in the nitrogen simulations. One clear difference is that we do not observe a two separate beam structure, but one single beam which moves upward and downward depending on the CEP value. This can be linked for example to Figure 5.22g showing that, for an initial CEP of 0, more injected electrons end up pointing upwards than downwards, resulting in a positive total beam pointing. This is because, as can be seen in Fig. 5.22c, a part of the electrons from the second injection, which occurs from the top and following the

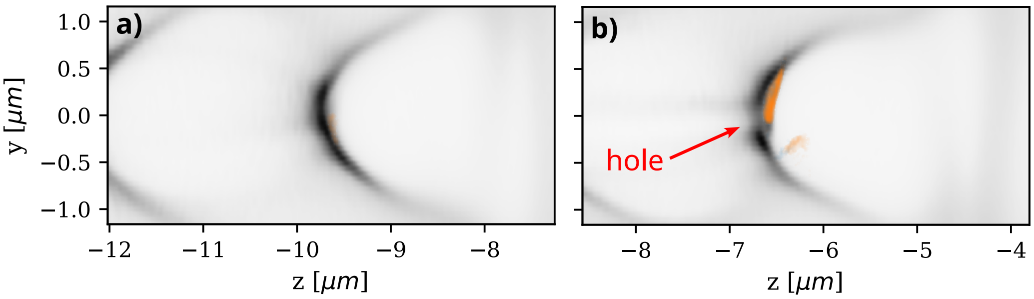

Figure 5.21 – *Illustration of the effect of the beamloading effect* . a) Wakefield before the injection of electrons. b) Wakefield after the injection of an electron bunch, showing a hole in the plasma wave.

same logic as earlier, should point downward, actually ends up with positive pointing. To explain this, we track two sub-bunches, injected at opposed transverse asymmetry values, during their propagation. The transverse and longitudinal momenta of the two bunches are plotted in Fig. 5.22e-f. The two bunches experience a similar trajectory, where they are injected with a non-zero transverse momentum, perform a single betatron oscillation before catching up with the laser and then oscillate in the laser electric field. Longitudinally, the electrons are accelerated over a distance of 13 µm and then keep an approximately stable longitudinal momentum for the rest of their propagation. Apart from the sign of their initial transverse momentum, related to their side of injection, what differentiates the two trajectories is the absolute value of P_y at injection, which is significantly higher in the case of the 'bunch +' (P_y = 0.58) than the 'bunch -' (P_y = -0.25) for an initial CEP of 0, leading to a similar difference in transverse momentum at the end of the simulation. This means that the 'bunch +' is pointing strongly upwards, while the 'bunch -' is almost centered, leading to a global positive beam pointing, and explaining why a part of the second injection ends up with a positive (orange) pointing. A similar reasoning can apply to the CEP = $\pi/2$ case. This difference in initial transverse momentum can be caused by the asymmetry of beam-loading effects. When an electron bunch is injected, its field perturbs the plasma wave and creates a hole in it, as showed in Figure 5.21. At the moment of injection of the 'bunch -', the previously injected electron bunch is now on the same side of the bubble after traveling upwards, and perturbs the plasma wave, leading to a reduced P_y at injection. One can notice this beam loading effect through the 'hole' in the plasma wave that can be seen in Fig 5.22a-b. This effect is more significant than in previous simulations in nitrogen, which could be associated to the lower plasma density which yields a lower peak density of the electron sheath that is more impacted by the injected bunch.

Scan in CEP and comparison to a test-beam injected on-axis

We then performed the same PIC simulations by changing the initial CEP between 0 and π, by increments of $\pi/4$. Because they are the perfect mirror of their π-shifted positive counterparts, negative CEP values were ignored. In order to validate the role of initial transverse momentum and position of injection of the bunches in their final beam pointing, an electron test-beam was injected on-axis with a zero P_y at the same time as the first real injection occurrence. The total charge of the test beam is chosen extremely low (1×10^{-30} C) so as not to interfere with the 'physical' electrons. The pointing of the physical beam in the simulations shows similar behavior as observed experimentally, with oscillations in the polarization direction when changing

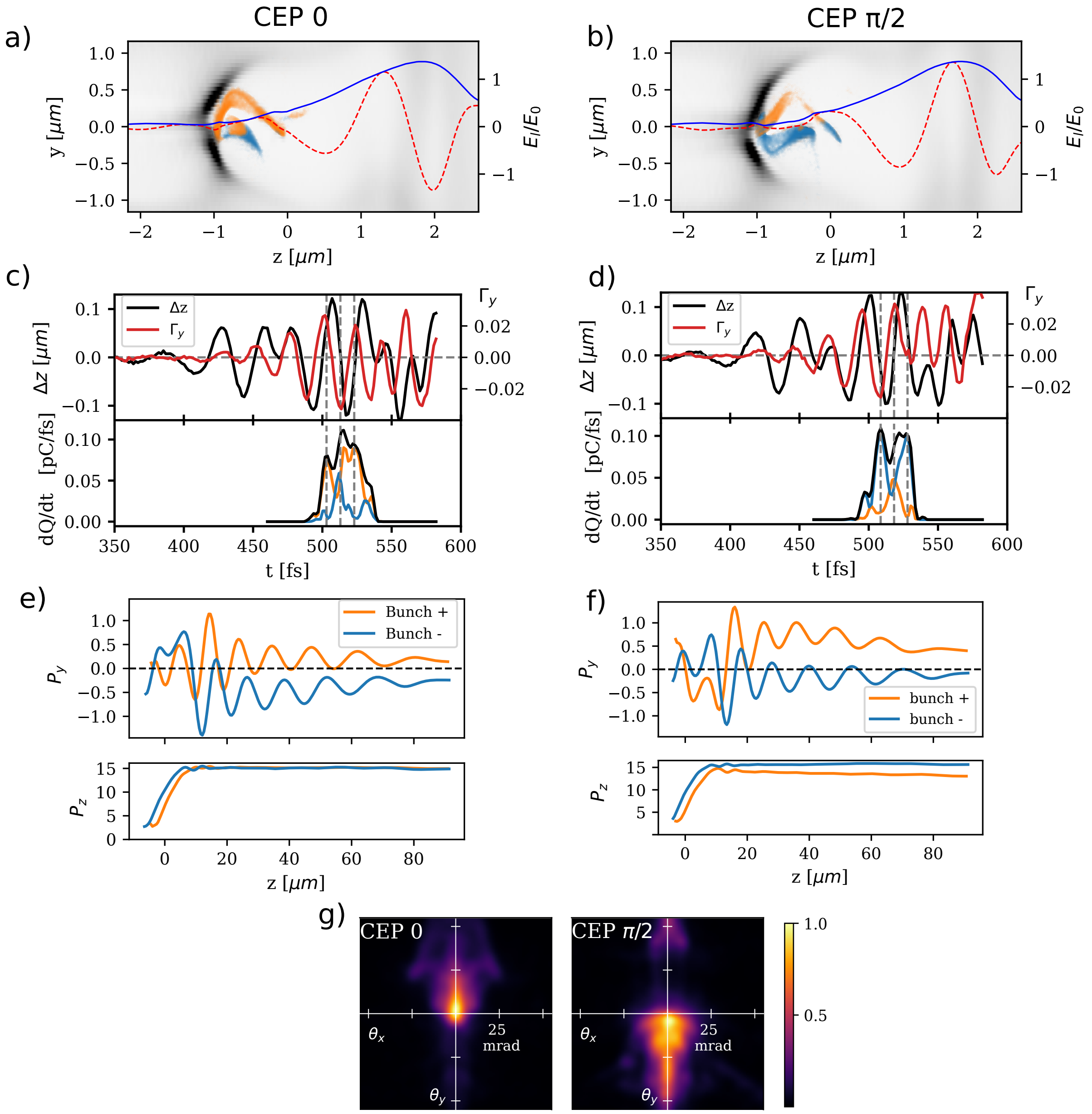

Figure 5.22 – Particle-in-cell simulation of a LPA driven by a 4.0 fs laser in a helium plasma. a)-b) Snapshot of the wakefield for a initial CEP of 0 and $\pi/2$, showing three different injected sub-bunches. Electron density in the z-y plane is shown in gray, and injected electrons are displayed in orange (blue) when their pointing is positive (negative) at the end of the simulation. The normalized laser electric field $E_l/E_0 = E_l/(m_e c\omega_0/e)$ (red) and its envelope (blue) are also shown. c)-d) Asymmetry of the wakefield in the y-direction Γ_y (red) and difference in the mean position of the bubble Δz between the top part (y>0) and the bottom part (y<0) of the wake (black). Charge injection rate for the two electron populations shown in a)-b) with corresponding colors, against the simulation time for an initial CEP of 0 and $\pi/2$. The gray dashed lines highlight the three main injection events. e)-f) Transverse (top) and longitudinal (bottom) momentum normalized to $m_e c$ as a function of propagation distance for two sub-bunches injected with a positive (bunch +) and negative (bunch -) initial transverse momentum, corresponding to opposite signs of Γ_y at the moment of injection. g) Output beams from simulations with initial CEP of 0 and $\pi/2$.

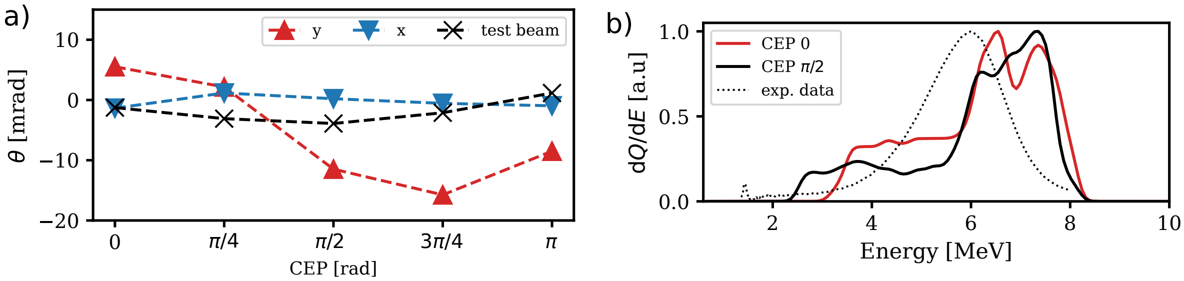

Figure 5.23 – a) Beam pointing in the simulations for different CEPs, in the y (polarization) direction (red triangles), in the x direction (blue triangles) and for the test-beam in the y-direction b) Spectra of the accelerated electrons in the simulations for two different CEPs (solid lines) compared to experimental spectrum (dotted).

the CEP, and a beam consistently centered in the perpendicular direction (see Fig. 5.23a). For the artificially injected test-beam, while a residual CEP-dependence of the beam pointing in the polarization direction to the CEP remains, it is of much lower (4 times) amplitude than for the physical beams. This clearly confirms once again that the pointing dependence on the CEP observed in the experiments can be attributed to the asymmetric injection, and not to the potential oscillations of the laser and plasma transverse fields during the accelerating process. Still, the residual pointing dependence observed on the test-beam can be explained by the fact that, due to the oscillating asymmetry of the bubble, they are not perfectly on its center when injected and therefore gain some transverse momentum.

The simulations also show only small variations in the electron spectra when changing the CEP, as presented in Fig. 5.23b, which is in accordance with the experimental results. The energy in the simulations is typically 1 MeV higher than experimentally measured, which can be explained by the idealized gaussian case used here, which tends to yield better performances, but still remains in good global agreement. The charge variation of 30% observed experimentally is not reproduced by these simulations, in which only a change in beam charge of the order of 5% is observed.

5.2.3 PIC simulations with an asymmetric laser spot

Beam pointing variations in the direction perpendicular to the laser polarization cannot be explained solely by an effect of the carrier-envelope phase. Indeed, the plasma wave asymmetry due to the near-single cycle pulse develops only in the polarization direction and leaves the perpendicular plane perfectly symmetric. Another source of asymmetry, coupled with CEP must therefore be responsible for this behaviour. We have remarked in section 5.2.1 that the laser focal spot corresponding to the experimental variations of θ_x with CEP is asymmetric in the horizontal direction, and therefore could be the source of this observation. To investigate this, we carried out PIC simulations in similar conditions as in Sec. 5.2.2, but now using the measured experimental laser spatial profile. The laser energy is slightly re-adjusted to 2.9 mJ. In these simulations, the accelerated charge is around 3.6 pC with energies in the range 5-7 MeV.

Firstly, these simulations reproduce the behavior observed in the experiment (see sec. 5.2.1) with the beam pointing varying in the polarization direction when changing the initial laser

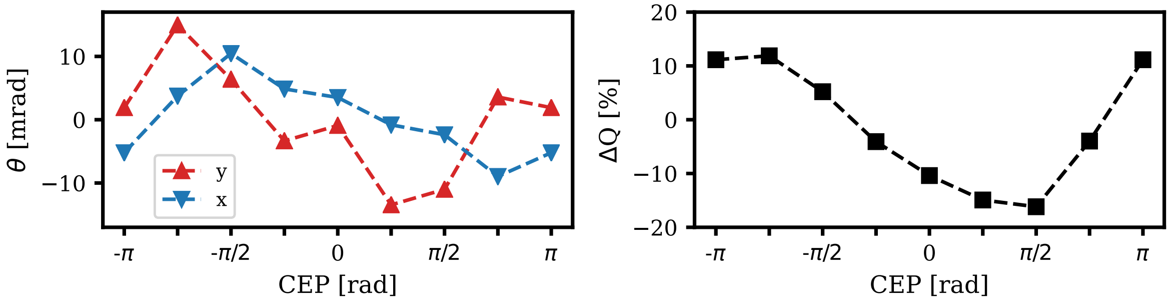

Figure 5.24 – a) Beam pointing in the simulations for different CEPs, in the y (polarization) direction (red triangles), in the x direction (blue triangles). b) Charge variation in the simulations plotted against the initial laser CEP. The mean charge ($\Delta Q = 0$) corresponds to Q = 3.6 pC.

CEP, as can be seen in Fig. 5.24a. Additionally we observe that the pointing in the other direction is also evolving but with a smaller amplitude. This is interesting, not only because it reproduces the experimental observations, but because it indicates a coupling mechanism between the asymmetry induced by the laser spot in the perpendicular direction, and the one induced by the different CEPs in the polarization direction. Moreover, this coupling seems to have a significant effect on injection, because it induces large variations on the injected charge with total variations up to 27% (see Fig. 5.24b).

In order to understand this coupling, we look at the geometry of the plasma wave and examine the dynamics of the electrons in the perpendicular plane (x,z). Contrarily to the gaussian laser case, here the plasma wave also presents asymmetries in the perpendicular plane. These asymmetries lead to off-axis injection and residual transverse momentum P_x for the injected electrons. Moreover, the bubble is a 3D structure, and these asymmetries vary depending on the positions in y at which the (x,z)-plane is observed. We have previously explained that the CEP-locked bubble oscillations lead to off-axis injection in the (y,z)-plane, on either positive or negative sides depending on the value of the CEP. Therefore, when injected on different sides of the y-axis depending on the CEP, the electrons will see a different asymmetry in the (x,z)-plane due to the asymmetric laser spot and obtain a different transverse momentum P_x, explaining how the pointing in the perpendicular direction can be correlated to CEP. Figure 5.25 highlights this effect by showing two (x,z) slices of the plasma bubble for different times corresponding to two successive injection events corresponding to opposed CEPs. The slices are taken at a position in y corresponding to the position of injection for each specific time. In the panel a) we observe a moderate upward asymmetry that will lead to injection of electrons with a low negative momentum $P_x < 0$, while in the panel b) the asymmetry is now leaning downwards and is much more pronounced, and results in off-axis injection of electrons with a positive transverse momentum $P_x > 0$ (see Fig.5.25c). This complex coupling can also be responsible for variations in the injected charge, with situations where electrons are injected at a position in y where the spot-induced asymmetry leads to a locally higher amplitude of the wave and thus higher charge than at the opposed position at which electron would be injected with a different CEP.

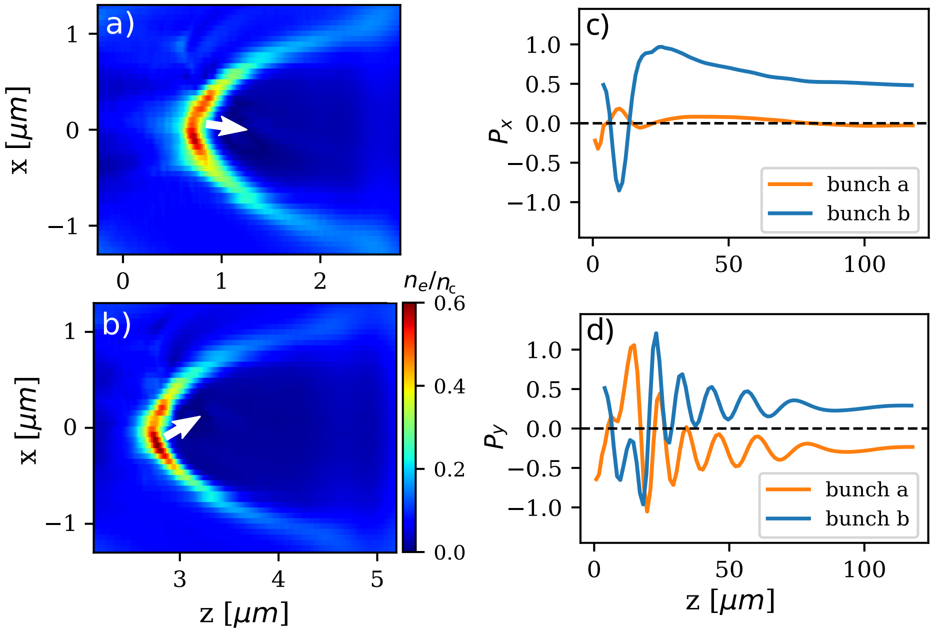

Figure 5.25 – Slices of the electron density of the wakefield in the (x,z)-plane (perpendicular to polarization) for two injection times corresponding to two opposite CEP values. Injection occurs therefore at two different positions y_1 and y_2 due to CEP-induced off-axis injection a) Slice for $y_1 = 0.2\mu m$ at a time where injection occurs from (y>0). b) Slice for $y_2 = -0.2\mu m$ at a time where injection occurs from (y<0). The two white arrows indicate the direction of injection of the electrons. c) Transverse momentum in the perpendicular direction P_x and (d) Transverse momentum in the polarization direction P_y for two beams injected at times corresponding to the panels (a) and (b).

5.2.4 Validation of the quasi-cylindrical geometry with full-3D PIC simulations

Most of the PIC simulations in this thesis were performed using FBPIC, which uses a spectral cylindrical representation, well suited to study problems with close-to-cylindrical symmetry. Even though our geometry is indeed quite close to a cylindrical symmetry, the very purpose of this work is to study in details how near-single cycle pulses induce a plasma response that deviates from this symmetry in the polarization plane. In this context, we made sure to use a sufficiently high number (5) of azimuthal Fourier modes in order to precisely model these asymmetries. Still, in order to validate this efficient approach to study CEP effects, we performed fully 3D PIC simulations with the code WarpX [180]. We reproduce the case of Section 5.2.2, in helium with a gaussian laser pulse. We use a 1024^3 cells simulation box, with a resolution $\Delta z = \lambda_0/34$ and $\Delta x = \Delta y = \lambda_0/19$. All the laser and plasma parameters are chosen identical to Section 5.2.2, but the initial laser position in the simulation is slightly different by a few microns, which does not affect the global laser propagation, but does change the value of the CEP at a given position for the same initial CEP due to dispersion. The principle of this section is therefore not to compare precisely CEP value by CEP value, but to verify that we retrieve (1) similar beam parameters (charge, spectrum, beam profile) and (2) similar asymmetric features and injection mechanisms to what was obtained with FBPIC.

Two 3D simulations were carried out, with initial CEP of 0 and $\pi/2$, with an accelerated charge of 2.7 pC and 2.8 pC (compared to 3 pC with FBPIC). The energy spectra is peaked betwteen

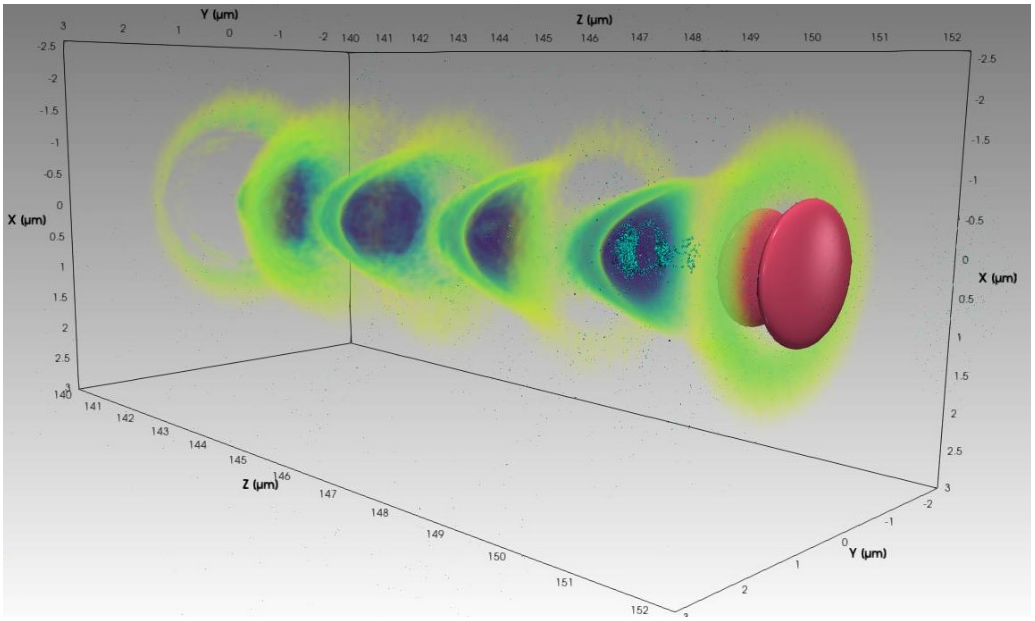

Figure 5.26 – Result of a 3D simulation. The plasma density is shown in a yellow (low) to blue (high) colormap. The laser intensity outline is shown in red.

6-8 MeV, with a lower energy tail, matching remarkably well the spectrum obtained in quasi-cylindrical simulations (see Fig. 5.27d). The beam shape is also globally similar, and the beam pointing evolves when changing the CEP: $\theta_y = -2.4$ mrad for a CEP of 0 and $\theta_y = 14.1$ mrad for a CEP of $\pi/2$. The beam pointings are different than for the same initial CEP in Section 5.2.2, because the CEP value at injection is different due to slightly different initial position of the laser pulse.

The panels (a) and (b) of Figure 5.27 show the wake and the injected electrons for the two cases with different initial CEP. In these 3D-simulations we find the exact same features of an asymmetric oscillating wakefield triggering periodic off-axis injection of several sub-bunches whose final pointing is associated to the asymmetry at the moment of injection. The plasma wave remains perfectly symmetric in the direction perpendicular to the polarization (not shown).

The correspondence between simulations carried out with the quasi-cylindrical code FBPIC and the fully 3D WarpX code is remarkably good. We are able to reproduce both integrated measurements such as charge and energy, while also observing the same asymmetric injection mechanism associated with CEP. This benchmark validates our use of FBPIC with 5 azimuthal Fourier modes for the study of CEP effects in laser-wakefield acceleration, allowing us to model the dynamics in 3D while benefiting from the fast-computing, cost-efficient quasi-cylindrical geometry.

5.3 Preliminary results on ionization injection in a helium-argon mixture

In the previous sections, the effects associated with the carrier-envelope phase were always associated with the oscillation of the transverse asymmetry of the plasma bubble. Yet, we have

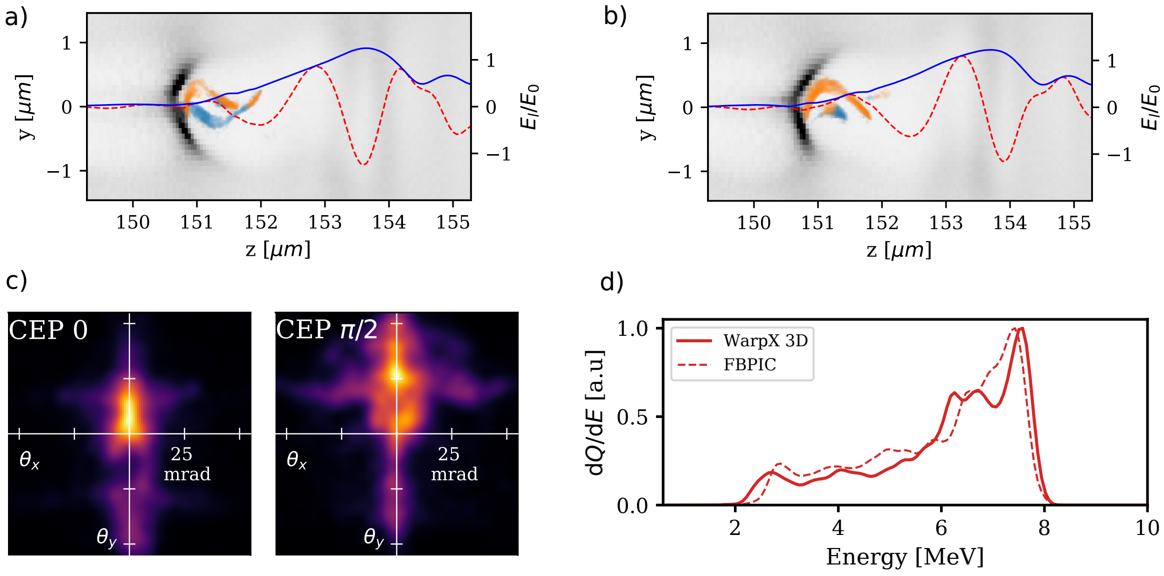

Figure 5.27 – 3D WarpX Particle-in-cell simulation of a LPA driven by a 4.0 fs laser in a helium plasma. a)-b) Snapshot of the wakefield for a initial CEP of 0 and $\pi/2$, showing three different injected sub-bunches. Electron density in the z-y plane is shown in gray, and injected electrons are displayed in orange (blue) when their pointing is positive (negative) at the end of the simulation. The normalized laser electric field $E_l/E_0 = E_l/(m_e c\omega_0/e)$ (red) and its envelope (blue) are also shown. c) Electron beams for the two different initial CEP. d) Comparison of the spectra in the 3D WarpX (CEP = 0) and quasi-cylindrical FBPIC (CEP = $\pi/2$) simulations. Initial CEPs were chosen so as to have the best match.

seen in Section 1.7 that another possibility for CEP to impact the dynamics of the accelerated electron beam is through ionization injection. However, after performing experiments in pure nitrogen, in which ionization injection is theoretically possible, we have concluded with the help of simulations that the laser intensity remained too low, and that this injection mechanism, and therefore the CEP effects associated with it remained marginal compared to self-injection. To circumvent this limitation, we first tried to perform experiments using a mixture of helium with 1% residual nitrogen in order to be able to achieve ionization injection by limiting the defocusing effect of pure nitrogen. But these experiments were not successful for the following reasons:

- When using higher plasma densities (similar to the densities used in previous section), the measured accelerated electron beam parameters were quasi-identical to the ones obtained in the pure helium case with matched density, indicating that self-injection was still the dominating mechanism, or at least that its impact was significant. This is also due to the fact that considering the high plasma density used in our experiment, ionization defocusing in helium might still be detrimental to the laser intensity which does not exceed the barrier-suppression level of nitrogen K-shell electrons.
- The alternative is to decrease the plasma density up to a point where self-injection cannot occur anymore, in order to isolate ionization injection, but in this case, the plasma density is too low to support the laser self-focusing, and therefore its intensity remain under the barrier-suppression ionization threshold, and no electrons are injected.

Isolating the ionization injection regime in a He/N_2 mixture with great confidence would require to be able to reach higher peak intensity without relying on the high plasma density necessary to achieve strong self-focusing, for example by increasing the laser energy. Alternatively, substituting helium with hydrogen would further decrease ionization defocusing. Another solution would be to decrease the high-Z atoms ionization levels to a point where the intensity achieved in our experiment is sufficient for ionization injection to massively occur. This is possible, by switching from using nitrogen to using argon in the mixture. The Table 5.2 compares the different ionization levels and associated barrier-suppression intensity for nitrogen and argon gas. It shows that argon has several ionization levels in the intensity range 1-5$\times 10^{18}$ W.cm^{-2} that can be used to trigger ionization injection in our typical experimental regime.

		1^+	2^+	3^+	4^+	5^+	6^+
N_2	E_i (eV) I_{bs} (W cm^{-2})	14.5 1.7×10^{14}	29.6 7.7×10^{14}	47.4 2.3×10^{15}	77.5 9.0×10^{15}	97.9 1.5×10^{16}	552.1 $\mathbf{1.0 \times 10^{19}}$
		7^+					
	E_i (eV) I_{bs} (W cm^{-2})	667.0 $\mathbf{1.6 \times 10^{19}}$					

		1^+	2^+	3^+	4^+	5^+	6^+
Ar	E_i (eV) I_{bs} (W cm^{-2})	15.8 2.5×10^{14}	27.6 5.8×10^{14}	40.7 1.2×10^{15}	59.8 3.2×10^{15}	75.0 5.1×10^{15}	91.0 7.6×10^{15}
		7^+	8^+	9^+	10^+	11^+	12^+
	E_i (eV) I_{bs} (W cm^{-2})	124.3 1.9×10^{16}	143.5 2.7×10^{16}	422.5 $\mathbf{1.6 \times 10^{18}}$	478.7 $\mathbf{2.1 \times 10^{18}}$	539.0 $\mathbf{2.8 \times 10^{18}}$	618.3 $\mathbf{4.1 \times 10^{18}}$

Table 5.2 – Ionization energies and corresponding barrier-suppression intensities for nitrogen and argon. Intensities potentially relevant for ionization injection are shown in bold. The ionization energies are from [44].

5.3.1 Experimental results

The experiment is carried out in the same conditions as the previous results in helium. We use a gas mixture with 99% helium, and 1% of argon in volume, with a backing pressure $P_{back} = 80\,\text{bar}$ corresponding to a plasma density $n_e \simeq 9.7 \times 10^{19}\,\text{cm}^{-3}$ after full ionization of helium and ionization of the eight first levels of argon. The laser polarization is vertical (along the y axis). Figure 5.28 summarizes the evolution of the electron beam parameters when varying the CEP. The beam structure is quite complex with different sub-beams horizontally creating an elongated structure in the direction perpendicular to the polarization (see Fig. 5.28b), which is counter-intuitive, especially in the case of ionization injection. The beam pointing varies in both directions and is correlated with CEP (see Fig. 5.28a). This can probably be attributed to a complex dynamics occurring due to couplings between different sources of asymmetry. The charge seems also correlated with CEP, even though additional random variations tends to mask the effect, but Figure 5.28d shows a clear difference with previous cases in pure helium or nitrogen, the measured energy spectrum varies significantly, with two distinct peaks, at 3 MeV and 4.5 MeV whose relative importance reverses when changing the CEP from to 0 π (see Fig. 5.28d). Note that here, the line of sampling pinholes of the spectrometer enables the measurement of the spectrum regardless of the variation of beam pointing in x, but gives only a local information at a fixed point in the y direction. This large variation of 50% of the peak energy indicates that the mechanism involving the CEP is probably different from the one in the previous section. In the work of Lifshitz *et al.* [84] where the effect of carrier-envelope phase on ionization injection is investigated through numerical simulations, the authors observe a correlation of the transverse direction of the electrons in the polarization direction, with their energy, associated with a different position of injection and E field sign at ionization. When the initial laser CEP is shifted by π, this direction is reversed, which could explain our experimental observation.

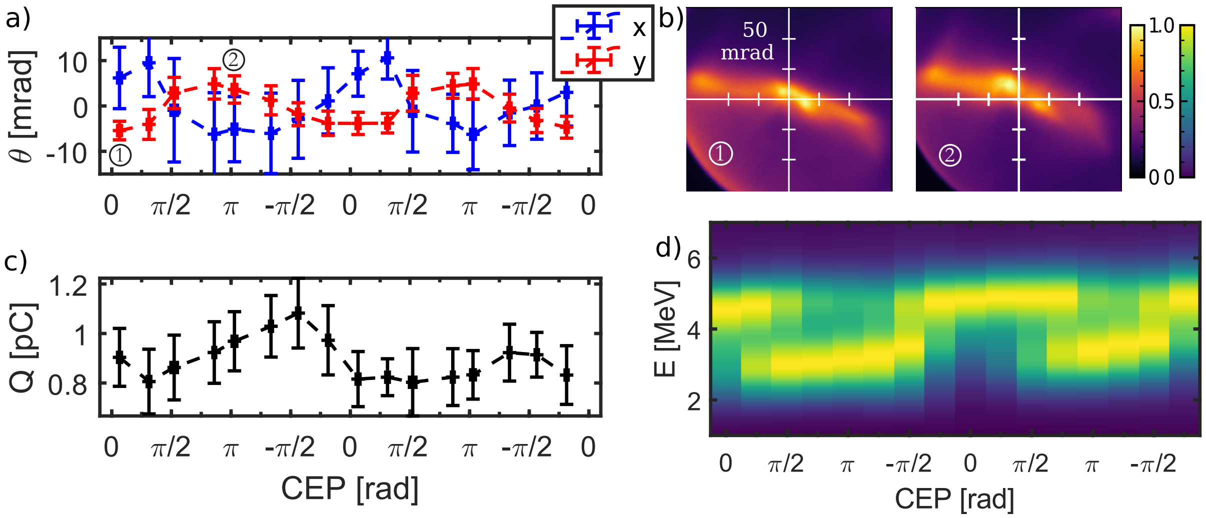

Figure 5.28 – Experimental results in a helium/argon mixture with $P_{back} = 80$ bar, corresponding to a plasma density $n_e = 9.7 \times 10^{19}$ cm^{-3}. a) Electron beam pointing θ plotted against CEP. a) Beam profiles for two different CEP of 0 and π, accumulated on 30 consecutive shots c) Electron beam charge plotted against CEP. d) Electron spectra plotted against CEP. Each point in pointing and charge corresponds to 20 measurements accumulating 30 consecutive shots (600 shots per point), the spectra are averaged on 20 measurements, each accumulating 300 shots (6000 shots per spectrum).

5.3.2 PIC simulation

We perform PIC simulations to verify that electrons are indeed injected via ionization, and to understand the behavior of the energy variations with CEP observed in the experiment. We use the experimental laser spot, and laser parameters matching the experiment to approach as closely as possible the intensity in the experiment, which is of paramount importance in the context of ionization injection. The plasma density is chosen to be $n_e = 1.1 \times 10^{20}$ cm^{-3}, and the simulation is initialized with 99% of neutral helium and 1% of neutral argon atoms. At the end of the simulation, a charge of 1 pC has been injected, matching very well the experiment. These electrons come exclusively from ionization levels Ar^{9+} and higher, indicating that ionization injection is the sole trapping mechanism at play. The beams are elongated in the polarization direction (see Fig. 5.29a) due to the residual transverse momentum associated with the value and sign of the ionizing electric field. The total beam pointing in the polarization direction is $\theta_y = -0.8$ mrad in the $-\pi/2$ case and $\theta_y = -5.7$ mrad in the $+\pi/2$ case. The beam are not perfectly centered in the perpendicular (x) direction because of the asymmetry of the experimental focal spot used in the simulation.

If we now look at the energy the electrons for two different cases with an initial CEP of $-\pi/2$ and $+\pi/2$ (the π-shift in CEP corresponding to a shift between the maximum and minimum energy case in the experiment), we remark in Figure 5.29b that when considering the spectrum integrated on the full beam, the two cases yield almost the same spectrum with a main peak at 4 MeV and and smaller one around 6 MeV. This is not surprising because, shifting the CEP by π results in the symmetric case, where the extrema of the electric field, and therefore ionization injection, occur at the same position but with opposed E value. Electrons injected at the same position will see the same accelerating fields and will end up with the same final energy. But in the experiment, the energy spectrum is not measured on the whole beam, but only at a specific position in (y) in the beam, and not necessarily perfectly centered. Figure 5.29c shows what happens to the energy spectra of the accelerated electrons when only the upper part (y>0) of the beam is measured. For the $-\pi/2$ case, there remains only the 4 MeV peak, while the main peak in the $\pi/2$ case is now the one at 6 MeV. The energy of the electrons is correlated to their time of injection: the higher energy electrons are injected first. But at some point the injected charge becomes sufficiently high to induce beamloading and reduce the bubble accelerating field and therefore the newly injected electron energy. In the meantime, the CEP has shifted, and thus the value of the electric field of the main ionization peak changed sign, leading to an opposite transverse momentum of the electrons. This clear dependence of the energy on the time of injection was not present in previous cases. Indeed, the plasma density is lower than in previous cases, leading to weaker self-focusing, and thus lower laser intensity. The plasma wave driven by the pulse is therefore weaker (possible because we do not rely on self-injection) and more strongly impacted by beamloading. Additionally, bunches injected via ionization all propagates close to the axis, leading to a stronger cumulative beamloading effect on the on-axis accelerating field than in the case where the electrons are injected off-axis.

This effect seems to explain quite well the behavior observed experimentally with a 2-peak spectrum whose relative amplitude shifts when changing the CEP from 0 to π. The fact that the absolute CEP values for these two energy extrema cases are different between the experiment and the simulations does not hold any meaning, because, as explained in Sec. 2.1.5, our experimental measurement does not allow to retrieve the absolute value of the CEP, but is only a relative measurement. Moreover, even if the initial CEP value were perfectly known, because it slips many times during propagation due to dispersion, even a slight difference in plasma density between simulations and experiment could yield different absolute CEP values at injection.

These results are important because they constitute the first clear experimental observation of a controlled effect of carrier-envelope phase on ionization injection in a LPA. But due several limitations and uncertainties of the experiment, they remain more of preliminary results that require to be confirmed and extended. Indeed, the beam constituted of several sub-beams horizontally does not corresponds to the elongated vertical shape typically expected for ionization injection. This could be associated with effects of transverse asymmetry evolving during propagation, leading to different beam pointing in (x) depending on the time of injection (also suggested by the observed pointing variations in (x) with CEP). A clear effect of the energy spectrum has been observed, but the sampling geometry of the spectrometer does not enable

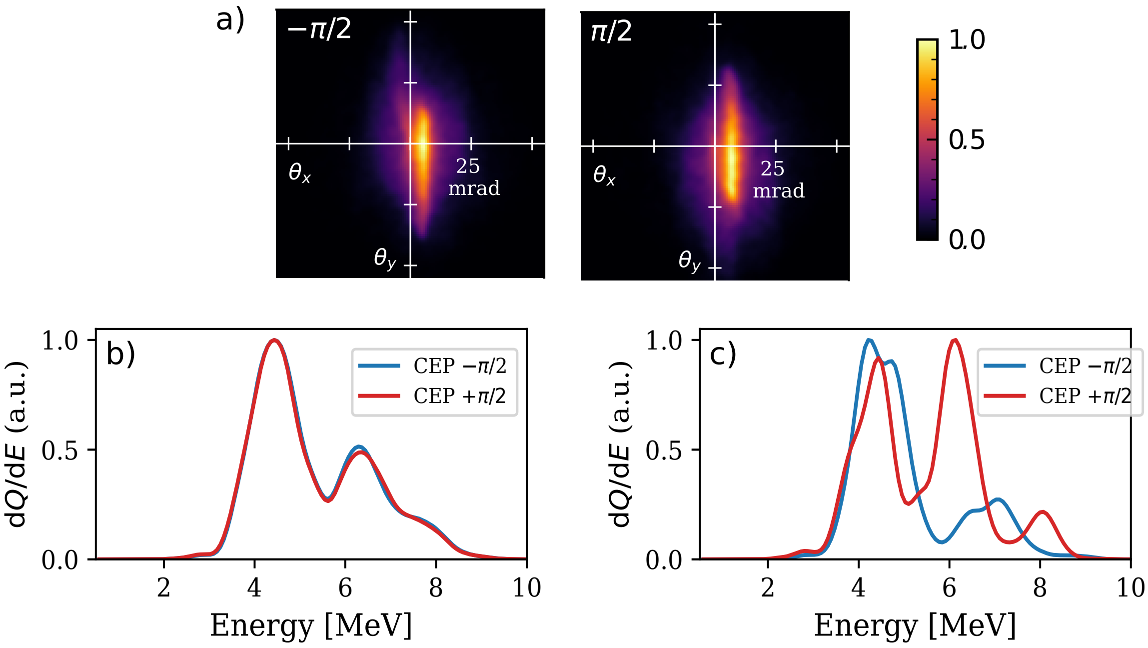

Figure 5.29 – Results of PIC simulations in a He/Ar mixture. a) Spectra of the full beam for an initial laser CEP of $-\pi/2$ and $+\pi/2$. b) Normalized spectra of the (y>0) part of the beam for two initial CEP of $-\pi/2$ and $+\pi/2$.

to decipher global energy variations from energy changes associated with different beam pointing related to the value of the ionizing electric field. Having a slit in the magnetic spectrometer, aligned with the laser polarization would gives us more information. Finally, while a helium/argon mixture ensures that we reach the ionization injection regime, its ionization levels between moderately relativistic intensities $I_{bs} = 1 \times 10^{18}\,\mathrm{W\,cm^{-2}}$ and $I_{bs} = 3 \times 10^{18}\,\mathrm{W\,cm^{-2}}$ make injection possible during an extended period, reducing the higher quality beam achievable by more localized injection, and possibly averaging out some CEP effects by injecting during several slippage lengths. Using a H_2/N_2 mixture could permit to reach sufficiently high intensities to ionize K-shell electrons of nitrogen by reducing ionization defocusing to a minimum, and could produce high quality, CEP-tunable electrons beams.

Conclusion

To conclude, we have demonstrated that the output beam of a laser-plasma accelerator driven by a near-single cycle pulse are impacted by the laser carrier-envelope phase. Two main sources for theses effects can be identified and were experimentally studied in this work:

- The transverse oscillation of the asymmetry of the wakefield associated with near-single cycle pulses can trigger periodic off-axis injection of bunches whose final pointing depends on the value of the asymmetry at the moment of injection. We have observed experimentally that this effect leads principally to a variation of the electron beam pointing in the polarization direction, but also to significant change in the injected charge in some

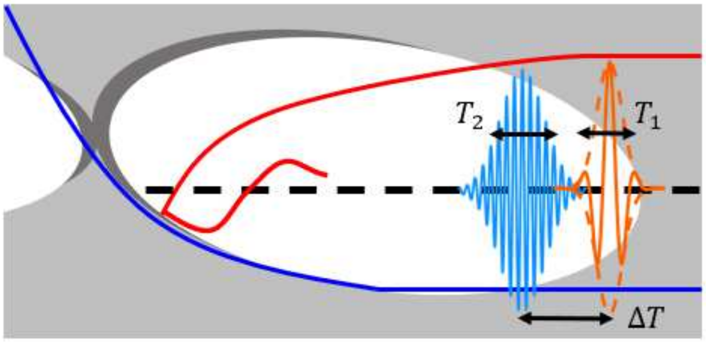

Figure 5.30 – Schematic of the proposition of Kim *et al.* extracted from [175], where a wakefield is driven by a multi-cycle, high energy pulse, while off-axis injection is triggered by a single-cycle, tightly focused, low-energy pulse.

cases. These observations demonstrate the breakdown of the ponderomotive approximation for near-single cycle pulses, and show the importance of considering the actual shape of the electric field in this case. Simulations indicate that this CEP-locked injection mechanism can lead to sub-femtosecond, ultra-low emittance sub-bunches that perform collective betatron oscillations and that could therefore be of particular interest for X-ray betatron radiation sources, though this source would not be very efficient, because the electrons perform only a single oscillation. But it was recently proposed to use a single-cycle pulse as an injector in combination with a longer pulse to subsequently drive the wakefield and accelerate the electrons to high energy [175], as represented in Figure 5.30.

— Ionization injection leads to the injection of electrons from the extrema of the laser electric field, and is therefore sensitive to the CEP. We have been able to observe preliminary experimental results of CEP effects on ionization injection using a He/Ar mixture indicating an energy dependence on the direction of the beam in the polarization plane. If a more thorough control was achieved, the CEP of a single-cycle pulse could be used in order to finely control the position of injection of electrons, for example in an accelerator driven by a particle beam (PWFA).

This work provides an experimental and numerical study of both regimes of CEP effects, but additional questions remain to address. It has been observed numerically in [78] that gradient injection reduces the impact of the carrier-envelope phase on injection, this is interesting in the context of minimizing the negative effects associated with the off-axis injection due to the transverse oscillation of the bubble, and would require experimental demonstration. In a similar way, it has been observed in [150] that using a laser with circular polarization reduces the final beam divergence by minimizing the transverse oscillations associated with CEP. Our setup with stabilized and controlled CEP would allow to quantify more precisely this effect, but achieving a clean circular polarization remains a challenge. Finally, a more detailed study of CEP effects in the context of ionization injection would be relevant. Our main limitation for this was that the laser intensities we are able to reach with our setup are at the limit of what is necessary to ionize K-shell electrons of nitrogen. Using a H_2/N_2 mixture might help to alleviate this constraint by reducing ionization defocusing to a minimum.

Conclusions and perspectives

Summary of the results

In the work presented in this thesis, we have studied kilohertz repetition rate laser-wakefield acceleration driven by few-mJ, near-single cycle pulses. It followed anterior experimental developments during previous thesis [35, 149] that led to the production of relativistic few MeV, few pC electron beams at a kilohertz repetition rate.

By performing an extensive scan in pulse duration and plasma density, we determined the optimal regime of operation of our LPA to achieve the best quality electron beams. This is done by using short sub-4 fs pulses ensuring sufficient laser intensity, and moderate plasma density $n_e \sim 10^{20}\mathrm{cm}^{-3}$ to approach resonance with the plasma wave while achieving self-focusing of the pulse. We have also taken the experiment to a new stage of exploitation by stabilizing and rationalizing the injection process by using newly designed one-sided shock nozzles that facilitate electron trapping via injection in a downward density transition. Indeed, we have demonstrated a 5h-long continuous, hands-off operation of our accelerator accumulating a record of more than 18 million consecutive shots, and good repeatability of the electron beam from one day to another. This newly acquired long-term stability allowed us to perform the first application experiment in radiobiology with our accelerator, where we demonstrated our capacity to irradiate biological samples with a controlled dose. We significantly increased the maximum energy of the electrons with spectra now peaked at 8 MeV, and beam divergence as low as 3 mrad, by implementing a differential pumping system that enabled the use of helium gas instead of nitrogen for the plasma, thus reducing the detrimental effect of ionization defocusing.

Secondly, we demonstrated and controlled the effects of the carrier-envelope phase of the laser pulse on the electron beam parameters, mainly through the observation of variation in the electron beam pointing when changing the CEP, but also significant charge fluctuations of up to 30% in some cases. By carrying out PIC simulations, we attributed these effects to the transverse oscillations of the wakefield in the polarization direction associated with the slippage of the CEP. These oscillations trigger periodic off-axis injection of several low-emittance, sub-femtosecond bunches of electrons that perform collective betatron oscillations. These experimental observations are significant from a fundamental point of view as they demonstrate the breakdown of the ponderomotive force for near-single cycle pulses and the appearance of an asymmetric response of the plasma to the electric field. Finally, we observed preliminary results of CEP variations in the angular dependence of the energy in the case of ionization injection using a helium and argon mixture.

Perspectives

The dramatic improvement of performances achieved by using a lighter gas calls naturally to continue on this path: using hydrogen gas instead of helium should enable to exceed the 10 MeV limit, as showed by the results achieved by a team of the University of Maryland where they accelerated electrons up to 15 MeV with few-mJ, near-single cycle pulses in a hydrogen plasma [150]. Our experimental set-up has been modified in order to be able to use high pressure, continuous flows of hydrogen safely, and experiments in hydrogen should be carried out in a very near future. Additionally, we observed that even if remarkable single shot performances can be achieved with very collimated few-mrad, few-pC beams, strong shot-to-shot fluctuations lead to larger beam divergences when accumulating on several shots while a beam is not necessarily detected on every shot. A possible explanation for these strong fluctuations could be the important transverse gradients existing in our micrometric-scale targets, and a transversely elongated slit-like geometry should be considered to limit these.

Ionization injection in a helium-argon mixture also proved to yield quite stable electron beams, that could be interesting for applications, but the several moderate intensity levels of argon between 1-4$\times10^{18}$W/cm^2 make ionization injection hard to localize and control, as electron are injected long before the laser reaches its peak intensity. Achieving ionization injection with nitrogen ($I_{bs} = 1.0 \times 10^{19}\,\mathrm{W\,cm^{-2}}$) proved to be difficult on our experiment due to the limited available intensity. By looking at less conventionally used atoms for ionization injection, we remark that carbon has two ionization levels in an intermediate range that could be interesting to trigger ionization injection in our experiment: $I_{bs} = 3.8 \times 10^{18}\,\mathrm{W\,cm^{-2}}$ for ionization into C^{5+} and $I_{bs} = 6.4 \times 10^{18}\,\mathrm{W\,cm^{-2}}$ for ionization into C^{6+}. This matches better the typical peak intensity reached in our experiments than for argon or nitrogen. It would thus be interesting to experiment a mixture of helium with a few percents of methane (CH4) or carbon dioxide (CO_2) to achieve controlled ionization injection. This would also allow to study more precisely the effects of carrier-envelope phase on ionization injection, to confirm the preliminary results observed in section 5.3, and achieve even finer control on the injection process. Using a slit instead of a pinhole array for the spectrometer, and turning the polarization in the direction of the slit would also permit to capture angular information on the spectrum associated with CEP effects.

In addition, we demonstrated a sufficient long-term stability for applications, and further radiobiology experiments should be carried out in the future years with the accelerator, notably investigating the effect of temporal fractionning of the dose. The first experiment tackling electron diffraction should also be carried out in a near future, starting by the re-focusing of the electron beam and the measurement of its emittance. With electron energies higher than 10 MeV, an X-ray source via Compton scattering becomes feasible. But this goal requires developing targets capable of supporting a high-repetition rate all-optical Compton source, such as gas plasma mirrors or liquid jets, or having a second intense laser pulse reaching $a_0 \sim 1$ available.

On a longer term, using two different laser beams, the transverse oscillations of the plasma bubble with the shifting of the CEP of a single-cycle pulse could be used to trigger injection of ultra-low emittance, sub-femtosecond bunches of electrons. These electrons could be then accelerated to high energy by a second longer and more energetic driver pulse as proposed in

[83]. This kind of injector would be interesting to generate high-brilliance X-rays via Betratron radiation thanks to the collective oscillation of the electrons following their off-axis position of injection.

Finally, high repetition rate LWFA will most probably progress in a near future with laser development and more energetic high repetition rate sources appearing. For instance, SYLOS 2 at ELI-ALPS provides 6 fs pulses with >30 mJ of energy, and the future LAPLACE-HC platform at LOA will be dedicated to laser-wakefield acceleration at 100 Hz with 20 fs, 300 mJ laser pulses to be upgraded up to 1 J [181]. These would allow to accelerate electron beams to several tens or hundreds of MeV at high repetition rate and provide appealing sources for applications.

Appendix A

Study of a potential all-optical kilohertz Compton source

In this appendix, we present the numerical study that was carried out to determine the feasibility of a single beam, all-optical Compton source operating at a kilohertz repetition rate using our experimental setup and the Salle Noire 2.0 laser system.

To produce X-rays via Compton scattering, a relativistic electron beam is collided with an intense counter-propagating laser pulse. The electrons oscillate in the laser field and radiate at a double Doppler shifted frequency. The resulting frequency of the scattered photons, assuming no angle between the electron and laser beam is [182, 183]:

$$\omega_c = \frac{4\gamma^2}{1 + \frac{a_0^2}{2} + \gamma^2\theta^2}\omega_0 \tag{A.1}$$

Where γ is the Lorentz factor of the electron, ω_0 the pulsation, a_0 the local normalized potential of the laser pulse, and θ the angle of emission of the photons. For electrons at 10 MeV, a laser wavelength of $\lambda_0 = 800\,\text{nm}$, and $a_0 = 1$, this yields scattered photons with a 2 keV energy on axis, and 7 keV at 20 MeV.

An X-ray Compton source requires the spatio-temporal superposition of a relativistic electron beam with an intense laser pulse [184, 185], and therefore laser-wakefield accelerators seem like good candidate to produce such sources. Usually, this scheme requires two separate laser beams, to drive the LWFA and scatter on the accelerated electrons [186, 187]. But in 2012, a team in LOA managed to generate gamma rays by using using the Compton Back-scattering scheme with a single beam from a 30 TW laser driving a LWFA [188]. The laser driving the plasma wave and accelerating the electrons was reflected using a solid thin foil, which was ionized by the front of the pulse and turned into a plasma mirror. The reflected pulse then interacted with the electron beam that was accelerated in its wakes and generated X-rays via Compton scattering. The principle of this scheme is illustrated in figure A.1.

But solid targets are not well suited for high-repetition rate experiments, as the surface is damaged on every shot so the target has to be moved, while it produces a large quantity of debris that can pollute the optics of the laser system. Adapting this single beam scheme to our kilohertz repetition rate laser (or even the 100 Hz laser system of the future LAPLACE-HC platform) will thus require to develop targets with over-critical densities and sharp gradients that

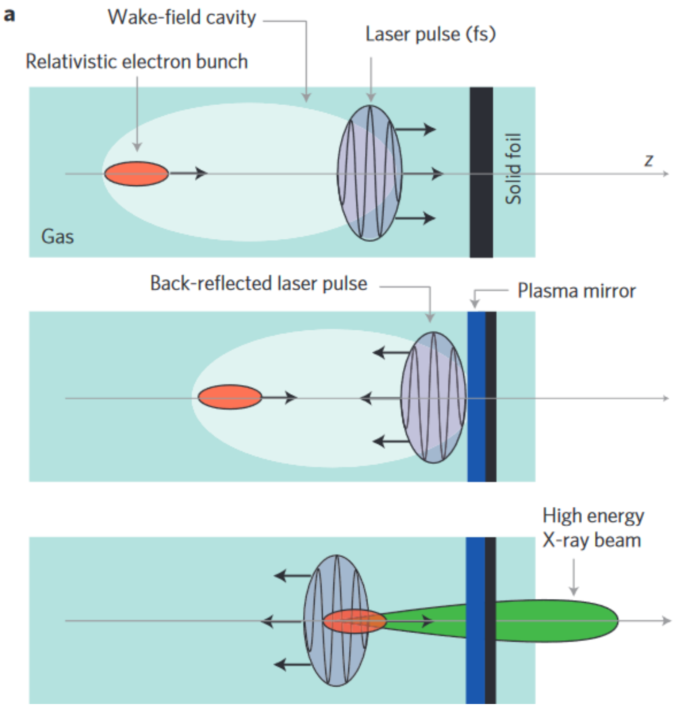

Figure A.1 – Principle of the all-optical Compton X-ray source from [188].

can support operation at high repetition rate. In this context we have carried out a study to investigate the feasibility of an inverse Compton scattering X-ray source using an over-critical gas target. The idea would be to use the sharp gradients induced by hydrodynamic shocks in supersonic flows to generate a 'gas plasma mirror' just after the electron acceleration zone. In a first instance, we study the feasibility of such a source by using analytical plasma profile with a critical density zone with gradients between 1-10 µm which could be achievable using hydrodynamic shocks. Laser-plasma interaction is modeled using FBPIC. In a second instance, we study the feasibility of such hydrodynamic structures providing a sub-critical plasma density of a few $10^{20}\,\mathrm{cm}^{-3}$ to accelerate electrons, followed by a sharp transition to overcritical density to reflect the laser using the CFD code FLUENT. The preliminary PIC study scanning density gradients and verifying that this scheme could provide X-rays in conditions similar (but optimistic, with double laser energy and starting from an already ionized plasma) to the one achieved in our experiment has been carried out by Daria Raspopova who was an intern in our group, supervised by Igor Andriyash at the time. Starting from her results I then looked at what we could reasonably expect with more realistic laser parameters and factoring ionization defocusing in simulations.

A.1 PIC simulations of a laser pulse reflected on a µm-scale over-critical density gradient

The typical plasma density profile used in the preliminary study, and then in my study is showed in Figure A.2. After a density up-ramp and a plateau at $n_e = 1.4 \times 10^{20}\,\mathrm{cm}^{-3}$, a density downramp to $n_e = 1.1 \times 10^{20}\,\mathrm{cm}^{-3}$ is used to inject electrons. Then there is a second plateau

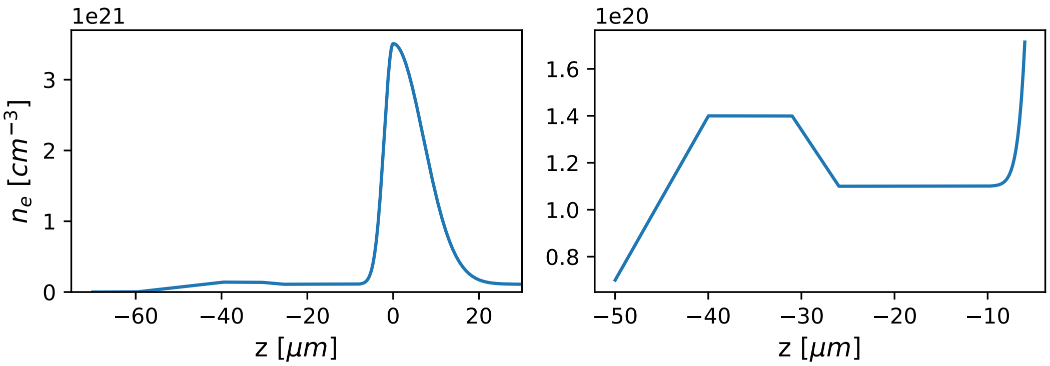

Figure A.2 – Left: Plasma density profile used in the PIC simulations, with a peak density $n_e = 2n_c$ and a steep gaussian profile with $\sigma = 3\,\mu m$. Right: Zoom on the injection and acceleration region.

to accelerate the injected electrons and finally, the density suddenly increases to $n_e = 2n_c$ with a gaussian up-ramp of variable width σ to reflect the laser pulse. The peak density has been set at $2n_c$ ($n_c = 1.7 \times 10^{21}\,\mathrm{cm}^{-3}$ at 800 nm at λ =800 nm) for two main reasons: (i) so that the density is critical even for the smaller wavelength of the broad spectrum (ii) for a given width of the up-ramp at $2n_c$, the effective width to reach n_c will thus be smaller.

In the preliminary study, the laser amplitude was set to $a_0 = 2.2$ with a waist $w_0 = 2\,\mu m$ and a pulse duration $\tau_{fwhm} = 5\,\mathrm{fs}$. The electrons were accelerated to energies between 5-20 MeV. The radiation of the electrons in the reflected laser field was computed using the software *Synchrad* developed by Igor Andriyash. This regime showed to be promising, with the generation of X-rays of a few keV, with wall gradients between 1-3 µm. The efficiency of the X-rays generation was showed to decrease for larger width of the gradient, but remained acceptable for $\sigma = 3\,\mu m$. Width smaller than 3 µm seems difficult to generate using hydrodynamic shocks, so we will use this a the minimum for the more realistic study. This preliminary study showed that an X-ray Compton source using a mJ-class laser and a density wall with a width potentially reachable using hydrodynamic shocks could be of interest. I then adapted this study to the actual laser parameters in Salle Noire 2.0 to see if this could be achieved with our experiment in its current form. These are the simulations results that will be presented in this section.

We simulate the propagation of a gaussian laser pulse with $a_0 = 1$, a waist $w_0 = 4.5\,\mu m$ and a duration $\tau_{fwhm} = 4\,\mathrm{fs}$, corresponding to an energy per pulse of 3.2 mJ. The plasma profile is chosen as showed in Fig. A.2, and the laser is focused at the end of the downramp at $z = -25\,\mu m$. The width σ of the gaussian up-ramp to critical density is varied among 3, 5 and 10 µm. The particles are initialized as neutral helium atoms, and ionization is computed using the ADK model.

Figure A.3 shows the wakefield, laser pulse and electrons in phase-space before and after the pulse being reflected by the overcritical plasma ($\sigma = 3\,\mu m$). The downward density transition triggers injection of electrons, not only in the first bucket of the plasma wave, but also in the following ones. This is particularly interesting in this case because a high charge will be more important than a high quality monoenergetic beam to generate a high brilliance X-ray source, but at the cost of a broader spectrum of emission. Additionally, because of the small plasma wavelength, the electrons injected in the first plasma bucket tend to overtake the laser pulse

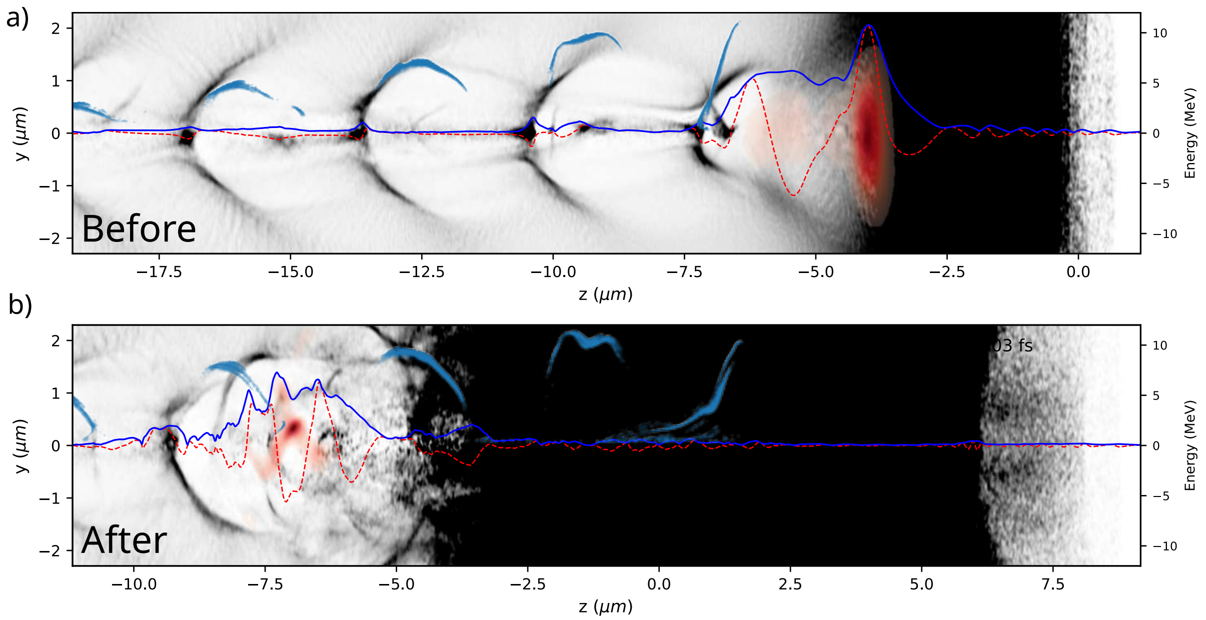

Figure A.3 – Plasma density (gray), laser on-axis electric field (red,dashed) and its envelope (solid,blue), laser intensity (red shaded area), and injected electrons in the (z, Ez) phase-space (a) before and (b) after the reflection of the laser on the critical plasma.

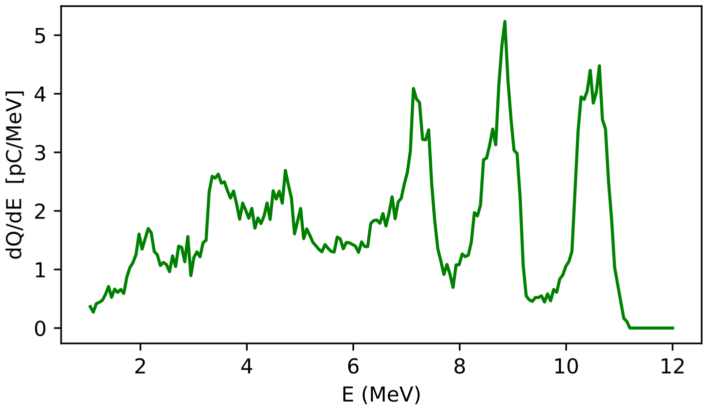

Figure A.4 – Spectrum of the electrons just before the laser reflection in the case $\sigma = 3\,\mu\text{m}$.

before it is reflected as it is strongly slowed down in the density up-ramp. We also observe that the back of the pulse is strongly redshifted in the near-critical density region, reaching approximately a 2 μm wavelength. In the bottom panel, we see that part of the beam has indeed been reflected, but the propagation in the near-critical part of the up-ramp has strongly degraded its profile. The peak on-axis amplitude of the reflected electric field is around 50% of the amplitude of the incident pulse. The energy spectrum of the electrons just before the reflection of the pulse is showed in Fig. A.4. There are notably three peaks at 7, 8.5 and 10.5 MeV corresponding respectively to the fourth, third and second plasma bucket. Electrons in the first bucket are injected slightly later and most of them do not have time to reach high energies. The total charge is 18 pC.

When crossing path with the reflected laser, the electrons oscillate in its electric field and radiate at a Doppler-shifted frequency. Using their trajectories, the light emitted is computed using *Synchrad*. The resulting spectrum and angular distribution of the light for the $\sigma = 3\,\mu\text{m}$ case is showed in Fig. A.5. The spectrum of the X-rays is peaked between 0.6 and 1.2 keV. The X-ray beam is relatively large, with a divergence of 50×80 mrad, and it is elongated and off-centered in the polarization direction (y). This could be caused by the reduced number of cycle in the laser pulse, leading to a preferred direction of irradiation depending on the value of the CEP of the pulse. The total number of photons in the beam is around 3.5×10^6. In the reference [188], the total photon number is measured to be 1×10^8 which is 30 times more, but if we consider the number of photons per second, now the kilohertz source would yield 35 times more than in [188], showing the interest this source could represent. Additionally, increasing the energy of the electrons to 15 or 20 MeV would not only increase the energy of the X-ray to several keV, but would also increase the photon yield of the source. In all cases, the peak energy of the X-rays is lower than we could expect with 10 MeV electrons, and the spectrum is broadband. This could be explained by three main reasons (i) the electron spectrum itself is broad with a significant amount of lower energy electrons (ii) the X-ray spectrum is integrated on the whole diverging beam, and equation A.1 indicates that the energy decreases with the angle of emission (iii) the laser is strongly redshifted which decreases the energy of the scattered photons.

Figure A.5c compares the X-ray yield when increasing the width of the transition to critical density. Increasing σ lowers the energy of the photons, but also the brightness of the source and photon number significantly. The performances for $\sigma = 10\,\mu\text{m}$ are largely degraded and the peak energy is now only 0.2 keV. This highlights the importance of achieving a profile with a steep gradient in order to reflect the laser.

A.2 Design of a potential gas plasma mirror using two colliding supersonic jets

To approach the desired plasma profile with a density plateau around 10^{20}cm^{-3} followed by a very steep over-critical density wall ($n_e > 1.7 \times 10^{21}\,\text{cm}^{-3}$) that will reflect the laser, we study a complex configuration of two tilted colliding supersonic nozzles with CFD simulations (FLUENT). The first one uses helium gas at moderate pressure (70 bar) and is designed to provide the density plateau at moderate density to accelerate electrons. The second nozzle is filled with nitrogen at high pressure (180 bar) and should provide an over-critical density. Both gas jets are de Laval, convergent-divergent nozzles with a throat diameter $\phi_t = 60\,\mu\text{m}$ and an exit diameter $\phi_e = 180\,\mu\text{m}$. The helium nozzle is tilted by 5° to the right, while the nitrogen nozzle is tilted by 15° to the left so that the two supersonic flows are colliding. The exit of both nozzles are separated by 100 µm. Figure A.6 shows that as the two supersonic flows collide, a double shock structure develops at their crossing, which notably results in a very steep transition to near-critical density ($n_{e,peak} = 1.5 \times 10^{21}\,\text{cm}^{-3}$) which could easily reach the critical density either by increasing slightly the nitrogen backing pressure or the throat diameter to increase the mass flux. The helium nozzle provides a density plateau at a density of $n_e > 7 \times 10^{19}\,\text{cm}^{-3}$ which also could be adjusted by increasing the backing pressure. This is followed by an intermediate density step to ($n_e > 1.8 \times 10^{20}\,\text{cm}^{-3}$) and a length of ∼15 µm due to the shock in helium before the large step in density towards critical values due to the shock in nitrogen.

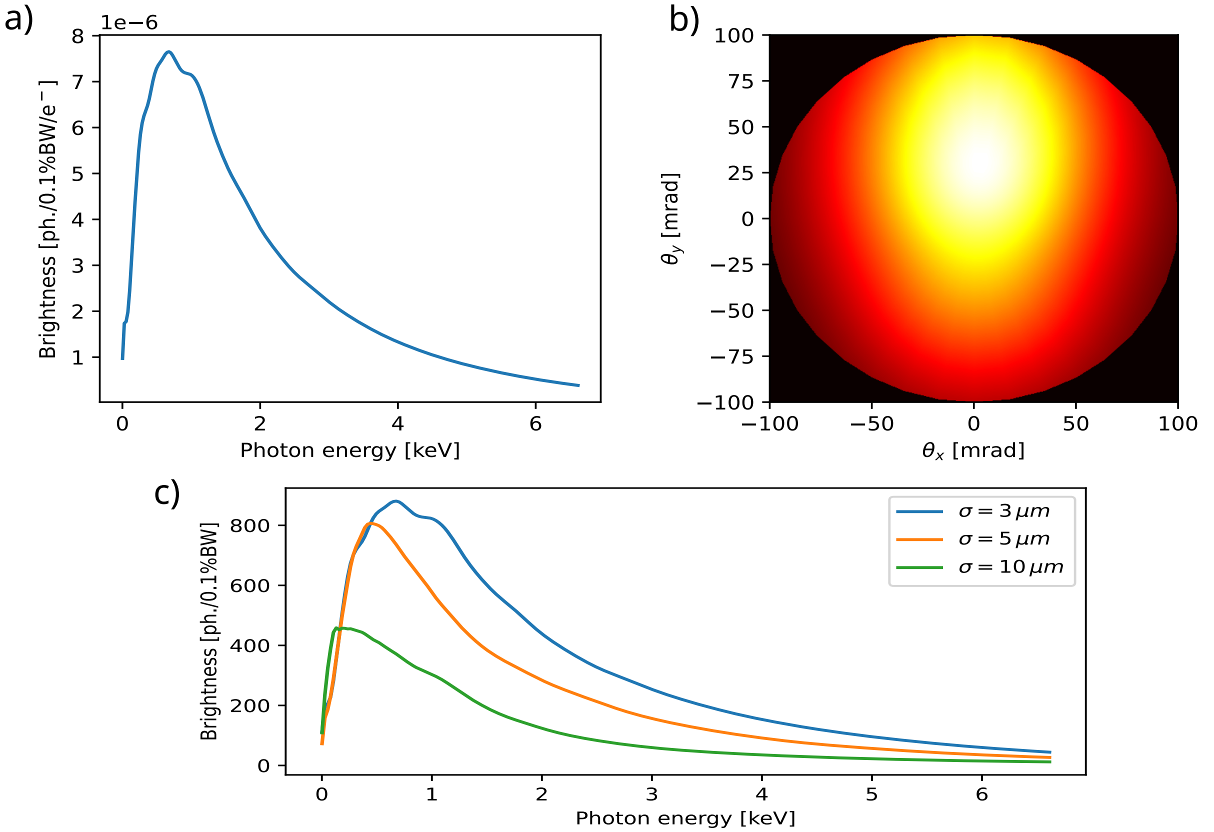

Figure A.5 – a) Brightness per electron of the radiated X-rays and b) Angular distribution of the X-rays in for $\sigma = 3\,\mu\text{m}$. c) Comparison of the total brightness for the three different up-ramp widths.

From afar, the density profile provided by this configuration (see Fig. A.6c) looks promising. Indeed, there is a zone of moderate plasma density around $10^{20}\,\text{cm}^{-3}$ followed by a steep step to critical density, but let us look at the parameters of this profile in more details. By fitting the critical density peak to a gaussian, we find $\sigma \simeq 10\,\mu\text{m}$. The impact of diverse parameters such as different tilt angles and the Mach number of the flows has been explored to reduce this gradient size, but no σ smaller than $10\,\mu\text{m}$ were ever obtained. As we have seen in the previous section, this size of gradient degrades significantly the quality of the X-ray source in a inverse Compton scattering configuration. Still, while it has been refined in this specific zone, the mesh resolution in the shock region is of the order of 2-3 μm. This is of the order of the expected shock dimensions, and therefore could lead to an overestimated shock width. But, with these 3D simulations, it is not possible to refine even more the mesh to a ∼1 μm size as the performance limit of the machine used to run the code have been reached, with the RAM fully used.

Another issue with this profile is the intermediate density plateau induced by the shock in helium. Indeed, if the density of the gas jet is set such as electrons are injected before this intermediate transition, then this plateau will be at relatively high density which will degrade the pulse and prevent a clean reflection afterwards. The pressure could also be set such as electrons are injected and accelerated on this plateau, but it is too short for them to reach sufficiently high energies before the density wall. This tends to indicate that this nozzle configuration, as it is,

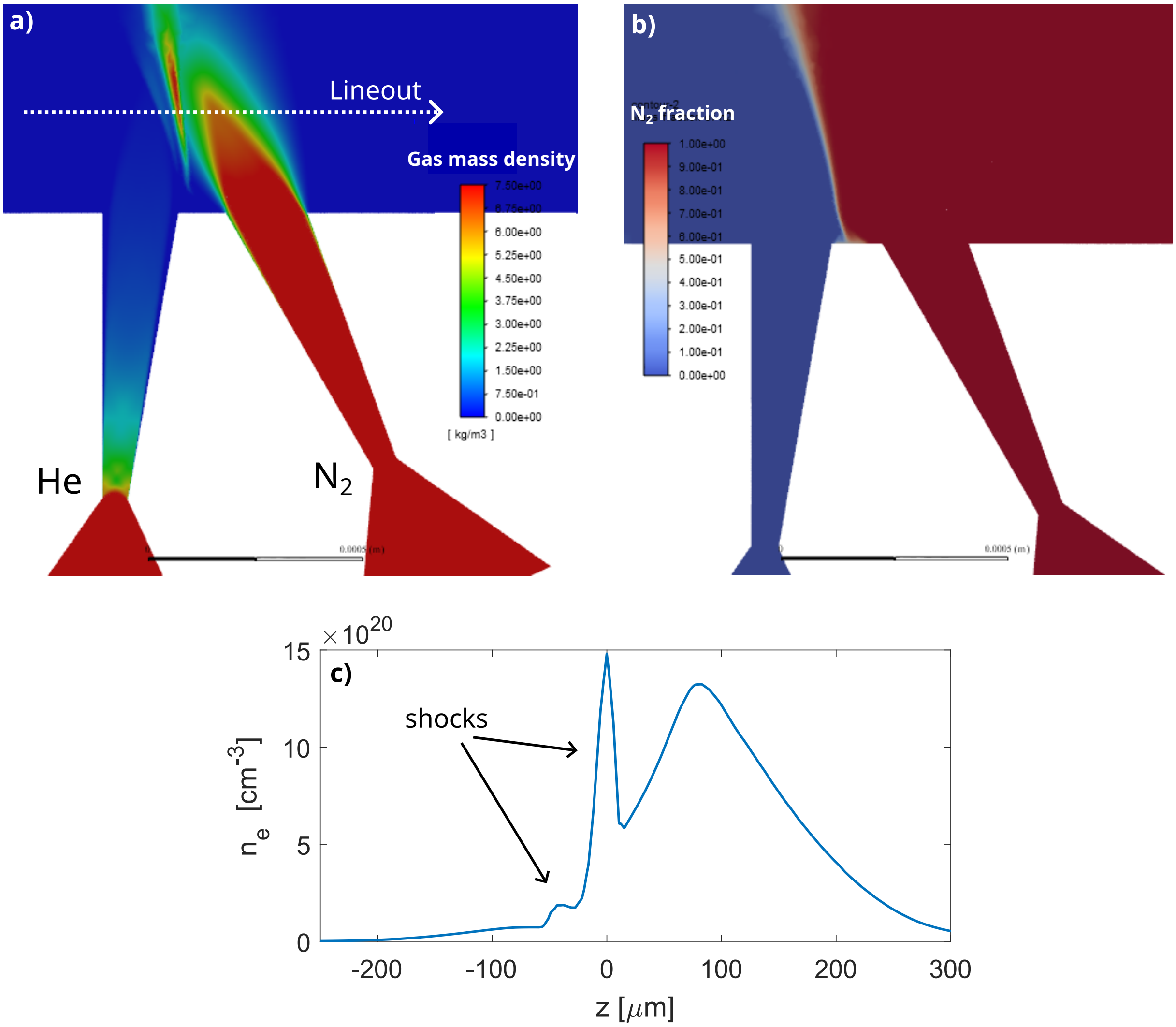

Figure A.6 – 3D CFD simulation with FLUENT of a double tilted jet configuration with helium with a backing pressure of 70 bar in the left nozzle, and nitrogen with a backing pressure of 180 bar in the right nozzle. a) Gas mass density in a centered 2D slice. b) Mass fraction of nitrogen in the 2D slice. c) Corresponding electron plasma density lineout at 250 µm from the nozzle exit (see lineout in first panel) after full ionization of helium and ionization of nitrogen up to N^{5+}.

does not provide sufficient condition to efficiently reflect the laser pulse and generate X-rays in a single-beam, inverse Compton scattering set-up. An alternative would be to use a liquid target [189] which could provide a plasma mirror at a sufficient repetition rate, with reduced pollution compared to solid targets, but still more than gas targets.

Conclusion

We have carried out a numerical feasibility study of an all-optical, single-beam inverse Compton X-ray source at high repetition rate using the few-mJ, few-cycle laser available at LOA. With PIC simulations, we have demonstrated that such a source could provide few-keV X-rays with good photon yield when taking into account the kilohertz repetition rate, while plasma mirrors of a few- µm gradient width which could potentially be achieved using gas targets. We have proposed a potential nozzle geometry to reach the desired plasma profile. It is based on two colliding supersonic flows with different gases. But while the general aspect of the gas profile looks promising, some specific parameters such as the steepness transition to critical density and an undesired density bump before this transitions are not suitable for this application. Further optimization of the gas profile, or a new geometry would be necessary to bring this idea to fruition.

Bibliography

[1] The Atlas Collaboration. “Observation of a new particle in the search for the Standard Model Higgs boson with the ATLAS detector at the LHC”. *Physics Letters B* 716.1 (2012), p. 1.

[2] P. Emma, R. Akre, J. Arthur, R. Bionta, C. Bostedt, J. Bozek, A. Brachmann, P. Bucksbaum, R. Coffee, F.-J. Decker, Y. Ding, D. Dowell, S. Edstrom, A. Fisher, J. Frisch, S. Gilevich, J. Hastings, G. Hays, Ph. Hering, Z. Huang, R. Iverson, H. Loos, M. Messerschmidt, A. Miahnahri, S. Moeller, H.-D. Nuhn, G Pile, D. Ratner, J. Rzepiela, D. Schultz, T. Smith, P. Stefan, H. Tompkins, J. Turner, J. Welch, W. White, J. Wu, G. Yocky, and J. Galayda. “First lasing and operation of an ångstrom-wavelength free-electron laser”. *Nature Photonics* 4.9 (2010), p. 641.

[3] C Kunz. *Synchrotron radiation: techniques and applications*. 1979.

[4] Vladimir A. Lobastov, Ramesh Srinivasan, and Ahmed H. Zewail. “Four-dimensional ultrafast electron microscopy”. *Proceedings of the National Academy of Sciences* 102.20 (2005), p. 7069.

[5] Germán Sciaini and R. J. Dwayne Miller. “Femtosecond electron diffraction: heralding the era of atomically resolved dynamics”. *Rep. Prog. Phys.* 74.9 (2011), p. 096101.

[6] R.W. Hamm and M.E. Hamm. *Industrial Accelerators And Their Applications*. 2012.

[7] T. Tajima and J. M. Dawson. “Laser Electron Accelerator”. *Phys. Rev. Lett.* 43.4 (1979), p. 267.

[8] D. Strickland and G. Mourou. “Compression of amplified chirped optical pulses”. *Opt. Comm.* 56 (1985), p. 219.

[9] C. A. Coverdale, C. B. Darrow, C. D. Decker, W. B. Mori, K.-C. Tzeng, K. A. Marsh, C. E. Clayton, and C. Joshi. “Propagation of intense subpicosecond laser pulses through underdense plasmas”. *Phys. Rev. Lett.* 74.23 (1995), p. 4659.

[10] A. Modena, A. E. Dangor, Z. Najmudin, C. E. Clayton, K. Marsh, C. Joshi, V. Malka, C. B. Darrow, D. Neely, and F. N. Walsh. “Electron acceleration from the breaking of electron plasma waves”. *Nature* 377 (1995), p. 606.

[11] D. Umstadter, S.-Y. Chen, A. Maksimchuk, G. Mourou, and R. Wagner. “Nonlinear optics in plasmas and laser wake field acceleration of electrons”. *Science* 273 (1996), p. 472.

[12] S. P. D. Mangles, C. D. Murphy, Z. Najmudin, A. G. R. Thomas, J. L. Collier, A. E. Dangor, E. J. Divall, P. S. Foster, J. G. Gallacher, C. J. Hooker, D. A. Jaroszynski, A. J. Langley, W. B. Mori, P. A. Norreys, F. S. Tsung, B. R. Walton, and K. Krushelnick. “Monoenergetic beams of relativistic electrons from intense laser-plasma interactions”. *Nature* 431 (2004), p. 535.

[13] C. G. R. Geddes, Cs. Toth, J. van Tilborg, E. Esarey, C. B. Schroeder, D. Bruhwiler, C. Nieter, J. Cary, and W. P. Leemans. "High-quality electron beams from a laser wakefield accelerator using plasma-channel guiding". *Nature* 431.7008 (2004), p. 538.

[14] J. Faure, Y. Glinec, A. Pukhov, S. Kiselev, S. Gordienko, E. Lefebvre, J.-P. Rousseau, F. Burgy, and V. Malka. "A laser–plasma accelerator producing monoenergetic electron beams". *Nature* 431.7008 (2004), p. 541.

[15] J. Faure, C. Rechatin, A. Norlin, A. Lifschitz, Y. Glinec, and V. Malka. "Controlled injection and acceleration of electrons in plasma wakefields by colliding laser pulses." *Nature* 444 (2006), p. 737.

[16] W. P. Leemans, B. Nagler, A. J. Gonsalves, Cs Tòth, K. Nakamura, C. G. R. Geddes, E. Esarey, C. B. Schroeder, and S. M. Hooker. "GeV electron beams from a centimetre-scale accelerator". *Nat. Phys.* 2 (2006), p. 696.

[17] A. J. Gonsalves, K. Nakamura, J. Daniels, C. Benedetti, C. Pieronek, T. C. H. de Raadt, S. Steinke, J. H. Bin, S. S. Bulanov, J. van Tilborg, C. G. R. Geddes, C. B. Schroeder, Cs. Tóth, E. Esarey, K. Swanson, L. Fan-Chiang, G. Bagdasarov, N. Bobrova, V. Gasilov, G. Korn, P. Sasorov, and W. P. Leemans. "Petawatt Laser Guiding and Electron Beam Acceleration to 8 GeV in a Laser-Heated Capillary Discharge Waveguide". *Phys. Rev. Lett.* 122.8 (2019), p. 084801.

[18] Wentao Wang, Ke Feng, Lintong Ke, Changhai Yu, Yi Xu, Rong Qi, Yu Chen, Zhiyong Qin, Zhijun Zhang, Ming Fang, Jiaqi Liu, Kangnan Jiang, Hao Wang, Cheng Wang, Xiaojun Yang, Fenxiang Wu, Yuxin Leng, Jiansheng Liu, Ruxin Li, and Zhizhan Xu. "Free-electron lasing at 27 nanometres based on a laser wakefield accelerator". *Nature* 595.7868 (2021), p. 516.

[19] Marie Labat, Jurjen Couperus Cadabag, Amin Ghaith, et al. "Seeded free-electron laser driven by a compact laser plasma accelerator". *Preprint* (2022).

[20] T. Kurz, T. Heinemann, M. F. Gilljohann, Y. Y. Chang, J. P. Couperus Cabadağ, A. Debus, O. Kononenko, R. Pausch, S. Schöbel, R. W. Assmann, M. Bussmann, H. Ding, J. Götzfried, A. Köhler, G. Raj, S. Schindler, K. Steiniger, O. Zarini, S. Corde, A. Döpp, B. Hidding, S. Karsch, U. Schramm, A. Martinez de la Ossa, and A. Irman. "Demonstration of a compact plasma accelerator powered by laser-accelerated electron beams". *Nature Communications* 12.1 (2021), p. 2895.

[21] John N Galayda. *The LCLS-II: A high power upgrade to the LCLS*. Tech. rep. SLAC National Accelerator Lab., (2018).

[22] Winfried Decking, Hans Weise, et al. "Commissioning of the European XFEL accelerator". In: *Proc. 8th Int. Particle Accelerator Conf.(IPAC'17)*. 8. (2017), p. 1.

[23] Z.-H. He, B. Hou, J. H. Easter, J. Faure, K. Krushelnick, J. A. Nees, and A. G. R. Thomas. "High repetition-rate wakefield electron source generated by few-millijoule, 30 femtosecond laser pulses on a density downramp". *New J. Phys.* 15 (2013), p. 053016.

[24] Z.-H. He, A. G. R. Thomas, B. Beaurepaire, J. A. Nees, B. Hou, V. Malka, K. Krushelnick, and J. Faure. "Electron diffraction using ultrafast electron bunches from a laser-wakefield accelerator at kHz repetition rate". *Appl. Phys. Lett.* 102.6 (2013), p. 064104.

[25] F. Salehi, A. J. Goers, G. A. Hine, L. Feder, D. Kuk, B. Miao, D. Woodbury, K. Y. Kim, and H. M. Milchberg. “MeV electron acceleration at 1kHz with <10mJ laser pulses”. *Opt. Lett.* 42.2 (2017), p. 215.

[26] D. Guénot, D. Gustas, A. Vernier, B. Beaurepaire, F. Böhle, M. Bocoum, M. Lozano, A. Jullien, R. Lopez-Martens, A. Lifschitz, and J. Faure. “Relativistic electron beams driven by kHz singel-cycle light pulses”. *Nature Photonics* 11 (2017), p. 293.

[27] A. Pukhov and J. Meyer-ter-Vehn. “Laser wake field acceleration: the highly non-linear broken-wave regime”. *Appl. Phys. B* 74 (2002), p. 355.

[28] E. N. Nerush and I. Yu. Kostyukov. “Carrier-Envelope Phase Effects in Plasma-Based Electron Acceleration with Few-Cycle Laser Pulses”. *Phys. Rev. Lett.* 103.3 (2009), p. 035001.

[29] Antonin Borot, Arnaud Malvache, Xiaowei Chen, Aurélie Jullien, Jean-Paul Geindre, Patrick Audebert, Gérard Mourou, Fabien Quéré, and Rodrigo Lopez-Martens. “Attosecond control of collective electron motion in plasmas”. *Nature Physics* 8.5 (2012), p. 416.

[30] Jonathan A Wheeler, Antonin Borot, Sylvain Monchocé, Henri Vincenti, Aurélien Ricci, Arnaud Malvache, Rodrigo Lopez-Martens, and Fabien Quéré. “Attosecond lighthouses from plasma mirrors”. *Nature Photon.* 6.12 (2012), p. 829.

[31] Dmitrii Kormin, Antonin Borot, Guangjin Ma, William Dallari, Boris Bergues, Márk Aladi, István B Földes, and Laszlo Veisz. “Spectral interferometry with waveform-dependent relativistic high-order harmonics from plasma surfaces”. *Nat. Commun.* 9.1 (2018), p. 1.

[32] DE Cardenas, TM Ostermayr, L Di Lucchio, L Hofmann, MF Kling, P Gibbon, J Shreiber, and L Veisz. “Sub-cycle dynamics in relativistic nanoplpasma acceleration”. *Sci. Rep.* 9 (2019), p. 7321.

[33] Olga Jahn, Vyacheslav E Leshchenko, Paraskevas Tzallas, Alexander Kessel, Mathias Krüger, Andreas Münzer, Sergei A Trushin, George D Tsakiris, Subhendu Kahaly, Dmitrii Kormin, et al. “Towards intense isolated attosecond pulses from relativistic surface high harmonics”. *Optica* 6.3 (2019), p. 280.

[34] Frederik Böhle, Maxence Thévenet, Maïmouna Bocoum, Aline Vernier, Stefan Haessler, and Rodrigo Lopez-Martens. “Generation of XUV spectral continua from relativistic plasma mirrors driven in the near-single-cycle limit”. *J. Phys. Photonics* 2.3 (2020), p. 034010.

[35] Dominykas Gustas. “High-repetition-rate relativistic electron acceleration in plasma wakefields driven by few-cycle laser pulses”. PhD thesis. 2018.

[36] J. Faure, D. Gustas, D. Guénot, A. Vernier, F. Böhle, M. Ouillé, S. Haessler, R. Lopez-Martens, and A. Lifschitz. “A review of recent progress on laser-plasma acceleration at kHz repetition rate”. *Plasma Phys. Control. Fusion* 61.1 (2018), p. 014012.

[37] Jared Maxson, David Cesar, Giacomo Calmasini, Alexander Ody, Pietro Musumeci, and David Alesini. “Direct Measurement of Sub-10 fs Relativistic Electron Beams with Ultralow Emittance”. *Phys. Rev. Lett.* 118.15 (2017), p. 154802.

[38] Fengfeng Qi, Zhuoran Ma, Lingrong Zhao, Yun Cheng, Wenxiang Jiang, Chao Lu, Tao Jiang, Dong Qian, Zhe Wang, Wentao Zhang, Pengfei Zhu, Xiao Zou, Weishi Wan, Dao Xiang, and Jie Zhang. "Breaking 50 Femtosecond Resolution Barrier in MeV Ultrafast Electron Diffraction with a Double Bend Achromat Compressor". *Phys. Rev. Lett.* 124.13 (2020), p. 134803.

[39] Hyun Woo Kim, Nikolay A. Vinokurov, In Hyung Baek, Key Young Oang, Mi Hye Kim, Young Chan Kim, Kyu-Ha Jang, Kitae Lee, Seong Hee Park, Sunjeong Park, Junho Shin, Jungwon Kim, Fabian Rotermund, Sunglae Cho, Thomas Feurer, and Young Uk Jeong. "Towards jitter-free ultrafast electron diffraction technology". *Nature Photonics* 14.4 (2020), p. 245.

[40] K. Ta Phuoc, S. Corde, C. Thaury, V. Malka, A. Tafzi, J.-P. Goddet, R. C.Shah, S. Sebban, and A. Rousse. "All-optical Compton gamma-ray source". *Nature Photonics* 6.5 (2012), p. 308.

[41] S. Chen, N. D. Powers, I. Ghebregziabher, C. M. Maharjan, C. Liu, G. Golovin, S. Banerjee, J. Zhang, N. Cunningham, A. Moorti, S. Clarke, S. Pozzi, and D. P. Umstadter. "MeV-Energy X Rays from Inverse Compton Scattering with Laser-Wakefield Accelerated Electrons". *Phys. Rev. Lett.* 110.15 (2013), p. 155003.

[42] S. Augst, D. Strickland, D. D. Meyerhofer, S. L. Chin, and J. H. Eberly. "Tunneling ionization of noble gases in a high-intensity laser field". *Phys. Rev. Lett.* 63.20 (1989), p. 2212.

[43] M. V. Ammosov, N. B. Delone, and V. P. Krainov. "Tunnel ionization of complex atoms and atomic ions by an alternating electromagnetic field". *Sov. Phys. JETP* 64 (1986), p. 1191.

[44] *CRC Handbook of Chemistry and Physics, 84th Edition Edited by David R. Lide (National Institute of Standards and Technology). CRC Press LLC: Boca Raton. 2003. 2616 pp. $139.95. ISBN 0-8493-0484-9.* Vol. 126. 5. 2004, p. 1586.

[45] V I Berezhiani and I G Murusidze. "Interaction of highly relativistic short laser pulses with plasmas and nonlinear wake-field generation". *Physica Scripta* 45.2 (1992), p. 87.

[46] E. Esarey, A. Ting, P. Sprangle, D. Umstadter, and X. Liu. "Nonlinear analysis of relativistic harmonic generation by intense lasers in plasmas". *IEEE Transactions on Plasma Science* 21.1 (1993), p. 95.

[47] W. Lu, M. Tzoufras, C. Joshi, F. S. Tsung, W. B. Mori, J. Vieira, R. A. Fonseca, and L. O. Silva. "Generating multi-GeV electron bunches using single stage laser wakefield acceleration in a 3D nonlinear regime". *Phys. Rev. ST Accel. Beams* 10.6 (2007), p. 061301.

[48] C. D. Decker, W. B. Mori, K. C. Tzeng, and T. Katsouleas. "The evolution of ultra-intense, short-pulse lasers in underdense plasmas". *Phys. Plasmas* 3.5 (1996), p. 2047.

[49] G. Sun, E. Ott, Y. C. Lee, and P. Guzdar. "Self-focusing of short intense pulses in plasmas". *Phys. Fluids* 30.2 (1987), p. 526.

[50] E. Esarey and M. Pilloff. "Trapping and acceleration in nonlinear plasma waves". *Phys. Plasmas* 2.5 (1995), p. 1432.

[51] C. B. Schroeder, E. Esarey, B. A. Shadwick, and W. P. Leemans. "Trapping, dark current, and wave breaking in nonlinear plasma waves". *Phys. Plasmas* 13.3 (2006), p. 033103.

[52] T. Katsouleas and W. B. Mori. “Wave-breaking amplitude of relativistic oscillations in a thermal plasma”. *Phys. Rev. Lett.* 61.1 (1988), p. 90.

[53] S. V. Bulanov, F. Pegoraro, A. M. Pukhov, and A. S. Sakharov. “Transverse-wake wave breaking”. *Phys. Rev. Lett.* 78.22 (1997), p. 4205.

[54] S. Corde, C. Thaury, A. Lifschitz, G. Lambert, K. Ta Phuoc, X. Davoine, R. Lehe, D. Douillet, A. Rousse, and V. Malka. “Observation of longitudinal and transverse self-injections in laser-plasma accelerators”. *Nat. Commun.* 4.1 (2013), p. 1501.

[55] I Kostyukov, E Nerush, A Pukhov, and V Seredov. “Electron self-injection in multidimensional relativistic-plasma wake fields”. *Phys. Rev. Lett.* 103.17 (2009), p. 175003.

[56] C. G. R. Geddes, Cs Tóth, J. van Tilborg, E. Esarey, C. B. Schroeder, D. Bruhwiler, C. Nieter, J. Cary, and W. P. Leemans. “High quality electron beams from a laser wakefield accelerator using plasma-channel guiding”. *Nature* 431 (2004), p. 538.

[57] S. Kalmykov, S. A. Yi, V. Khudik, and G. Shvets. “Electron Self-Injection and Trapping into an Evolving Plasma Bubble”. *Phys. Rev. Lett.* 103.13 (2009), p. 135004.

[58] S. Bulanov, N. Naumova, F. Pegoraro, and J. Sakai. “Particle injection into the wave acceleration phase due to nonlinear wake wave breaking”. *Phys. Rev. E* 58.5 (1998), R5257.

[59] A. V. Brantov, T. Zh. Esirkepov, M. Kando, H. Kotaki, V. Yu. Bychenkov, and S. V. Bulanov. “Controlled electron injection into the wake wave using plasma density inhomogeneity”. *Phys. Plasmas* 15.7 (2008), p. 073111.

[60] C. G. R. Geddes, K. Nakamura, G. R. Plateau, Cs Tóth, E. Cormier-Michel, E. Esarey, C. B. Schroeder, J. R. Cary, and W. P. Leemans. “Plasma-Density-Gradient Injection of Low Absolute-Momentum-Spread Electron Bunches”. *Phys. Rev. Lett.* 100 (2008), p. 215004.

[61] J. Faure, C. Rechatin, O. Lundh, L. Ammoura, and V. Malka. “Injection and acceleration of quasimonoenergetic relativistic electron beams using density gradients at the edges of a plasma channel”. *Phys. Plasmas* 17.8 (2010), p. 083107.

[62] K. Schmid, A. Buck, C. M. S. Sears, J. M. Mikhailova, R. Tautz, D. Herrmann, M. Geissler, F. Krausz, and L. Veisz. “Density-transition based electron injector for laser driven wakefield accelerators”. *Phys. Rev. ST Accel. Beams* 13.9 (2010), p. 091301.

[63] C. Thaury, E. Guillaume, A. Lifschitz, K. Ta Phuoc, M. Hansson, G. Grittani, J. Gautier, J.-P. Goddet, A. Tafzi, O. Lundh, and V. Malka. “Shock assisted ionization injection in laser-plasma accelerators”. *Scientific Reports* 5.1 (2015), p. 16310.

[64] K. K. Swanson, H.-E. Tsai, S. K. Barber, R. Lehe, H.-S. Mao, S. Steinke, J. van Tilborg, K. Nakamura, C. G. R. Geddes, C. B. Schroeder, E. Esarey, and W. P. Leemans. “Control of tunable, monoenergetic laser-plasma-accelerated electron beams using a shock-induced density downramp injector”. *Phys. Rev. Accel. Beams* 20.5 (2017), p. 051301.

[65] Min Chen, Zheng-Ming Sheng, Yan-Yun Ma, and Jie Zhang. “Electron injection and trapping in a laser wakefield by field ionization to high-charge states of gases”. *Journal of Applied Physics* 99.5 (2006), p. 056109.

[66] A. Pak, K. A. Marsh, S. F. Martins, W. Lu, W. B. Mori, and C. Joshi. “Injection and Trapping of Tunnel-Ionized Electrons into Laser-Produced Wakes”. *Phys. Rev. Lett.* 104.2 (2010), p. 025003.

[67] C. McGuffey, A. G. R. Thomas, W. Schumaker, T. Matsuoka, V. Chvykov, F. J. Dollar, G. Kalintchenko, V. Yanovsky, A. Maksimchuk, K. Krushelnick, V. Yu. Bychenkov, I. V. Glazyrin, and A. V. Karpeev. “Ionization Induced Trapping in a Laser Wakefield Accelerator”. *Phys. Rev. Lett.* 104.2 (2010), p. 025004.

[68] M. Chen, E. Esarey, C. B. Schroeder, C. G. R. Geddes, and W. P. Leemans. “Theory of ionization-induced trapping in laser-plasma accelerators”. *Physics of Plasmas* 19.3 (2012), p. 033101.

[69] S. C. Rae. “Ionisation-induces defocusing of intense laser-pulses in high-pressure gases”. *Opt. Comm.* 97.1 (1993), p. 25.

[70] B. Beaurepaire, A. Lifschitz, and J. Faure. “Electron acceleration in sub-relativistic wakefields driven by few-cycle laser pulses”. *New J. Phys.* 16 (2014), p. 023023.

[71] I. H. Malitson. “Interspecimen Comparison of the Refractive Index of Fused Silica∗,†”. *J. Opt. Soc. Am.* 55.10 (1965), p. 1205.

[72] W. B. Mori. “The physics of the nonlinear optics of plasmas at relativistic intensities for short-pulse lasers”. *IEEE J. Quant. Elec.* 33.11 (1997), p. 1942.

[73] P. Sprangle, C.-H. Tang, and E. Esarey. “Relativistic self-focusing of short-pulse radiation beams in plasmas”. *IEEE Trans. Plasma Sci.* PS-15.2 (1987), p. 145.

[74] C. Ren, B. J. Duda, R. G. Hemker, W. B. Mori, T. Katsouleas, T. M. Antonsen Jr, and P. Mora. “Compressing and focusing of a short laser pulse by a thin plasma lens”. *Phys. Rev. E* 63.2 (2001), p. 26411.

[75] F. S. Tsung, C. Ren, L. O. Silva, W. B. Mori, and T. Katsouleas. “Generation of ultra-intense single-cycle laser pulses by using photon deceleration”. *Proc. Nat. Acad. Science* 99.1 (2002), p. 29.

[76] J. Faure, Y. Glinec, J. J. Santos, F. Ewald, J.-P. Rousseau, S. Kiselev, A. Pukhov, T. Hosokai, and V. Malka. “Observation of laser pulse shortening in nonlinear plasma waves”. *Phys. Rev. Lett.* 95 (2005), p. 205003.

[77] P. Chessa, E. De Wispelaere, F. Dorchies, V. Malka, J.-R. Marquès, G. Hamoniaux, P. Mora, and F. Amiranoff. “Temporal and angular resolution of the ionization-induced refraction of a short laser pulse in a Helium gas”. *Phys. Rev. Lett.* 82.3 (1999), p. 552.

[78] Julius Huijts, Igor A Andriyash, Lucas Rovige, Aline Vernier, and Jérôme Faure. “Identifying observable carrier-envelope phase effects in laser wakefield acceleration with near-single-cycle pulses”. *Physics of Plasmas* 28.4 (2021), p. 043101.

[79] Michael Geissler, Jörg Schreiber, and Jürgen Meyer-ter-Vehn. “Bubble acceleration of electrons with few-cycle laser pulses”. *New Journal of Physics* 8.9 (2006), p. 186.

[80] Alexei Zhidkov, Takashi Fujii, and Koshichi Nemoto. “Electron self-injection during interaction of tightly focused few-cycle laser pulses with underdense plasma”. *Phys. Rev. E* 78.3 (2008), p. 036406.

[81] David H. Whittum, William M. Sharp, Simon S. Yu, Martin Lampe, and Glenn Joyce. “Electron-hose instability in the ion-focused regime”. *Phys. Rev. Lett.* 67.8 (1991), p. 991.

[82] P. Sprangle, J. Krall, and E. Esarey. “Hose-modulation instability of intense laser pulses in plasmas”. *Phys. Rev. Lett.* 73 (1994), p. 3544.

[83] Jihoon Kim, Tianhong Wang, Vladimir Khudik, and Gennady Shvets. "Subfemtosecond Wakefield Injector and Accelerator Based on an Undulating Plasma Bubble Controlled by a Laser Phase". *Phys. Rev. Lett.* 127.16 (2021), p. 164801.

[84] A. F. Lifschitz and V. Malka. "Optical phase effects in electron wakefield acceleration using few-cycle laser pulses". *New J. Phys.* 14.5 (2012), p. 053045.

[85] G.A. Mourou, N.M. Naumova, E.P. Power, V. Yanovsky, and J.A. Nees. "Relativistic optics in the lambda-cubed regime and applications to attosecond physics". In: *CLEO/Europe. 2005 Conference on Lasers and Electro-Optics Europe, 2005.* 2005, p. 691.

[86] Marie Ouillé. "Génération d'impulsions laser proches du cycle optique en durée pour l'interaction laser-matière relativiste à haute cadence". PhD Thesis. Institut Polytechnique de Paris, 2022.

[87] Marie Ouillé, Aline Vernier, Frederik Böhle, Maïmouna Bocoum, Aurélie Jullien, Magali Lozano, Jean-Philippe Rousseau, Zhao Cheng, Dominykas Gustas, Andreas Blumenstein, Peter Simon, Stefan Haessler, Jérôme Faure, Tamas Nagy, and Rodrigo Lopez-Martens. "Relativistic-intensity near-single-cycle light waveforms at kHz repetition rate". *Light. Sci. Appl.* 9.1 (2020), p. 1.

[88] Aurélie Jullien, Olivier Albert, Frédéric Burgy, Guy Hamoniaux, Jean-Philippe Rousseau, Jean-Paul Chambaret, Frédérika Augé-Rochereau, Gilles Chériaux, Jean Etchepare, Nikolay Minkovski, and Solomon M. Saltiel. "10^{10} temporal contrast for femtosecond ultraintense lasers by cross-polarized wave generation". *Opt. Lett.* 30.8 (2005), p. 920.

[89] M. Nisoli, S. De Silvestri, O. Svelto, R. Szipöcs, K. Ferencz, Ch Spielmann, S. Sartania, and F. Krausz. "Compression of high-energy laser pulses below 5 fs". *Opt. Lett.* 22 (1997), p. 522.

[90] S. Sartania, Z. Cheng, M. Lenzner, G. Tempea, Ch. Spielmann, F. Krausz, and K. Ferencz. "Generation of 0.1-TW 5-fs optical pulses at a 1-kHz repetition rate". *Opt. Lett.* 22.20 (1997), p. 1562.

[91] Akira Suda, Masatoshi Hatayama, Keigo Nagasaka, and Katsumi Midorikawa. "Generation of sub-10-fs, 5-mJ-optical pulses using a hollow fiber with a pressure gradient". *Applied Physics Letters* 86.11 (2005), p. 111116.

[92] Miguel Miranda, Cord L. Arnold, Thomas Fordell, Francisco Silva, Benjamín Alonso, Rosa Weigand, Anne L'Huillier, and Helder Crespo. "Characterization of broadband few-cycle laser pulses with the d-scan technique". *Opt. Express* 20.17 (2012), p. 18732.

[93] Esmerando Escoto, Ayhan Tajalli, Tamas Nagy, and Günter Steinmeyer. "Advanced phase retrieval for dispersion scan: a comparative study". *J. Opt. Soc. Am. B* 35.1 (2018), p. 8.

[94] L. Xu, Ch. Spielmann, A. Poppe, T. Brabec, F. Krausz, and T. W. Hänsch. "Route to phase control of ultrashort light pulses". *Opt. Lett.* 21.24 (1996), p. 2008.

[95] Jörn Stenger and Harald R. Telle. "Intensity-induced mode shift in a femtosecond laser by a change in the nonlinear index of refraction". *Opt. Lett.* 25.20 (2000), p. 1553.

[96] Masayuki Kakehata, Hideyuki Takada, Yohei Kobayashi, Kenji Torizuka, Yoshihiko Fujihira, Tetsuya Homma, and Hideo Takahashi. "Single-shot measurement of carrier-envelope phase changes by spectral interferometry". *Opt. Lett.* 26.18 (2001), p. 1436.

[97] Fabian Lücking, Vincent Crozatier, Nicolas Forget, Andreas Assion, and Ferenc Krausz. "Approaching the limits of carrier-envelope phase stability in a millijoule-class amplifier". *Opt. Lett.* 39.13 (2014), p. 3884.

[98] S. Agostinelli et al. "Geant4—a simulation toolkit". *Nuclear Instruments and Methods in Physics Research Section A: Accelerators, Spectrometers, Detectors and Associated Equipment* 506.3 (2003), p. 250.

[99] Y. Glinec, J. Faure, A. Guemnie-Tafo, V. Malka H. Monard, J. P. Larbre, V. De Waele, J. L. Marignier, and M. Mostafavi. "Absolute calibration for a broad range single shot electron spectrometer". *Rev. Sci. Instrum.* 77 (2006), p. 103301.

[100] K Halbach and R F Holsinger. "SUPERFISH - a computer program for evaluation of rf cavities with cylindrical symmetry". *Part. Accel.* 7 (1976), p. 213.

[101] S. Semushin and V. Malka. "High density gas jet nozzle design for laser target production". *Rev. Sci. Instrum.* 72 (2001), p. 2961.

[102] G. Pretzier, H. Jäger, T. Neger, H. Philipp, and J. Woisetschläger. "Comparison of Different Methods of Abel Inversion Using Computer Simulated and Experimental Side-On Data". *Zeitschrift für Naturforschung A* 47.9 (1992), p. 955.

[103] Björn Landgraf, Michael Schnell, Alexander Sävert, Malte C. Kaluza, and Christian Spielmann. "High resolution 3D gas-jet characterization". *Review of Scientific Instruments* 82.8 (2011), p. 083106.

[104] L. Rovige, J. Huijts, A. Vernier, I. Andriyash, F. Sylla, V. Tomkus, V. Girdauskas, G. Raciukaitis, J. Dudutis, V. Stankevic, P. Gecys, and J. Faure. "Symmetric and asymmetric shocked gas jets for laser-plasma experiments". *Review of Scientific Instruments* 92.8 (2021), p. 083302.

[105] J. Primot and L. Sogno. "Achromatic three-wave (or more) lateral shearing interferometer". *J. Opt. Soc. Am. A* 12.12 (1995), p. 2679.

[106] Jérôme Primot and Nicolas Guérineau. "Extended Hartmann test based on the pseudoguiding property of a Hartmann mask completed by a phase chessboard". *Applied optics* 39.31 (2000), p. 5715.

[107] R.D. Zucker and O. Biblarz. *Fundamentals of Gas Dynamics*. 2002.

[108] John M. Dawson. "Particle simulation of plasmas". *Rev. Mod. Phys.* 55.2 (1983), p. 403.

[109] Boris J. P. "Relativistic plasma simulation-optimization of a hybrid code". *Proc. 4th Conf. Num. Sim. Plasmas* (1970), p. 3.

[110] Rémi Lehe, Manuel Kirchen, Igor A. Andriyash, Brendan B. Godfrey, and Jean-Luc Vay. "A spectral, quasi-cylindrical and dispersion-free Particle-In-Cell algorithm". *Comput. Phys. Commun.* 203 (2016), p. 66.

[111] A. F. Lifschitz, X. Davoine, E. Lefebvre, J. Faure, C. Rechatin, and V. Malka. "Particle-in-Cell modelling of laser–plasma interaction using Fourier decomposition". *J. Comp. Phys.* 228 (2009), p. 1803.

[112] Kane Yee. "Numerical solution of initial boundary value problems involving maxwell's equations in isotropic media". *IEEE Transactions on Antennas and Propagation* 14.3 (1966), p. 302.

[113] Brendan B Godfrey. "Numerical Cherenkov instabilities in electromagnetic particle codes". *Journal of Computational Physics* 15.4 (1974), p. 504.

[114] R. Lehe, A. Lifschitz, C. Thaury, V. Malka, and X. Davoine. "Numerical growth of emittance in simulations of laser-wakefield acceleration". *Phys. Rev. ST Accel. Beams* 16.2 (2013), p. 021301.

[115] Igor A. Andriyash, Remi Lehe, and Agustin Lifschitz. "Laser-plasma interactions with a Fourier-Bessel particle-in-cell method". *Physics of Plasmas* 23.3 (2016), p. 033110.

[116] P. Tomassini, M. Galimberti, A. Giulietti, D. Giulietti, L. A. Gizzi, L. Labate, and F. Pegoraro. "Production of high-quality electron beams in numerical experiments of laser wakefield acceleration with longitudinal wave breaking". *Phys. Rev. ST Accel. Beams* 6.12 (2003), p. 121301.

[117] H. Suk, N. Barov, J. B. Rosenzweig, and E. Esarey. "Plasma Electron Trapping and Acceleration in a Plasma Wake Field Using a Density Transition". *Phys. Rev. Lett.* 86.6 (2001), p. 1011.

[118] J. U. Kim, N. Hafz, and H. Suk. "Electron trapping and acceleration across a parabolic plasma density profile". *Phys. Rev. E* 69.2 (2004), p. 026409.

[119] J. Ferri, S. Corde, A. Döpp, A. Lifschitz, A. Doche, C. Thaury, K. Ta Phuoc, B. Mahieu, I. A. Andriyash, V. Malka, and X. Davoine. "High-Brilliance Betatron γ-Ray Source Powered by Laser-Accelerated Electrons". *Phys. Rev. Lett.* 120.25 (2018), p. 254802.

[120] Xing-Long Zhu, Min Chen, Su-Ming Weng, Tong-Pu Yu, Wei-Min Wang, Feng He, Zheng-Ming Sheng, Paul McKenna, Dino A. Jaroszynski, and Jie Zhang. "Extremely brilliant GeV γ-rays from a two-stage laser-plasma accelerator". *Science Advances* 6.22 (2020), eaaz7240.

[121] Vidmantas Tomkus, Valdas Girdauskas, Juozas Dudutis, Paulius Gečys, Valdemar Stankevič, Gediminas Račiukaitis, Isabel Gallardo González, Diego Guénot, Jonas Björklund Svensson, Anders Persson, and Olle Lundh. "Laser wakefield accelerated electron beams and betatron radiation from multijet gas targets". *Scientific Reports* 10.1 (2020), p. 16807.

[122] T. Katsouleas. "Physical mechanisms in the plasma wake-field accelerator". *Phys. Rev. A* 33.3 (1986), p. 2056.

[123] P. Sprangle, B. Hafizi, J. R. Peñano, R. F. Hubbard, A. Ting, C. I. Moore, D. F. Gordon, A. Zigler, D. Kaganovich, and T. M. Antonsen. "Wakefield generation and GeV acceleration in tapered plasma channels". *Phys. Rev. E* 63.5 (2001), p. 056405.

[124] E. Guillaume, A. Döpp, C. Thaury, K. Ta Phuoc, A. Lifschitz, G. Grittani, J.-P. Goddet, A. Tafzi, S. W. Chou, L. Veisz, and V. Malka. "Electron Rephasing in a Laser-Wakefield Accelerator". *Phys. Rev. Lett.* 115.15 (2015), p. 155002.

[125] J. Osterhoff, A. Popp, Zs Major, B. Marx, T. P. Rowlands-Rees, M. Fuchs, M. Geissler, R. Hörlein, B. Hidding, S. Becker, E. A. Peralta, U. Schramm, F. Grüner, D. Habs, F. Krausz, S. M. Hooker, and S. Karsch. "Generation of Stable, Low-Divergence Electron Beams by Laser-Wakefield Acceleration in a Steady-State-Flow Gas Cell". *Phys. Rev. Lett.* 101.8 (2008), p. 085002.

[126] T.-Y. Chien, C.-L. Chang, C.-H. Lee, J.-Y. Lin, J. Wang, and S.-Y. Chen. "Spatially Localized Self-Injection of Electrons in a Self-Modulated Laser-Wakefield Accelerator by Using a Laser-Induced Transient Density Ramp". *Phys. Rev. Lett.* 94.11 (2005), p. 115003.

[127] A. Buck, J. Wenz, J. Xu, K. Khrennikov, K. Schmid, M. Heigoldt, J. M. Mikhailova, M. Geissler, B. Shen, F. Krausz, S. Karsch, and L. Veisz. "Shock-Front Injector for High-Quality Laser-Plasma Acceleration". *Phys. Rev. Lett.* 110.18 (2013), p. 185006.

[128] L. Fan-Chiang, H.-S. Mao, H.-E. Tsai, T. Ostermayr, K. K. Swanson, S. K. Barber, S. Steinke, J. van Tilborg, C. G. R. Geddes, and W. P. Leemans. "Gas density structure of supersonic flows impinged on by thin blades for laser–plasma accelerator targets". *Physics of Fluids* 32.6 (2020), p. 066108.

[129] Florian Mollica. "Interaction laser-plasma ultra-intense à densité proche-critique pour l'accélération d'ions." Theses. Université Paris Saclay (COmUE), 2016.

[130] K. Schmid and L. Veisz. "Supersonic gas jets for laser-plasma experiments". *Rev. Sci. Intstrum.* 84 (2012), p. 053304.

[131] D. Gustas, D. Guénot, A. Vernier, S. Dutt, F. Böhle, R. Lopez-Martens, A. Lifschitz, and J. Faure. "High-charge relativistic electron bunches from a kHz laser-plasma accelerator". *Phys. Rev. Accel. Beams* 21.1 (2018), p. 013401.

[132] H.W. Liepmann and A. Roshko. *Elements of Gas Dynamics*. Dover Books on Aeronautical Engineering. 2013.

[133] Richard Courant and Kurt Otto Friedrichs. *Supersonic flow and shock waves*. Vol. 21. 1999.

[134] David C Wilcox et al. *Turbulence modeling for CFD*. Vol. 2. 1998.

[135] Florian Menter. "Zonal two equation kw turbulence models for aerodynamic flows". In: *23rd fluid dynamics, plasmadynamics, and lasers conference*. 1993, p. 2906.

[136] Andrius Marcinkevičius, Saulius Juodkazis, Mitsuru Watanabe, Masafumi Miwa, Shigeki Matsuo, Hiroaki Misawa, and Junji Nishii. "Femtosecond laser-assisted three-dimensional microfabrication in silica". *Opt. Lett., OL* 26.5 (2001), p. 277.

[137] Vidmantas Tomkus, Valdas Girdauskas, Juozas Dudutis, Paulius Gečys, Valdemar Stankevič, and Gediminas Račiukaitis. "High-density gas capillary nozzles manufactured by hybrid 3D laser machining technique from fused silica". *Opt. Express, OE* 26.21 (2018), p. 27965.

[138] B. Beaurepaire, A. Vernier, M. Bocoum, F. Böhle, A. Jullien, J-P. Rousseau, T. Lefrou, D. Douillet, G. Iaquaniello, R. Lopez-Martens, A. Lifschitz, and J. Faure. "Effect of the Laser Wave Front in a Laser-Plasma Accelerator". *Phys. Rev. X* 5 (2015), p. 031012.

[139] L. Rovige, J. Huijts, I. A. Andriyash, A. Vernier, M. Ouillé, Z. Cheng, T. Asai, Y. Fukuda, V. Tomkus, V. Girdauskas, G. Raciukaitis, J. Dudutis, V. Stankevic, P. Gecys, R. Lopez-Martens, and J. Faure. "Optimization and stabilization of a kilohertz laser-plasma accelerator". *Physics of Plasmas* 28.3 (2021), p. 033105.

[140] S. Gordienko and A. Pukhov. "Scalings for ultrarelativistic laser plasmas and quasimonoenergetic electrons". *Phys. Plasmas* 12 (2005), p. 043109.

[141] J. Osterhoff, A. Popp, Zs. Major, B. Marx, T. P. Rowlands-Rees, M. Fuchs, R. Hörlein, F. Grüner, D. Habs, F. Krausz, S. M. Hooker, and S. Karsch. “Stable Laser-Driven Electron Beams from a Steady-State-Flow Gas Cell”. *AIP Conference Proceedings* 1086.1 (2009), p. 125.

[142] Andreas R. Maier, Niels M. Delbos, Timo Eichner, Lars Hübner, Sören Jalas, Laurids Jeppe, Spencer W. Jolly, Manuel Kirchen, Vincent Leroux, Philipp Messner, Matthias Schnepp, Maximilian Trunk, Paul A. Walker, Christian Werle, and Paul Winkler. “Decoding Sources of Energy Variability in a Laser-Plasma Accelerator”. *Phys. Rev. X* 10.3 (2020), p. 031039.

[143] L. Rovige, J. Huijts, I. Andriyash, A. Vernier, V. Tomkus, V. Girdauskas, G. Raciukaitis, J. Dudutis, V. Stankevic, P. Gecys, M. Ouille, Z. Cheng, R. Lopez-Martens, and J. Faure. “Demonstration of stable long-term operation of a kilohertz laser-plasma accelerator”. *Phys. Rev. Accel. Beams* 23.9 (2020), p. 093401.

[144] J. Faure, B. van der Geer, B. Beaurepaire, G. Gallé, A. Vernier, and A. Lifschitz. “Concept of a laser-plasma-based electron source for sub-10-fs electron diffraction”. *Phys. Rev. Accel. Beams* 19.2 (2016), p. 021302.

[145] Y. Ma, D. Seipt, S. J. D. Dann, M. J. V. Streeter, C. A. J. Palmer, L. Willingale, and A. G. R. Thomas. “Angular streaking of betatron X-rays in a transverse density gradient laser-wakefield accelerator”. *Physics of Plasmas* 25.11 (2018), p. 113105.

[146] Daniel E. Mittelberger, Maxence Thévenet, Kei Nakamura, Anthony J. Gonsalves, Carlo Benedetti, Joost Daniels, Sven Steinke, Rémi Lehe, Jean-Luc Vay, Carl B. Schroeder, Eric Esarey, and Wim P. Leemans. “Laser and electron deflection from transverse asymmetries in laser-plasma accelerators”. *Phys. Rev. E* 100.6 (2019), p. 063208.

[147] B. B. Pollock, F. S. Tsung, F. Albert, J. L. Shaw, C. E. Clayton, A. Davidson, N. Lemos, K. A. Marsh, A. Pak, J. E. Ralph, W. B. Mori, and C. Joshi. “Formation of Ultrarelativistic Electron Rings from a Laser-Wakefield Accelerator”. *Phys. Rev. Lett.* 115.5 (2015), p. 055004.

[148] T. Z. Zhao, K. Behm, C. F. Dong, X. Davoine, S. Y. Kalmykov, V. Petrov, V. Chvykov, P. Cummings, B. Hou, A. Maksimchuk, J. A. Nees, V. Yanovsky, A. G. R. Thomas, and K. Krushelnick. “High-Flux Femtosecond X-Ray Emission from Controlled Generation of Annular Electron Beams in a Laser Wakefield Accelerator”. *Phys. Rev. Lett.* 117.9 (2016), p. 094801.

[149] Benoit Beaurepaire. “Développement d’un accélérateur laser-plasma à haut taux de répétition pour des applications à la diffraction ultra-rapide d’électrons”. Theses. Université Paris Saclay (COmUE), 2016.

[150] F Salehi, M Le, L Railing, M Kolesik, and HM Milchberg. “Laser-Accelerated, Low-Divergence 15-MeV Quasimonoenergetic Electron Bunches at 1 kHz”. *Physical Review X* 11.2 (2021), p. 021055.

[151] Marco Cavallone. “Application of laser-plasma accelerated beams to high dose-rate radiation biology”. Theses. Institut Polytechnique de Paris, 2020.

[152] Marco Cavallone, Lucas Rovige, Julius Huijts, Émilie Bayart, Rachel Delorme, Aline Vernier, Patrik Gonçalves Jorge, Raphaël Moeckli, Eric Deutsch, Jérôme Faure, and Alessandro Flacco. "Dosimetric characterisation and application to radiation biology of a kHz laser-driven electron beam". *Applied Physics B* 127.4 (2021), p. 57.

[153] Jones Bleddyn and Morgan David AL. "4-Radiotherapy fractionation". In: *Radiobiological Modelling in Radiation Oncology*. 2015, p. 51.

[154] Vincent Favaudon, Laura Caplier, Virginie Monceau, Frédéric Pouzoulet, Mano Sayarath, Charles Fouillade, Marie-France Poupon, Isabel Brito, Philippe Hupé, Jean Bourhis, Janet Hall, Jean-Jacques Fontaine, and Marie-Catherine Vozenin. "Ultrahigh dose-rate FLASH irradiation increases the differential response between normal and tumor tnumber in mice". *Science Translational Medicine* 6.245 (2014), 245ra93.

[155] Jean Bourhis, Wendy Jeanneret Sozzi, Patrik Gonçalves Jorge, Olivier Gaide, Claude Bailat, Fréderic Duclos, David Patin, Mahmut Ozsahin, François Bochud, Jean-François Germond, Raphaël Moeckli, and Marie-Catherine Vozenin. "Treatment of a first patient with FLASH-radiotherapy". *Radiotherapy and Oncology* 139 (2019), p. 18.

[156] William F Morgan and Marianne B Sowa. "Effects of ionizing radiation in nonirradiated cells". *Proceedings of the National Academy of Sciences* 102.40 (2005), p. 14127.

[157] Gabriel Adrian, Elise Konradsson, Michael Lempart, Sven Bäck, Crister Ceberg, and Kristoffer Petersson. "The FLASH effect depends on oxygen concentration". *The British Journal of Radiology* 93.1106 (2020), p. 20190702.

[158] Pierre Montay-Gruel, Lydia Meziani, Chakradhar Yakkala, and Marie-Catherine Vozenin. "Expanding the therapeutic index of radiation therapy by normal tnumber protection". *The British Journal of Radiology* 92.1093 (2019), p. 20180008.

[159] Jean Bourhis, Pierre Montay-Gruel, Patrik Gonçalves Jorge, Claude Bailat, Benoît Petit, Jonathan Ollivier, Wendy Jeanneret-Sozzi, Mahmut Ozsahin, François Bochud, Raphaël Moeckli, Jean-François Germond, and Marie-Catherine Vozenin. "Clinical translation of FLASH radiotherapy: Why and how?" *Radiotherapy and Oncology* 139 (2019), p. 11.

[160] Maria Grazia Andreassi, Andrea Borghini, Silvia Pulignani, Federica Baffigi, Lorenzo Fulgentini, Petra Koester, Monica Cresci, Cecilia Vecoli, Debora Lamia, Giorgio Russo, et al. "Radiobiological effectiveness of ultrashort laser-driven electron bunches: Micronucleus frequency, telomere shortening and cell viability". *Radiation research* 186.3 (2016), p. 245.

[161] Lydia Laschinsky, Michael Baumann, Elke Beyreuther, Wolfgang Enghardt, Malte Kaluza, Leonhard Karsch, Elisabeth Lessmann, Doreen Naumburger, Maria Nicolai, Christian Richter, et al. "Radiobiological effectiveness of laser accelerated electrons in comparison to electron beams from a conventional linear accelerator". *Journal of Radiation Research* (2012), p. 11080.

[162] Melanie Oppelt, Michael Baumann, Ralf Bergmann, Elke Beyreuther, Kerstin Brüchner, Josefin Hartmann, Leonhard Karsch, Mechthild Krause, Lydia Laschinsky, Elisabeth Leßmann, et al. "Comparison study of in vivo dose response to laser-driven versus conventional electron beam". *Radiation and environmental biophysics* 54.2 (2015), p. 155.

[163] LA Gizzi, L Labate, F Baffigi, F Brandi, GC Bussolino, L Fulgentini, P Koester, D Palla, and F Rossi. "Laser–plasma acceleration of electrons for radiobiology and radiation sources". *Nuclear Instruments and Methods in Physics Research Section B: Beam Interactions with Materials and Atoms* 355 (2015), p. 241.

[164] Elke Beyreuther, Wolfgang Enghardt, Malte Kaluza, Leonhard Karsch, Lydia Laschinsky, Elisabeth Lessmann, Maria Nicolai, Jörg Pawelke, Christian Richter, Roland Sauerbrey, et al. "Establishment of technical prerequisites for cell irradiation experiments with laser-accelerated electrons". *Medical physics* 37.4 (2010), p. 1392.

[165] Maria Nicolai, Alexander Sävert, Maria Reuter, Michael Schnell, Jens Polz, Oliver Jäckel, Leonhard Karsch, Michael Schürer, Melanie Oppelt, Jörg Pawelke, et al. "Realizing a laser-driven electron source applicable for radiobiological tumor irradiation". *Applied Physics B* 116.3 (2014), p. 643.

[166] E. Bayart, A. Flacco, O. Delmas, L. Pommarel, D. Levy, M. Cavallone, F. Megnin-Chanet, E. Deutsch, and V. Malka. "Fast dose fractionation using ultra-short laser accelerated proton pulses can increase cancer cell mortality, which relies on functional PARP1 protein". *Scientific Reports* 9.1 (2019), p. 10132.

[167] K H Chadwick and H P Leenhouts. "A molecular theory of cell survival". *Physics in Medicine and Biology* 18.1 (1973), p. 78.

[168] Albrecht M. Kellerer and Harald H. Rossi. "A Generalized Formulation of Dual Radiation Action". *Radiation Research* 75.3 (1978), p. 471.

[169] Eric J Hall, Amato J Giaccia, et al. *Radiobiology for the Radiologist*. Vol. 6. 2006.

[170] L. Pommarel, B. Vauzour, F. Mégnin-Chanet, E. Bayart, O. Delmas, F. Goudjil, C. Nauraye, V. Letellier, F. Pouzoulet, F. Schillaci, F. Romano, V. Scuderi, G. A. P. Cirrone, E. Deutsch, A. Flacco, and V. Malka. "Spectral and spatial shaping of a laser-produced ion beam for radiation-biology experiments". *Phys. Rev. Accel. Beams* 20.3 (2017), p. 032801.

[171] Dominykas Gustas. "High-repetition-rate relativistic electron acceleration in plasma wakefields driven by few-cycle laser pulses". PhD thesis. 2018.

[172] J. Faure, D. Gustas, D. Guénot, A. Vernier, F. Böhle, M. Ouillé, S. Haessler, R. Lopez-Martens, and A. Lifschitz. "A review of recent progress on laser-plasma acceleration at kHz repetition rate". *Plasma Physics and Controlled Fusion* 61.1 (2019), p. 014012.

[173] Julius Huijts, Lucas Rovige, Igor A. Andriyash, Aline Vernier, Marie Ouillé, Jaismeen Kaur, Zhao Cheng, Rodrigo Lopez-Martens, and Jérôme Faure. "Waveform Control of Relativistic Electron Dynamics in Laser-Plasma Acceleration". *Phys. Rev. X* 12.1 (2022), p. 011036.

[174] Lucas Rovige, Joséphine Monzac, Julius Huijts, Igor A. Andriyash, Aline Vernier, Jaismeen Kaur, Marie Ouillé, Zhao Cheng, Vidmantas Tomkus, Valdas Girdauskas, Gediminas Raciukaitis, Juozas Dudutis, Valdemar Stankevic, Paulius Gecys, Rodrigo Lopez-Martens, and Jérôme Faure. "Carrier-envelope phase controlled dynamics of relativistic electron beams in a laser-wakefield accelerator". *The European Physical Journal Special Topics* (2022).

[175] Jihoon Kim, Tianhong Wang, Vladimir Khudik, and Gennady Shvets. "Subfemtosecond Wakefield Injector and Accelerator Based on an Undulating Plasma Bubble Controlled by a Laser Phase". *Phys. Rev. Lett.* 127.16 (2021), p. 164801.

[176] MJ De Loos and SB Van Der Geer. "General Particle Tracer: A new 3D code for accelerator and beamline design". In: *5th European Particle Accelerator Conference*. 1996, p. 1241.

[177] A. E. Siegmann. *Lasers*. Mill Valey, 1986.

[178] L. Cicchitelli, H. Hora, and R. Postle. "Longitudinal field components for laser beams in vacuum". *Phys. Rev. A* 41.7 (1990), p. 3727.

[179] B. Quesnel and P. Mora. "Theory and simulation of the interaction of ultra-intense laser pulses with electrons in vacuum". *Phys. Rev. E* 58 (1998), p. 3719.

[180] A. Myers, A. Almgren, L.D. Amorim, J. Bell, L. Fedeli, L. Ge, K. Gott, D.P. Grote, M. Hogan, A. Huebl, R. Jambunathan, R. Lehe, C. Ng, M. Rowan, O. Shapoval, M. Thévenet, J.-L. Vay, H. Vincenti, E. Yang, N. Zaïm, W. Zhang, Y. Zhao, and E. Zoni. "Porting WarpX to GPU-accelerated platforms". *Parallel Computing* 108 (2021), p. 102833.

[181] A. Pellegrina, A. Jeandet, L. Lavenu, S. Ricaud, C. Simon-Boisson, A. Vernier, A. Flacco, and J. Faure. "High average power TiSa amplifier for high energy, high repetition rate laser plasma accelerator". In: *Optica High-brightness Sources and Light-driven Interactions Congress 2022*. 2022, HW4B.6.

[182] Frederic V Hartemann. *High-field electrodynamics*. 2001.

[183] S. Corde, K. Ta Phuoc, G. Lambert, R. Fitour, V. Malka, and A. Rousse. "Femtosecond X-rays from laser-plasma accelerators". *Rev. Mod. Phys.* 85 (2013), p. 0034.

[184] R. W. Schoenlein, W. P. Leemans, A. H. Chin, P. Volfbeyn, T. E. Glover, P. Balling, M. Zolotorev, K.-J. Kim, S. Chattopadhyay, and C. V. Shank. "Femtosecond X-ray Pulses at 0.4 Angstroms Generated by 90 degrees Thomson Scattering: A Tool for Probing the Structural Dynamics of Materials". *Science* 274.5285 (1996), p. 236.

[185] W.P. Leemans, R.W. Schoenlein, P. Volfbeyn, A.H. Chin, T.E. Glover, P. Balling, M. Zolotorev, K.-J. Kim, S. Chattopadhyay, and C.V. Shank. "Interaction of relativistic electrons with ultrashort laser pulses: generation of femtosecond X-rays and microprobing of electron beams". *IEEE Journal of Quantum Electronics* 33.11 (1997), p. 1925.

[186] H. Schwoerer, B. Liesfeld, H.-P. Schlenvoigt, K.-U. Amthor, and R. Sauerbrey. "Thomson-Backscattered X Rays From Laser-Accelerated Electrons". *Phys. Rev. Lett.* 96 (1 2006), p. 014802.

[187] F. V. Hartemann, D. J. Gibson, W. J. Brown, A. Rousse, K. Ta Phuoc, V. Mallka, J. Faure, and A. Pukhov. "Compton scattering x-ray sources driven by laser wakefield acceleration". *Phys. Rev. ST Accel. Beams* 10 (1 2007), p. 011301.

[188] K. Ta Phuoc, S. Corde, C. Thaury, V. Malka, A. Tafzi, J. P. Goddet, R. C. Shah, S. Sebban, and A. Rousse. "All-optical Compton gamma-ray source". *Nature Photonics* 6.5 (2012), p. 308.

[189] Sterling Backus, Henry C. Kapteyn, Margaret M. Murnane, David M. Gold, Howard Nathel, and William White. "Prepulse suppression for high-energy ultrashort pulses using self-induced plasma shuttering from a fluid target". *Opt. Lett.* 18.2 (1993), p. 134.

Publications and presentations

Publications

- **L. Rovige**, J. Monzac, J. Huijts, I. A. Andriyash, A. Vernier, J. Kaur, M. Ouillé, Z. Cheng, V. Tomkus, V. Girdauskas, G. Raciukaitis, J. Dudutis, V. Stankevic, P. Gecys, R. Lopez-Martens, and J. Faure. *Carrier-envelope phase controlled dynamics of relativistic electron beams in a laser-wakefield accelerator.* Eur. Phys. J. Spec. Top. (2022)
- J. Huijts*, **L. Rovige***, I. A. Andriyash, A. Vernier, M. Ouillé, J. Kaur, Z. Cheng, R. Lopez-Martens, and J. Faure. *Waveform control of relativistic electron dynamics in laser-plasma acceleration.* Physical Review X, 12, 011036 (2022). *co-first authors
- **L. Rovige**, J. Huijts, I. A. Andriyash, A. Vernier, M. Ouillé, Z. Cheng, T. Asai, Y. Fukuda, V. Tomkus, V. Girdauskas, G. Raciukaitis, J. Dudutis, V. Stankevic, P. Gecys, R. Lopez-Martens, and J. Faure. *Optimization and stabilization of a kilohertz laser-plasma accelerator.* Physics of Plasmas, 28, 033105. (2021)
- **L. Rovige**, J. Huijts, A. Vernier, I. Andriyash, F. Sylla, V. Tomkus, V. Girdauskas, G. Raciukaitis, J. Dudutis, V. Stankevic, P. Gecys, and J. Faure. *Symmetric and asymmetric shocked gas jets for laser-plasma experiments.* Review of Scientific Instruments, 92, 083302. (2021)
- **L. Rovige**, J. Huijts, I. Andriyash, A. Vernier, V. Tomkus, V. Girdauskas, G. Raciukaitis, J. Dudutis, V. Stankevic, P. Gecys, M. Ouille, Z. Cheng, R. Lopez-Martens, and J. Faure. *Demonstration of stable long-term operation of a kilohertz laser-plasma accelerator.* Phys. Rev. Accel. Beams, 23, 093401. (2020)
- M. Cavallone, **L. Rovige**, J. Huijts, É. Bayart, R. Delorme, A. Vernier, P. Gonçalves Jorge, R. Moeckli, E. Deutsch, J. Faure and A. Flacco. *Dosimetric characterisation and application to radiation biology of a kHz laser-driven electron beam.* Applied Physics B, 127, 57. (2021)
- J. Huijts, I. A. Andriyash, **L. Rovige**, A. Vernier, J. Faure. *Identifying observable carrier-envelope phase effects in laser wakefield acceleration with near-single-cycle pulses.* Physics of Plasmas, 28, 043101. (2021)

Presentations

— **L. Rovige**, J. Huijts, J. Monzac, I. A. Andriyash, A. Vernier, J. Kaur, M. Ouillé, Z. Cheng, R. Lopez-Martens, and J. Faure. 2022. Carrier-envelope phase control of a kilohertz laser-wakefield accelerator. Oral presentation : EuroNNAc Special Topics Workshop, Portoferraio, Italy.

— **L. Rovige**, J. Huijts, J. Monzac, I. A. Andriyash, A. Vernier, J. Kaur, M. Ouillé, Z. Cheng, R. Lopez-Martens, and J. Faure. *et al.* 2022. Carrier-envelope phase controlled electron dynamics in a laser-wakefield accelerator. Oral presentation : 48^{th} EPS Plasma Conference, Online.

— **L. Rovige**, J. Huijts, I. Andriyash, A. Vernier, V. Tomkus, V. Girdauskas, G. Raciukaitis, J. Dudutis, V. Stankevic, P. Gecys, M. Ouille, Z. Cheng, R. Lopez-Martens, and J. Faure. 2021. Kilohertz laser-plasma acceleration : long-term stability and control of CEP effects. Oral presentation : 11^{e} Forum interaction laser-plasma, Belgodère, France.

— **L. Rovige**, J. Huijts, I. Andriyash, A. Vernier, V. Tomkus, V. Girdauskas, G. Raciukaitis, J. Dudutis, V. Stankevic, P. Gecys, M. Ouille, Z. Cheng, R. Lopez-Martens, and J. Faure. 2021. Optimization and long-term stability of a kHz laser-plasma accelerator. Seminar: LPA Online seminars.

— **L. Rovige** J. Huijts, A. Vernier, and J. Faure. 2019. Micrometric gas jets for high-repetition rate laser-wakefield acceleration. Oral presentation: GDR APPEL workshop on targets for laser-plasma experiments. Orsay, France.

ECOLE
DOCTORALE

Titre : Optimisation, stabilisation et contrôle via la phase optique d'un accélérateur laser-plasma à haut taux de répétition

Mots clés : accélérateur laser-plasma, faisceaux d'électrons, phase optique, kilohertz, haute intensité

Résumé : Cette thèse de doctorat présente un travail expérimental sur le développement d'un accélérateur laser-plasma à haut taux de répétition (kHz) utilisant des impulsions laser de quelques milijoules, et de durée proche du cycle optique. Nous explorons un large ensemble de paramètres expérimentaux pour optimiser l'accélérateur en contrôlant la densité et le profil plasma, la durée des impulsions, le type de gaz et le mécanisme d'injection utilisés dans les expériences. Nous démontrons une amélioration significative des performances, notamment avec d'importants progrès réalisés sur la stabilité et la fiabilité à long terme de l'accélérateur, avec un fonctionnement continu et stable de l'accélérateur pendant plusieurs heures, accumulant un record de 18 millions de tirs consécutifs. Ce gain de stabilité est obtenu en utilisant un nouveau type de jet de gaz qui utilise un choc hydrodynamique oblique permettant l'injection d'électrons dans le gradient de densité de la région choquée. L'énergie typique du faisceau d'électrons a également été augmentée d'un facteur deux, jusqu'à 8 MeV, tandis que des divergences mono-tir du faisceau d'électrons aussi faibles que 3mrad sont obtenues en utilisant de l'hélium au lieu de l'azote pour créer le plasma. Nous présentons ensuite les résultats d'une première expérience d'application en radiobiologie où notre accélérateur est utilisé pour irradier des cellules cancéreuses, en profitant de la stabilité nouvellement acquise.

Dans un second temps, nous étudions les spécificités de l'interaction des impulsions de durée proche du cycle optique avec un plasma sous-dense se produisant dans notre accélérateur, principalement par l'effet de la phase porteuse-enveloppe (CEP). Nous observons et contrôlons expérimentalement pour la première fois les effets de la CEP dans un accélérateur laser-plasma, qui se manifestent notamment par une dépendance du pointé du faisceau d'électrons à la phase optique du laser. Des variations de charge significatives (jusqu'à 30%) lorsque l'on change la valeur de la CEP sont également observées dans certains cas. En effectuant des simulations particle-in-cell, nous expliquons ces effets par une injection périodique hors axe de plusieurs sous-faisceaux d'électrons déclenchée par l'oscillation transverse de l'asymétrie de l'onde plasma dans la direction de polarisation du laser due au glissement de la CEP pendant la propagation.

Title : Optimization, stabilization and optical phase control of a high-repetition rate laser-wakefield accelerator

Keywords : laser-plasma accelerator, electron beams, carrier-envelope phase, kilohertz, high intensity

Abstract : This PhD thesis presents experimental work on the development of a high-repetition rate (kHz) laser-wakefield accelerator using few milijoules, near-single cycle laser pulses. We explore a large set of experimental parameters to optimize the accelerator by controlling the plasma density and profile, pulse duration, type of gas and injection mechanism used in experiments. We demonstrate significant performances improvement, notably with progress made on the long-term stability and reliability of the accelerator with continuous and stable operation of the accelerator for several hours accumulating a record of 18 million consecutive shots. We achieve this gain in stability by using a newly designed type of gas target resulting in an asymmetric hydrodynamic oblique shock enabling injection in the downward density transition of the shocked region. The typical electron beam energy has also been increased by a factor of two, up to 8 MeV, while a single-shot beam divergence as low as 3mrad is achieved using helium instead of nitrogen to form the plasma. We then present the results of a first application experiment in radiobiology where our accelerator is used to irradiate cancerous cells, taking advantage of the newly acquired stability. Secondly, we study the specificities of the interaction of near-single cycle pulses with an underdense plasma that occurs in our accelerator, mainly through the effect of the carrier-envelope phase (CEP). We observe and control experimentally for the first time CEP effects in a laser-wakefield accelerator, that manifest through a dependence of the electron beam pointing to the laser initial optical phase. We also show significant (up to 30%) charge variations in some cases when changing the value of the CEP. By carrying out particle-in-cell simulations, we explain these effects by the periodic off-axis injection of several electron sub-bunches triggered by the transverse oscillations of the asymmetry of the plasma wave in the laser polarization direction due to the CEP shifting during propagation.

Institut Polytechnique de Paris
91120 Palaiseau, France